CIVIL ENGINEERING JOURNAL

číslo 2/2021

Obsah:

CIVIL ENGINEERING JOURNAL

Article no. 28

THE CIVIL ENGINEERING JOURNAL 2-2021

STUDY ON ADJUSTABLE CONNECTOR OF RECIPROCAL FRAME

Lin Qi, Zifei Li, Lingtong Li, Hui Pan, Zhenzhou Xie and Xin Huang

Civil Aviation University of China, Tianjin, China; qilin1208@vip.163.com

ABSTRACT

In this paper, we design an adjustable connector of reciprocal frame, and a three-dimensional solid model of this connector with Circular Hollow Section has been created in the FEM software Abaqus CAE to study its mechanical properties. When the plastic hinge is formed at the end of the Circular Hollow Section, the connector is still in an elastic state. It is concluded that the adjustable connector of reciprocal frame has high strength and rigidity, realizing the goal for designing higher connector strength over Circular Hollow Section strength. Then parametric analysis is used to analyse the influence of the connector about each part on the mechanical properties, and the flexural rigidity of the connector has been derived. A three-dimensional wire model of reciprocal frames has been created in the FEM software Abaqus CAE, and a full-scale test model of the structure is designed. The numerical simulation results agree well with the test results. It is verified that the reliability of the modeling method and the accuracy of the connector mechanical model.

KEYWORD

Reciprocal frame, Connector of reciprocal frame, Numerical model of connector, Mechanical model of connector, Full-scale test

INTRODUCTION

Reciprocal frame is a special structure [1]. In reciprocal frames, members are mutually supported, to be more specific, a member supports an adjacent counterpart and is supported by another in return [2-4]. Figure1 indicates a common circular reciprocal frame [4]. Thanks to its unique and mutually supported feature, the members and connectors of reciprocal frame are in a simple and unified structure [5]. Therefore, reciprocal frame can simplify the on-site assembling process and draws an extensive attention in the field of prefabricated building [6-8].

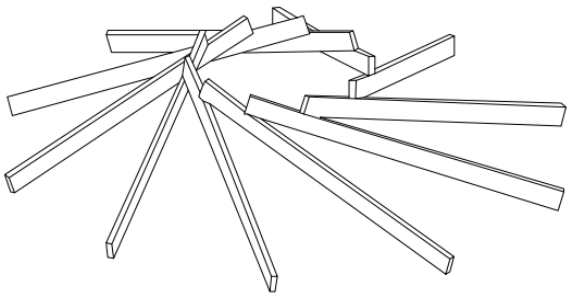

Fig. 1 - A circular reciprocal frame

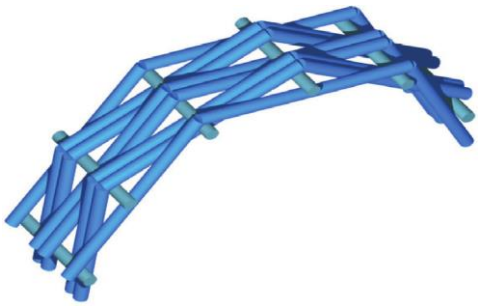

Fig.2 - Model of Chinese laminated beam bridge

Due to the unique construction nature of reciprocal frame, the function of connector is attached with great importance. The stability and reliability of a reciprocal frame directly influence its

performance. Reciprocal frame has various types of joints. Figure 2 is a model of laminated beam bridge in ancient China [9], and Figure 3 shows an example of woven closed geodesic basket [10]. The joints of the two reciprocal frame models mentioned above are inter-locked, depending on the frictional force to ensure the strong connection of whole frame. The connection process of this friction-driven joints is simple, but the strength and rigidity of the joints are weak which proposes limitation on the size of reciprocal frame [11-13]. New methods of connection such as lashed connection (Figure 4.) and notched connection (Figure 5.) have appeared with the advancement of reciprocal frame. However, because of the weak strength and rigidity of these two methods, the strength and rigidity of reciprocal frame are greatly reduced at the same time [14-15] New methods of connection such as lashed connection (Figure 4.) and notched connection (Figure 5.) have appeared with the advancement of reciprocal frame. However, because of the weak strength and rigidity of these two methods, the strength and rigidity of reciprocal frame are greatly reduced at the same time [14-15].

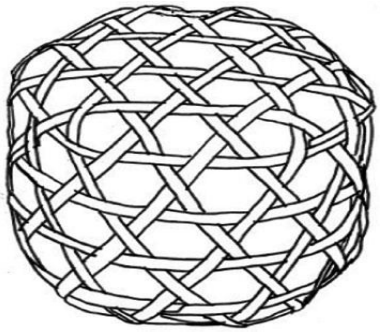

Fig.3 - Woven closed basket

Fig. 4 - Lashed connections

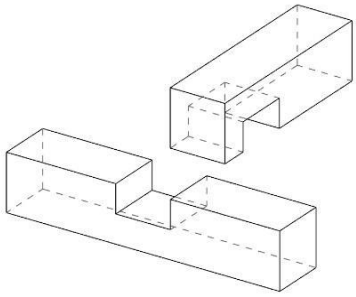

Fig. 5 - Notched connection

In 1976, Bijnen published the first patent concerning with reciprocal frame's connector Bolted Connectors [16]. He suggested to loop steel pipes via threaded pins to form a closed-circuit structure. As can be seen from Figure 6, the joint is achieved in a simple way, and the strength and rigidity are high. On the contrary, this connector requires high accuracy in terms of connecting threaded pins and reserved holes. As a result, it presents difficulties for on-site construction and reduces construction efficiency. Moreover, two members connected by one threaded pin can rotate around the pin, affecting the rigidity of the entire structure [17-18]. In recent years, temporary reciprocal-frame buildings have received wide attention, and the application of scaffolding swivel couplers can be observed in reciprocal frame (Figure 7). Scaffolding swivel coupler has great tolerance for error, but this connector is of little strength and rigidity. It is mostly used for temporary buildings as it is difficult to ensure the stability, rigidity and seismic performance of the structure [19-20] Figure 8 is an example of coupler connector [14]. Coupler connector owns the features of large strength and rigidity and high construction accuracy. What is more, it can only be applied to vertically connected members, and the application scope of its connector is limited as well [15].

Fig. 6 - Bolted connectors

Fig. 7 - Scaffolding swivel couplers

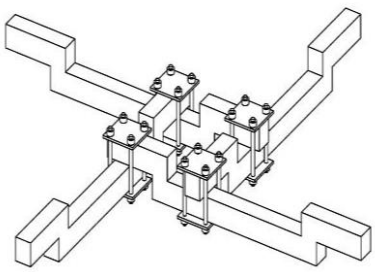

Fig.8 - Coupler connectors

In conclusion, though there are various types of connections of reciprocal frame, most of them face the issues of poor strength and rigidity or limited application scope. Consequently, it is crucial to conduct studies on exploring new types of reciprocal frame connector of better strength and rigidity and wider application scope.

ADJUSTABLE CONNECTOR OF RECIPROCAL FRAME

In order to overcome the connector of reciprocal frame's existing problems of low strength and rigidity and small range of application, this paper designs an adjustable connector of reciprocal frame with higher strength and rigidity, and this connector can compensate for the installation error of the reciprocal frame members. As shown in Figure 9, the connector consists of upper and lower semi-connectors, each of which is composed of a sleeve (1), a nut (2) and a connecting plate (3) with four arc-shaped holes.

The inner diameter of the sleeve fits with the outer diameter of the Circular Hollow Section. Besides, a certain length of thread is machined on the outer walls of both ends of the Circular Hollow Section for adjusting the relative position between Circular Hollow Section and sleeve when there are errors in the freedom of the point during installation and therefore the member bar and sleeve can be tightened by nut.

The connecting plates of the upper and lower hemi-connectors are connected by bolts that pass through the arc-shaped holes on the connecting plate. Since the arc-shaped connecting hole is larger than the diameter of the bolt rod, the upper and lower connecting plates can rotate relatively to each other in order to eliminate the error during installation. After properly adjusting the relative rotation angle of the connecting plate between upper and lower hemi-connectors, arc-shaped holes will be filled with FastSteel.

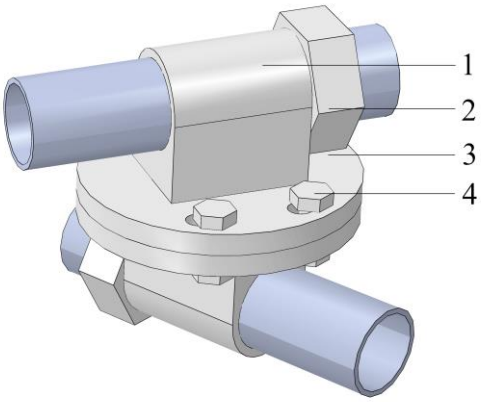

Fig. 9 - The model adjustable connector of reciprocal frame

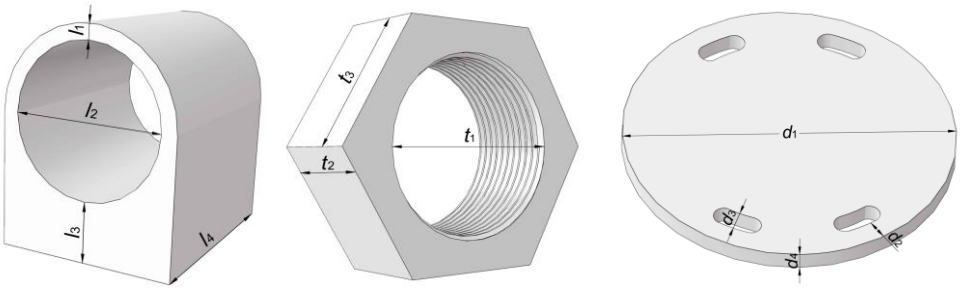

（1）Sleeve *（2）Nut* *（3）Connecting plate*

Fig.10 - The geometric parameters of the parts in the connector of reciprocal frame

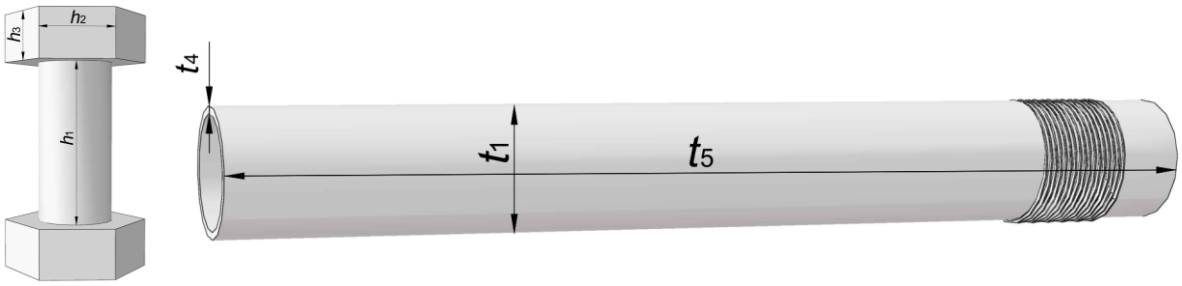

（4）Bolt （5）Circular Hollow Section

Fig.10 - The geometric parameters of the parts in the connector of reciprocal frame

NUMERICAL ANALYSIS OF ADJUSTABLE CONNECTOR OF RECIPROCAL FRAME

Mechanical characteristics of connector

A three-dimensional solid model of the connector has been created in the FEM software Abaqus CAE to study the mechanical properties of the connector. The parameters of each part of the connector are shown in Table 1.

Tab.1 - The geometric parameters of the connector/mm

Geometric Parameters	d_1	d_2	d_3	d_4	l_1	l_2	l_3	l_4	t_1	t_2	t_3	t_4	t_5	h_1	h_2	h_3
Value	180	16	16	15	6	60	30	90	60	46	30	6	490	30	12	10

This connector is made of Q235 steel and it applies with Class 10.9 M16 bolts. The upper and lower connector plates, the sleeve and the Circular Hollow Sections, and the bolt and the connector plate are connected in a hard contact way.

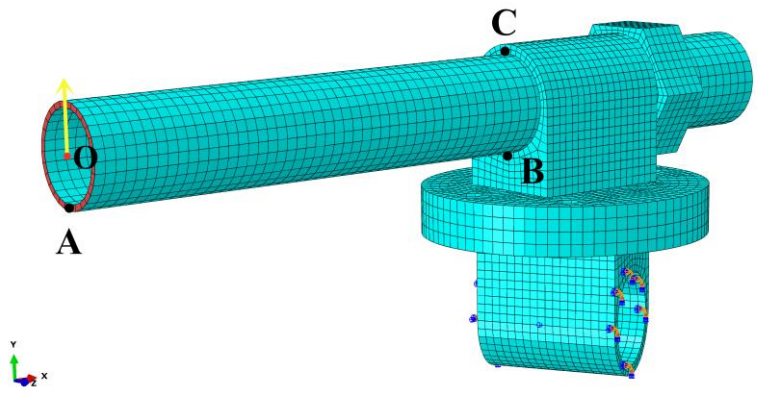

Fig. 11 - Finite element numerical model under Y-direction shearing force

The reciprocal frame members are mainly subjected to lateral loads which cause bending moments and shearing forces in the members. A shearing force parallel to the Y-axis is applied to the end section of the Circular Hollow Section as shown in Figure 11. In order to study the force characteristics and failure mechanism of this connector, the applied shearing force is continuously increased until the plastic deformation of the whole Circular Hollow Section has formed. Based on the analysis, the intersection of the Circular Hollow Section and the sleeve is the maximum force section of the Circular Hollow Section. When the shearing force parallel to the Y-axis reaches

12.12kN, the whole section of the intersection of the Circular Hollow Section and the sleeve produces plastic deformation. At this time, the stress nephogram of the connector can be shown in Figure 12.

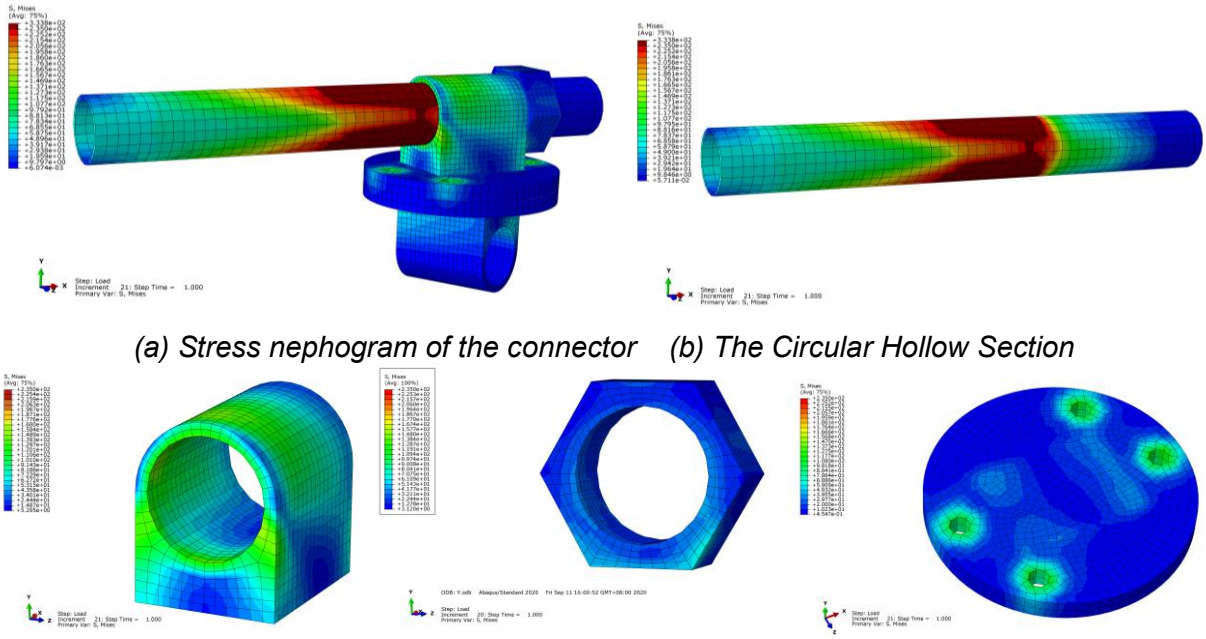

(a) Stress nephogram of the connector (b) The Circular Hollow Section

（c）The sleeve (d) The nut （e）The connecting plate

Fig. 12 - Stress nephogram of connector under Y-direction shearing force

It can be seen from Figure 12(b) that when the Y-direction shearing force reaches 12.12kN, the stress of the whole intersection of the Circular Hollow Section and the sleeve exceeds the material yield stress (235MPa), forming a plastic hinge. From Figure 12(c-e), the sleeve, nut and connecting plate are all in an elastic state. And the maximum stress of the sleeve is 175.7MPa, which is located on the inner wall of the sleeve near the external force. The maximum stress of the nut is 65.1MPa, which is located below the outer surface of the external force. The maximum stress of the connecting plate is 134.2MPa, which is located in the bolt hole far away from the external force. Take the rotation angle of the line around Z-axis connecting the sleeve's central point in front with its central point in the rear as the rotation angle of the connector around Z-axis. At this time, the rotation angle of this connector is only 8.3×10^{-4}rad, and the flexural rigidity of the connector around the Z-axis is very high. It can be seen that the structural damage is mainly caused by the plastic hinge formed at the end of the Circular Hollow Section when the members are subjected to the Y-direction shearing force. The adjustable connector of reciprocal frame has high strength and is still in an elastic state. The rigidity of the connector around the Z-axis is also great. When a plastic hinge is formed at the end of the Circular Hollow Section, the rotation angle of the connector around the Z-axis is minimal.

Under the condition of a shearing force parallel to the Z-axis being applied to the end section of the Circular Hollow Section, the applied shearing force is continuously increased until the plastic deformation of the whole Circular Hollow Section has formed in order to study the force characteristics and failure mechanism of the connector. Based on the analysis, the intersection of the Circular Hollow Section and the sleeve is still the maximum force section of the Circular Hollow Section. When the shearing force parallel to the Z-axis reaches 12.16kN, the whole section of the intersection of the Circular Hollow Section and the sleeve produces plastic deformation. At this time, the stress nephogram diagram of the connector is shown in Figure 13.

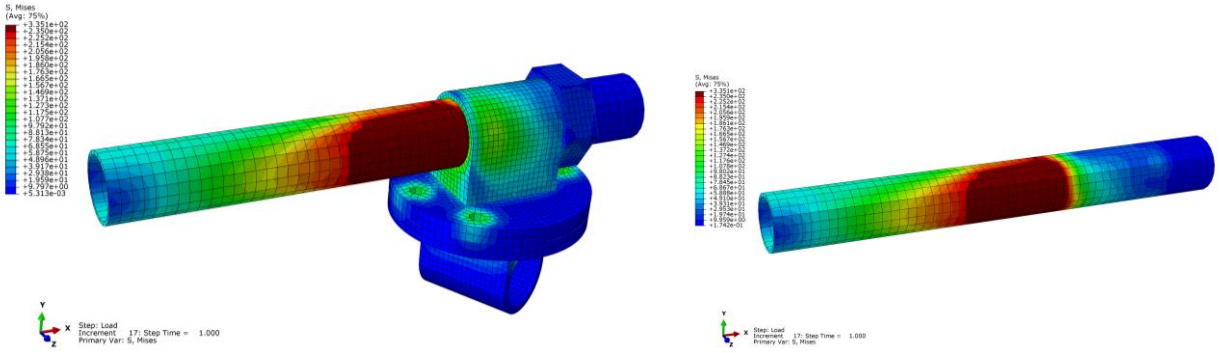

(a) Stress nephogram of the connector *（b）The Circular Hollow Section*

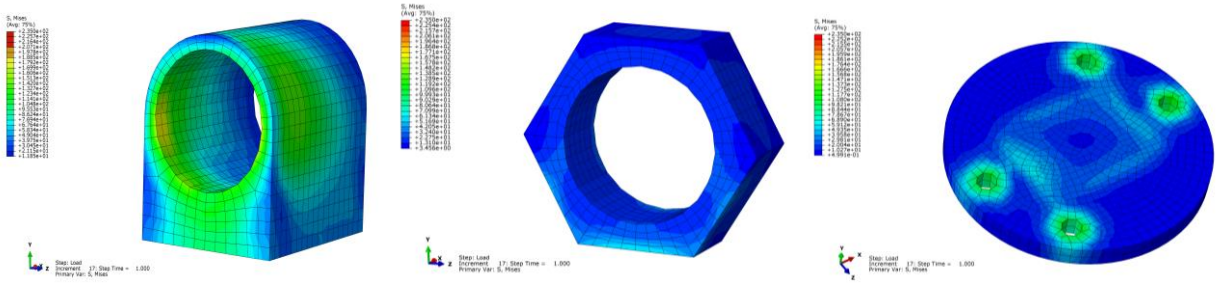

(b) The Circular Hollow Section (c) The sleeve (d) The nut (e)The connecting plate

Fig. 13 - Stress nephogram of connector under Z-direction shearing force

It can be seen from Figure 13(b) that when the Z-direction shearing force reaches 12.12kN, the stress of the whole intersection of the Circular Hollow Section and the sleeve exceeds the yield stress of the material by 235MPa, forming a plastic hinge. It can be seen from Figures 13 (c), 13 (d) and 13 (e) that the sleeve, nut and connecting plate are all in an elastic state. The maximum stress of the sleeve is 206.2MPa, which is located on the left side of the inner wall near the side where the external force is applied. The maximum stress of the nut is 63.1MPa, which is located at the bottom end of the surface near the side where the external force is applied. The maximum stress of the connecting plate is 127.7MPa, which is located in the bolt hole away from the external force. Take the rotation angle of the line around Y-axis connecting the sleeve's central point in front with its central point in the rear as the rotation angle of the connector around Y-axis. At this time, the rotation angle of the connector is only 1.01×10^{-3}rad, and the flexural rigidity of the connector around the Y-axis is very high. It can be seen that the structural damage is mainly caused by the plastic hinge formed at the end of the Circular Hollow Section when the members are subjected to Z-direction shearing force. The adjustable connector of reciprocal frame has high strength and is still in an elastic state. The rigidity of the adjustable connector of reciprocal frame around the Y-axis is also very large. When the end of the Circular Hollow Section forms a plastic hinge, the rotation angle of the connector around the Y-axis is minimal.

It can be concluded from the above-mentioned analysis that the strength of the adjustable connector of reciprocal frame is relatively high. When the reciprocal frames are subjected to the ultimate load, the damage is mainly caused by the plastic hinge formed at the end of the members, and the adjustable connector of reciprocal frame is still in an elastic state, which has realized the goal for designing higher connector strength over members strength. The rigidity of the adjustable connector of reciprocal frame is very large. When the plastic hinge is formed at the end of the Circular Hollow Section, the rotation angle of the connector is very small and can be ignored. Therefore, the rigid connector model can be used to simulate the adjustable connector of reciprocal frame.

Calculation model of the connector

The adjustable connector of reciprocal frame is composed of 4 parts, and the mechanical characteristics of the connector directly affect the entire mechanical response of the reciprocal frame. In order to calculate the response of reciprocal frame under various forces, the calculation model of adjustable connector should be established first. The parameterized calculation method is adopted to establish the calculation model of the connector. The reciprocal frame member mainly bears lateral load and thus the connector of reciprocal frame mainly bears the bending moment around the Z-axis. This section mainly discusses the calculation model of the connector around the Z-axis. The fastening bolts have tightened the upper and lower connecting plates according to the analysis, and the parameters in the connecting plates barely impact the bending resistance of the connector. The bottom of the sleeve is welded to the connecting plate, and the thickness l_3 of the lower wall of the sleeve has little effect on the flexural rigidity of the connector. The five parameters d_1、d_2、d_3、d_4 and l_3 in Figure 10 create minimal effect on the flexural rigidity of the connector around the Z-axis. The parameters d_1=360mm，d_2=16mm，d_3=20mm，d_4=25mm，and l_3=30mm, are fixed values. For the sake of parametric analysis, the values of l_1、l_2、l_4 and f are changed singly and 20 sets of numerical models are established. The 20 sets of model parameters are shown in Table 2.

Tab. 2 - Numerical model parameters

No.	1	2	3	4	5	6	7	8	9	10
l_1/*mm*	6	9	12	15	18	12	12	12	12	12
l_2/mm	120	120	120	120	120	60	90	120	150	180
l_4/*mm*	150	150	150	150	150	150	150	150	150	150
f	Q235	Q235	Q235	Q235	Q235	Q235	Q235	Q235	Q235	Q235
No.	11	12	13	14	15	16	17	18	19	20
l_1/*mm*	12	12	12	12	12	12	12	12	12	12
l_2/*mm*	120	120	120	120	120	120	120	120	120	120
l_4/*m*	90	120	150	180	210	150	150	150	150	150
f	Q235	Q235	Q235	Q235	Q235	Q235	Q255	Q275	Q295	Q345

A bending moment around the Z-axis is applied to the connector sleeve. Take the rotation angle of the line around Z-axis connecting the sleeve's central point in front with its central point in the rear as the rotation angle of the connector around Z-axis, and the bending moment of model 1~model 5 is calculated. As shown in Figure 14(a). The bending moment-rotation angle curve of model 6~model 10 is shown in Figure 14(b). The bending moment-rotation angle curve of model 11~model 15 is shown in Figure 14(c). The bending moment-rotation angle curve of model 16~model 20 is shown in Figure 14(d). From Figure 14 (a-d), it can be seen that the bending moment of the adjustable connector and the rotation angle is in a linear relation.

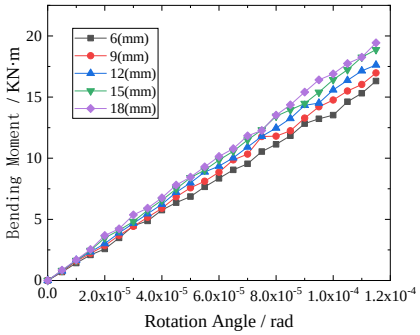

No. 1~5 Bending moment-rotation angle

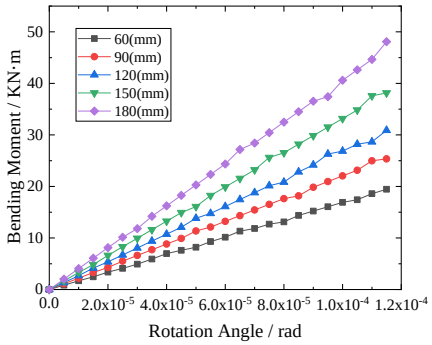

(b)No.6~10 Bending moment-rotation angle

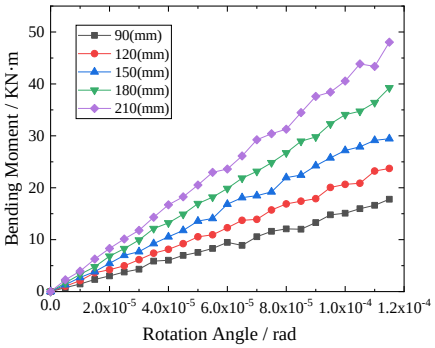

(c) No. 11~15 Bending moment-rotation angle

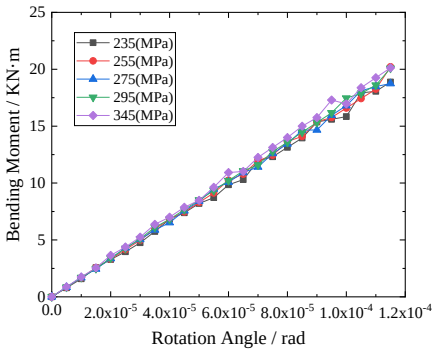

(d) No.16~20 Bending moment-rotation angle

Fig. 14 - Bending moment--rotation angle curve of the connector

According to Figure 14, the slope of each curve, that is the flexural rigidity of each connector model around the Z-axis, can be calculated by the least square method. In Model 1~Model 5, the effect of l_1 on the flexural rigidity of the connector around the Z-axis is achieved by changing the parameter of l_1. The flexural rigidity k of the connector around the Z-axis is shown in Table 3. The relation between l_1 and k is shown in Figure15.

Tab. 3 - Flexural rigidity of the connector model 1~5

No.	1	2	3	4	5
l_1/mm	6	9	12	15	18
k/(N·m/rad)	139226	147586	155864	164166	169000

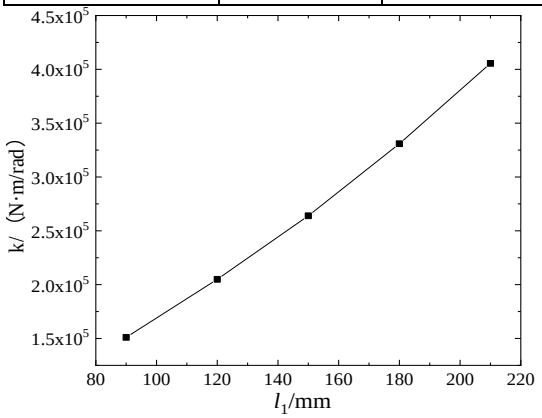

Fig. 15 - Relation curve between l_1 and k

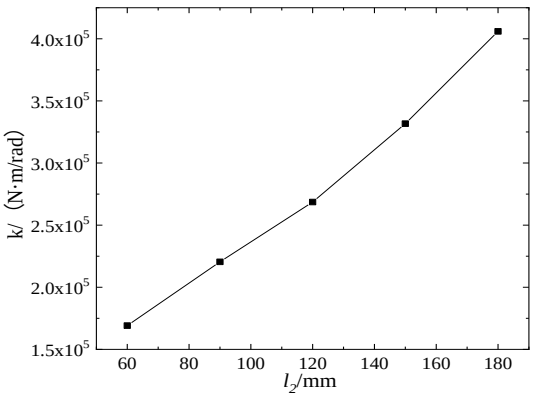

Fig. 16 - Relation curve between l_1 and k

Only the parameter l_2 has been changed in Model 6~Model 10. The flexural rigidity k of the connector around the Z-axis is shown in Table 4, and the relation curve between l_2 and k is shown in Figure 16.

Tab. 4 - Flexural rigidity of the connector model 6~10

No.	6	7	8	9	10
l_2/mm	60	90	120	150	180
k/(N·m/rad)	169116	220468	268590	331686	405976

Only the parameter l_4 has been changed in Model 11 ~ Model 15. The flexural rigidity l_4 of the connector around the Z-axis is shown in Table 5, and the relation curve between l_4 and k is shown in Figure 17.

Tab. 5 - Flexural rigidity of the connector model 11~15

No.	11	12	13	14	15
l_4/mm	90	120	150	180	210
k/(N·m/rad)	151036	204966	263960	330896	405544

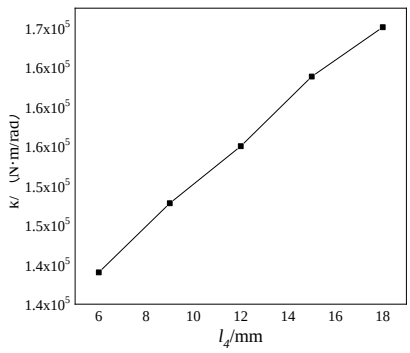

Fig. 17 - Relation curve between l4 and k

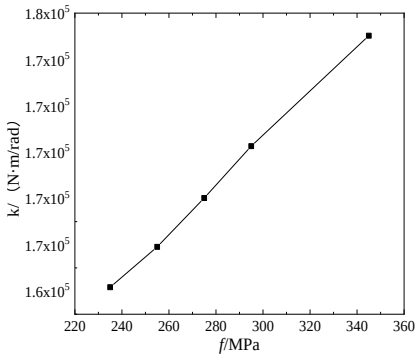

Fig.18 -Relation curve between f and k

In Model 16 ~ Model 20, only the parameter f has been changed. The flexural rigidity k of the connector around the Z-axis is shown in Table 6, and the curve of the relation between f and k is shown in Figure -18.

Tab. 6 - Flexural rigidity of the connector model 16~20

No.	16	17	18	19	20
f/MPa	235	255	275	295	345
k/(N·m/rad)	164166	165908	168018	170256	175026

It can be seen from Figure 15~Figure 18 that the flexural rigidity of the connector has a positive linear relation with the sleeve wall thickness l_1, the sleeve inner diameter l_2, the sleeve length l_4, and the material yield strength f. In order to study the quantitative relationship between the flexural rigidity of the connector and the related parameters, the same dimension parameters $k/\left(l_2 \cdot l_4 \cdot f\right)$ and l_1 are constructed. The relation between the two parameters is shown in Figure 19.

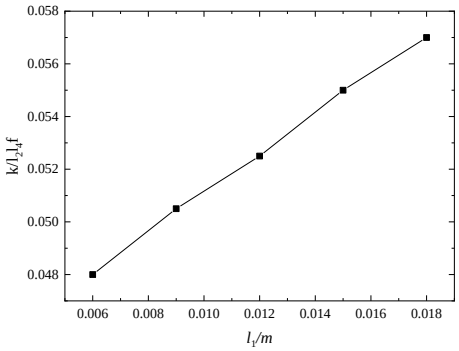

Fig. 19 - Relation curve between $k/\left(l_2 \cdot l_4 \cdot f\right)$ *and* l_1

$k/\left(l_2 \cdot l_4 \cdot f\right)$ and l_1 are in a linear relation from Figure 19, and the least square method is used for analysis to get a formula and correlation efficient as follows:

$$\frac{k}{l_2 \cdot l_4 \cdot f} = 0.75 l_1 \tag{1}$$

Correlation coefficient $R^2 = 0.9985$。

Therefore, the flexural rigidity of the adjustable connector of reciprocal frame is:

$$k = 0.75 l_1 l_2 l_4 f \tag{2}$$

NUMERICAL ANALYSIS OF RECIPROCAL FRAME

The members of the reciprocal frame mainly bear lateral loads. According to the analysis in section 3, the adjustable connector of reciprocal frame is of semi-rigid. Accurate numerical models should be established to research the mechanical characteristics of the connector. A three-dimensional wire model of reciprocal frame has been created in the FEM software Abaqus CAE. The members are simulated by beam elements, while the joints are simulated by UJoint connectors, and the UJoint connectors can be set rigidity value. Defining the UJoint connectors, according to the relation curve in Figure 19 and the formula (2) in Section 3.2, and the calculation model of reciprocal frame considering joint rigidity can be established. The support is hinged, that is, translational freedom of the support is constrained and rotational freedom is released. The members are Circular Hollow Section of Q235 with an outer diameter of 60mm, wall thickness of 3mm and length of 1500mm. The dimensions of each part in the adjustable connector of reciprocal frame are t_1=90mm, t_2=62mm, t_3=40mm, l_1=8mm, l_2=90mm, l_3=30mm, l_4=120mm, d_1=270mm, d_3=16mm, d_4=20mm. The angle between the member and the horizontal plane is 8°. A concentrated force of 540N, 840N and 1140N is applied at each joint in turn. A finite element model of reciprocal frame is shown in Figure 20.

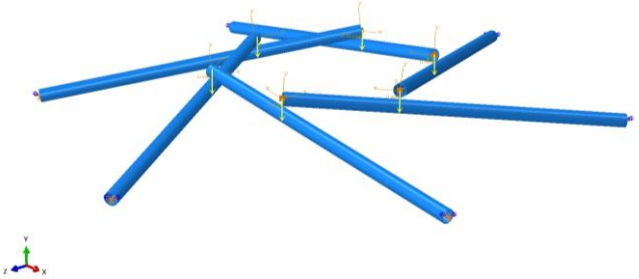

Fig. 20 - A finite element model of the reciprocal frame

After the static analysis, the deformation of the structure was amplified by 30 times to show the result of the members under the different concentrated force.

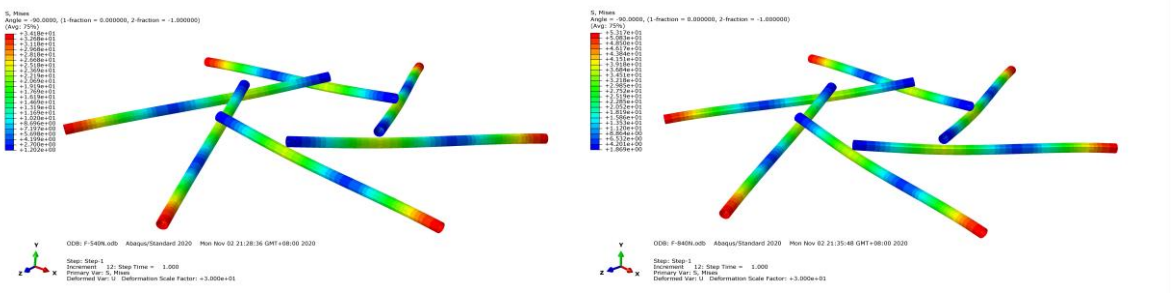

（a）Concentrated force of 540N *（b）Concentrated force of 840N*

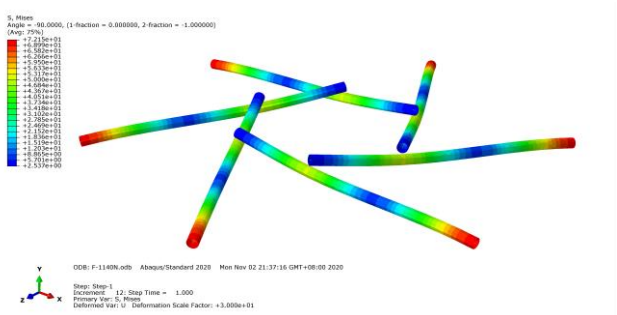

（c）Concentrated force of 1140N

Fig. 21 - Nephogram of structural stress under different concentrated forces

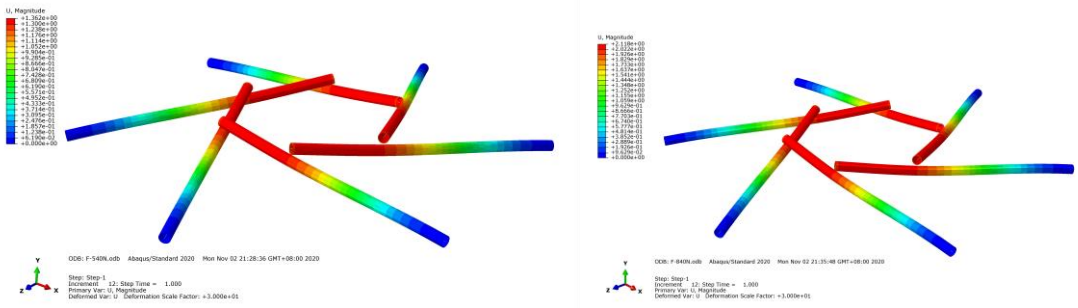

（a）Concentrated force of 540N *（b）Concentrated force of 840N*

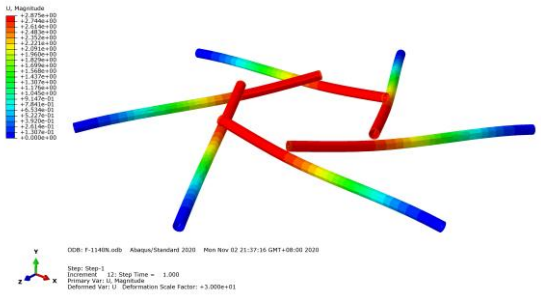

（c）Concentrated force of 1140N

Fig. 22 - Nephogram of structural vertical displacement under different concentrated forces

As seen in Figure 22, reciprocal frame is of rotational symmetry, which makes stress and deformation of each member uniform. The position of the maximum vertical displacement is at the joint and the position of the maximum stress is at the support. See Tables 6 and 7. The stress decreases first and then increases from the joint to the support of the member. The vertical displacement values of members between adjacent joint is uniform and larger than the rest.

Tab. 6 - Stress of the members under different concentrated force

Concentrated Force	540N	840N	1140N
maximum stress	34.2	53.2	72.1
stress at joint	24.1	37.4	50.8

Tab.7 - Vertical displacement of the joints under different concentrated force

Concentrated Force	540N	840N	1140N
Deformation	1.36	2.12	2.88

FULL-SCALE TEST

In order to verify the validity of the mechanical model and structural modeling method of the connector, carrying out a full-scale test including connectors and members. The full-scale test model is shown in Figure 21. The test model was fixed on a regular hexagon pedestal with great stiffness, and the end of members are welded to the pedestal. The size of members and connectors of the full-scale test model are the same as the numerical model in Section 4. The test model was loaded with weights.

The members are numbered A~F, and three measuring points are installed at the bottom of each member, which are respectively located at the joint of the member, the center of the joint and internal endpoint, and the center of the joint and external endpoint. There are 18 measuring points. For A~F members, measuring points are numbered successively from 1 to 18. According to electrical measures, the strain changes of each measurement point in the structure are measured through resistance strain gauge. According to the formula Hooke's law $\sigma = \mathrm{E} \cdot \varepsilon$, the stress of each measuring point can be calculated. Displacement meters are installed below the measuring points 2, 5, 8, 11, 14 and 17 in Figure 21 (a). The change of vertical displacement at the joints of members in the structure is measured.

（a） (b) (c)

Fig.21 - (a) Location of strain gage (b) Loading diagram (c) Displacement meter

As shown in Figure 21(b), a concentrated force of 540N, 840N and 1140N is applied at each joint respectively. The data of stress and vertical displacement at the joint points in members A~F are shown in Table 8 and Table 9.

Tab. 8 - Stress of the members under different concentrated forces/MPa

Member	Concentrated Force		
	540N	840N	1140N
A	36.6	56.2	76.3
B	34.2	49.6	79.4
C	36.5	57.5	69.6
D	35.7	51.2	78.9
E	35.5	55.3	64.
F	32.2	63.4	77.4
average	35.1	58.9	74.3

Tab. 9 - Vertical displacement of the joint under different concentrated forces/mm

Member	Concentrated Force		
	540N	840N	1140N
A	1.42	2.27	2.91
B	1.36	2.19	2.85
C	1.26	2.58	2.93
D	1.33	2.07	2.52
E	1.24	2.31	3.14
F	1.35	2.02	2.65
average	1.33	2.24	2.84

COMPARISON OF TEST RESULTS AND NUMERICAL SIMULATION RESULTS

Comparison of the results of stress between test and numerical simulation

Tab. 10 - Comparison under 540N concentrated force at the joints/MPa

member	A	B	C	D	E	F
test results	36.6	34.2	36.5	35.7	35.5	32.2
simulation results	34.2	34.2	34.2	34.2	34.2	34.2
relative error	6.5%	0	6.3%	4.2%	3.7%	6.2%

Tab. 11 - Comparison under 840N concentrated force at the joints/MPa

member	A	B	C	D	E	F
test results	56.2	49.6	57.5	51.2	55.3	63.4
simulation results	53.2	53.2	53.2	53.2	53.2	53.2
relative error	5.3%	7.3%	7.5%	3.9%	3.8%	16%

Tab. 12 - Comparison under 1140N concentrated force at the joints/MPa

member	A	B	C	D	E	F
test results	76.3	79.4	69.9	78.9	64.2	77.4
simulation results	72.1	72.1	72.1	72.1	72.1	72.1
relative error	5.5%	9.2%	3.1%	8.6%	12.3%	6.8%

It can be seen from the table that under different concentrated forces, the test results at the joints of each member are very close to the simulation results, and the error is very small.

Comparison of the results of vertical displacement between test and numerical simulation

Tab. 13 - Comparison under 540N concentrated force at the joints

member	A	B	C	D	E	F
test results /mm	1.42	1.36	1.26	1.33	1.24	1.35
simulation results /mm	1.36	1.36	1.36	1.36	1.36	1.36
relative error	4.2%	0	7.9%	2.3%	9.7%	0.7%

Tab. 14 - Comparison under 840N concentrated force at the joints

member	A	B	C	D	E	F
test results /mm	2.27	2.19	2.58	2.07	2.31	2.02
simulation results /mm	2.12	2.12	2.12	2.12	2.12	2.12
relative error	6.6%	3.2%	17.8%	2.4%	8.2%	4.9%

Tab. 15 - Comparison under 1140N concentrated force at the joints

member	A	B	C	D	E	F
test results /mm	2.91	2.85	2.93	2.52	3.14	2.65
simulation results /mm	2.88	2.88	2.88	2.88	2.88	2.88
relative error	1.0%	1.1%	0.7%	14.3%	8.3%	8.7%

It can be seen from the tables that under different concentrated forces, the test results at the joints of each member are very close to the simulation results, and the error is very little.

CONCLUSION

(1) In this paper, we design an adjustable connector of reciprocal frame which consists of a sleeve, a nut, two connecting plates and four bolts. A three-dimensional solid model of this connector with Circular Hollow Section has been created in the FEM software Abaqus CAE to study the mechanical properties of the connector. When the plastic hinge is formed at the end of the Circular Hollow Section, the connector is still in an elastic state. It is verified that the adjustable connector of reciprocal frame has high strength and rigidity, realizing the goal for designing higher connector strength over Circular Hollow Section strength.

(2) Under lateral load, parametric analysis is used to analysis the influence of the connector about each part on the mechanical properties. There is a linear relation between flexural rigidity and material yield strength, sleeve diameter, sleeve length, and wall thickness of the sleeve. Then the flexural rigidity of the connector is derived.

(3) A three-dimensional wire model of reciprocal frame has been created in the FEM software Abaqus CAE, and full-scale test model of the structure is designed. The numerical simulation results agree well with the test results. It is verified that the reliability of the modeling method and the accuracy of the mechanical model.

ACKNOWLEDGEMENTS

Financial supports from Fundamental Research Funds for Central Universities (3122019104) is gratefully acknowledged.

REFERENCES

[1] Fan Binghe, Luo Chao, Xu Xiaoyan, etc. Structural configuration analysis and detailing of wooden Rainbow Bridge[J].SPATIAL STRUCTURE,2018,24(01):91-96.doi: 10.13849/j. issn.1006-6578. 2018.01.091
[2] Yan Su, Makoto Ohsaki, Yue Wu, Jingyao Zhang. A numerical method for form finding and shape optimization of reciprocal structures[J]. Engineering Structures,2019,198
[3] Baverel, O., and H. Nooshin. 2007. Nexorades based on regular polyhedra. Nexus Network Journal 9(2): 281–299. doi: 10.1007/s00004-007-0043-0
[4] Bertin V. Leverworks : one principle, many forms [M]. Beijing: China Architecture & Building Press, 2012. 11-11.
[5] Larsen, Olga Popovic.Reciprocal Frame (RF) Structures: Real and Exploratory[J].Nexus network journal: Architecture and mathematics,2014,16(1):119-134. doi: 10.1007/s00004 -014-0181-0
[6] Bernard Vaudeville,Simon Aubry,Simon Gelez.Nexorade or Reciprocal Frame System Applied to the Design and Construction of a 850 m2 Archaeological Shelter [J]. International journal of space structures,2011,26(4):303-311. doi: 10.1260/0266-3511. 26.4.303
[7] Song, P.,-Wing Fu, C.,Goswami, P., et al.Reciprocal frame structures made easy[J].ACM Transactions on Graphics,2013,32(4 CD/ROM):94-1-94-10. doi: 10.1145/2461912.246 1915
[8] Alejandro Bernabeu Larena,David García Ménendez, et al.Extension of Euskalduna Conference Centre and Concert Hall: A Contemporary Application of Irregular Reciprocal Frames[J].Structural Engineering International,2014,24(1):63-67. doi: 10.2749/10168 66 14X13830788506233
[9] Yan Su,Makoto Ohsaki,Yue Wu,Jingyao Zhang. A numerical method for form finding and shape optimization of reciprocal structures[J]. Engineering Structures,2019,198. doi:10.1016/j.engstruct. 2019.109510
[10] Aicher, S., Garrecht, H., Reinhard, H.-W. (2014): Materials and Joints in Timber Structures. Springer, New York, pp. 129-134.
[11] Rizzuto J P, Popovic O L. Connection Systems in Reciprocal Frames and Mutually Supported Elements Space Structure Networks[J]. International Journal of Space Structures, 2010, 11(4): 243-256. doi: 10.1260/0266-3511.25.4.243
[12] Baverel, O., and H. Nooshin. 2007. Nexorades based on regular polyhedra. Nexus Network Journal 9(2): 281–299. doi: 10.1007/s00004-007-0043-0
[13] Bijnen A. Een geodetiese knoopkonstruktie[P]. Octrooiraad Nederland, Terinzagelegging. Aanvrage, No 7603046. 1976.
[14] JOEL GUSTAFSSON. Connections in Timber Reciprocal Frames[D]. Gothenburg, Sweden: CHALMERS UNIVERSITY OF TECHNOLOGY,2016.
[15] Liu Xuechuan,Shang Zixuan, Zhang Dongjie,etc.Research key points and present situation analysis of prefabricated multi-story and high-rise steel structures[J].Industrial Construction, 2018, 48(05):1-10. doi: 10.13204/j.gyjz201805001
[16] O. Baverel,O . Popovic Larsen. A Review of Woven Structures with Focus on Reciprocal Systems Nexorades[J]. International journal of space structures,2011,26(4):281-288. doi:10.1260/0266-351 1.26.4.281
[17] Rizzuto J P. The Structural Behaviour of Mutually Supported Elements in Space Structures[D]. Coventry: Coventry University, 2005.
[18] J. P. RIZZUTO. Rotated Mutually Supported Elements In Truncated Icosahedric Domes [J] Journal of the international association for shell and spatial structures, 2007, 48(1):3-17.
[19] Maziar Asefi, Mahnaz BahremandiTolou. Design challenges of reciprocal frame structures in architecture[J]. Journal of Building Engineering,2019,26.
[20] Larsen, Olga. (2014). Reciprocal Frame (RF) Str Exploratory. Nexus Network Journal. 16. 10.1007/s00004-014-0181-0. doi: 10.1007/s00004-014-0181-0

CIVIL ENGINEERING JOURNAL

Article no. 29

THE CIVIL ENGINEERING JOURNAL 2-2021

STUDY ON REINFORCEMENT OF FABRICATED HOLLOW SLAB BRIDGE BY POLYURETHANE-CEMENT COMPOSITE (PUC)

Zhang Kexin[1], Qi Tianyu[1], Zhu Zhimin[2], Xue Xingwei[1], Shen Xinyuan[1]

1. *School of Traffic Engineering, Shenyang Jianzhu University, Shenyang, 110168, PR of China; jt_zkx@sjzu.edu.cn*
2. *Liaoning Urban Construction Design Institute Co. LTD, Shenyang, 110000, PR of China*

ABSTRACT

In this paper, a new polyurethane-cement composite (PUC) material is used to reinforce a 25-year hollow slab bridge. PUC material is composed of polyurethane and cement, which has good mechanical properties. After pouring PUC material at the bottom of the hollow slabs, the traffic can be restored in a short time. Ultimate bearing capacity was discussed based on the concrete structures. The bending failure mode of concrete reinforced T-beam bridges strengthened with PUC was controlled through PUC design strength. The main construction process was introduced, including concrete surface treatment, supporting template and pouring. To investigate the effectiveness of PUC in strengthening bridges, load tests were conducted before and after the reinforcement. The test results showed that PUC possibly removed the bridge load and increase the stiffness of the hollow slabs. The maximum carrying capacity and stiffness of the main girder were increased by about 20% and 28% after PUC material was poured. Meanwhile, the width of the cracks was reduced in different degrees.

KEYWORDS

Polyurethane-cement composite (PUC), Strengthening, Hollow slab, Strength analysis, Field application, Load test

INTRODUCTION

Concrete bridges are uninterruptedly unprotected to external environments. During their life spans, concrete bridges frequently experience situations that cannot be predicted during design. The durability of a concrete bridge is reduced by construction defects, overloaded vehicles, material characteristics, and environmental variations [1,2]. Replacing bridges to improve bridge performance can cause economic loss and inconvenient vehicle traffic [3]. Many researchers have studied proper repair and strengthening methods to solve the problems that occur in concrete structures [4,5].

To improve the working ability of concrete bridges, many techniques have been used in strengthening. The most common methods for strengthening beams have been the use of Carbon Fibre Reinforced Polymer (CFRP), steel plate bonding, high strength wire mesh reinforcement and others; these methods are widely used at present [6]. CFRP has good performance, high strength and light weight, but there are some disadvantages of CFRP reinforcement, the most important is

the high cost of CFRP reinforcement [7,8]. Bonding steel plates have the disadvantages of weakened bonding caused by steel corrosion, increased dead load weight and difficulties in adapting to the concrete surface profile [9,10]. High-strength steel wire mesh has the advantages of convenient construction and small section size [4]. Usually, high-strength steel strand is bonded and anchored to the main beam concrete by mortar or composite mortar, but mortar or composite mortar has low adhesion, which is prone to the peeling and destruction of the reinforcement layer and the main beam, leading to the de-crease of material utilization [11-12].

The introduction of new construction materials such as polyurethane-cement composite (PUC) to civil engineering can provide a potential solution. PUC is a polymer material made from a mixture of polyurethane raw materials and cement [13-15]. Polyurethane (PU) is a high performance polymer elastic material mainly based on the chemical compounds of polyisocyanate and polyester polyol. PUC has the advantages of light quality, significant strength in compressive and blending strength [13,14]. PUC has excellent bonding and adhesive properties with concrete materials, and it does not need additional adhesive for beam reinforcing [15].

PUC has been successfully used in strengthening T-beam girders, as proven through comprehensive laboratory tests. Haleem reported 10 beams strengthened with PUC under different load conditions, and the results showed a significant improvement of beam -bearing capacity. An experimental study on strengthening reinforced concrete T-beams using PUC [15]. The increment values of compressive strength were from 5 MPa to 60 MPa of PUC with density 400 kg/m^3 density and 1650 kg/m^3 respectively, while the flexural tensile strength was increased from 3.3 MPa to 44.3 MPa of PUC with 400 kg/m^3 and 1650 kg/m^3 density respectively indicating highly improvement in compressive and bending tensile strength compare with conventional concrete [14]. Nevertheless, these research projects were performed with laboratory-scale tests and corresponding analyses. Applying and obtaining the application results in engineering are essential.

The cross section of the plate made hollow is called hollow plate. The hollow slab bridge is composed of a number of hollow slabs connected horizontally. The hollow slab is lighter than the solid slab of the same span, convenient for transportation and installation, and the building height is smaller than the T beam of the same span, so it is used more in the small span bridge. This study describes PUC as a material used to strengthen a 25-year-old fabricated reinforced concrete hollow slab bridge, including design, field application, field test and analysis.

ANALYSIS AND DESIGN

Bridge description

Fig. 1 - Lateral view of Piao Fa Bridge

Figure 1 shows a lateral view of Piao Fa Bridge. The bridge was built in 1995 and carries an average daily traffic of 800 vehicles. The bridge has 5 spans, each span being 20 meters of simply supported hollow slabs. Central supports consist of reinforced concrete bents, each supported by two circular columns. The total width is 12.0 m, and the width of the driveway is 11.0 m. The bridge has two lanes and carries one lane of traffic in each direction. The cross section of the superstructure consists of 9 hollow slabs with a width of 1.25m Figure 2.

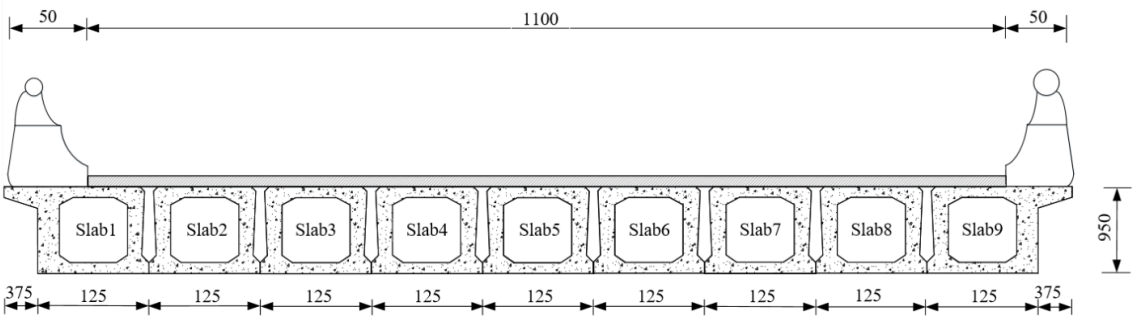

Fig. 2 - Cross-section of the bridge

The bridge has different degrees of damage caused by aging, overload, surging traffic and environment. During routine inspection, salt infiltration was observed in the bridge superstructure. Many hollow plates have the phenomenon of alkali spreading. Many vertical cracks appear on the bottom of the hollow slabs across the middle area. Serious cracks occurred in the edge-beam, as water from the pavement cracks affected the durability of the girder. Reinforcing the structure was selected because the owner did not agree to replace the bridge or limiting traffic. PUC strengthening method was chosen based on its application of being the least intrusive with traffic and being the most practical.

MATERIAL CHARACTERISTICS

This project adopts polyurethane cement material with good mechanical properties with a density of 1500kg/m^3 to strengthen the hollow plate. The bending stress-strain curves of PUC with the same density are approximately the same. Bending test for PUC material is shown in Figure 3. The density of PUC mixed in the construction site was 1,524 kg/m^3. The bending stress-strain curves of five groups of stirred PUC specimens at the construction site are shown in Figure 4. Ultimate strength (f_{Pu})was about 42.3MPa. Design strength (f_{Pu})was designed to be 3/4 of the ultimate strength, and the corresponding strain was 0.006 under the design strength. The minimum modulus of elasticity (E_{Pd}) was 5MPa. Table 1 shows the properties of PUC.

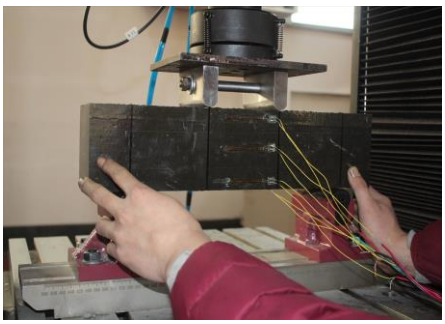

Fig. 3 - Bending test for PUC material

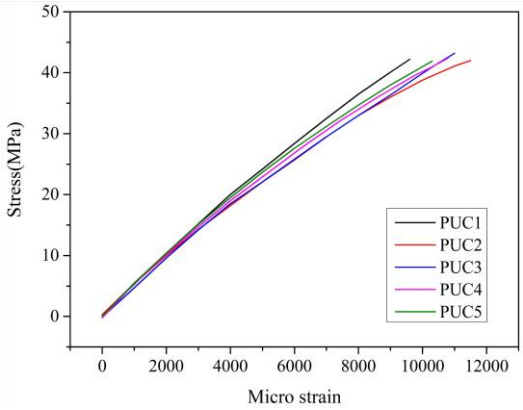

Fig. 4 - Blending stress–strain curve of the PUC

Basic properties such as the concrete compression strength and steel yield strength were assumed because the owner of the bridge did not allow coring to obtain the on-site strengths of the materials from the bridge girder. These basic properties f_c f_s were assumed as described by JTJ023-85 [16] for bridges of that age because no sample could be obtained onsite. The parameters of steel strand refer to the standard drawing of the same span in the same year. The strength and elastic modulus of materials such as steel bar, strand, concrete and PUC are shown in Table 1.

Tab. 1 - Material properties

Material	Property	Value
PUC	f_{Pu} (MPa)	42.3
	f_{Pd} (MPa)	31.7
	E_{Pd} (GPa)	5.0
Concrete	f_c (MPa)	30
	E_c (GPa)	30
Steel	f_s (MPa)	335
	E_s (GPa)	200

STRENGTHEN ANALYSIS

The service capacity of the inspected bridge is insufficient due to cracks, rain erosion and so on. Moreover, the owner of the bridge asked to complete the strengthening work with minimum interference to traffic. Therefore, the PUC material is designed to reinforce the hollow slab bridge. The hollow slab blending bearing capacity was analysed through the assumption that the plane section remained to be planar until failure. Blending bearing capacity was evaluated based on force equilibrium and strain compatibility until failure Figure 5.

The failure of the prestressed hollow slab strengthened with PUC material was slab bending failure because of the strong bonding performance between PUC material and concrete. The flexural capacity of the PUC -reinforced member depended on the concrete crushing or the PUC

material's design strength. Two kinds of failure modes exist for PUC -strengthened the prestressed hollow slab according to Fig. (5) and plane assumption.

According to strain compatibility, the strain of steel bar ε_s can be expressed as follows.

$$\varepsilon_s = \frac{h_s - x_c}{h_p - x_c}\varepsilon_p \tag{1}$$

where h_s represents the depth from the centroid of steel bars to the top of the T-cross section, h_P represents the depth from the centroid of the PUC section to the top of the hollow slab section, x_c represents the depth of the neutral axis and ε_p represents the strain of the centroid of the PUC section. When concrete crushing failed, the ultimate compressive strain for the concrete was assumed to be 0.003, and the steel strand has been in a yield situation.

According to strain compatibility, the strain of the centroid of the PUC section ε_p can be expressed as follows.

$$\varepsilon_p = \frac{h_p - x_c}{x_c}\varepsilon_{cu} \tag{2}$$

The PUC material and steel strand were treated as a nearly linear material, and the stress of the PUC material can be calculated by the following:

$$\sigma_{PUC} = E_{PUC}\varepsilon_{PUC} \tag{3}$$

$$\sigma_p = E_p\varepsilon_p \tag{4}$$

The standard equilibrium equation is listed in Equation (5)

$$\alpha_1 f_c b_f x = f_y A_s + \sigma_p A_p + f_{PUC}A_{PUC} \tag{5}$$

where $x = 0.8x_c$, $\alpha_1 = 1$, A_s represents the area of the steel bars, f_y represents the yield strain of the steel bars and ε_s represents the strain of the steel bars. ε_s can be calculated from a combination of equations (1) to (5), and ε_s goes beyond the allowance strain of steel rebars, which is 0.01 according to Design Code of Concrete Structures [17]. Therefore, beam failure is not controlled by concrete crushing failure.

The ultimate strain of PUC is about 0.006 when the strength of the PUC material is design strength. The steel bar strain is larger than the yield sign strain and less than 0.01 according to strain compatibility.

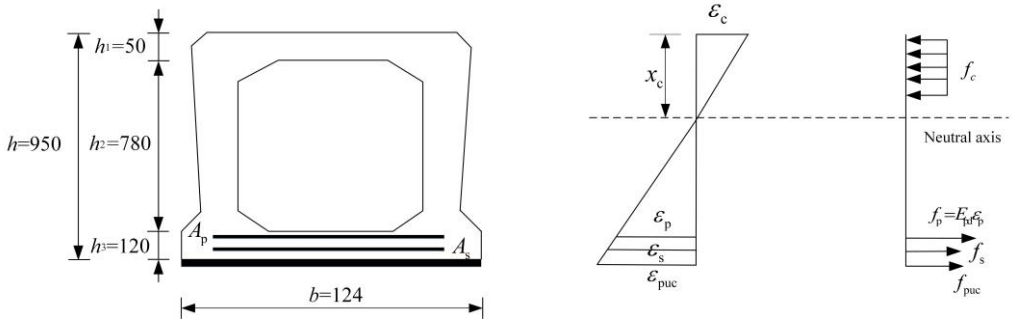

(a) Reinforced concrete section *(b) Strain distribution* *(c) Stress distribution*

Fig. 5 - Internal strain and stress distribution for a hollow slab shape section

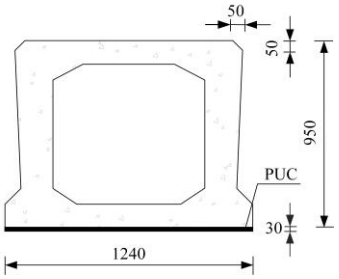

Fig. 6 - Hollow slab section strengthened with PUC material

$$\alpha_1 f_c b_f x = f_y A_s + f_p A_p + f_{PUC} A_{PUC} \quad (6)$$

$$M_u = f_{PUCd} A_{PUC} \left(h_p - \frac{x}{2} \right) + f_y A_s \left(h_s - \frac{x}{2} \right) + f_{Py} A_p \left(h_s - \frac{x}{2} \right) \quad (7)$$

where A_p represents the cross-sectional area of the PUC material, and f_{Pd} represents the design strength of the PUC material. The flexural strength of the beams after strengthening can be calculated through a combination of Equations (6) and (7).

The above mentioned analysis shows that the bearing capacity of the strengthened beam is controlled by the design strength of the PUC material. The flexural strength increased to 1543.7 kN.m through the pouring of the PUC material. The section of PUC is shown in Figure 6.

STRENGTHENING PROCEDURE

PUC strengthening is similar to the enlarging section method [18,19], but the curing time of the PUC strengthening method is significantly less than the enlarging section method. First, degenerate materials are removed from the concrete surface, and the visible cracks in the surface of the girders are closed through a chemical method. Second, the concrete surface is chiselled to ensure that its roughness meets the China Construction Code of Concrete Structure. Loose materials, which affect the bonding performance of the PUC material, are removed through high - pressure water washing.

In achieving a better bonding effect, sufficient time must be ensured to dry the concrete surface naturally. The construction templates were made depending on the design of the dimensions of the PUC material. The template was installed in the location specified Figure 8. The mixing ratio of the PUC components (polyol: polyisocyanate: cement) was 1:1:2 by weight. The mixed PUC material was poured into the templates. First, a water drill is used to form a round hole with a diameter of 40 mm at the hinge joint position. Then, at the deck location, the PUC material is dumped through the circular hole. The templates were removed after two hours Figure 7c.

(a) Mixed the PUC material (b) Support formwork and PUC casting (c) Template removal
Fig. 7 - The PUC material casting

LOAD TEST

Before strengthening and two months after strengthening, load tests were performed to obtain the service ability of the bridge. These tests are repeated once a year, and they will continue over a period of three years. Three-axle trucks are used as live load. The details of the trucks are shown in Figure 10. The gross rail loads before and after strengthening are listed in Table 2. The bridge test was performed under four conditions. The two trucks were used at different locations for each condition and were assigned with unique letters A and B.

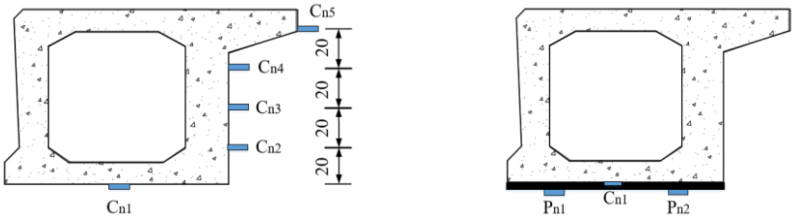

(a) Strain gages mounted oncConcrete *(b) Strain gages mounted on PUC*

Fig. 9 - Locations of Strain Gages Mounted on the Slabs (n is the slab number

Tab. 2 -Gross axle load of trucks before and after strengthening

Load-test trucks		Force axle t_1 (kN)	Force axle t_2 (kN)	Back axle t_3 (kN)	Back axle t_4 (kN)
Before	(A)	79.5	79.3	157.4	157.4
	(B)	78.4	78.8	157.9	157.9
After	(A)	79.7	79.5	157.5	157.5
	(B)	79.7	79.9	157.6	157.6

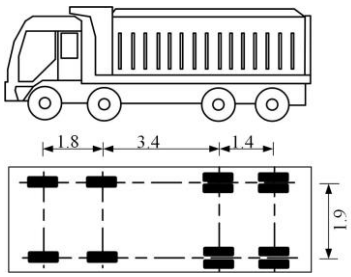

Fig. 10 - Load-test truck configuration

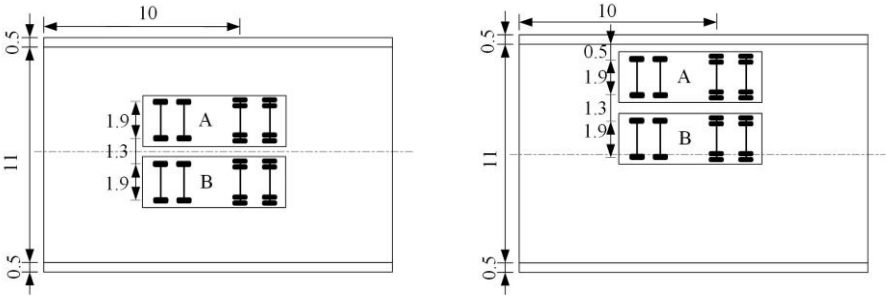

(a) Condition 1 *(b) Condition 2*

Fig. 11 - Distribution of load-test trucks on the bridge deck at different

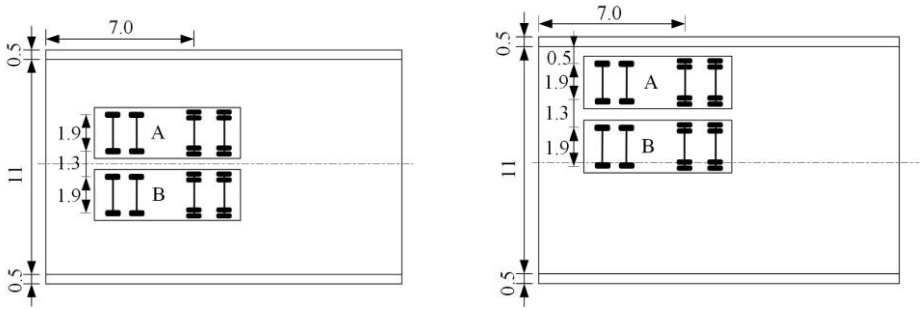

(c) Condition 3 *(d) Condition 4*

Fig. 11 - Distribution of load-test trucks on the bridge deck at different

The testing of each condition was sequenced as follows: Truck A, Truck A + B, Truck B. The four conditions are shown in Figure 11. For condition 1, the two trucks were symmetrical with the centre of the bridge, and the distance from the outside wheels to the pavement edge was 2.95 m. For condition 2, the two trucks deviated from the centre line of the bridge, and the distance from the outside wheels to the pavement edge was 0.5m. For both conditions 1 and conditions 2, the third axle of the vehicles are in the middle of the span. For condition 3, the two trucks were symmetrical with the centre of the bridge, and the distance from the outside wheels to the pavement edge was 2.95 m. For condition 4, the two trucks deviated from the centre line of the bridge, and the distance from the outside wheels to the pavement edge was 0.5m. For both conditions 3 and conditions 4, the four axles of the vehicles are in the middle of the span.

STRAIN MEASUREMENT

Strain gages were placed and arranged at the bottom of the mid-span, as shown in Figure 9a. The letter n represents the hollow slab number, and the letter C represents the concrete strain gages. Strain gauges (C_{n1}) were installed on the bottom of the hollow slab before strengthening, as the bottom of the hollow slabs was covered with PUC after strengthening. The strain gages of the PUC surface are shown in Figure 9b. The letter P represents the PUC strain gages. The gage P_{n2} and the gage C_{n1} were installed at the same horizontal position. The strains were collected at a rate of two readings per second.

Figure 12 shows the concrete strain on the bottom concrete surface under live load in condition 1 before and after strengthening. The strain was the largest in the middle slab. The maximum strain of slab 5 were 75 microstrains for the two trucks (Trucks A + B) before strengthening because of the damage and the weak interaction between the slabs. After strengthening, the maximum strain of slab 5 were 60 microstrains for the two trucks (Trucks A + B). The maximum strains of hollow slab 3 were 50 microstrains and 45 microstrains before and after strengthening, respectively. The strain was reduced to about 5 microstrains. The maximum strains of slab 1 were 31 microstrains and 25 microstrains before and after strengthening, respectively. Therefore, the concrete strain can be reduced after the PUC material is poured. For condition 2, the concrete strains on the bottom concrete surface under live load before and after strengthening are shown in Figure 12. The strain of beam 1 was the largest for the two trucks (Trucks A + B) because the two trucks approached the side of the bridge. The maximum strain of beam 1 were 88 microstrains before strengthening, and the strain became 69 microstrains after strengthening. Before strengthening, the strains of beam 3 and beam 5 were 83 and 76 microstrains, respectively, and after strengthening, the strains were 68 and 63 microstrains, respectively. In comparing the strains before and after strengthening, the concrete strain is reduced to some degree.

Figure 13 shows the concrete strain on the bottom concrete surface under live load in condition 3 before and after strengthening. The strain was the largest in the middle slab. The maximum strain of slab 5 was 60 microstrains for the two trucks (Trucks A + B) before strengthening because of the damage and the weak interaction between the slabs. After strengthening, the maximum strain of slab 5 was 52 microstrains for the two trucks (Trucks A + B). The maximum strains of hollow slab 3 were 40 microstrains and 36 microstrains before and after strengthening, respectively. The strain was reduced to about 4 microstrains. The maximum strains of slab 1 were 25 microstrains and 20 microstrains before and after strengthening, respectively. Therefore, the concrete strain can be reduced after the PUC material is poured. For condition 4, the concrete strains on the bottom concrete surface under live load before and after strengthening are shown in Figure 13. The strain of beam 1 was the largest for the two trucks (Trucks A + B) because the two trucks approached the side of the bridge. The maximum strain of beam1 was 68 microstrains before strengthening, and the strain became 56 microstrains after strengthening. Before strengthening, the strains of beam 3 and beam 5 were 67 and 61 microstrains, respectively, and after strengthening, the strains were 56 and 52 microstrains, respectively. In comparing the strains before and after strengthening, the concrete strain is reduced to some degree.

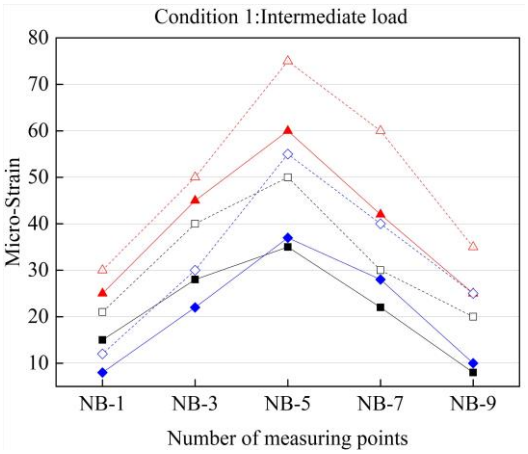

(a) Strains in the condition 1

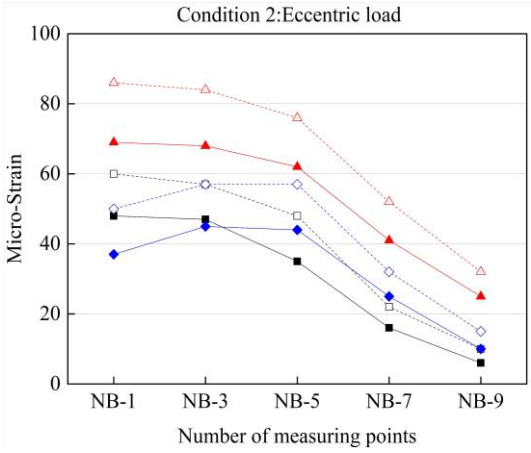

(b) Strains in the condition 1

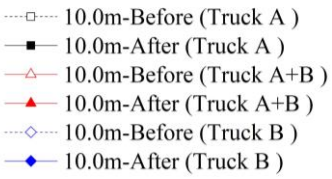

(c) Annotation explanation

Fig. 12 - Recorded concrete strains of hollow slabs in condition 1 and condition 2

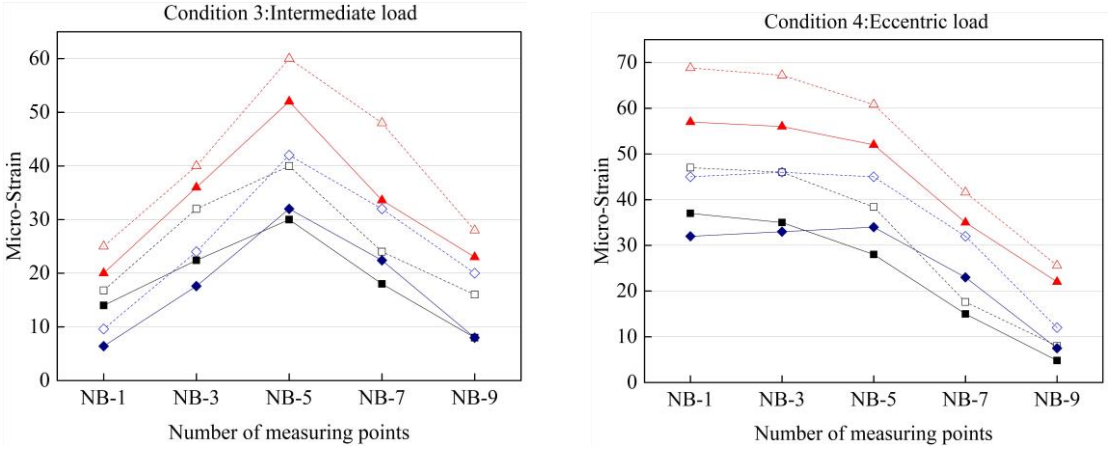

(a) Before strengthening *(b) After strengthening*

(c) Annotation explanation

Fig. 13 - Recorded concrete strains in condition 2

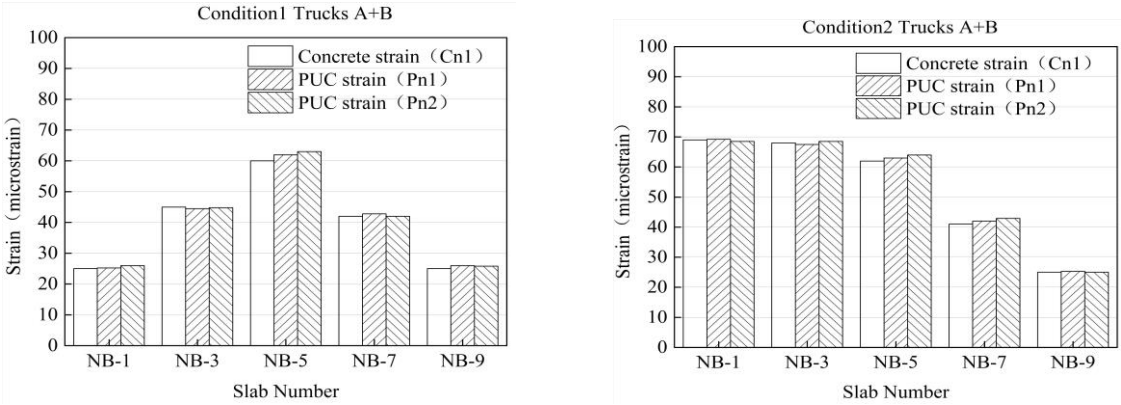

(*a) Condition1 (Trucks A+B)* *(b) Condition2 (Trucks A+B)*

Fig. 14 - Concrete Strains and PUC Strains at Different Positions

The recorded strain values of gages C_{n1}, P_{n2} and P_{n1} for the five slabs in condition 1 and condition 2 are shown in Figure 14. In comparing the recorded concrete strains (gage C_{n1}) and PUC strains (gage P_{n1} and gage P_{n2}), the concrete strain values are close to the PUC strain values on the same horizontal height. Therefore, PUC strain compatibility is well at the live load. In comparing the PUC strains (gage P_{n1} and gage P_{n2}) with those recorded on the concrete (gage C_{n1}), the PUC strains are approximately the same as that of concrete strains. Strain compatibility

leads to the higher PUC strain than the concrete strain because the bottom PUC is physically located below the bottom concrete in the beam section.

Measured concrete strains of slab 1 and slab 9 in the flange plate position are listed in Table 3. Two trucks (Trucks A + B) were parked on the bridge in the condition 1 and condition 2. From this table, in comparing the strains for the given gages before and after pouring PUC, the compressive strains in the concrete were higher after the PUC was poured. In investigating this matter further, the axes were determined as shown in Table 4. Two trucks (Trucks A + B) were parked on the bridge in condition 1. From this table, as expected, the neutral axes of slab1 and slab5 migrated downwards by about 56mm and 55 mm, respectively, after the PUC was poured in condition1.

Tab. 3 - Measured compressive strain on slab 1 and slab 9

Condition	Gage C15 strain (με)		Gage C95 strain (με)	
	Before	After	Before	After
1	-19	-21	-18	-20
2	-27	-31	-11	-13

Tab. 4 - Neutral axis investigation on condition 2

Slab number	Before strengthening (με)			After strengthening (με)		
	Gage Cn1 strain (με)	Gage Cn5 strain (με)	Neutral axis location (mm)	Gage Cn1 strain (με)	Gage Cn5 strain (με)	Neutral axis location (mm)
1	85	-27	193	69	-31	248
9	32	-11	205	27	-13	260

DEFLECTION MEASUREMENT

Displacement meters were installed on the bottom of the hollow slabs to measure the midspan deflection in the different conditions. The midspan deflection of all the slabs before strengthening in condition 1 is shown in Figure 15a. The deflection of slab 5 was the maximum under the symmetrical loads. The maximum deflections were 3.9 mm and 2.8 mm for two trucks (Trucks A + B) before and after strengthening, respectively. The deflection was reduced by 3mm compared with that before reinforcement. The deflection for slab 1 and slab 5 were 1.5 mm and 2.7 mm before strengthening, respectively. The deflection for slab 1 and slab 5 were 1.1 mm and 2.2 mm after strengthening, respectively. Figure 15b shows the midspan deflection of all the slabs after strengthening in condition 2. The maximum deflections of slab 1 were 4.6mm before strengthening. After strengthening, the deflection was 3.8 mm for the two trucks (Trucks A + B). As expected, a certain decrease in deflection after the application of PUC reinforcement could be observed.

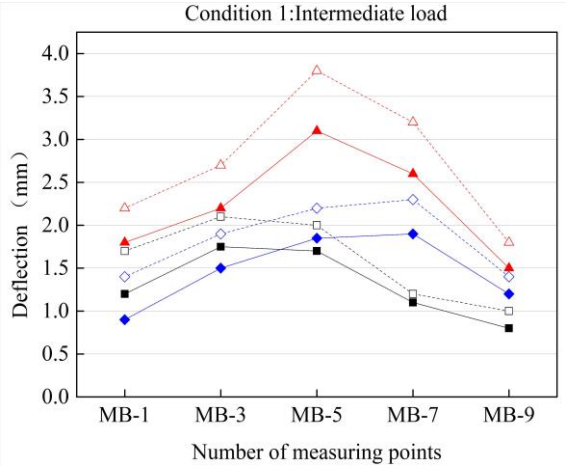

(a) Deflections in the condition 1

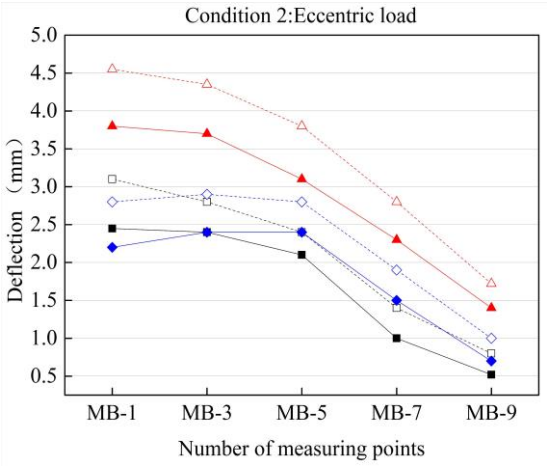

(b) Deflections in the condition 2

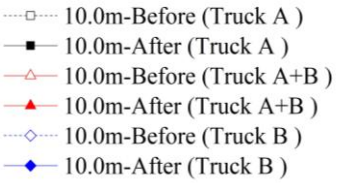

(c) Annotation explanation

Fig. 15 - Measured deflection of hollow slabs in condition 1 and condition 2

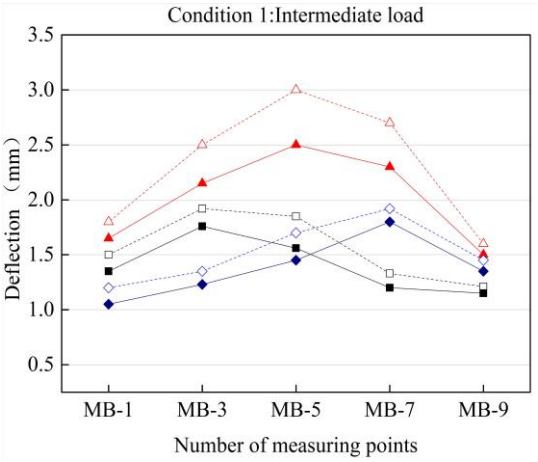

(a) Deflections in the condition 3

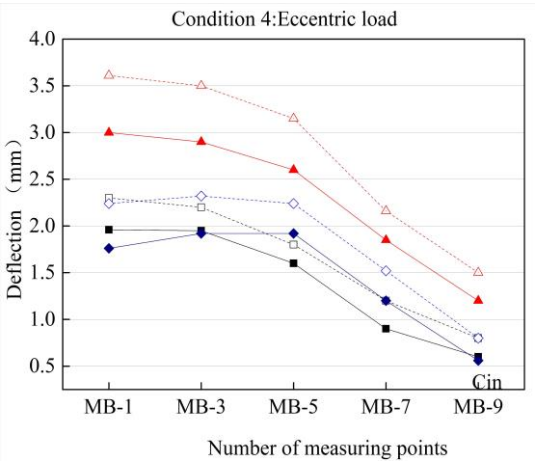

(b) Deflections in the condition 4

Fig. 16 - Measured deflection of hollow slabs in condition 1 and condition 2

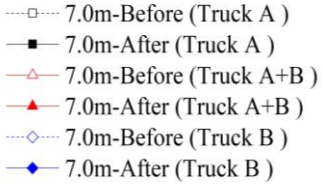

(c) Annotation Explanation

Fig. 16 - Measured deflection of hollow slabs in condition 1 and condition 2

Figure 16a and Figure 16b show the midspan deflection of all the beams before and after strengthening in condition 3 and condition 4, respectively. In condition 3, the deflections of slab 5 were 3.0 mm and 2.5 mm for the two trucks (Trucks A + B) before and after strengthening, respectively. The deflection decreased by about 0.5 mm after strengthening. Before strengthening, the deflections of slab 1 and slab 3 were 1.7 mm and 2.5mm, respectively. After strengthening, the deflections of slab 1 and slab 3 were 1.7 mm and 2.2 mm, respectively. In condition 4, the deflections of slab 1 were 3.7 mm and 3.0 mm for the two trucks (Trucks A + B) before and after strengthening, respectively. The deflection decreased by about 0.7 mm after strengthening. Before strengthening, the deflections of slab 3 and slab 5 were 3.5 mm and 3.2 mm, respectively. After strengthening, the deflections of slab 1 and slab 3 were 2.2 mm and 2.8 mm, respectively.

These findings represent an initially good performance, although the long-term performance will be monitored throughout the next year.

CRACKS

In the load test before retrofitting, the width of the cracks increased with the test load, but no new cracks appeared. These cracks had affected the durability of the bridge and would have further reduced the performance of the bridge if no actions were taken. In observing the development of the cracks after reinforcement, a crack (2-2 measure point) in the side slab for slab 9 was selected to be the observation crack of the load test. The width of the crack on the bottom concrete is 0.15mm before strengthening. The depth from the observation location to the bottom concrete surface was 10cm. The width of the crack at the observation location is 0.08mm. Its width was unchanged for one truck (Truck A), 0.01mm for two trucks (Trucks A + B) in condition 2 and closed when the trucks were moved from the deck. Furthermore, periodical inspections were conducted to observe the development of the crack. The crack was found to be stable.

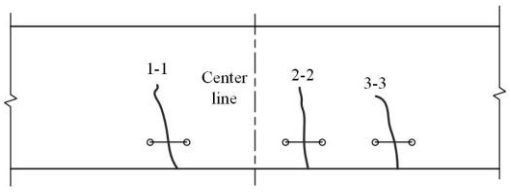

Fig. 17 - Schematic diagram of fracture observation

LIVE-LOAD DISTRIBUTION FACTORS

Many techniques are available in determining transverse live-load distribution or girder distribution factors (DFs). Khaloo et al. [20] analysed the DFs by using the finite element method

considering four different parameters. Field testing could also provide information on live-load DFs for a given bridge type and geometry [21-23]. As the geometric size of all the hollow slabs is almost the same, the stiffness of every slab can be considered as having an equal value. The DFs can be determined from field. measurements using the following:

$$DF_i = \delta_i / \sum \delta_i \tag{8}$$

where δ_i is the maximum static deflection in the i th slab, and $i = 1 \sim 5$. The deflection measurements shown in Figure 18 for Pia oFa Bridge in condition 2 were used to determine the live-load DFs according to Equation (7). From the horizontal hinged plate method [24], live-load DFs that can be compared with the measured DFs Figure 18 were provided. The slab 9 deflected by 2.5 mm for one truck (Truck A) in condition 2. The total deflection of all of the slabs was 8.5mm for a live-load DF of about 2.5/8.5 or 0.29. The live-load DF is 0.30 using the horizontal hinged plate method. The live-load DFs depend on slabs spacing, span, girder bending stiffness and girder torsional stiffness. The slab 9 deflected by 3.8 mm for the two trucks (Truck A + B) in condition 2. The total deflection of all of the girders was 14.3 mm for a live-load DF of about 3.8/14.3 or 0.27. The live-load DF is 0.28 using the horizontal hinged plate method. Thus, the horizontal hinged plate method is applicable for calculating the live-load DFs of T-beam bridges.

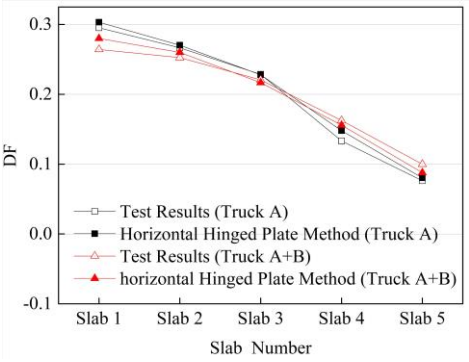

Fig. 18 - Live -load DFs calculated from test results and horizontal hinged plate method in condition 2

CONCLUSION

This paper uses an innovative method to strengthen a 25-year bridge with polyurethane cement composite material. The main construction process was described. Load tests were conducted before and after strengthening to evaluate the performance of this bridge and the effectiveness of the reinforcement method. Based on load test and analysis, the main results obtained in this study are listed below:

The blending strength of the hollow slab bridge strengthened with PUC can be determined by force equilibrium, strain compatibility and controlled failure modes. The fabricated hollow slab bridge strengthened with PUC is governed by the PUC design strength.

The maximum carrying capacity of the main girder was increased by about 20% after PUC material was poured. The main girder deflection was reduced by about 28%. The width of the cracks was reduced in different degrees. Repeated load tests will be conducted to observe long-term performance.

The PUC strain deformation complies with strain coordination under the static load. The neutral axis of hollow slab migrated downwards after the PUC was poured.

The transverse connection between slabs was proven by the hinged joints. The live-load DFs of the strengthened bridge calculated by experimental results were in good agreement with the modified eccentric-pressed method.

REFERENCES

[1] Michael H Faber and Dimitri V Val and Mark G Stewart. Proof load testing for bridge assessment and upgrading[J]. Engineering Structures, 2000.

[2] Kim T H , Lee K M , Chung Y S , et al. Seismic damage assessment of reinforced concrete bridge columns[J]. Engi-neering Structures, 2005, 27(4):p.576-592.

[3] J. Campos E. Matos, J. R. Casas & J. Figueiras. A new methodology for damage assessment of bridges through in-strumentation: application to the Sorraia River Bridge[J]. Structure and Infrastructure Engineering, 2005.

[4] G. H. Xing, T. Wu, B. Q. Liu and H. Huang, “Experimental Investigation of Reinforced Concrete T-Beams Strengthened with steel Wire Mesh Embedded in Polymer Mortar Overlay”,Advances in structural Engineering, vol.13, no. 1, pp. 69-79, 2010.

[5] G. Wu, Z. S. Wu, W. Yang and J. B. Jiang, “Flexural strengthening of RC beams using distributed prestressed high strength steel wire rope: theoretical analysis”, Structure and Infrastructure Engineering, vol.10, no. 2, pp. 160-171, 2012.

[6] Chen W C . Some experimental investigations in the drilling of carbon fiber-reinforced plastic (CFRP) composite laminates[J]. International Journal of Machine Tools and Manufacture, 1997, 37(8):1097-1108.

[7] Wenwei W, Guo L . Experimental study and analysis of RC beams strengthened with CFRP laminates under sus-taining load[J]. International Journal of Solids and Structures, 2006, 43(6):1372-1387.

[8] Zhang J , Zhou P , Guan C , et al. An ultra-lightweight CFRP beam-string structure[J]. Composite Structures, 2020, 257(1):113149.

[9] Dong L , Guangyuan C , Yuquan C , et al. Experimental research and numerical simulation of RC beams strength-ened with bonded steel plates[J]. ence China Technological ences, 2012, 55(012):3270-3277.

[10] Vincenzo Colotti Giuseppe Spadea. Shear Strength of RC Beams Strengthened with Bonded Steel or FRP Plates[J]. Journal of Structural Engineering, 2001.

[11] Hua Huang, Jianling Hou. Mechanism of Debonding Failure between Reinforced Layer with Stainless Steel Wire Mesh and Polymer Mortar and RC Structures[J]. Advanced Materials Research, 2010:163-167.

[12] Hua Huang, Boquan Liu, Kailin Xi. Interfacial tensile bond behavior of permeable polymer mortar to concrete[J]. Construction and Building Materials, 2016, 212:210-221.

[13] L. Guiwei and O.Hisanori,“A foundational study on static mechanical characteristics of the super lightweight and high strength material using fly-ash”,Journal of the Society of Materials Science, vol.55, no. 8, pp. 738-745, 2006.

[14] K. Haleem, L. Guiwei and Y. Wenyong, “Experimental study to investigate mechanical properties of newmaterial polyurethane-cement composite (PUC)”,Construction and Building Materials, vol. 50, no. 15, pp. 200-208, 2014.

[15] K. Haleem, Z.Lianzhenand L. Guiwei,“An experimental study on strengthening reinforced concrete T-beams using new material poly-urethane-cement (PUC)”,Construction and Building Materials, vol.40, pp. 104-117, 2013.

[16] Ministry of Communications of China, Design Code of Highway Reinforced Concrete and Prestressed Concrete Bridge (JTJ023-85). Beijing: China Communication Press, 1985.

[17] Ministry of Construction of China, Design Code of Concrete Structures (GB50010). Beijing: China Building Industry Press, 2010.

[18] Chappuis J L , Veldman M S , Taylor H S . Surgical instrumentation and method for forming a passage in bone hav-ing an enlarged cross-sectional portion: US.

[19] Yang B , Chen S H . Methods for Calculating Shear Capacity on Oblique Section of Bending Members Strengthened with Enlarged Section[J]. Journal of Highway & Transportation Research & Development, 2016, 11(3):71-78.
[20] A. Khaloo, and H.Mirzabozorg, “Load Distribution Factors in Simply Supported Skew Bridges”, Journal of Bridge Engineering, vol.8, no. 4, pp. 241-244, 2003.
[21] M. Schwarz, and J.Laman, “Response of Prestressed Concrete I-Girder Bridges to Live Load”, Journal of Bridge Engineering, vol.1, no. 1, pp. 1-8, 2001.
[22] S. Kim, and A.Nowak, “Load Distribution and Impact Factors for I-Girder Bridges”, Journal of Bridge Engineering, vol.3, no. 97, pp. 97-104, 1997.
[23] Seo J , Kidd B . Parametric study of deteriorating precast concrete double-tee girder bridges using computational models[J]. Engineering Structures, 2021, 230(3):111714.
[24] Ministry of Communications of China, General Specification for Highway Bridge and Culvert Design (JTG D60). Beijing: China Communication Press, 2015.

CIVIL ENGINEERING JOURNAL

Article no. 30

THE CIVIL ENGINEERING JOURNAL 2-2021

TORSIONAL SHEAR STRESS WITH ARBITRARY CROSS-SECTIONS IN HOMOGENEOUS ISOTROPIC ELASTIC MATERIAL USING FINITE ELEMENT METHOD

Dang-Bao Tran[1,2]

1. *VSB–Technical University of Ostrava, Faculty of Civil Engineering, Department of Structures, Ludvíka Podéště 1875/17, 708 00 Ostrava, Czech Republic; dang.bao.tran@vsb.cz*
2. *Thu Dau Mot University, Faculty of Architecture, Department of Civil Engineering, Tran Van On 06, 75000 Binh Duong Province, Vietnam;baotd@tdmu.edu.vn*

ABSTRACT

Determining the shear stress of a structural element caused by torsion is a vital problem. The analytical solution of the Saint-Venant torsion is only suitable for simple cross-sections. The numerical methods to evaluate the shear stress due to torsion of complicated cross-sections is indispensable. Many scientists have studied the torsion problem with various numerical methods. This paper aims to present an efficient finite element method for assessing the shear stress with arbitrary cross-sections in homogeneous isotropic elastic material due to torsion. MATLAB is the language for programming the numerical method. The validation examples were performed to show the reliability and efficiency of the author's numerical method.

KEYWORDS

Torsional shear stress, Isoparametric eight-noded quadrilateral elements, Saint-Venant torsion, Warping function

INTRODUCTION

Torsion in the structure occurs due to asymmetrical loads, either by geometric dimensions or by interconnections between members. In many cases, torsion can be governing design factors. It is, therefore, essential to accurately determine the shear stress caused by torsion. Saint-Venant analysed the torsion problem using the semi-inverse method, assuming an unknown displacement to satisfy the equilibrium equations and boundary conditions. Prandtl then introduced the stress function of the Saint-Venant torsion and the method of membrane analogy [1]. However, determining the shear stress due to torsion by the analytic solution is complicated for a complex single connected domain or multiply connected domain. A single connected domain is a domain where the cross-section is bounded by a closed. The multiply connected domain is the domain where the cross-section is bordered by several closed.

Nowadays, structural elements such as beams and columns are more and more complicated in their shapes. Hence the use of numerical methods to determine shear stress due to torsion is indispensable. Various numerical methods to assess torsional shear stress have been performed by many researchers [2-22]. Ely, J. F., and Zienkiewicz, O. C. [2] first solved Poisson's equation of Prandtl's stress function using the finite difference method and investigated the rectangular section with and without holes. Herrmann, L. R. [3] utilized the finite element method to calculate the warping function of the torsion of irregular sectional shapes. Based on the Hellinger–Reissner principle, Xiao, Q. Z., et al. [4] developed a 4-node element with four stress parameters to determine the shear

stress for the polygonal section. Gruttmann, F. et al. [5] used the finite element method to evaluate shear stress using the warping function, which is more convenient than using Prandtl's stress function when considering a multiply connected domain. Gruttmann's numerical method has been implemented into an enhanced version of the program FEAP [6], which used isoparametric four-noded quadrilateral elements. Fialko, S.Y. et al. [7] developed a numerical method using constant triangular elements to solve the Saint Venant problem of torsion, and torsionless bending of prismatic bars is realized in the SCAD software [8]. Jog, S. et al. [9] presented a finite-element formulation for Saint Venant torsion with a multiply-connected domain in an anisotropic material. Recently, Beheshti, A. [10] derived a finite element from strain-gradient elasticity for torsion of prismatic bars with minimal dimensions.

Besides the finite difference and finite element method, many authors have applied other numerical methods such as the boundary element method (BEM) [11-16], line element-less method (LEM) [17-18], a null-field integral technique [19], and finite-volume method [20-21] to analyse the torsion problem. Katsikadelis, J. T. et al. [11] examined the torsion of general composite bars by BEM while Gaspari, D. et al. [12] tackled orthotropic beams with a polygonal cross-section. Barone, G. et al. [13] implemented the Complex Variable Boundary Element Method to examine the torsion problem in the single connected domain. Lee, J.W. et al. [14] obtained a new BEM from the general Cauchy integral formula derived from the Borel–Pompeiu formula to analyse the torsion problem. Paradiso, M. et al. [15] achieved an efficient method to determine the warping function parameter with the general cross-section. Chen, K. H. et al. [16] introduced a new error estimation technique in BEM to optimise the torsion problem with a multiply-connected domain. Di Paola, M. et al. [17] proposed LEM to deal with shear stress in torsion problem with isotropic material and arbitrary cross-section. Santoro, R. [18] handled the Saint Venant torsion problem for orthotropic beams with a general cross-section by LEM. Chen, J-T. et al. [19] introduced the null-field integral technique to analyse the torsion problem of circular cross-sections with round holes. Chen, H. et al. [20-21] developed a new finite-volume based on Bansal and Pindera's work to investigate Saint Venant's torsion problems of homogeneous and composite prismatic bars with multiply connected domain.

In summary, all of the works show the feasibility and effectiveness in academia. Currently, to the author's knowledge, Gruttmann's method [5] has been developed into the FEAP program [6] of the University of California, Berkeley, and Allplan Bridge [22]. Fialko's method [7] is similar to Gruttmann, developed as a module in the SCAD commercial software [8]. It means the methods of Gruttmann and Fialko are practical. However, due to the use of the four-noded quadrilateral element in FEAP and the constant strain triangle element in SCAD, to achieve high accuracy, it is necessary to mesh very smoothly, which affects the calculation speed. So, this research aims to develop a new numerical method (NMB) based on the work of Gruttmann by using the isoparametric eight-noded quadrilateral element. The validation examples were performed to show the reliability and efficiency of NMB.

FINITE ELEMENT METHOD PROCEDURE

Figure 1 shows the arbitrary cross-section of prismatic beam in homogeneous isotropic elastic material, the longitudinal axis is the x-axis, the cross-section denoted Ω is in yz plane. The multiply connected domain Ω is bounded by Γ_1, Γ_2,..., Γ_{n-1}, Γ_n . S is the centre of gravity. On Γ_1, Γ_2,..., Γ_{n-1}, Γ_n the right-handed orthogonal basis system is defined with tangent vector **t** and outward normal vector $\mathbf{n}=[n_y, n_z]^T$. With **t** the orientation of the associated coordinate *s* is uniquely defined.

The displacement field $\mathbf{u}=[\mathrm{u_x}, \mathrm{u_y}, \mathrm{u_z}]^T$ is expressed as [1]

$$u_x = \alpha\omega^T, u_y = -\beta_x z, \; u_z = -\beta_x y, \tag{1}$$

where β_x: torsion angle, $\alpha = \frac{d\beta_x}{dx}$, $\omega^T(y,z)$: warping function for torsion. Here, the constraint of the warping for torsion is

$$\int_{\Omega} \omega^T dA = 0. \tag{2}$$

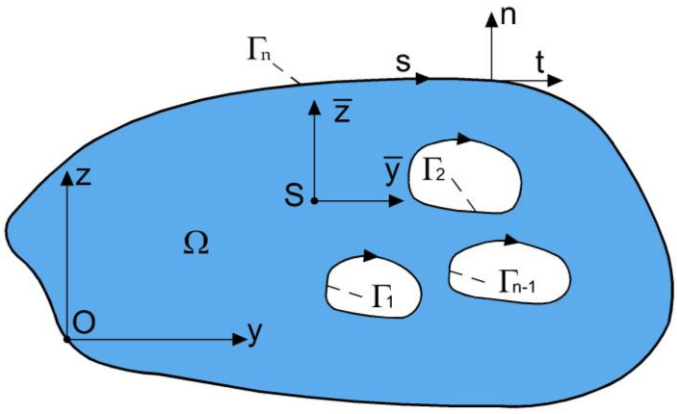

Fig. 1 - Cross-section of a prismatic bar.

The shear stresses are given as

$$\tau_{xy} = G\alpha\left(\frac{\partial\omega^T}{\partial y} - z\right),\ \tau_{xz} = G\alpha\left(\frac{\partial\omega^T}{\partial z} + y\right). \tag{3}$$

The polar second moment of area can be written as

$$I_T = \int_{\Omega}\left[\left(\frac{\partial\omega^T}{\partial z} + y\right)y - \left(\frac{\partial\omega^T}{\partial y} - z\right)z\right]dA. \tag{4}$$

The governing differential equation for the Saint-Venant torsion is expressed as

$$\frac{\partial^2\omega^T}{\partial^2 y} + \frac{\partial^2\omega^T}{\partial^2 z} = 0 \quad in\ \Omega. \tag{5}$$

Meanwhile, the boundary condition is given as

$$n_y\frac{\partial\omega^T}{\partial y} + n_z\frac{\partial\omega^T}{\partial z} = n_y z - n_z y \quad on\ \Gamma_i (i = 1,2,...,n), \tag{6}$$

$$\text{where } n_y = \frac{dz}{ds},\ n_z = -\frac{dy}{ds}. \tag{7}$$

The governing differential equation (5) is transformed into the weak form by using the Galerkin's method as below

$$G(\omega^T,\eta) = \int_{\Omega}\left[\frac{\partial\omega^T}{\partial y}\frac{\partial\eta}{\partial y} + \frac{\partial\omega^T}{\partial z}\frac{\partial\eta}{\partial z}\right]dA - \oint_{\partial\Omega}(n_y z - n_z y)\eta ds = 0, \tag{8}$$

with test function $\eta \in H^1(\Omega)$.

The equation (8) is approximated by using the finite element method. Gruttmann's method used isoparametric four-noded quadrilateral elements. To improve the computation speed, NMB used isoparametric eight-noded quadrilateral elements. The $\mathbf{x}=[y,z]^T$, the unknown function ω^T and the test function η are interpolated in the local coordinate system as follows

$$\mathbf{x}^h=\sum_{i=1}^{8}N_i(\xi,\eta)\mathbf{x}_i\ ,\ (\omega^T)^h=\sum_{i=1}^{8}N_i(\xi,\eta)\omega_i^T\ ,\ (\eta)^h=\sum_{i=1}^{8}N_i(\xi,\eta)\eta_i, \tag{9}$$

where *h* denotes the approximate solution of the finite element method, $N_i(\xi,\eta)$ denotes the shape function of the element. Figure 2 shows the isoparametric eight-noded quadrilateral element used in NMB. The shape functions of this element can be described as follows [23, 24]

$$\begin{aligned}
N_1(x,h)&=\frac{1}{4}(1-x)(1-h)(-1-x-h),\ N_2(x,h)=\frac{1}{4}(1+x)(1-h)(-1+x-h),\\
N_3(x,h)&=\frac{1}{4}(1+x)(1-h)(-1+x+h),\ N_4(x,h)=\frac{1}{4}(1-x)(1+h)(-1+x+h),\\
N_5(x,h)&=\frac{1}{2}(1-x^2)(1-h),\ N_6(x,h)=\frac{1}{2}(1+x)(1-h^2),\\
N_7(x,h)&=\frac{1}{2}(1-x^2)(1+h),\ N_8(x,h)=\frac{1}{2}(1-x)(1-h^2).
\end{aligned} \tag{10}$$

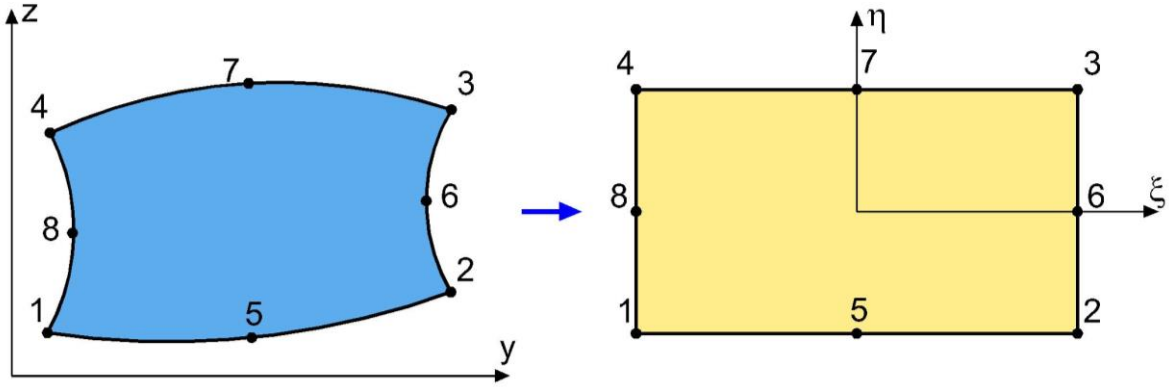

Fig 2 -. Isoparametric eight-noded quadrilateral element.

Inserting the derivatives of $(\omega^T)^h$ and η^h into the equation (8) reads as

$$\bigcup_{e=1}^{numel}\sum_{i=1}^{8}\sum_{j=1}^{8}(K_{ij}^e\omega_j^T-F_i^e)=0. \tag{11}$$

Here, $\bigcup$ denotes the assembly operator with *numel* the total number finite elements. The stiffness part K_{ij}^e to the nodes *i* and *j* and the right hand F_i^e read

$$\begin{aligned}
K_{ij}^e&=\int_{\Omega_e}\left(\frac{\partial N_i}{\partial y}\frac{\partial N_j}{\partial y}+\frac{\partial N_i}{\partial z}\frac{\partial N_j}{\partial z}\right)dA_e=\int_{-1}^{1}\int_{-1}^{1}\left(\frac{\partial N_i}{\partial y}\frac{\partial N_j}{\partial y}+\frac{\partial N_i}{\partial z}\frac{\partial N_j}{\partial z}\right)|\mathbf{J}|d\xi d\eta,\\
K_{ij}^e&=\sum_{p=1}^{P}\sum_{q=1}^{Q}w_pw_q\left(\frac{\partial N_i}{\partial y}(\xi_p,\eta_q)\frac{\partial N_j}{\partial y}(\xi_p,\eta_q)+\frac{\partial N_i}{\partial z}(\xi_p,\eta_q)\frac{\partial N_j}{\partial z}(\xi_p,\eta_q)\right)\left|\mathbf{J}(\xi_p,\eta_q)\right|.
\end{aligned} \tag{12}$$

$$F_i^e = \int_{\Omega_e} \left(\frac{\partial N_i}{\partial y} z - \frac{\partial N_i}{\partial z} y \right) dA_e = \int_{-1}^{1} \int_{-1}^{1} \left(\frac{\partial N_i}{\partial y} z - \frac{\partial N_i}{\partial z} y \right) |\mathbf{J}| d\xi d\eta,$$
$$F_i^e = \sum_{p=1}^{P} \sum_{q=1}^{Q} w_p w_q \left(\frac{\partial N_i}{\partial y}(\xi_p, \eta_q) z - \frac{\partial N_i}{\partial z}(\xi_p, \eta_q) y \right) |\mathbf{J}(\xi_p, \eta_q)|. \quad (13)$$

where $\mathbf{J}$ denoted as Jacobian matrix defined as

$$\mathbf{J} = \begin{bmatrix} \frac{\partial y}{\partial x} & \frac{\partial z}{\partial x} \\ \frac{\partial y}{\partial h} & \frac{\partial z}{\partial h} \end{bmatrix} \quad (14)$$

w_p and w_q are the weights and ξ_p and η_q are the integration points of the Gaussian integration technique. NMB uses 3 x 3 Gauss quadrature derived from the 1D case, where the quadrature points are located at $-\sqrt{3/5}$, 0 and $\sqrt{3/5}$, and the corresponding weights are equal to 5/9, 8/9, and 5/9, respectively (see [23, 24]). The value ω_i^T of one arbitrary nodal point *i* has to be value 0.

VALIDATION EXAMPLES

The objective of this section is to demonstrate the reliability and effectiveness of NMB. For this purpose, four validation examples derived from [1, 5, 9] were examined, and their results are compared with those analyzed by NMB implemented in MATLAB R2015a.

A bar of square cross-section subjected to the torsion moment $M_T = 1$ kN.m with the length of the edge 2 m is analysed in the first example. Jog, C.S. et al. [9] investigated this problem using 16 isoparametric nine-noded quadrilateral elements. To achieve convergence values of the shear stress and the polar second moment of area, the square cross-section is divided into 16, 64, 256 elements with uniform mesh by NMB, respectively. Figure 3 shows the discretization of the square cross-section with 16 eight-noded quadrilateral elements. The points, A, B, C, D, correspond with the coordinates (0, 1), (2, 1), (0, 0), (0, 2), respectively.

The analytical results of maximum shear stress and polar second moment of area obtained from [1, 9] are $\tau_{\max} = 0.592$ kPa, $I_T = 2.24923$ m^4, respectively. Table 1 shows the comparison of the results of the maximum shear stress, the polar second moment of area between the methods. The results of NMB-16 elements and Jog, C.S. et al. [9] are the same. When the square cross-section is refined into 256 elements, NMB is in good agreement with analytical solutions.

Tab. 1 - The maximum shear stress $\tau_{\max}$ and the polar second moment of area I_T of square cross-section

Factors	Analytical solutions	Jog, C.S. et al. [9]	NMB- 16 elements	NMB- 256 elements
$\tau_{\max}^{(a)}$ [kPa]	0.592	0.6173	0.619174	0.601461
$I_T^{(b)}$ [m^4]	2.24923	2.2519	2.25187	2.24925
Error$^{(a)}$, (%)	-	4.273	4.590	1.598
Error$^{(b)}$, (%)	-	0.1187	0.1173	0.000

Figure 4 depicts the distribution of shear stress τ_{xz} for square cross-section, which decreases the magnitude gradually from the midpoint of the edge to the centre of gravity along the y-axis [1].

Figure 5 and 6 present the variation of the shear stress τ_{xz} along the AB and CD segment, respectively. With 16 elements, NMB and Jog, C.S. et al. [9] cannot capture precisely the shear stress distribution along the CD segment. When the mesh is fine enough, in this case, 256 elements, the results of NMB and theory harmonize very well.

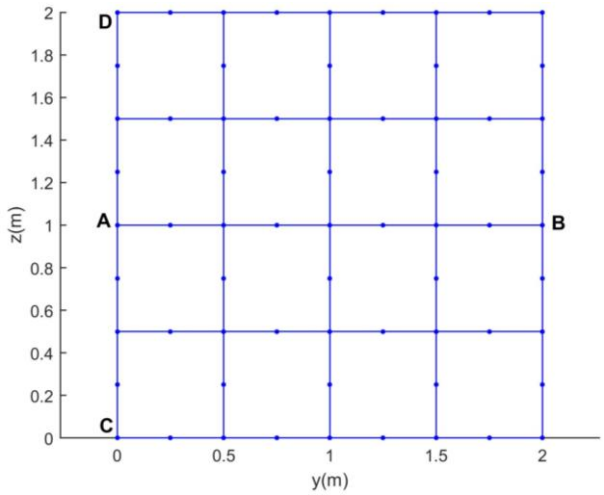

Fig. 3 - Discretization of the square cross-section with 16 elements.

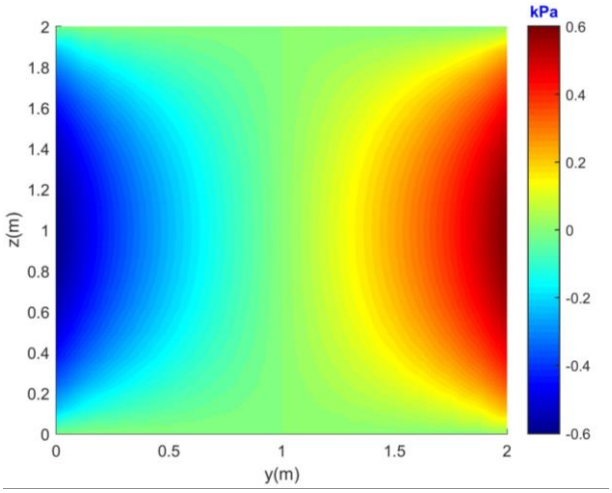

Fig. 4 - Distributed shear stresses τ_{xz} for square cross-section.

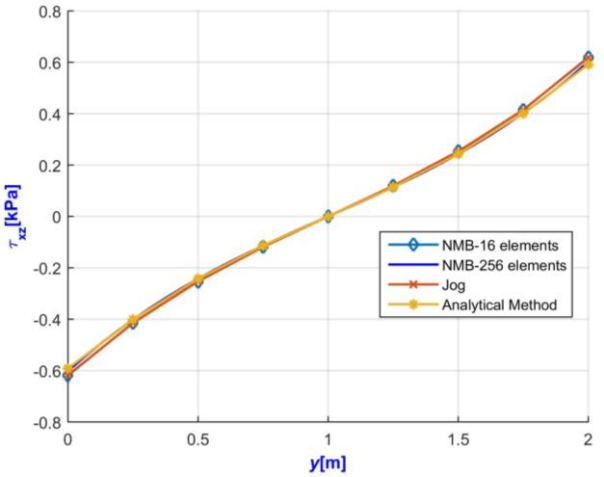

Fig. 5 - The variation of shear stress τ_{xz} along the AB segment.

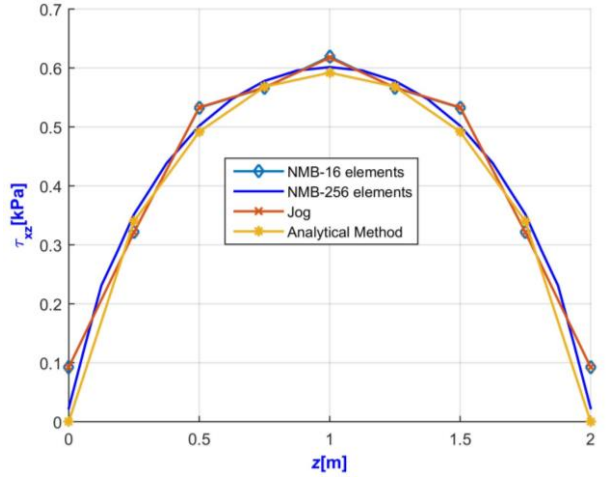

Fig. 6 - The variation of shear stress τ_{xz} along the CD segment.

The second example is an equilateral triangle subjected to the torsion moment $M_T = 1$ kN.m with the height of the triangle 0.2 m. The analytical results of maximum shear stress $\tau_{\max}$ and polar second moment of area I_T are 1.62380 MPa and 6158.40 cm^4, respectively [1]. The triangular cross-section was discretized 4, 8, 14, 37, 57, 109, 658 eight-noded quadrilateral elements with non-uniform mesh to obtain the convergence results.

Tab. 2 - The maximum shear stress τ_{max} and the polar second moment of area I_T of triangular cross- section

Factors	Analytical solution	NMB- 658 elements	Error, (%)
τ_{max} [MPa]	1.62380	1.6247	0.055
I_T [cm^4]	6158.40	6158.40	0.000

It is clear from Table 2 that the results of the maximum shear stress, the polar second moment of area obtained from NMB are in good agreement with the theoretical solution [1]. Figure 7 shows the triangular cross-section divided by 14 eight-noded quadrilateral elements. The points, E, F, correspond with the coordinates (0, $\frac{0.2}{\sqrt{3}}$), (0.2, $\frac{0.2}{\sqrt{3}}$), respectively.

Figure 8 depicts the stress distribution τ_{xy} for triangular cross-section, where magnitude values do not exist along with segment EF [1]. Figure 9 presents the stress distribution τ_{xz} for triangular cross-section. It can observe from Figure 10 that the result of the variation of shear stress τ_{xz} along the EF segments of NMB and analytical method is very well matched.

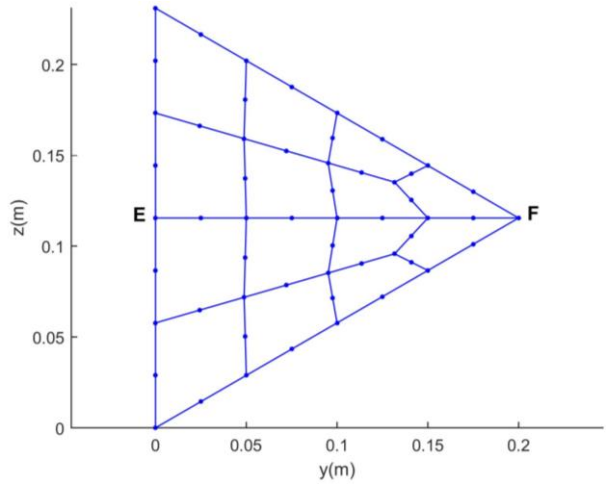

Fig. 7 - Discretization of the triangular cross-section with 14 elements.

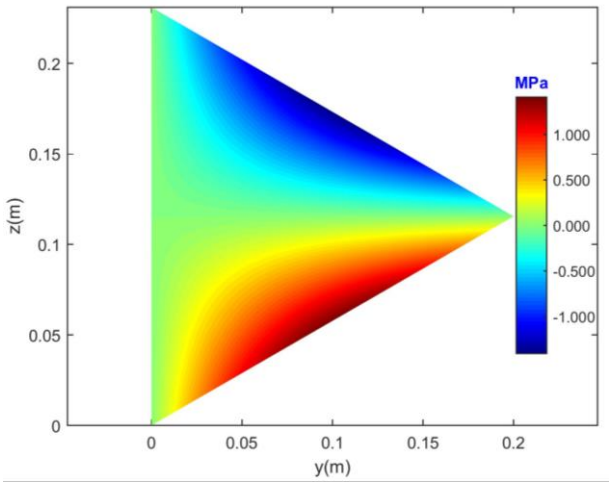

Fig. 8 - Distributed shear stresses τ_{xy} for triangular cross-section.

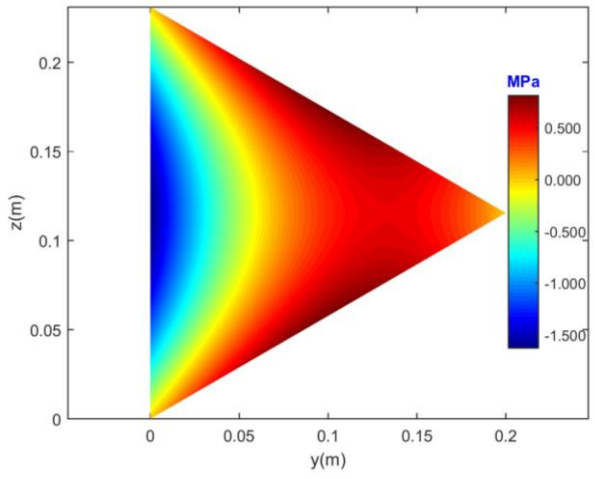

Fig. 9 - Distributed shear stresses τ_{xz} for triangular cross-section.

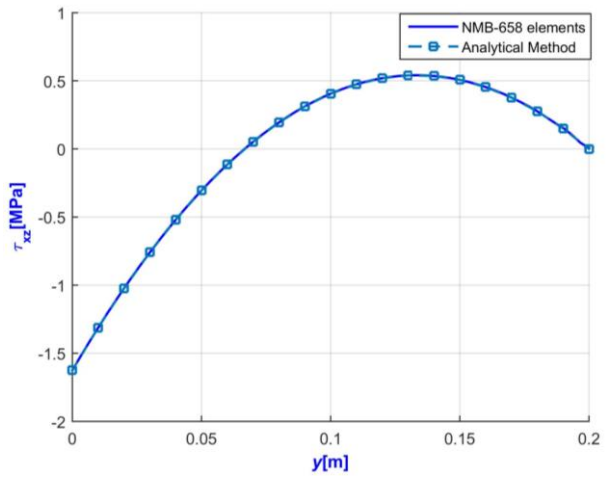

Fig. 10 - The variation of shear stress τ_{xz} along the EF segment with NMB-109 element.

The third example concerns a bar of square cross-section with hole applied to the torsion moment $M_T = 1$ kN.m. Figure 11 shows the geometrical dimensions and the meshing to 96 isoparametric eight-noded quadrilateral elements by NMB of the square cross-section with hole. The points, G, H, I, J, correspond with the coordinates (0, 1), (1.6, 1), (0, 0), (0, 2), respectively.

Jog, C.S. et al. [9] analysed this problem using 96, 1536, 6144 isoparametric nine-noded quadrilateral elements, respectively. Figure 12 depicts the variation of polar second moment of area corresponding to 96, 1536, 6144 discretization elements investigated by NMB. In Table 3, the convergence of the polar second moment of area value by NMB is presented as a comparison with that obtained from Jog, C.S. et al. [9]. Figure 13 and 14 present the stress distribution τ_{xy}, τ_{xz} for square cross-section with hole, respectively. Figure 15 and 16 plot the variation of shear stress τ_{xz} along the segments, GH, IJ, respectively, evaluated with the two methods, Jog, C.S. et al. [9], and NMB. From the figures and table mentioned above, the reliability of the NMB is once more verified.

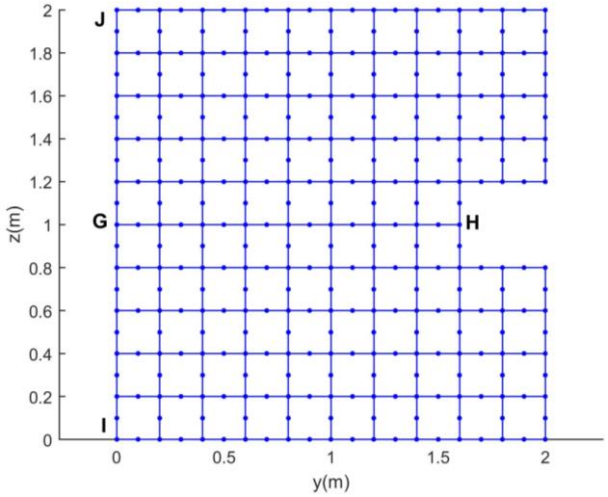

Fig. 11 - The dimension and the discretization to 96 elements of the square cross-section with hole.

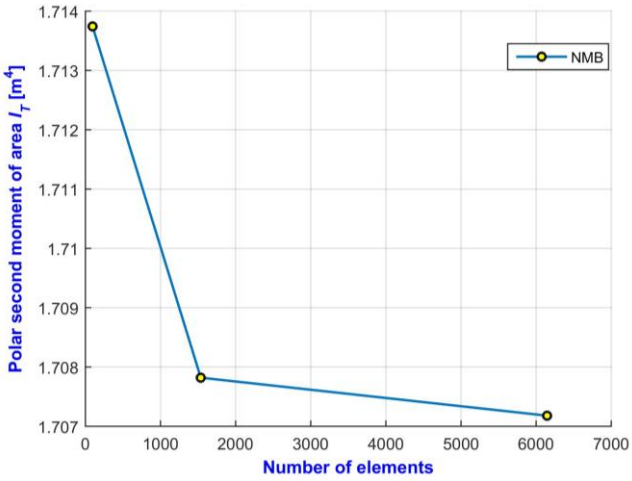

Fig. 12 - The variation of polar second moment of area corresponding to discretization elements.

Tab. 3 - The polar second moment of area of square cross-section with hole

Factors	Jog, C.S. et al.- 6144 elements [9]	NMB- 6144 elements	Error, (%)
I_T [m^4]	1.707	1.70718	0.01054

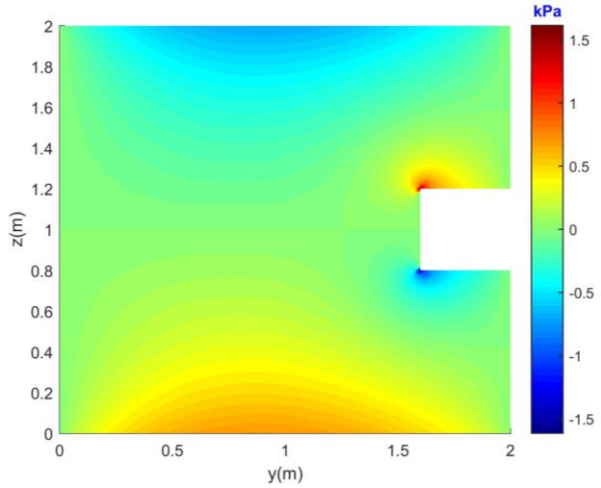

Fig. 13 - Distributed shear stresses τ_{xy} for the square cross-section with hole.

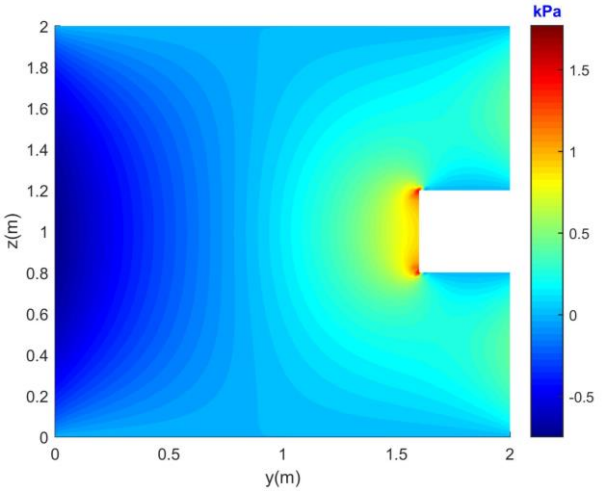

Fig. 14 - Distributed shear stresses τ_{xz} for the square cross-section with hole.

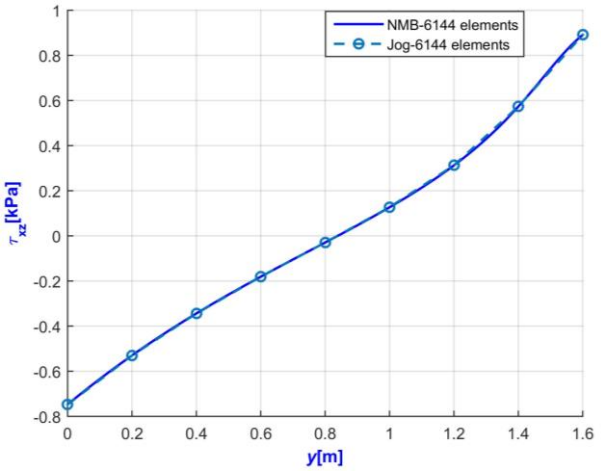

Fig. 15 - The variation of shear stress τ_{xz} along the GH segment.

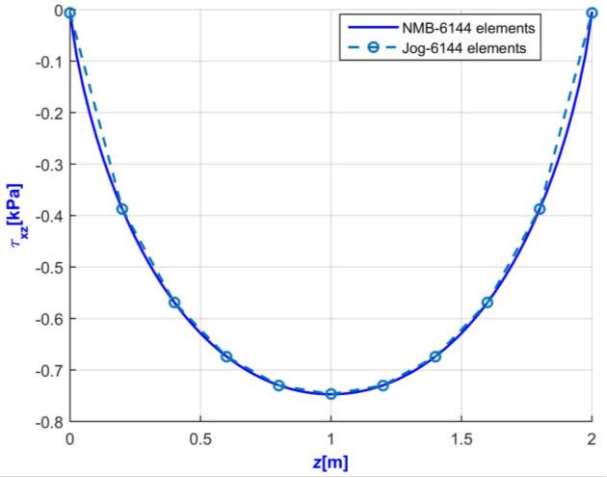

Fig. 16 - The variation of shear stress τ_{xz} along the IJ segment.

According to Figure 17, the bridge cross-section is an example for multiply connected domains was considered the fourth example. With this example, the polar second moment of area of the bridge cross-sections neglected the cantilever part obtained by the analytical solution is 40.0 m^4 [5]. A comparison with a theoretical explanation is not possible. The comparison between NMB and FEAP [5,6], implemented Gruttmann's numerical method by using isoparametric four-noded quadrilateral element, was performed on the convergence speed. The bridge cross-section was divided into 50000 nodes with a uniform mesh by FEAP to obtain the convergence of the results.

In NMB, the bridge cross-section is meshed with 80, 406, 1892, 4634, 11414 nodes to investigate the convergence result. Figure 18 shows the bridge cross-section divided into 80 nodes by NMB. Figure 19 depicts the convergence of the polar second moment of area obtained by NMB with 4634 nodes.

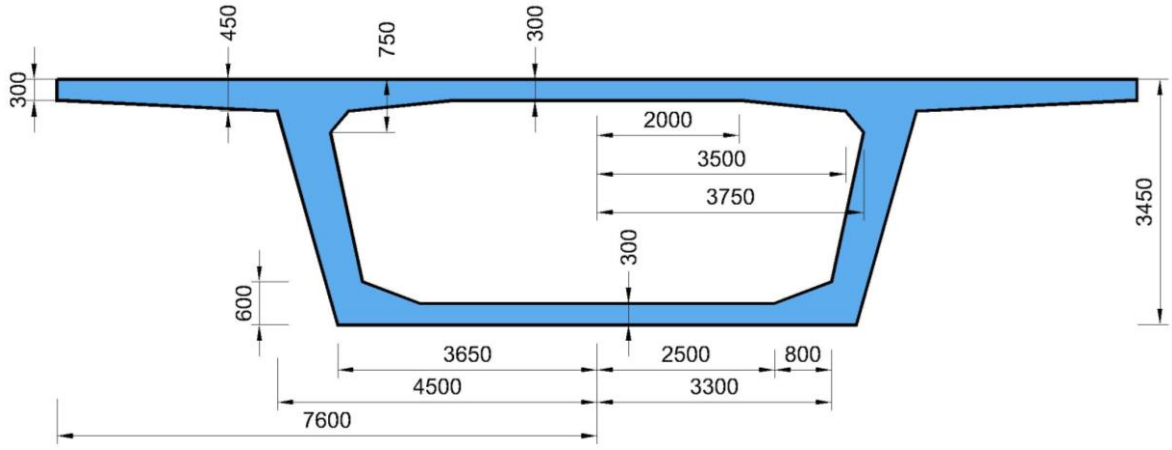

Fig. 17 - Bridge cross-section, with measurements in [m].

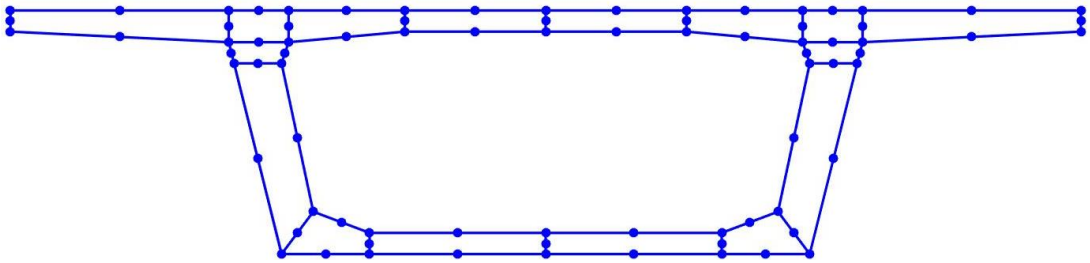

Fig.18 - Discretization of the bridge cross-section to 80 nodes by NMB.

The comparison of the polar second moment of area between the two methods was performed. In Table 4, we can see that the error of the value of the polar second moment of area between the two methods is 1.904%. It should be emphasized that there is no exact analytical solution for this example, and the number of nodes required for the convergence problem of NMB is 10.8 times smaller than that of FEAP. From Table 4, the efficiency of NMB is verified. Figure 20 shows the shear flow of the bridge cross-section under torsion $M_T = 1$ kN.m of NMB. As expected, shear stress is mainly concentrated in the closed part of the section [5].

Tab. 4 - The polar second moment of area of bridge cross-section

Factors	FEAP- 50000 nodes [5,6]	NMB- 4634 nodes	Error, (%)
I_T [m^4]	42.487	43.2963	1.904

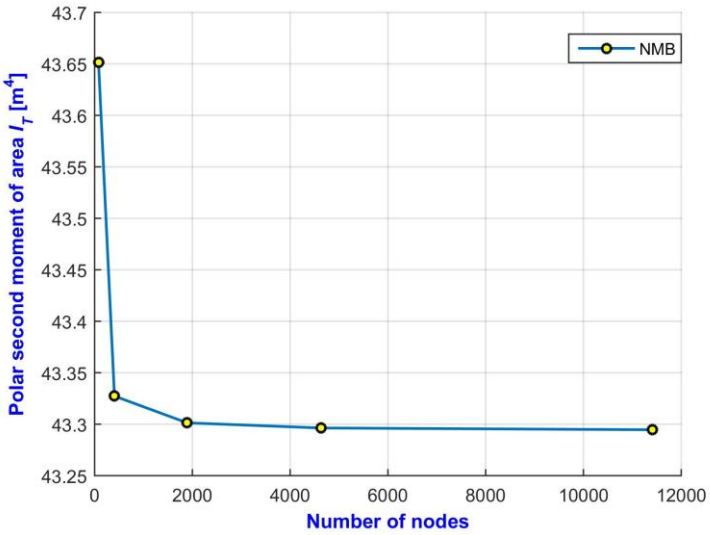

Fig.19 - The values of polar second moment of area with respect to the number of nodes in bridge cross-section.

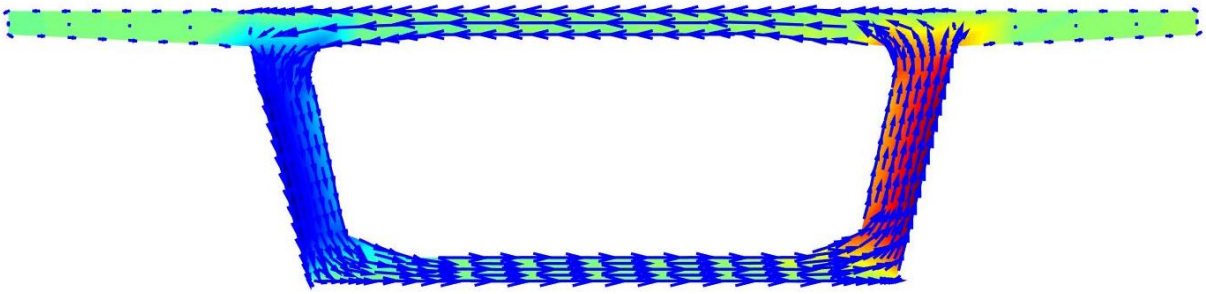

Fig.20.- Shear flow for the bridge cross-section under torsion of NMB.

CONCLUSION

Gruttmann [5] proposed an excellent finite element method for evaluating shear stress due to torsion with arbitrary cross-sections in homogeneous isotropic elastic material based on the Saint-Venant theory. However, the use of isoparametric four-noded quadrialeral elements made the method not reach the best optimization. NMB has been improved Gruttmann's work by using isoparametric eight-noded quadrilateral elements. Through 4 validated examples represented by single connected domain and multiply connected domains, it can conclude that NMB is reliable and efficient in assessing shear stress due to torsion. The shear stress research due to torsion of the arbitrary reinforced concrete section is desirable in the future.

ACKNOWLEDGEMENTS

The works were supported from the Student Grant Competition VSB-TUO. The registration number of the project is SP2021/77 "Nonuniform torsion in prismatic beams with arbitrary cross-sections using FEM".

REFERENCES

[1] Timoshenko, S., Goodier, J. N. Theory of Elasticity, by S. Timoshenko and JN Goodier,... McGraw-Hill book Company, 1951.
[2] Ely, J. F., and Zienkiewicz, O.C. "Torsion of compound bars—A relaxation solution." *International Journal of Mechanical Sciences* 1.4 (1960): 356-365.
[3] Herrmann, L.R. "Elastic torsional analysis of irregular shapes." *Journal of the Engineering Mechanics Division* 91.6 (1965): 11-19.
[4] Xiao, Q. Z., et al. "An improved hybrid-stress element approach to torsion of shafts." *Computers & structures* 71.5 (1999): 535-563.
[5] Gruttmann, F., Sauer, R. and Wagner, W. "Shear stresses in prismatic beams with arbitrary cross-sections." *International journal for numerical methods in engineering* 45.7 (1999): 865-889.
[6] 2021. Available online: http://projects.ce.berkeley.edu/feap/ (accessed on 08 June 2021).
[7] Fialko, S.Y. and Lumelskyy, D.E. "On numerical realization of the problem of torsion and bending of prismatic bars of arbitrary cross section." *Journal of Mathematical Sciences* 192.6 (2013): 664-681.
[8] Scadsoft. Available online: https://scadsoft.com/en (accessed on 08 June 2021).
[9] Jog, C.S. and Mokashi, I.S. "A finite element method for the Saint-Venant torsion and bending problems for prismatic beams." *Computers & Structures* 135 (2014): 62-72.
[10] Beheshti, A. "A numerical analysis of Saint-Venant torsion in strain-gradient bars." *European Journal of Mechanics-A/Solids* 70 (2018): 181-190.
[11] Katsikadelis, J.T. and Sapountzakis, E.J. "Torsion of composite bars by boundary element method." *Journal of engineering mechanics* 111.9 (1985): 1197-1210.
[12] Gaspari, D. and Aristodemo, M. "Torsion and flexure analysis of orthotropic beams by a boundary element model." *Engineering analysis with boundary elements* 29.9 (2005): 850-858.
[13] Barone, G., Iacono, F.L. and Navarra, G. "Complex potential by hydrodynamic analogy for the determination of flexure–torsion induced stresses in De Saint Venant beams with boundary singularities." *Engineering Analysis with Boundary Elements* 37.12 (2013): 1632-1641.
[14] Lee, J.W., Hong, H.K. and Chen, J.T., "Generalized complex variable boundary integral equation for stress fields and torsional rigidity in torsion problems." *Engineering Analysis with Boundary Elements* 54 (2015): 86-96.
[15] Paradiso, M., et al. "A BEM approach to the evaluation of warping functions in the Saint Venant theory." *Engineering Analysis with Boundary Elements* 113 (2020): 359-371.
[16] Chen, K. H., et al. "A new error estimation technique for solving torsion bar problem with inclusion by using BEM." *Engineering Analysis with Boundary Elements* 115 (2020): 168-211.
[17] Chen, J.T. and Lee, Y.T. "Torsional rigidity of a circular bar with multiple circular inclusions using the null-field integral approach." *Computational Mechanics* 44.2 (2009): 221-232.
[18] Di Paola, M., Pirrotta, A. and Santoro, R. "Line element-less method (LEM) for beam torsion solution (truly no-mesh method)." *Acta Mechanica* 195.1 (2008): 349-364.
[19] Santoro, R. "The line element-less method analysis of orthotropic beam for the De Saint Venant torsion problem." *International journal of mechanical sciences* 52.1 (2010): 43-55.
[20] Chen, H., Gomez, J. and Pindera, M.J. "Saint Venant's torsion of homogeneous and composite bars by the finite volume method." *Composite Structures* 242 (2020): 112128.
[21] Chen, H., Gomez, J. and Pindera, M.J. "Parametric finite-volume method for Saint Venant's torsion of arbitrarily shaped cross sections." *Composite Structures* 256 (2021): 113052.
[22] Allplan Bridge Features. Available online: https://www.allplan.com/products/allplan-bridge-2019-features/ (accessed on 08 June 2021).
[23] Zienkiewicz, O.C., Taylor, R.L. and Zhu, J.Z. *The finite element method: its basis and fundamentals. Elsevier*, 2005.
[24] Bathe, K.J. "Finite Element Procedures Prentice-Hall." *New Jersey* 1037 (1996).

CIVIL ENGINEERING JOURNAL

Article no. 31

THE CIVIL ENGINEERING JOURNAL 2-2021

FACTORS' SELECTION EFFECT AND COMPRESSIVE STRENGTH PREDICTION OF SCC USING A HYBRID NETWORK BASED ON GA

Wei Liang[1,2,3], Ming Lin[1,3], Jiangfeng Dong[2], Shucheng Yuan[1,3]

1. *Sichuan Agricultural University, College of Civil Engineering, Dujiangyan, 611830, Chengdu, China.*
2. *Failure Mechanics & Engineering Disaster Prevention and Mitigation, Key Laboratory of Sichuan Province, Sichuan University, 610065, Chengdu, China.*
3. *Sichuan Higher Education Engineering Research Center for Disaster Prevention and Mitigation of Village Construction, Sichuan Agricultural University, Dujiangyan, 611830, Chengdu, China.E-mail addresses: liangwei9090950@163.com*

ABSTRACT

Compressive strength is the most important evaluation index for concrete. In order to predict the compressive strength of self-compacting concrete, two kinds of artificial neural networks (ANNs), including the BP (Back-propagation) networks and the hybrid networks DRGA-BP (Dimenssion reduction back-propagation based on genetic algorithm), were designed and applied in this study. With DRGA-BP, the most representative variables were selected out from many initial inputs to reduce data dimensions and also the weights and thresholds of BP model were optimized. The results showed that the hybrid model presented better prediction accuracy with the R^2 (coefficient of determination) of 0.9602, and appeared to well agree with the experimental data and was quite reliable. Finally, a mix ratio design method based on DRGA-BP model was proposed for reducing material waste and saving time in the process of concrete production with continuous adjustment.

KEYWORDS

Self-compacting concrete, Artificial neural network, Genetic algorithm, Compressive strength

INTRODUCTION

Self-compacting concrete (SCC) is a kind of high-performance concrete that can flow through gaps of steel bars and fill corners of molds by its own weight, and can be compacted without additional mechanical vibration during the casting process.[1-2]. SCC has the advantages of eliminating noise of vibration, reduction in labor cost and increasing casting speed. For these reasons, SCC has been widely applied in concrete structures [3-5].

However, the performance of SCC is affected by many complex factors, and mixture ratio as one of the most important factors is still designed by empirical method [6]. At present, the mix design of SCC mainly includes the following steps: (1) Select coarse aggregate and its dosage; (2) Calculate the mortar dosage; (3) Calculate the amount of sand and the paste content; (4) Calculate the water-binder ratio according to the design strength of SCC; (5) Calculate the dosage of binding material according to the volume of paste, apparent density of cementing material, water-binder ratio, etc.; (6) Calculate the amount of water; (7) Determine the dosage of additives; (8) Trial matching and adjustment of mix ratio. Okamura et al.[1] suggested the following parameters : the

amount of coarse aggregate, which accounts for about 50% of the total aggregate volume; the amount of fine aggregate, which accounts for about 40% of the mortar volume; low water-cement ratio and use of superplasticizer. Domone[6] provided the median value of the mix ratio through a large number of data statistics : the amount of coarse aggregate, which accounts for 31.2% of the total volume; the amount of fine aggregate , which accounts for 47.5% of the total volume; the content of paste , which accounts for 34.8% of the volume; the dosage of binding material is 500kg/m^3; the water-cement mass ratio is 0.34. The experience statistical data and empirical formulas, can offer some reference value for design of SCC mix proportion, and help to narrow the scope of each parameter. However, due to the variety of raw materials that can be used in SCC, especially the increasing use of mineral admixtures such as fly ash, silica powder and blast furnace slag, the influencing factors are more complex compared to common concrete. Therefore, various mixing ratio parameters still need to be adjusted and tested in practical engineering. In addition, there is a nonlinear relationship between these parameters and concrete strength, so the mix proportion design method based on empirical linear formula is no longer applicable. Therefore, if a more efficient and accurate mix ratio design method of SCC can be proposed, a large number of trial materials and time can be effectively saved.

Artificial neural network (ANN) is a model that imitate human brain to process data. Outside information is transmitted between neurons in ANN and adjusted by leaning. Eventually, the trained ANN has an ability to react to the input data and obtain the desired output [7-8]. In recent years, ANN has been applied to many different fields, such as chemical engineering, medical industry, food technology and civil engineering, to solve nonlinear problems for modelling and optimization [9]. This method has also been applied to concrete strength prediction and mix ratio design in the past years. Lai et al.[10] concluded that the neural network performance was independent of the number of neurons in the hidden layer in the range of 4-8. Yeh [11-12] proposed a method of optimizing concrete mixture using ANN. For the prediction of concrete compressive strength, the Back-propagation (BP) neural network is the most used kind of ANN models [13-14]. Past research results show that the prediction results of ANN are more accurate than the traditional regression results[15], and the use of ANN makes it more convenient and simpler to analyze the influence of various factors on mix ratio. However, there are too many initial parameters that can be applied as input data in ANNs. These parameters are usually raw material types and their proportions, and most of them are chosen based on experience. Duan et al.[16] used 14 parameters as input data, such as water, cement, sand, natural aggregate, recycle aggregate, fineness modulus of sand, maximum size of coarse aggregate, water–cement ratio, type of coarse aggregate, impurity content, water absorption of coarse aggregate, saturated surface dry specific gravity of coarse aggregate, replacement ratio by volume and conversion coefficient. Ghafari et al.[17] used cement, sand, silica fume, quartz flour, water, superplasticizer and steel fiber as input data. Chithra et al.[18] applied six mix constituents as input data, such as cement content, nano silica content, fine aggregate content, copper slag content, age of specimen and super plasticizer dosage. These variable parameters affected the prediction accuracy a lot, but there were few investigations tried to find out the critical ones in the past. Due to the fact that the effect factors are many and not independent mutually, it is easy to occur the overfitting phenomena and cause the problems of low accuracy and time-consuming process of networks. In order to solve this problem, these factors need to be optimized and selected to find out the factors which can best reflect the relationship between inputs and outputs.

Genetic algorithm (GA) simulate the evolutionary processes of species in the nature. It can be used to acquire a global optimal solution to solve nonlinear problems and optimize the initial weights and thresholds in BP network [19]. In this paper, a hybrid ANN model, DRGA-BP (Dimenssion Reduction Back-propagation based on Genetic Algorithm), is constructed to optimize the inputs and improve the prediction accuracy of compressive strength of SCC.

DATA COLLECTION AND NORMALIZATION

The experimental data sets were obtained from the research of Nepomuceno [20], including 60 mixes and corresponding compressive strength data of SCC at 28 days. In this paper, 40 sets of data were used in the training set, while the other 20 sets of data were used-to test the accuracy of the prediction.

The input data were divided into 10 categories, including the amount of raw materials (cement, mineral admixtures, water, superplasticizer, fine aggregate and coarse aggregate) and binding materials (cement and mineral admixtures), and the ratio among the raw materials (water-binder ratio, sand ratio and mineral admixtures replacement ratio). In addition, the type of cement was Portland cement with a density of 3040~3140 kg/m^3; the mineral admixtures included single or combined limestone powder, fly ash and granite ash, with densities of 2380~2720 kg/m^3; the superplasticizer was polycarboxylic acid superplasticizer with a density of 1050 kg/m^3; the fine aggregate was natural sand, with a density of 1598 kg/m^3 and a fineness of 2.22; the coarse aggregate was granite crushed stone, with a density of 1642 kg/m^3 and a fineness of 5.78. Table 1 shows the range of these input and output data sets.

Tab. 1: Input and output data

Parameters type	Code	Description	Dosages in kg for solids and in liters for water and SP per cubic meter		
			Minimum	Maximum	Average
Input	C	Cement	276	670	477
	M	Mineral admixture	0	376	140
	W	Water	154	184	169
	P	Superplasticizer	4.8	20.8	12.6
	B	Binding material	547	672	617
	S	Superplasticizer	656	846	757
	G	Coarse aggregate	729	875	784
	W/B	Water-binder ratio	0.24	0.32	0.28
	SR	Sand ratio	0.43	0.54	0.49
	RR	Mineral admixture replacement ratio	0	0.57	0.22
Output	$f_{c,28}$	Compressive strength (MPa)	38.3	86.8	65.2

Because the units of the input data are different and some of the data value range is larger, if the collected data is directly inputted into the network, it will lead to the problem of long training time and slow convergence, and the range of activation functions is also limited. Therefore, it is necessary to normalize the data before training the network and map the data to the interval of [0,1] or [-1,1]. The normalization algorithm adopted in this paper was $y = 2*(x-\min)/(\max-\min)-1$. '$x$' is the input vector, 'min' is the minimum value of 'x', 'max' is the maximum of 'x', and 'y' is the normalized output vector.

IMPROVED ANN MODEL BASED ON GA

Genetic Algorithm

In this paper, GA and BP network are combined to improve the shortcomings of traditional BP network. At the same time, it is expected to screen out the factors that have little influence on the strength of self-compacting concrete by reducing dimension of independent variables, so as to simplify input data and improve learning efficiency and prediction accuracy.

The implementation process of genetic algorithm is shown in Figure 1. After selection, crossover and mutation, population P reaches the requirements of environmental fitness and forms a new population Pn. The three most important steps are as follows[21]:

(1) Selection. Select individuals with high fitness from the current population. And these individuals will have a greater chance of being passed on to the next generation.

(2) Crossover. Individuals in the group are randomly paired with each other to obtain new individuals.

(3) Mutation. There is a certain probability that an individual's genes will change and a new individual will be born.

In this paper, the roulette algorithm is used to select individuals. The higher the individual fitness, the greater the probability of selection. Specific operations are as follows:

(1) Calculate the probability of each individual being selected:

$$P(X_i) = \frac{f(X_i)}{\sum_{i=1}^{m} f(X_i)} \tag{1}$$

where, $f(X_i)$ is the fitness of individual i; m is the population size, that is, the number of individuals in the population.

(2) Calculate the cumulative probability of each individual:

$$q_i = \sum_{i=1}^{m} P(X_i) \tag{2}$$

(3) Generate the random number r in (0,1). If $q_{i-1} < r \le q_i$, then the individual i is selected.

(4) Repeat the operation (3) for m times.

According to the above operations, if an individual has high fitness, then that individual will be selected many times, thus its gene ratio will expand in the population.

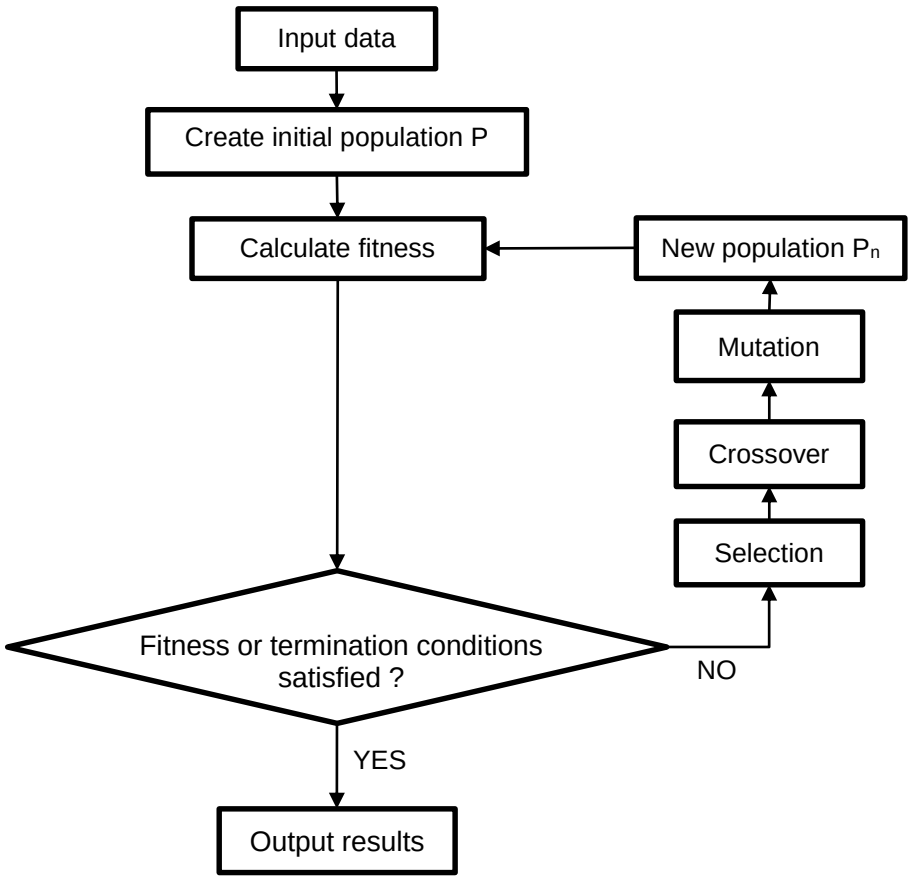

Fig. 1 – The implementation process of GA

In crossover operations, arithmetic crossover is used. Pairs of individuals in the population are randomly paired, and for each pair of individuals, two new individuals are generated according to the following formula:

$$c_1 = p_1 \times a + p_2 \times (1-a) \tag{3}$$

$$c_2 = p_1 \times (1-a) + p_2 \times a \tag{4}$$

where, p_1 and p_2 are the parent individuals respectively; c_1 and c_2 are the offspring after the crossover operation; a is a random number between 0 and 1, namely the crossover probability.

In this paper, the nonuniform variation method is used. The process by which a gene in an individual is randomly disturbed in a small probability to produce a new individual. Suppose $x = (x_1, x_2, ..., x_i, ..., x_n)$ is a set of chromosomes, that is, an individual, and one of the genes x_i is selected as the mutation object, so the new individual is $x' = (x_1, x_2, ..., x_i', ..., x_n)$. This process can be expressed as:

$$x_i' = \begin{cases} x_i + \Delta(g, u_i - x_i) & \text{if } t = 0 \\ x_i + \Delta(g, x_i - l_i) & \text{if } t = 1 \end{cases} \tag{5}$$

where, u_i and l_i are the upper and lower bounds of value respectively; t is a random value, 0 or 1. And $\Delta(g, y)$ is calculated by the following formula:

$$\Delta(g, y) = y\left(1 - r^{(1-\frac{g}{G})^b}\right) \tag{6}$$

where, g is the current number of evolutionary generations; G is the maximum number of evolutionary generations; b is the a parameter that determines the degree of nonuniform variation; r is a random number in the range [0,1].

DRGA-BP model

The hybrid neural network DRGA-BP for dimension reduction is shown in Figure 2. After normalization processing, each group of data is input into the computing network as an individual. During population initialization, genes in each individual chromosome are randomly coded with '1' or '0'. In BPNN-A, which represents the back-propagation neural network "A", the optimal weights and thresholds are obtained by genetic algorithm, and then substituted into BPNN-A as initial weights and thresholds for training. In process (a), the influence of initial weights and thresholds on the prediction results is reduced because the initial weights and thresholds are not obtained randomly. At the same time, the problem of BP neural network falling into local optimal is avoided. In process (b), several factors that have a greater impact on concrete strength are selected and input into BPNN-B (back-propagation neural network "B") as input data. Finally, the data are trained in BPNN-B and the prediction results can be obtained.

In this paper, the reciprocal of the Sum of the Squared Errors (SSE) is taken as the fitness function:

$$f(X) = \frac{1}{sse(T_p - T_a)} = \frac{1}{\sum_{i=1}^{n_1}(t_{p,i} - t_{a,i})^2} \tag{7}$$

where, $T_p = \{t_{p,1}, t_{p,2}, ..., t_{p,n_1}\}$ is the predicted value in the training phase; $T_a = \{t_{a,1}, t_{a,2}, ..., t_{a,n_1}\}$ is the actual value in the training phase; n_1 is the number of samples in the training phase.

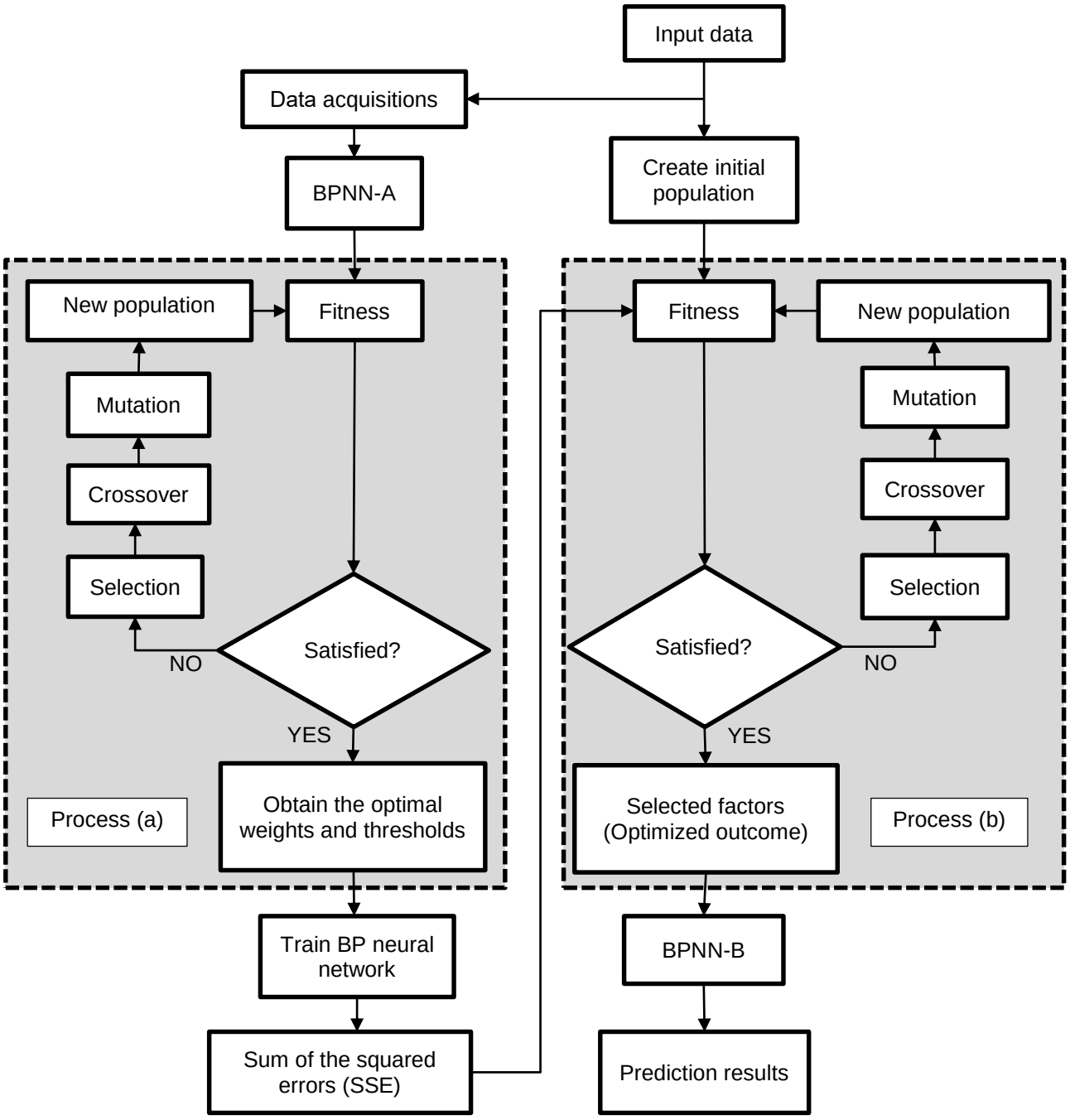

Fig. 2 – Working diagram of DRGA-BP

After several iterations, when a certain termination condition is met, individuals with optimal fitness survive and form a new population. This means that the most representative and effective variables are selected from the initial input data. Then, the selected factors are used as input data for training and testing in the new BP network (BPNN-B). Finally, the prediction results are obtained.

Final selected factors

In this hybrid neural network, the BPNN was set as a three-layer neural network with 8 hidden neurons. Levenberg-marquardt algorithm was used to train the data. The training termination conditions of this hybrid neural network were set as follows:

(1) Maximum number of iterations: 1000

(2) Training target error: 0.001

(3) Maximum number of verification checks: 10

If any of the above conditions were satisfied, the training was terminated. The population size m in Formula (1) was set as 8. To make sure that the whole process does not go on endless, the maximum evolutionary algebra was set as 50, that means every 8 individuals formed a population, and the evolution process stopped after up to 50 times even if the above termination conditions had not been met. The 10 factors listed in Table 1 were used as input data for prediction.

In process (b), typical evolutionary process is shown in Figure 3. As can be seen that the average fitness of individuals in the population increased with the growth of evolutionary generations, and the difference between optimal fitness and average fitness became smaller and smaller. Eventually, after many iterations, fitness values tended to be constant. It can be considered that the evolutionary process had been completed. And the individuals with the best fitness, that was, the factors that had the greatest influence on the compressive strength, formed new populations as optimized parameters.

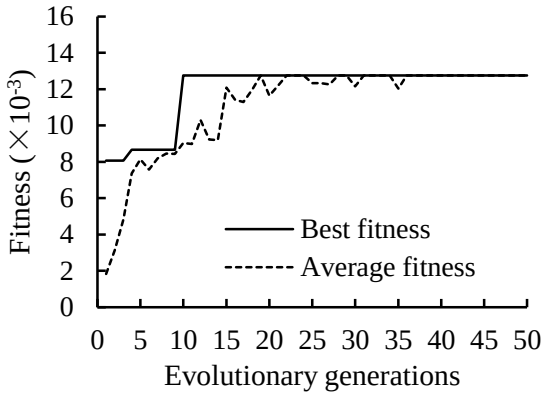

Fig. 3 – Typical evolutionary process

MODEL VERIFICATION AND COMPARATIVE ANALYSIS

In BPNN-B, the best effect achieved in the training process was in the 14th training session, which mean-square error (MSE) was only 0.0009841. The training results are shown in Figure 4. As can be seen, the training results were very consistent with the actual values, which meant the training effect was good. Besides, in total of five variables as the final selected factors had survived in the evolutionary process, including cement (C), mineral admixture (M), water-binder ratio (W/B), sand ratio (SR) and mineral admixture replacement ratio (RR). It shows that these five factors have great influence on the compressive strength of SCC, and similar conclusion can be obtained from relevant literatures[22]. These five optimal variables, as input data, participated in network BPNN-B for compressive strength prediction.

In order to compare and confirm the five selected factors were reasonable and could improve the accuracy of the prediction, the five selected factors and all ten original factors respectively as two groups of input data were applied to a conventional three-layer BP neural network with eight of hidden neurons for test, namely BPNN-5 and BPNN-10, as listed in Table 2.

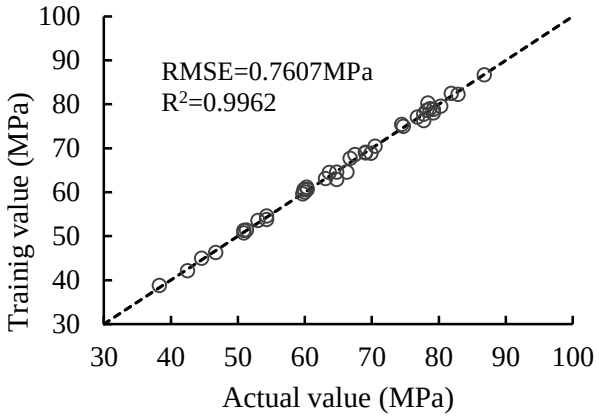

Fig. 4 – Training results of BPNN-B in the hybrid neural network DRGA-BP

The prediction results of the compressive strength with hybrid network DRGA-BP and comparison BP network BPNN-5 and BPNN-10 are shown in Table 2 and Figure 5. In the table, RMSE is the root mean square error, which is the square root of the squared deviation between the predicted value and the actual value and the ratio of prediction times 'n'. It is very sensitive to the very large or very small errors in a set of measurements, and can well reflect the precision of the prediction. The expression of RMSE is as follows:

$$RMSE = \sqrt{\frac{\sum_{i=1}^{n}(T_i - P_i)^2}{n}} \tag{8}$$

R^2 is the determining coefficient, which measures the overall fitting degree of the regression equation and represents the overall relationship between the dependent variables and all independent variables. The closer R^2 is to 1, the higher the reference value of the relevant equations will be. The closer to 0, the lower the reference value. Its expression is:

$$R^2 = 1 - \frac{\sum_{i=1}^{n}(T_i - P_i)^2}{\sum_{i=1}^{n}(T_i - \overline{T_i})^2} \tag{9}$$

where, P_i is the predicted value; T_i is the actual value; $\overline{T_i}$ is the average of all actual values; n is the number of samples.

It can be seen that the prediction results of hybrid network DRGA-BP proposed in this paper were closest to the real value and had the best prediction effect. When the same 10 factors were used as the initial input data, compared with network BPNN-10, the prediction results of DRGA-BP had a very high accuracy, and the RMSE was 2.2329 MPa and R2 was 0.9602. Besides, by comparing the prediction results of BPNN-10 and BPNN-5, it can be seen that using the selected factors as the initial input data in the same BP neural network had effectively improved the accuracy of prediction. In addition, the comparison test showed that the prediction effect of BP neural network was very sensitive to the initial input data, so the improved network DRGA-BP using genetic algorithm can effectively suppress the impact of initial weight and threshold on the prediction effect.

Tab. 2: Prediction results of ANN

Code	Number of hidden neurons	Initial input factors	Optimized output factor as selected factors	RMSE (MPa)	R^2
DRGA-BP	8	C, M, W, SP, B, S, G, W/B, SR, RR	C, M, W/B, SR, RR	2.2329	0.9602
BPNN-10	8	C, M, W, SP, B, S, G, W/B, SR, RR	/	6.5197	0.6610
BPNN-5	8	C, M, W/B, SR, RR	/	4.2972	0.8527

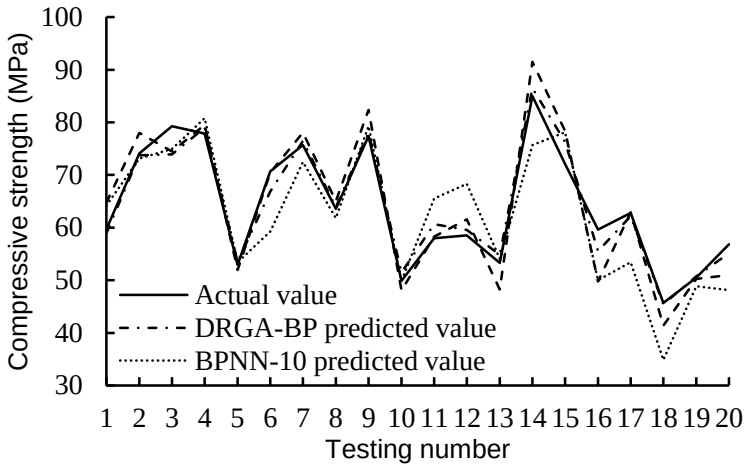

Fig. 5 – The actual value versus the predicted value

MIX RATIO DESIGN METHOD BASED ON DRGA-BP MODEL

Five key factors, including cement (C), mineral admixture (M), water-binder ratio (W/B), sand ratio (SR) and mineral admixture replacement ratio (RR), were selected out by DRGA-BP as control factors affecting the compressive strength of SCC. The predicted values with DRGA-BP and experimental values (actual values with experiments) were respectively interpolated to draw the relationship diagram of water-binder ratio and replace ratio, water-binder ratio and sand ratio on the compressive strength of SCC, as shown in Figure 6 and Figure 7. It can be seen that the experimental values and the predicted values showed the same influence trend, and the value of water-binder ratio, replacement ratio and sand ratio was not a simple linear relation to the compressive strength of SCC. In addition, when the mineral admixture replacement ratio was higher than 0.48, the corresponding strength of SCC decreased significantly.

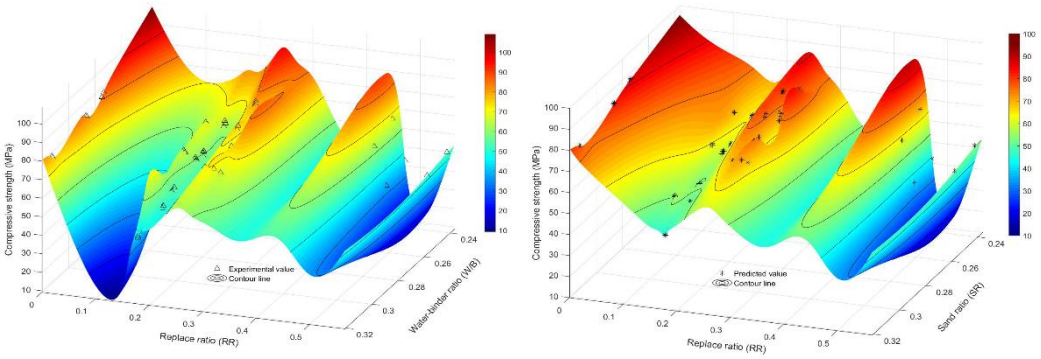

(a) Experimental values *(b) Predicted values*

Fig. 6 – Effect of W/B and RR on the compressive strength of SCC

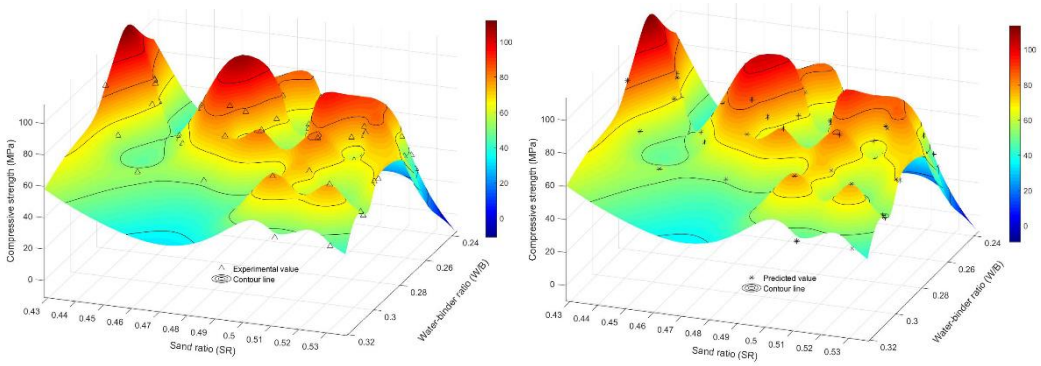

(a) Experimental values *(b) Predicted values*

Fig. 7 – Effect of W/B and SR on the compressive strength of SCC

The influence relation of water-binder ratio, replacement ratio and sand ratio on the compressive strength can provide reference for the mix ratio design of SCC with a certain strength. The main steps are as follows: (1) Determine the design compressive strength of SCC; (2) Determine the total binder amount and aggregate amount; (3) Select water-binder ratio, sand ratio and mineral admixture replacement ratio; (4) Calculate the specific dosage of water, cement, mineral admixture, fine aggregate and coarse aggregate; (5) Determine the dosage of additives; (6) Trial matching and adjustment of mix ratio.

Taking the mix ratio design of SCC with 40 MPa of compressive strength at 28 day as an example, the total colloidal quantity is 560 kg/m^3, the total coarse and fine aggregate quantity is 1600 kg/m^3. And the control factors can be determined in a small range as follows: water-binder ratio is 0.31-0.32, sand ratio is 0.44-0.50, and mineral admixture replacement ratio is 40%-50%. Finally, the water-binder ratio is determined as 0.31, the sand ratio is determined as 0.50, and the mineral admixture replacement ratio is determined as 40%. The specific amount of each material is calculated: cement is 336 kg/m^3, fly ash is 224 kg/m^3, fine aggregate is 800 kg/m^3, coarse aggregate is 800 kg/m^3, and water is 174 kg/m^3. By substituting the above data into the artificial neural network DRGA-BP, the 28-day strength is predicted to be 44.7 MPa, which can provide reference value for the preparation of SCC and effectively reduce the matching work and adjustment time.

CONCLUSIONS

In this paper, a new hybrid network DRGA-BP was studied to predict the compressive strength of SCC. The following conclusions could be drawn from this study:

1. DRGA-BP network improved by genetic algorithm can reduce the influence of initial input data, initial weight and threshold on the prediction results, and can predict the compressive strength of SCC with high level of accuracy. The prediction is quite reliable for application in concrete industry to decrease the time-consuming laboratory tests.
2. DRGA-BP network can effectively screen out the main factors that affect the strength of SCC, including cement, mineral admixture, water-binder ratio, sand ratio and mineral admixture replacement ratio.
3. DRGA-BP can provide reference for the design of SCC mix ratio. However, it still needs a lot of experimental data to study and verify, so as to improve its prediction accuracy continuously.

CONFLICT OF INTEREST

The authors declare that they have no conflict of interest.

REFERENCES

[1] Okamura, H.; Ouchi, M. Self-compacting concrete. J ADV CONCR TECHNOL **2003,** 1 (1), 5-15.
[2] Su, N.; Hsu, K. C.; Chai, H. W. A simple mix design method for self-compacting concrete. CEMENT CONCRETE RES **2001,** 31, 1799-1807.
[3] Han, L. H.; Yao, G. H.; Zhao, X. L. Tests and calculations for hollow structural steel (HSS) stub columns filled with self-consolidating concrete (SCC). J CONSTR STEEL RES **2005,** 61 (9), 1241-1269.
[4] Nikbin, I. M.; Beygi, M. H. A.; Kazemi, M. T.; Vaseghi Amiri, J.; Rahmani, E.; Rabbanifar, S.; Eslami, M. Effect of coarse aggregate volume on fracture behavior of self compacting concrete. CONSTR BUILD MATER **2014,** 52, 137-145.
[5] Gencel, O.; Brostow, W.; Datashvili, T.; Thedford, M. Workability and Mechanical Performance of Steel Fiber-Reinforced Self-Compacting Concrete with Fly Ash. COMPOS INTERFACE **2011,** 18 (2), 169-184.
[6] Domone, P. L. Self-compacting concrete: An analysis of 11 years of case studies. CEMENT CONCRETE COMP **2006,** 28 (2), 197-208.
[7] Erdem, H. Predicting the moment capacity of RC beams exposed to fire using ANNs. CONSTR BUILD MATER **2015,** 101, 30-38.
[8] Yeh, I. C. Modeling slump flow of concrete using second-order regressions and artificial neural networks. CEMENT CONCRETE COMP **2007,** 29 (6), 474-480.
[9] Astray, G.; Gullón, B.; Labidi, J.; Gullón, P. Comparison between developed models using response surface methodology (RSM) and artificial neural networks (ANNs) with the purpose to optimize oligosaccharide mixtures production from sugar beet pulp. IND CROP PROD **2016,** 92, 290-299.
[10] Lai, S.; Serra, M. Concrete strength prediction by means of neural network. CONSTR BUILD MATER **1997,** 11(2), 93-98.
[11] Yeh, I.-C. Design of high-performance concrete mixture using neural networks and nonlinear programming. Journal of Computing in Civil Engineering **1999,** 13(1), 36-42.
[12] Yeh, I. C. Computer-aided design for optimum concrete mixtures. CEMENT CONCRETE COMP **2007,** 29 (3), 193-202.
[13] Topçu, İ. B.; Sarıdemir, M. Prediction of properties of waste AAC aggregate concrete using artificial neural network. Computational Materials Science **2007,** 41 (1), 117-125.
[14] Oztaş, A.; Pala, M.; Ozbay, E. a.; Kanca, E. a.; Çag˘lar, N.; Bhatti, M. A. Predicting the compressive strength and slump of high strength concrete using neural network. CONSTR BUILD MATER **2006,** 20 (9), 769-775.
[15] Yeh, I.-C. Modeling of strength of high-performance concrete using artificial neural networks. CEMENT CONCRETE RES **1998,** 28(12), 1797-1808.
[16] Duan, Z. H.; Kou, S. C.; Poon, C. S. Prediction of compressive strength of recycled aggregate concrete using artificial neural networks. CONSTR BUILD MATER **2013,** 40, 1200-1206.
[17] Ghafari, E.; Bandarabadi, M.; Costa, H.; Júlio, E. Prediction of Fresh and Hardened State Properties of UHPC: Comparative Study of Statistical Mixture Design and an Artificial Neural Network Model. Journal of Materials in Civil Engineering **2015,** 27 (11), 04015017.
[18] Chithra, S.; Kumar, S. R. R. S.; Chinnaraju, K.; Alfin Ashmita, F. A comparative study on the compressive strength prediction models for High Performance Concrete containing nano silica and copper slag using regression analysis and Artificial Neural Networks. CONSTR BUILD MATER **2016,** 114, 528-535.
[19] Yu, W.; Li, B.; Jia, H.; Zhang, M.; Wang, D. Application of multi-objective genetic algorithm to optimize energy efficiency and thermal comfort in building design. Energy and Buildings **2015,** 88, 135-143.
[20] Nepomuceno, M. C. S.; Pereira-de-Oliveira, L. A.; Lopes, S. M. R. Methodology for the mix design of self-compacting concrete using different mineral additions in binary blends of powders. CONSTR BUILD MATER **2014,** 64, 82-94.
[21] Esmaeili, R.; Dashtbayazi, M. R. Modeling and optimization for microstructural properties of Al/SiC nanocomposite by artificial neural network and genetic algorithm. Expert Systems with Applications **2014,** 41 (13), 5817-5831.
[22] Prasad, B. K. R.; Eskandari, H.; Reddy, B. V. V. Prediction of compressive strength of SCC and HPC with high volume fly ash using ANN. CONSTR BUILD MATER **2009,** 23 (1), 117-128.

CIVIL ENGINEERING JOURNAL

Article no. 32

THE CIVIL ENGINEERING JOURNAL 2-2021

RESEARCH ON THE KEY TECHNOLOGY OF TIED-ARCH BRIDGE INCREMENTAL LAUNCHING METHOD CONSTRUCTION

Kexin Zhang[1], Tianyu Qi [1], Xingwei Xue[1] and Zhimin Zhu [2]

1. *Shenyang Jianzhu University, School of Traffic Engineering, Department of Bridge, Shenyang, NO. 25 Hunnan Middle Road, PR of China; jt_zkx@sjzu.edu.cn; 1579339669@qq.com; gdansys@163.com*
2. *Liaoning Urban Construction Design Institute Co. LTD, Shenyang, NO.77-1 Jinfeng Street, PR of China; minzdragon@126.com*

ABSTRACT

Steel tied arch bridge has been widely used in modern bridge construction due to its beautiful shape, high material utilization rate and overall structural stiffness. However, there are few cases in which the tied-arch bridge is constructed by incremental launching. Based on the steel tied arch bridge project, this paper uses finite element software to establish the finite element simulation analysis of the construction process and monitors the construction process of the bridge. The test results show that it is in the most unfavourable state when the cantilever at the end of the bridge reaches the maximum. At this time, the stress at the 117 m position of the beam reaches the maximum, the stress at the top edge is 33.7 MPa, and the stress at the bottom edge is -58.2 MPa. The stress in other sections did not exceed 30 MPa, and the beam was under uniform stress. When the foot of the internal arch passes through the temporary pier, the supporting force of the pier is maximum, which is about 6000 kN. The reasonable range of α is between 0.55 and 0.65, which is the ratio between the length Ln of launching nose and the maximum span L of incremental launching. The research results can provide reference for the construction of similar bridges.

KEYWORDS

Tied-arch bridge, Incremental launching method, Construction monitoring, Temporary pier, Launching nose

INTRODUCTION

Tied arch bridge has a beautiful shape, the curve is round, its construction history is relatively long. The cost of arch bridge is economical and has a good crossing ability. Meanwhile, the maintenance and repair are convenient and the cost is less. However, the arch bridge has some disadvantages. The main arch ring is mainly pressured during the use of the arch bridge, and its mechanical characteristics determine that there will be relatively large horizontal thrust at the foot of the arch. Therefore, the construction of the arch bridge has strict requirements on the foundation. Different from the arch bridge, the beam bridge is mainly subjected to the action of bending moment and there is no horizontal thrust. By combining the arch and beam in a reasonable design, their respective advantages can be fully exerted and the influence of force defects can be reduced. The mechanical performance of the bridge structure is optimized, so that the span capability of the bridge is increased and the use effect is better. The superstructure of girder and arch composite bridge usually includes arch rib, longitudinal beam, tie rod and vertical column, etc. The tie bar is mainly

used to balance most or all of the horizontal thrust at the arch foot of the completed bridge. Therefore, the horizontal thrust at the arch foot of the girder arch composite structure bridge does not exist or is much smaller than the thrust at the arch foot under the same conditions, which can greatly reduce the requirements of foundation bearing capacity. In addition, in some special site environments, such as the bridge across the river navigation requirements are high, the bridge under the bridge navigation height is high, the combined system bridge will reflect a greater advantage. Due to the good application value of such bridges, a lot of such bridges have been built in recent years, which also promotes the faster development of bridge structures. With the emergence of various bridges with novel structures and unique shapes, the construction methods of bridges are also constantly innovating and developing. In the actual bridge construction, the choice of construction method is targeted. According to the structural characteristics of the bridge, construction technology and equipment, site environment and economic, to determine the most suitable construction method. There are many bridge construction methods, and each method has different applicable conditions. Due to the difference of site environment and construction conditions, the construction method selected will also be very different. When the bridge construction site environment is relatively complex and has a great impact on the bridge construction, the bridge structure can be prefabricated and assembled in sections, and then the assembled well-formed bridge structure can be jacked forward gradually along the direction of the bridge, making the bridge slowly pass through each temporary pier to complete the bridge construction. This construction method is called push - up construction.

The incremental launching method is used more in the construction of prestressed concrete bridges and less in the construction of steel bridges. With its unique and novel shape, beam and arch composite structure can be well integrated with the surrounding environment and has good crossing ability, which is increasingly widely applied in practical engineering, especially in the design and application of urban and landscape bridges. As a new bridge construction technology, the incremental launching method has few practical applications, and there are still some problems to be solved. Therefore, it is very necessary to analyze the force of the whole incremental launching construction process of the bridge by combining with the engineering practice.

PROJECT PROFILE

Fig.1 - Elevation drawing of push process

The bridge is 191.339 m in length and 38 m in width. The main bridge structure adopts steel truss arch beam structure with main span of 106 m to cross the river. The lower arch rib is 19.27 m high, the span ratio is 1/5.5, and the height of vault truss is 3.5m. Fixed support is set at one end of the bridge towards the arch foot, and sliding support is set at the other end. The overall structure is non-thrust system. The arch ribs are box girder structure and the material is Q345QC. A structure in which the main beam is the main longitudinal beam, steel beam and secondary longitudinal beam are under joint stress. The bridge deck is orthogonal special-shaped plate, and the beam height at

the center line of the bridge is 2.57 m. The steel type is Q345Qc. The middle pier adopts the form of pile foundation extended by pile caps. The pile foundation is a bored pile with a diameter of 1.8 m.

The main girder adopts the structure form of all welded steel box girder. The box girder adopts a single box with a three-compartment section, with a height of 3.5 m and a cantilever length of 4.0 m outside the box girder. The beam is 39.0 m wide at the top and 18.5 m wide at the bottom. The steel box girder roof thickness is 16 mm, the bottom plate thickness is 14 mm. U - shaped longitudinal stiffeners are used for the top and bottom plates, and plate stiffeners are used for the rest. The longitudinal spacing of the cable anchor points is 9 m, and a beam is set at the corresponding lifting point. The arch ribs of the main bridge are in the form of steel truss. The upper and lower arch ribs are connected as a whole by vertical and oblique ventral rods, and two truss frames are arranged laterally. The trusses are connected by transverse braces to enhance lateral stability. The upper arch rib span is about 142 m, and the sagittal height is 23.5 m. The rib span of the lower arch is about 103 m and the vector height is 20 m. The net sagittal height of the truss arch is 19.288 m, the sagittal span ratio is 1:5.5, and the height difference between the upper and lower arch ribs is 3.5 m. The steel arch rib section adopts a closed box section with a section height of 1.2 m and a width of 1.2 m. The thickness of steel plates in the standard section of arch rib is 30 mm, the thickness of steel plates in the reinforced section of arch foot is 40 mm, and a diaphragm is set every 1m in the arch rib. The arch truss girders are the I-shaped sections, the section height is 1.2 m, the flange width is 0.4 m, and the plate thickness is 16 mm. The sling of this bridge adopts parallel steel wire sling, and the whole bridge is arranged with 30 slings. The sling is made of 85 parallel steel wires with a diameter of 7 mm, with a standard strength of 1670 MPa. The elevation of the bridge is shown in Figure 2, the span arrangement is 22 m+106 m+22 m.

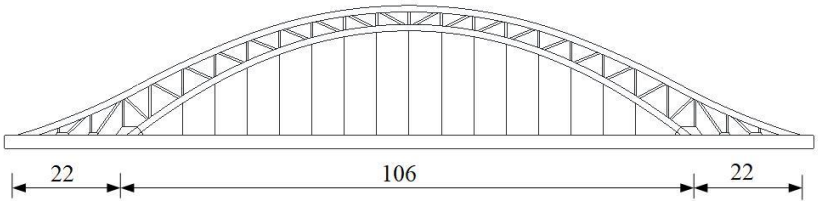

Fig.2 - Vertical view

CONSTRUCTION SEQUENCE

As the river has navigation requirements, supports cannot be set up in the river, so the steel truss arch bridge is recommended to use the push method for construction. The main construction steps are as follows:

Step 1: Two temporary piers shall be built between the 2 # and 3 # main piers, the slide beam shall be installed, and the vertical and horizontal jack adjustment devices and the incremental launching equipment shall be installed for debugging.

Step 2: In the assembly site, the steel box girder structure of arch bridge is assembled, and the arch rib steel tube, derrick and launching nose are installed. After installing the boom, preapply a certain tension of the sling. At the same time, the pier incremental launching traction system and deviation correction system are installed, and the debugging incremental launching system is ready.

Step 3: Start the incremental launching system and push forward. After pulling the anchor near the pier, pause the incremental launching and drag the strand to the next pier to be installed, and continue pushing forward. Remove the steel strand when the next anchor is close to the pier, then pull the anchor backward and change it. The changed steel strand shall be pre-tightened again and continue to push.

Step 4: When the launching nose is pushed to pier 1, remove the launching nose. Carry out system conversion, drop the whole bridge on permanent support, and complete incremental launching method construction.

Step 5: Demolish the temporary piers and incremental launching equipment, drop the beam to the design elevation, and complete the incremental launching method construction.

The push process is shown in Figure 2. During the welding process of the arch ribs, support piers should be installed. Five support piers should be installed on each side of the arch ribs, and the support piers should be removed after the top of the bridge is pushed into place.

A finite element model of the construction process was established, as shown in Figure 3. The bridge has a total of 1680 units and 1371 nodes. The arch and beam are simulated by beam element, the sling is simulated by tension element only, and the temporary pier is simulated by supporting boundary condition. The incremental launching method process is divided into 30 working conditions, as shown in Table 1. The incremental launching distance of each working condition is 5m, and the total incremental launching is 150 m. The support piers in the incremental launching process are shown in Figure 4. L1~L6 are temporary support piers and the remaining four are permanent bridge piers. The determination of temporary pier distance is mainly based on the stress of the jacking structure in the maximum cantilever state. When the structure reaches the maximum cantilever state, the stress cannot exceed the allowable stress value in the construction process. The length of the slideway in the support position is 5 m, and a push cycle is 2.5m .

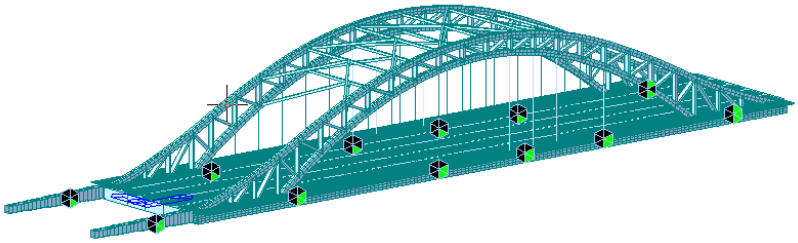

Fig.3 - Finite element model of bridge

Tab. 1 - Working condition of pusher

Construction Stage	Pushing Distance (m)	Construction Stage	Pushing Distance (m)	Construction Stage	Pushing Distance (m)
CS0	0	CS12	60	CS24	120
CS1	5	CS13	65	CS25	125
CS2	10	CS14	70	CS26	130
CS3	15	CS15	75	CS27	135
CS4	20	CS16	80	CS28	140
CS5	25	CS17	85	CS29	145
CS6	30	CS18	90	CS30	150
CS7	35	CS19	95	CS31	Demolition of nose
CS8	40	CS20	100	CS32	bridge deck pavement
CS9	45	CS21	105		
CS10	50	CS22	110	CS33	Demolition of temporary pier
CS11	55	CS23	115		

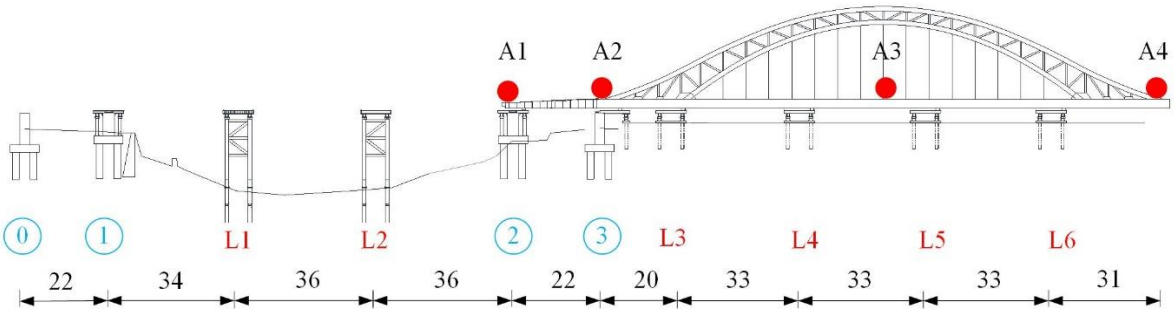

Fig.4 - Supporting pier diagram

MONITORING POINTS DURING CONSTRUCTION

The construction process control system mainly includes construction process simulation, construction process monitoring and construction process correction and adjustment. Among them, construction process monitoring is the core of the whole control system. By monitoring the important structural design parameters and state parameters, the data and technical information reflecting the actual construction state can be obtained, and then the construction path can be modified and adjusted reasonably according to the monitoring data results, so as to achieve the purpose of safe and smooth control in the construction process.

The key parameters of construction process monitoring can reflect the mechanical behaviour of the structure and its construction support system in any construction stage. Generally, monitoring key parameters can be divided into two categories: load parameters (such as temperature, thrust, etc.) and response parameters (such as stress, deformation, etc.). In the construction process, through the real-time monitoring of these key parameters, the results can be obtained together with the construction support system's stress behaviour and shape characteristics, so as to achieve the purpose of safety control in the construction process. The response parameters in this project include stress and deformation. The stress measurement points of beam and arch are shown in Figure 5, and the deflection measurement points of main beam and launching nose are shown in Figure 4. The stress measuring points of the beam and arch are arranged at the two ends, the middle point and the quarter point.

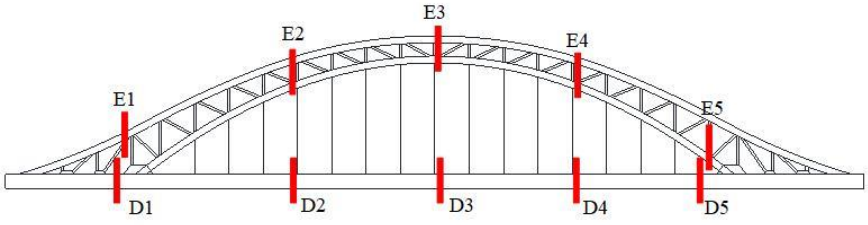

Fig. 5 - Arrangement of stress measuring points of beams and arches

(a) Arch rib measuring point (b) Main girder measuring point

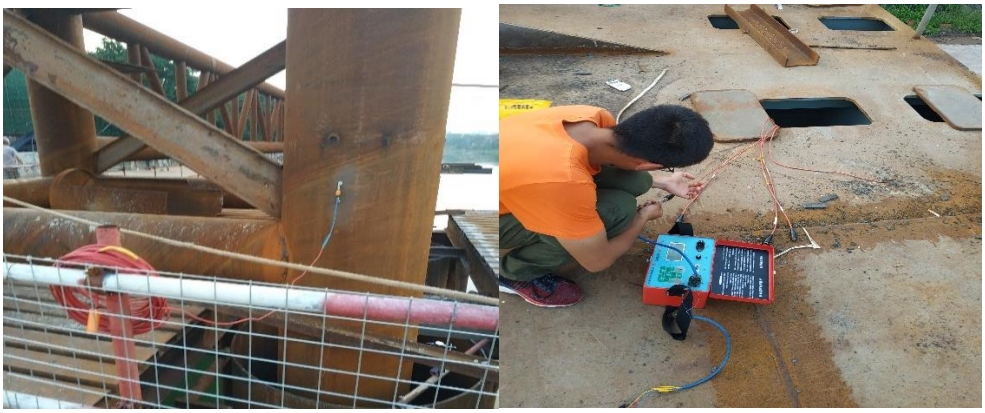

(c) Temporary pier measuring point (d) Stress data acquisition

Fig. 6 - Stress measuring

PUSH PROCESS ANALYSIS

Stress of main beam during incremental launching

In the whole process of incremental launching method, the measured and theoretical stress values of beam at different incremental launching method conditions are shown in Figure 7. Under the condition of CS11, the theoretical stress at the bottom edge of measuring point D1 is at most 21.3 MPa, and the measured stress is at 11.0 MPa. When it is pushed to CS22 working condition, the theoretical maximum stress at the bottom edge of the beam is -19.5 MPa, and then the measured stress is -13.7 MPa. When the working condition of CS22 is jacked, the maximum theoretical stress of the top edge is 18.2 MPa, and the measured value is 15.1 MPa at this time. The measured stress at the top edge and bottom edge during the whole process of incremental launching method is less than the theoretical stress. When pushed to CS22, the maximum theoretical stress of the top edge of D2 measuring point is 22.5 MPa, and the corresponding measured value is 18.3 MPa; the maximum theoretical stress of the bottom edge is -30.5 MPa, and the corresponding measured value is -18.9 MPa. The D2 measured stress at the top edge and bottom edge of beam in the whole process of incremental launching method is less than the theoretical stress.

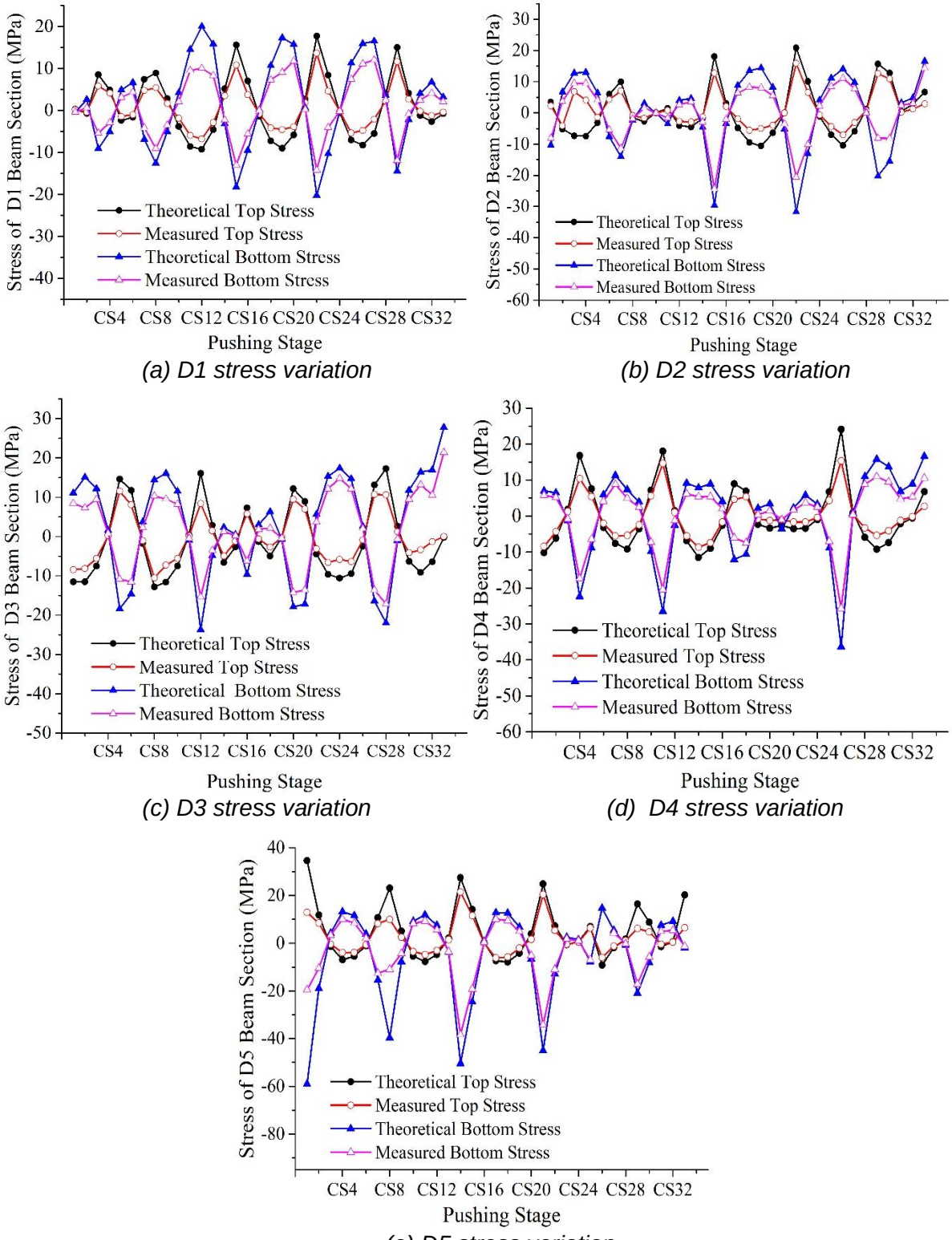

(a) D1 stress variation *(b) D2 stress variation*

(c) D3 stress variation *(d) D4 stress variation*

(e) D5 stress variation

Fig. 7 - Measured value and theoretical value of beam stress measuring point

Under the working condition of CS12, the maximum theoretical stress at the bottom edge of the measuring point D3 is 23.4 MPa, and the measured stress is 14.2 MPa. When it is pushed to CS32 working condition, the theoretical maximum stress of bottom edge is 32.3 MPa, and the

measured stress is 24.0 MPa. The measured stress at the top edge and bottom edge during the whole process of incremental launching method is less than the theoretical stress. When pushed to CS26, the maximum theoretical stress value of the top edge at the measuring point D4 was 25.2 MPa, and the corresponding measured value was 17.2 MPa; the maximum theoretical stress value of the bottom edge was -33.8 MPa, and the corresponding measured value was -23.5 MPa. The measured stress at the top edge and bottom edge of D4 measuring point in the whole process of incremental launching method is less than the theoretical stress. When pushed to CS1, the maximum theoretical stress of the top edge at the measuring point D5 was 35.6 MPa, and the corresponding measured value was 13.4 MPa; the maximum theoretical stress of the bottom edge was -58.6 MPa, and the corresponding measured value was -19.6 MPa. The measured stress at the top edge and bottom edge of measuring point D4 in the whole process of incremental launching method is less than the theoretical stress.

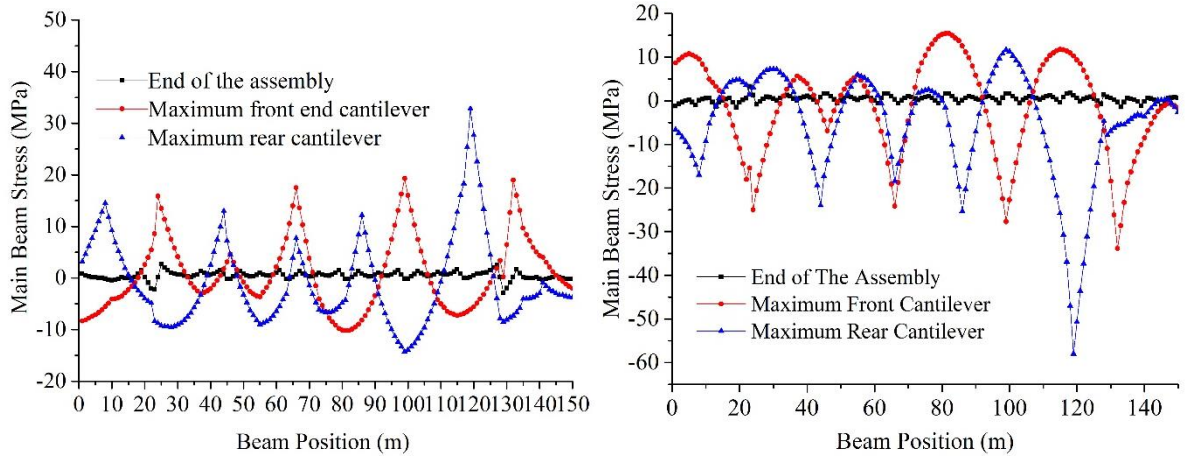

(a)Top Edge Stress *(b) Bottom Edge Stress*

Fig. 8 - Stress at top edge and bottom edge of beam at worst

In the process of incremental launching method, the most unfavourable condition of structural force will occur. The maximum state of the cantilever at the front end of the bridge and the maximum state of the cantilever at the rear end of the bridge in this project are the most unfavourable conditions. The stress of the top edge and bottom edge of the beam under the most unfavourable conditions is shown in Figure 8. When the cantilever at the end of the bridge is the largest, the stress at 117 m of the beam is the largest, the stress at the top edge is 33.7 MPa, and the stress at the bottom edge is -58.2 MPa. The stress in other sections did not exceed 30 MPa, and the beam was under uniform stress.

Stress of arch rib for incremental launching method

In the whole process of incremental launching method, the measured and theoretical stress values at the five measuring points of E1~E5 under different incremental launching method conditions are shown in Figure 9. Under the condition of CS33, the maximum theoretical stress of arch rib at the measuring point E1 was -41.3 MPa, and the measured stress was 28.0 MPa. The measured stress of arch rib was slightly less than the theoretical value, and the variation trend was consistent. Under the condition of CS33, the maximum theoretical stress of arch rib at measuring point E2 was -40.8 MPa, and the measured stress was 25.6 MPa. The measured stress of the arch rib was slightly less than the theoretical one, and the variation trend was consistent. When pushed up to the CS6 working condition, the arch rib stress at the measuring point E2 was -7.2 MPa at most, and the measured stress was 4.3 MPa at this time. Compared with the other four measuring points, the stress change at the measuring point E2 was uniform and did not exceed 10 MPa. The maximum stress at the measuring points E4 and E5 occurred under the working condition of CS33. Due to the

removal of the temporary pier beam in the water, the cable force of the sling increased, which increased the axial force of the arch rib.

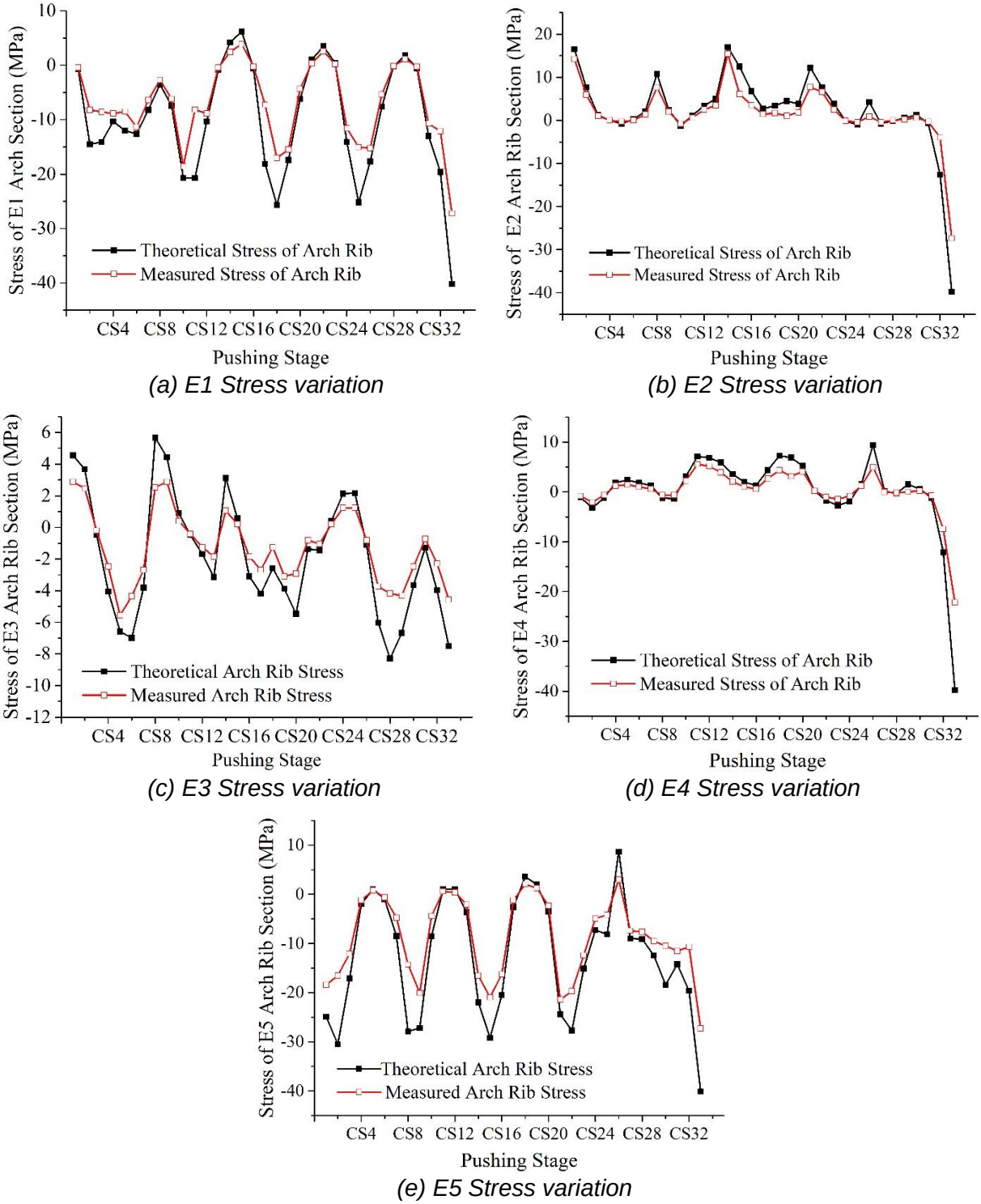

(a) E1 Stress variation

(b) E2 Stress variation

(c) E3 Stress variation

(d) E4 Stress variation

(e) E5 Stress variation

Fig. 9 - Measured value and theoretical value of beam stress measuringpPoint

Temporary pier counterforce

The temporary pier is supported by steel tube lattice column and the stress of steel tube is measured by vibrating string strain gauge affixed to the surface of the steel tube. L1 and L2 are temporary support piers in water, L3~L6 are temporary support piers on shore, and 1~4 are permanent support piers. The temporary pier buttress reaction varies with the change of the incremental launching position, and the maximum of the buttress reaction is about 6000 kN. The maximum bracing reaction of L1, L2, 2 and 3 temporary piers occurs at the arch foot position inside the head, while the maximum bracing reaction of L3-L6 temporary piers occurs at the arch foot position inside the tail. The test value of L2 and L3 temporary pier support reaction force is basically consistent with the theoretical value, and the test value is slightly less than the theoretical value.

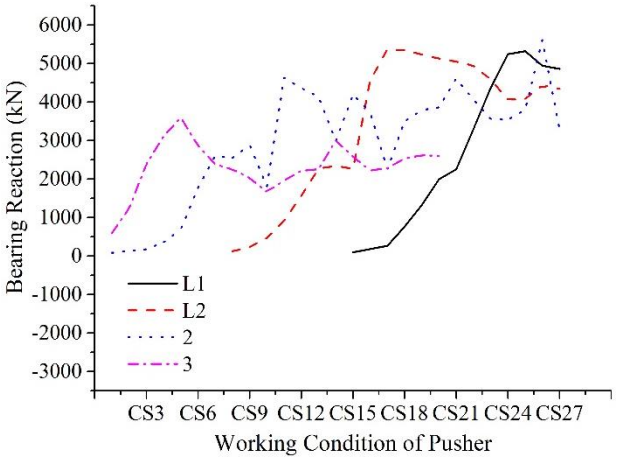

(a) Reaction values of piers L1、L2、2 and 3

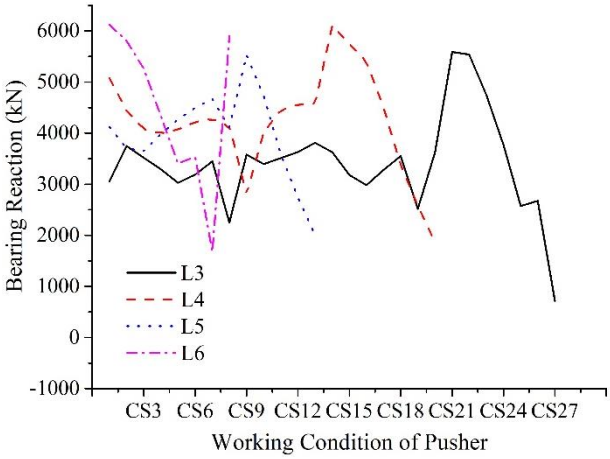

(b) Reaction values of piers L3、L4、L5 and L6

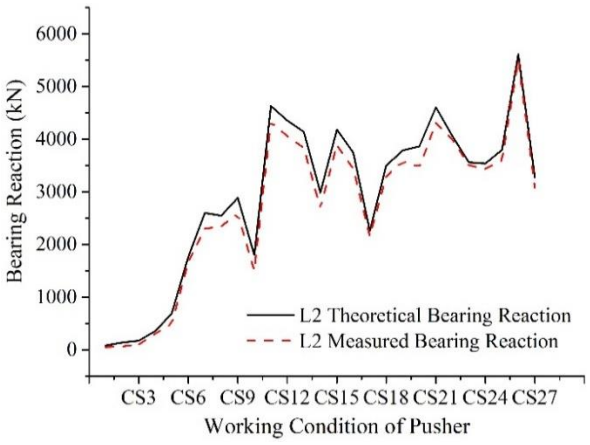

(c) Theoretical and measured values of L2 pier

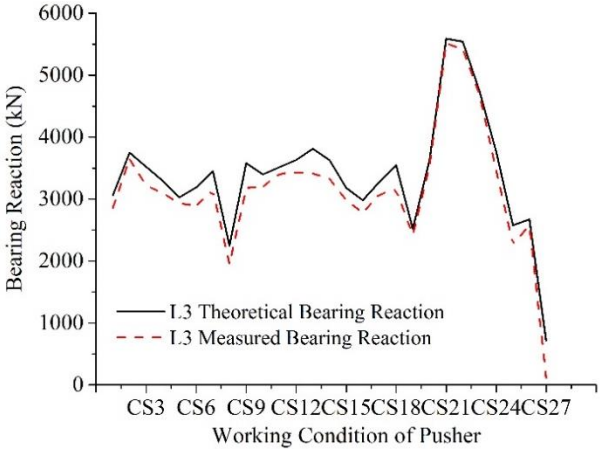

(d) Theoretical and measured values of L2 pier

Fig.10 - Temporary pier support reaction

Deflection of incremental launching process

During the whole incremental launching process, the deflection measurement points of the main beam and launching nose are shown in Figure 4. The deflection measurement point of the launching nose end is A1, the deflection measurement point of the beam mid-span is A3, and the deflection measurement points of the beam end are A2 and A4. The deflection range of the launching nose during the top pushing is -30mm~10mm, the deflection of the measuring point at the beam end is -35mm~0mm, and the deflection of the beam mid-span is -47.6 mm~0 mm. The deflection of the mid-span of the beam is almost unchanged before the temporary pier is removed.

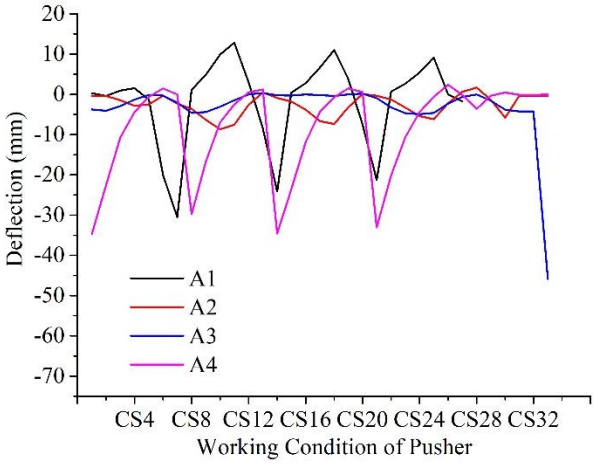

Fig.11 - Deflection value of main beam

Sling force

In the incremental launching process, the cable force value is about the mid-span symmetry of the bridge. The measured value is basically consistent with the theoretical value, and the error between the theoretical value and the measured value is within 5%.

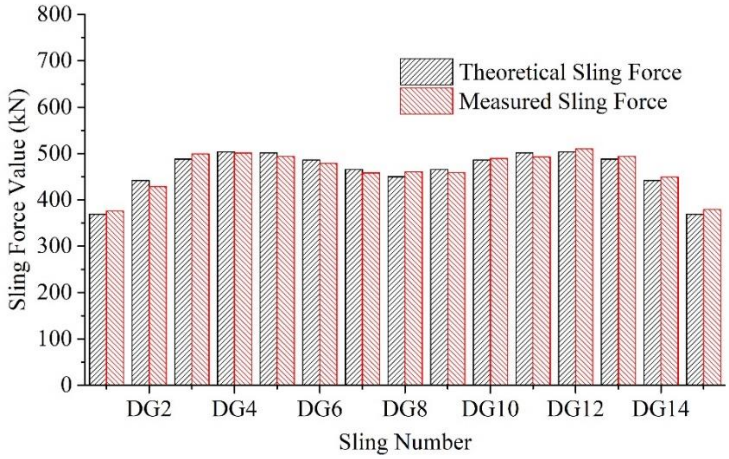

Fig.12 - Cable force of the sling

Launching nose parameter analysis

In the process of incremental launching construction, the structural system of the bridge is constantly changing, and each section should bear the action of positive and negative bending moments alternately. The application of launching nose effectively reduces the cantilever length of the main beam, improves the stress condition of the main beam, and also plays a role in increasing the structural stability and preventing overturning and instability. In the analysis of launching nose, the parameters such as the length, stiffness and the mass of the length of the launching nose have great influence on the stress of the main beam.

Although the structural form of girder and arch composite bridge is complex, its stiffness and dead weight are not uniformly distributed along the longitudinal direction, which is very different from the continuous beam with equal section, so it is difficult to configure launching nose according to the method of equal section beam. The model under different construction conditions was established by finite element software, and the influence of the variation of launching nose parameters on the bridge stress was studied from two aspects: the ratio of the length of launching nose to the maximum span of thrust (α), the ratio of the dead weight load per unit length of launching nose and the dead

weight load per unit length of main beam (β). It provides a reference for the selection of design parameters for the overall incremental launching construction launching nose. In addition, the design of the launching nose can only be studied if the temporary support is set up first.

During the incremental launching process, if the length of the launching nose is too short, the structure may be damaged due to excessive stress under the maximum cantilever condition. If the length is too long, the launching nose will not play its role and the economy is poor. Therefore, an appropriate launching nose length should be selected. The length of the launching nose in this project is 23 m, and the ratio of the length of the launching nose L_n to the maximum span L of the thrust is α =0.7. Assuming that the cross-section and structural form of the launching nose remain unchanged and the length of the launching nose is changed, the value of is taken to be 0.45, 0.55, 0.65, 0.75 and 0.85, respectively. Bending moments of the upstream main beam and arch rib are listed, as shown in Figure 13 and Figure 14. When is 0.45~0.75, the bending moment of the main beam has little change, while when is 0.55~0.85, the negative bending moment of the main arch has little change. The maximum stress of the upstream main beam and arch rib is shown in Figure 15 and Figure 16. As the length of launching nose increases, the variation trend of stress is consistent. When is 0.75 and 0.85, the compressive stress of main beam is larger, with a maximum of -50 MPa; when is 0.75 and 0.85, the stress of arch rib is larger, with a maximum of 50 MPa. The appropriate range for α is 0.55~0.65 and the deflection of the launching nose is 21.1mm~22.8mm.

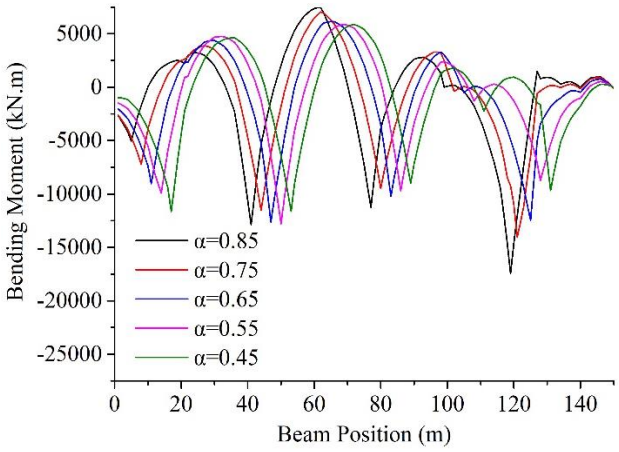

Fig. 13 - Beam bending moment of different guide beam length

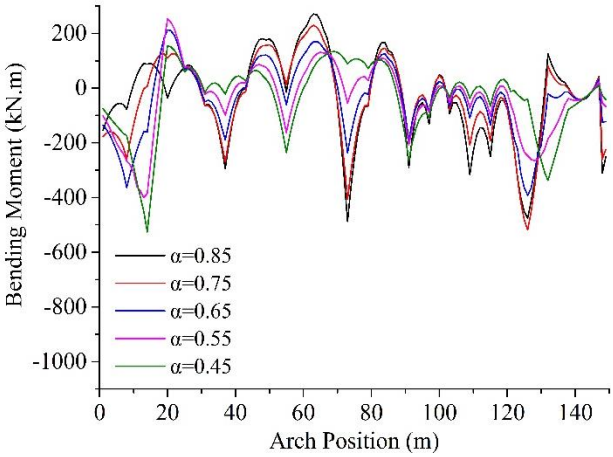

Fig.14 - Arch bending moments of different guide beam lengths

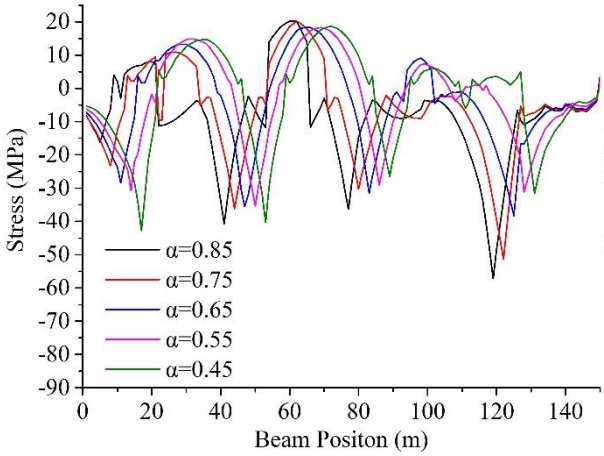

Fig.15 - Beam bending moment of different guide beam length

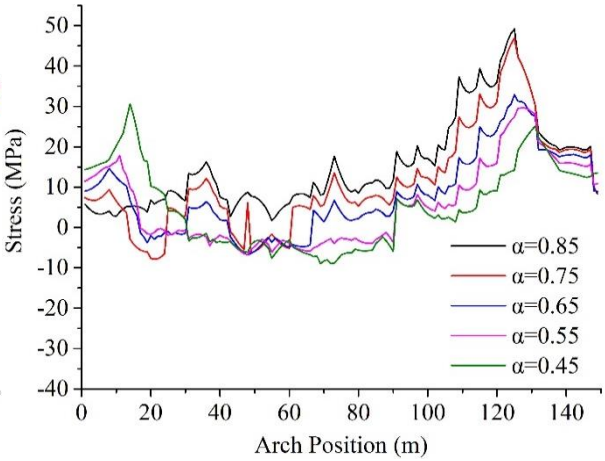

Fig.16 - Arch stress of different lengths of launching nose

Tab.2- Deflection of launching nose at different lengths

α	0.85	0.75	0.65	0.55	0.45
Deflection (mm)	22.7	25.8	22.8	21.1	20.6

It is assumed that the stiffness and length of the launching nose remain unchanged. The values of β were 0.2, 0.4, 0.6, 0.8 and 1. In view of these conditions, the influence of the dead weight per unit length of the launching nose on the structure is studied under the maximum cantilever condition. In finite element software, the change of value is achieved by changing the bulk density of the launching nose material. As shown in Figure 17 and Figure 18, when the launching nose weight per unit length is taken as different values, the stress variation trend of main beam and arch rib is the same and almost unchanged. As shown in Table 2, the deflection of the launching nose increases with the increase of density, and the maximum value is 25.8mm.

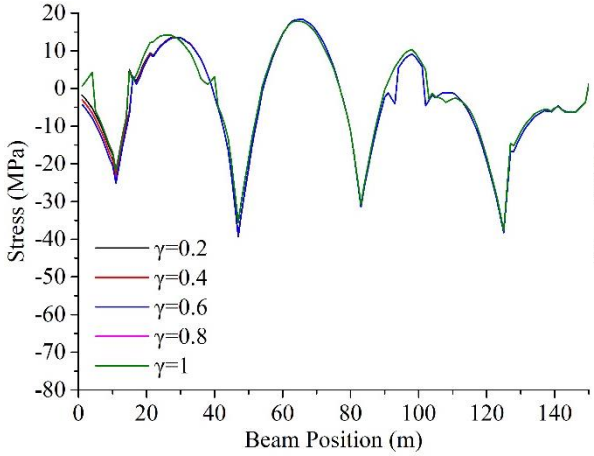

Fig.17 - Beam stress under different density Beam

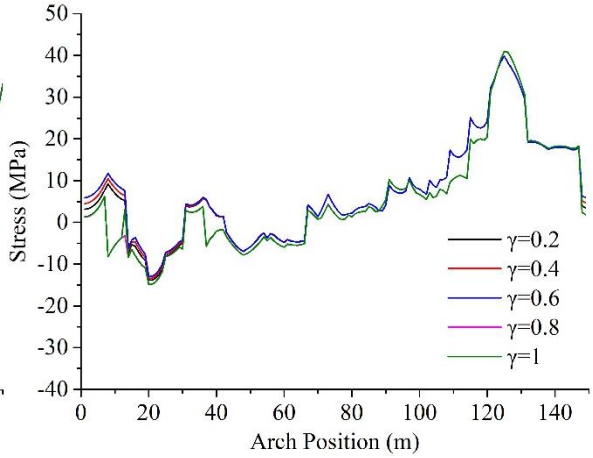

Fig.18- Arch stress under different density of guide of launching nose

Fig. 3 - Deflection of launching nose under different launching nose density

β	0.2	0.4	0.6	0.8	1
Deflection (mm)	5.9	10.1	14.3	19.4	25.8

CONCLUSION

At present, there are few researches on the overall incremental launching construction of the beam arch composite bridge, and the stress form of its temporary members in the incremental launching construction is not fully understood. Based on the research background of the whole incremental launching construction of the supported tie bar arch combination structure, this paper studies the temporary members in the incremental launching construction by establishing the finite element model, which provides reference experience for the temporary design of the same type of beam arch combination structure. The research results of this paper can provide reference for the construction of similar bridges. The conclusions of this paper are as follows:

In the process of incremental launching construction, the measured and theoretical stress values of the beam and arch have a high degree of coincidence, the stress is between -30.4 MPa and 16.5 MPa, all within the safe range. The field monitoring results show that the stress changes slowly in the measuring points of the bridge, which indicates that the external force is applied slowly and evenly in the construction process.

When the cantilever at the end of the bridge reaches the maximum, it is in the most unfavourable state. At this time, the stress at the 117 m position of the beam reaches the

maximum, the stress at the top edge is 33.7 MPa, and the stress at the bottom edge is -58.2 MPa. The stress in other sections did not exceed 30 MPa, and the beam was under uniform stress.

The temporary pier buttress reaction varies with the change of the incremental launching position, and the maximum of the buttress reaction is about 6000 kN. When the front foot of the internal arch passes by, the maximum supporting reaction of each temporary pier at the beginning of the incremental launching appears at the rear foot of the internal arch. The maximum supporting reaction of each temporary pier at the beginning of the incremental launching occurs when the arch foot in the front of the internal arch passes, while the maximum supporting reaction of each temporary pier at the beginning of the incremental launching occurs when the arch foot in the rear of the internal arch passes.

During the incremental launching process, if the length of the launching nose is too short, the structure may be damaged due to excessive stress under the maximum cantilever condition. If the length is too long, the launching nose will not play its role and the economy is poor. Therefore, an appropriate launching nose length should be selected. The reasonable range of α is 0.55~0.65, which is the ratio between the length Ln of launching nose and the maximum span L of incremental launching.

ACKNOWLEDGEMENTS

Thanks for the support of the Open Fund project of key Laboratory of Ministry of Education for Disaster and Control of Major Engineering (20200904012).

REFERENCES

[1] Jung K H , Kim K S , Sim C W , et al. Verification of Incremental Launching Construction Safety for the Ilsun Bridge, the World's Longest and Widest Prestressed Concrete Box Girder with Corrugated Steel Web Section[J]. Journal of Bridge Engineering, 2011, 16(3):453-460.

[2] Marzouk M , El-Dein H Z , El-Said M . Application of computer simulation to construction of incremental launching bridges[J]. Statyba, 2007, 13(1):27-36.

[3] Sampaio A Z , Martins O P . The application of virtual reality technology in the construction of bridge: The cantilever and incremental launching methods[J]. Automation in Construction, 2014, 37(jan.):58-67.

[4] Yong-Hong C . Incremental Launching Construction of Steel Box Girder of Self-Anchored Suspension Bridge of Pingsheng Bridge[J]. Bridge Construction, 2006.

[5] Xu, Ming K . Incremental Launching Construction Method for Steel Truss Suspension Bridge[J]. Advanced Materials Research, 2011, 204-210:842-845.

[6] Wang W , Zheng H , Zeng X . Optimum Design of Launching Nose during Incremental Launching Construction of Same-Span Continuous Bridge[J]. World Academy of Science, Engineering & Technology, 2011(72):861.

[7] Lin, J, P, et al. Evaluation of Long Multi-Span Steel U-Shaped Girder During Incremental Launching Construction[J]. Journal of Testing and Evaluation: A Multidisciplinary Forum for Applied Sciences and Engineering, 2015, 43(2).

[8] Jiang T Y , Tian Z C , Xu J H . Key Technologies of Whole Incremental Launching Construction Control for Inclined Continuous Box Girder with Steep Longitudinal Gradient[J]. Applied Mechanics & Materials, 2012, 204-208:2034-2039.

[9] Dai J , Di J , Qin F J , et al. Finite Element Analysis on Incremental Launching Construction for Steel Box Girder[J]. Advanced Materials Research, 2013, 671-674(1):974-979.

[10] Roeder C W , Macrae G , Crocker P . Dynamic Response and Fatigue of Steel Tied-Arch Bridge[J]. Journal of Bridge Engineering, 2000, 5(1):14-21.

[11] Cheng K M , Ketchum R A , Drouillard R . Nanning Butterfly Tied Arch Bridge Over the Yong River in China[J]. Structural engineering international, 2010, 20(3):P.308-311.

[12] Kim, Woo, Jong, et al. Gyopo Bridge: A Double-Tied Arch Bridge in Poseung-Pyeongtaek Railroad[J]. Structural Engineering International, 2012.
[13] Duan Y F , Li Y , Xiang Y Q . Strain-temperature correlation analysis of a tied arch bridge using monitoring data[C]// 2011 International Conference on Multimedia Technology. IEEE, 2011.
[14] Bai J C . Construction Control Technique for Special-Shaped Tied-Arch Bridge with Anti-Symmetric Reinforced Concrete Arch Ribs[J]. Bridge Construction, 2018, 48(3):116-120.
[15] Bangwu Y , Feng Y , Xiangrong G , et al. Influence of temperature deformation on vehicle-bridge dynamic response of long-span steel box-girder tied-arch bridge[J]. Journal of Railway Science and Engineering, 2013.

CIVIL ENGINEERING JOURNAL

Article no. 33

THE CIVIL ENGINEERING JOURNAL 2-2021

BENEFIT FROM CHAINED MASONRY WALLS TO IMPROVE THE SEISMIC RESPONSE OF REINFORCED CONCRETE BUILDINGS

Abdelkader Nour[1], Abdelkader Benanane[1] and Humberto Varum[2]

1. *Laboratory Materials and Processes of Construction, Faculty of Science & Technology, University of Mostaganem, Algeria; abdelkader.nour@univ-mosta-dz, abdelkader.benanane@univ-mosta-dz*

2. *CONSTRUCT-LESE, Department of Civil Engineering, Faculty of Engineering, University of Porto, Portugal; hvarum@fe.up.pt*

ABSTRACT

The multiple earthquakes have proved the effect of chained masonry walls on the seismic behaviour of multistorey reinforced concrete buildings. The chained masonry walls have been considered one of the types of masonry infill walls but without gaps between the wall and the surrounding frame. This participation came intending to study this effect through the modeling of several two-dimensional frames for a multistorey reinforced concrete building, taking into account the hollow brick walls, which represent the most common type in Algeria. We analyzed the proposed models using ETABS finite element software, relying on the response spectrum method and respecting the most important requirements according to the applicable Algerian Seismic Code. After analysis of the different models, the results have been compared according to the parameters of the period, base shear, lateral displacement, and stiffness. Through a critical synthesis of the results, we concluded that these walls could significantly affect the seismic behaviour of this type of buildings. Moreover, the neglect of these walls in the modeling process can lead designers to have a false perception of the behaviour of these buildings towards seismic loadings.

KEYWORDS

Chained masonry wall, Seismic behaviour, Reinforced concrete building, Hollow brick, Algerian Seismic Code

INTRODUCTION

The need to infill the spaces between columns and beams, is a necessary issue in building and construction processes, especially in multi-storey buildings, this type of building is widely used in most parts of the world, especially in Algeria. Also, the most well-known types of infill walls are those which are mainly made of hollow red bricks due to their lightness and multiple properties.

Based on the multiple earthquakes that have hit various parts of the world, it can be said that these have caused severe damage to these types of buildings and caused many of them to collapse completely.

If we looked at the direct causes of these earthquakes, we would find that they do not deviate from two basic questions:

First, it is necessary to ensure the proper design of buildings to be constructed by finding models that simulate the actual behaviour of buildings when exposed to potential earthquakes. This allows us to reduce the damage that these inevitable disasters can cause.

Secondly, the strict implementation of the previously prepared designs, ensuring that the appropriate materials are brought in for the construction operations, and continuous monitoring of the work to ensure that the completed buildings conform to what was designed.

To shine more light and scrutinize, we have tried to address the first reason, which revolves around the following question: how to achieve the best simulation of what will be accomplished in the site?

To answer this question, we can say that the only way to achieve this is to try to model the largest possible number of constituent elements of this building, taking into account the importance and behaviour of each component to know its role in strength or rigidity.

In addition to what will be detailed in this article, masonry infill walls, cannot be neglected in the analysis of reinforced concrete or steel buildings, nor be considered as non-structural elements, because the reality lies and the best proof of all that we have said is the loss and damage, which has been recorded across different countries.

In an attempt to understand the behaviour of these walls, we have listed the most important approaches used in the structural analysis of reinforced concrete buildings, which were the results of the most important research and experiments based on real models or scaled-down models.

These approaches can be summarized in three main families, which are simplistic models (macro-models) [1-3], average models (meso-models) [3-7], as well as precise models (micro-models) [1-5,8-10]. To highlight evidence of this diversity, we can say that it results from the different characteristics of the different components of these masonry walls without forgetting the interaction between them and the surrounding environment [3-5,11-13].

Following the Boumerdes earthquake on May 21, 2003, and at the invitation of Mr. Mohamed Nadir HAMIMIDE, Minister of Housing and Urban Planning, Mr. Victor DAVIDOVICI went to Algeria from Wednesday, May 28 to Sunday, June 1, 2003 [19].

The objective of this mission was to make an independent analysis of the causes of the multiple damages and collapses of buildings and to propose priority actions to be put in place in the immediate [19].

Through this mission, this researcher drew up a preliminary report, where he tried to present the most important reasons that caused, in one way or another, the collapse of important parts of the buildings that were subjected to the earthquake, and he focused on particular on the walls of the masonry infill most used in our country, which builds walls and connects them rigidly to the frames that surround it (Figure 1 & Figure 2) [19]. This article has therefore focused on this particular type, which represents the most responded type in Algeria and hence the term chained masonry which has been used in this article.

Although the Algerian seismic code [17] does not give any method to model masonry infill walls, this earthquake engineering consultant also explained that not modeling these walls in the design processes causes the building to lose additional stiffness and resistance. This led us to think about presenting a reliable model on this aspect, through which we can treat the seismic behaviour of these infill walls.

Fig. 1 – Rigid connection, BOUMERDES earthquake of May 21, 2003

The subject of the study that we will present below is limited to the importance of the role played by the chained masonry wall. This type represents the case of masonry infill without gaps, either with the columns or with the beams, in hollow bricks interconnected by a cement-based mortar, these walls occupy the void for the reinforced concrete frame in high seismicity area, according to the current codes in Algeria [14].

Fig. 2 – Chained masonry, BOUMERDES earthquake of May 21, 2003

In the following, we have carried out a parametric study by analyzing several models of a two-dimensional multistorey reinforced concrete frame using the response spectrum method.

With ETABS finite element software [15], we analyzed the proposed models and compared the results by a critical synthesis to assess the seismic response of these models by the study of the positive role paled by the chained masonry infill walls.

METHODS

The study presented in this article concerns the numerical modeling of 2D reinforced concrete frames, using ETABS software [15], by the response spectrum method recommended in the Algerian Seismic Code (ASC99v2003) [17].

The analysis of the models is summarized as follows:

Modeling the frames and extracting the results for the period, base shear, lateral displacement, and stiffness, so this is a linear dynamic analysis.

Presentation of the analyzed models

The span lengths are 3.00, 4.50, 6.00, and 7.50m and the number of spans is 2, 4, and 6 for all models. The number of storeys is fixed at 11 storeys and the storey height is 3.06m.

The characteristics of concrete and steel of columns and beams are taken from the Algerian Code of Reinforced Concrete [16]. The compressive strength of concrete is 25000 kN/m^2, the elastic limit of steel is 500000 kN/m^2.

The masonry used in this study is the hollow brick cited in the Algerian Code of Masonry [14], with an elastic modulus of 2000000 kN/m^2, and compressive strength of 2000 kN/m^2. The wall thickness of the chained masonry is 0.30m, which represents a double leaf wall, with a bloc of 0.10m, bloc of 0.15m, and 0.05m of space between two pieces of hollow bricks as shown in Table 1.

Tab. 1 - Geometric and mechanical characteristics of frames

Designation	Values or type
Concrete strength (kN/m^2)	25000
Modulus of elasticity of concrete, E_c (kN/m^2)	32164000
Steel tensile yield strength (kN/m^2)	500000
Storey height (m)	3.06
Number of storey	11
Building height (m)	33.66m
Span length (m)	3.00m, 4.50m, 6.00m and 7.00m
Number of spans	2, 4 and 6
Masonry compressive strength, f_m (kN/m^2)	2000
Modulus of elasticity of masonry, E_m (kN/m^2)	2000000
Thickness of masonry walls, t_m (m)	0.30

The cross-sections of columns and beams are grouped in Table 2.

Tab. 2 - Cross-sections of beams and columns

Number of storey	Length Span (m)			
	3.00m	4.50m	6.00m	7.50m
	Beam's Dimensions (m)			
	0.30 x 0.30	0.30 x 0.40	0.30 x 0.50	0.30 x 0.60
	Column's Dimensions (m)			
11	0.45 x 0.45			
10	0.45 x 0.45			
9	0.50 x 0.50			
8	0.50 x 0.50			
7	0.50 x 0.50			
6	0.55 x 0.55			
5	0.55 x 0.55			
4	0.55 x 0.55			
3	0.60 x 0.60			
2	0.60 x 0.60			
1	0.60 x 0.60			

For the loads used in the analysis of all frames, we have 6kN/m^2 as dead loads and 1.50kN/m^2 as live loads.

For the response spectrum, we referred to the Algerian Seismic Code (ASC99v2003) [17], by using a spectrum for a zone of high seismicity (zone III), a user group of 2, a loose soil (S3), and a behaviour factor of 3.5.

For the source of the mass, we took the totality of the dead loads plus 20% of the live loads [17].

Validation of the proposed model

For the validation of the proposed model, we used the famous SEISMOSTRUCT software [18], which offers a great possibility of modeling the masonry infill walls, of a 7-storey frame, and then we compared the results with the use of the ETABS software of the same frame mentioned above [15].

The model of Seismostruct software, has validated experimentally. In Seismostruct software, the infill is considered as a four-node masonry panel element developed and initially programmed by Crisafulli (1997) [..] and implemented in Seismostruct by Blandon (2005) to see the nonlinear response of infill panels in frames. Each panel is represented by six struts; each diagonal direction represents two struts capable of taking axial loads along two opposite diagonal corners and a third to take shear from the top to the bottom of the panel. This last link acts only across the diagonal which is in compression, therefore it's (activation) depends on the deformation of the infill panel. The connecting strut under axial loads use the hysteresis model of masonry connecting struts developed by Crisafulli et all (2000) [..].

RESULTS

In this section, we proceeded to compare, comment, and discuss the results according to the period, the base shear, the lateral displacement, and stiffness.

Comparison of analyzed models in term of period

Tab. 3- Period of analyzed frames

Number of spans	Span length (3.00m)			Span length (4.50m)			Span length (6.00m)			Span length (7.50m)		
	Bare Frame	Fully Infilled	Ratio (%)	Bare Frame	Fully Infilled	Ratio (%)	Bare Frame	Fully Infilled	Ratio (%)	Bare Frame	Fully Infilled	Ratio (%)
2	1.485	0.589	60.34%	1.456	0.538	63.05%	1.427	0.514	63.98%	1.405	0.501	64.34%
4	1.457	0.487	66.58%	1.446	0.471	67.43%	1.427	0.465	67.41%	1.413	0.462	67.30%
6	1.448	0.454	68.65%	1.442	0.451	68.72%	1.427	0.450	68.47%	1.416	0.451	68.15%
Used unit in Seconds												

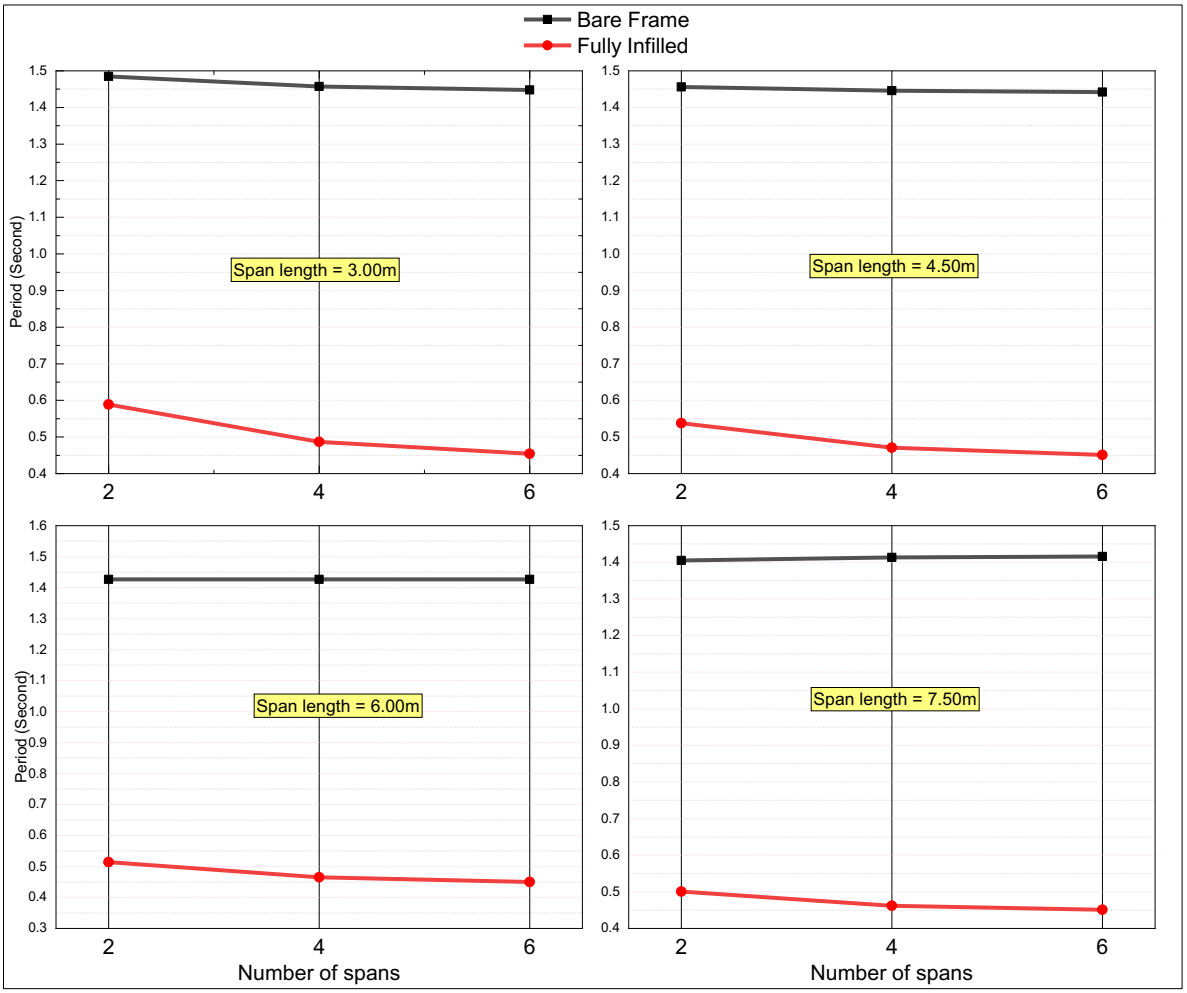

Fig. 3 – Period of analyzed frames

Table 3 and Figure 3 represent the comparison of the results between the different models that were analyzed in terms of the period of vibration, which can be summarized as follows:

This allows us to notice that all fully infilled frames recorded much lower period values than their fully bare counterparts, indicating that the introduction of chained masonry infill walls in the modeling processes of reinforced concrete frames, has significantly contributed to the decrease in period values and thus helps these frames exhibit better strength to seismic loadings.

If we want to deepen the analysis of the results obtained, we can say that the values of the period of all models fully infilled frames, decreased by more than 60% compared to their fully bare counterparts.

These significant values recorded by all fully infilled frames undoubtedly demonstrated the significant contribution of chained masonry infill walls to improving the performance of these frames when exposed to seismic loadings.

Comparison of analyzed models in term of base shear

Tab. 4 - Base shear of analyzed frames

Number of spans	Span length (3.00m)			Span length (4.50m)			Span length (6.00m)			Span length (7.50m)		
	Bare Frame	Fully Infilled	Ratio (%)	Bare Frame	Fully Infilled	Ratio (%)	Bare Frame	Fully Infilled	Ratio (%)	Bare Frame	Fully Infilled	Ratio (%)
2	191.18	376.52	*1.97*	272.66	577.01	*2.12*	361.59	785.84	*2.17*	454.91	1003.95	*2.21*
4	371.16	848.59	*2.29*	532.95	1263.20	*2.37*	707.50	1691.14	*2.39*	891.26	2132.80	*2.39*
6	552.15	1337.98	*2.42*	791.36	1956.15	*2.47*	1053.37	2596.26	*2.46*	1324.90	3257.49	*2.46*
Used unit is kN												

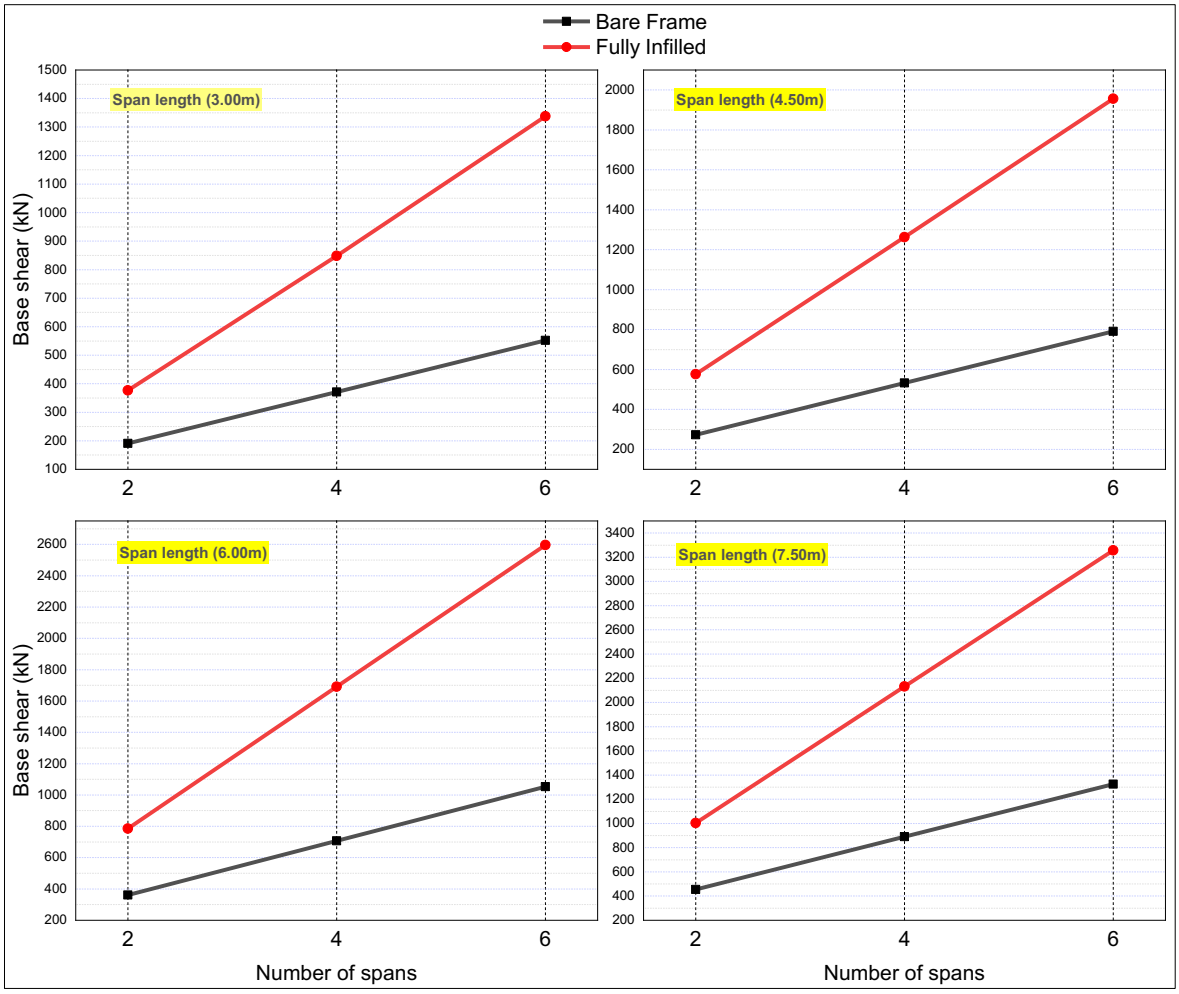

Fig. 4 – Base shear of analyzed frames

Table 4 and Figure 4 summarize the results of the different models that had analyzed in terms of the base shear, which can be interpreted as follows:

These results allow us to note that all fully infilled frames had recorded much larger base shear values than their fully bare counterparts. This comes down to the consideration of the chained masonry infill walls by their inclusion in the modeling of the reinforced concrete frames, which participated significantly in the increase of the basic shear values and therefore increases the strength of these frames to seismic loadings.

If we want to detail the analysis of the aforementioned results, we can say that the base shear values of all models of fully infilled frames have increased by more than 2 times compared to their fully bare counterparts.

These significant values recorded by all fully infilled frames demonstrated the important contribution of chained masonry infill walls to improving the performance of these frames when exposed to seismic loadings.

Comparison of analyzed models in term of lateral displacement

Tab. 5 - Lateral displacement of analyzed frames

Number of spans	Span length (3.00m)			Span length (4.50m)			Span length (6.00m)			Span length (7.50m)		
	Bare Frame	Fully Infilled	Ratio (%)	Bare Frame	Fully Infilled	Ratio (%)	Bare Frame	Fully Infilled	Ratio (%)	Bare Frame	Fully Infilled	Ratio (%)
2	0.0710	0.0224	*68.45%*	0.0682	0.0194	*71.55%*	0.0661	0.0179	*72.92%*	0.0646	0.0170	*73.68%*
4	0.0683	0.0167	*75.55%*	0.0671	0.0158	*76.45%*	0.0658	0.0151	*77.05%*	0.0648	0.0148	*77.16%*
6	0.0677	0.0148	*78.14%*	0.0666	0.0144	*78.38%*	0.0657	0.0142	*78.39%*	0.0649	0.0141	*78.27%*
Used unit is m												

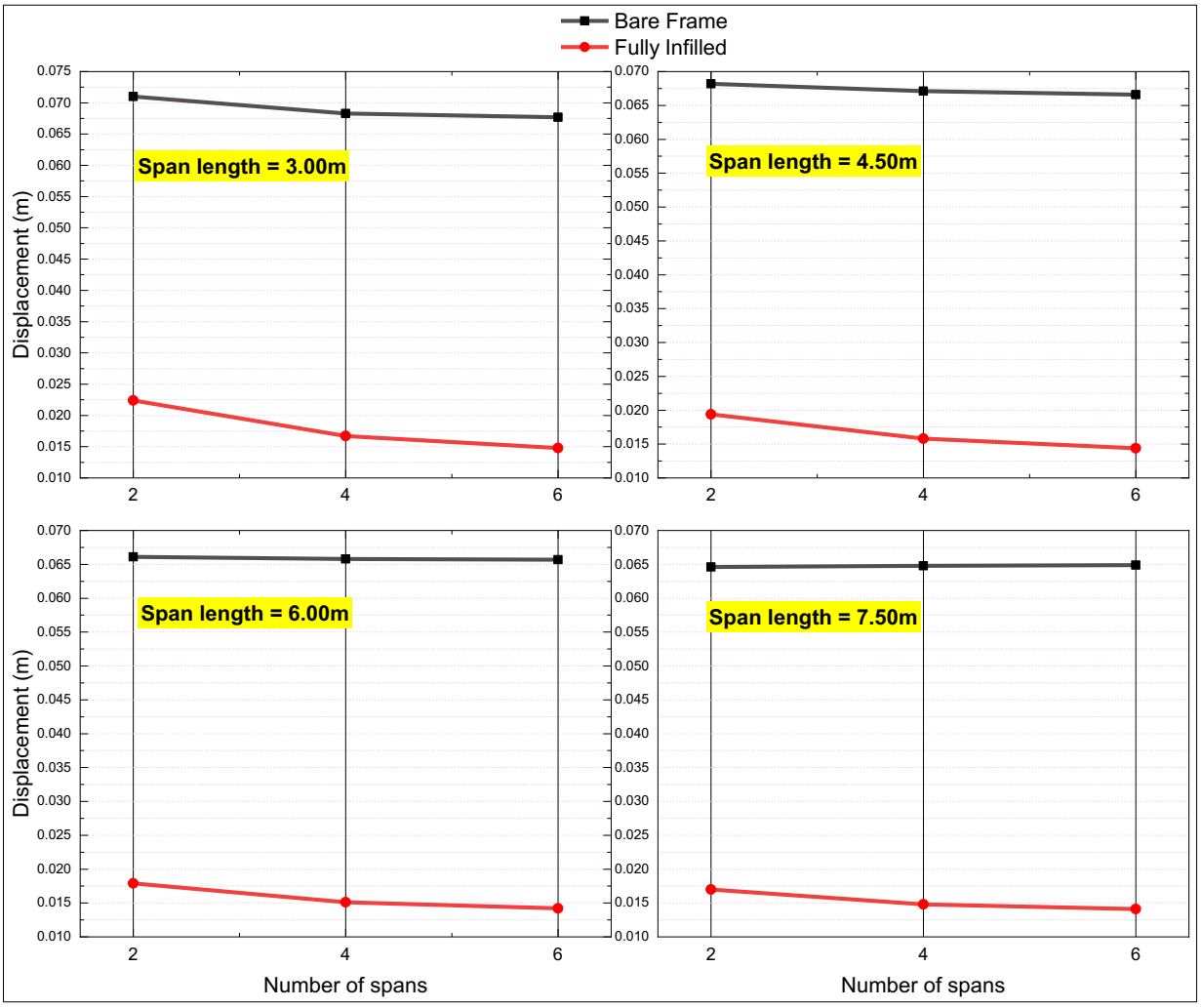

Fig. 5 – Lateral displacement of analyzed frames

Through Table 5 and Figure 5, which represent the results obtained within the framework of the analysis of the seismic response in terms of the lateral displacement of the reinforced concrete frames, we can read the following:

All fully infilled frames recorded small values compared to their fully bare counterparts. This decrease in the lateral displacement values is the result of the introduction of chained masonry infill walls, in the modeling processes of the reinforced concrete frames that have been proposed.

These results can be detailed by reading the percentages, which have been recorded in the table above, where we can notice that all the percentages varied between 68% and 78%, which are important percentages, which cannot be neglected and which have indicated the great change in seismic behaviour of these frames. This leads us to say that the inclusion of these walls in the modeling process can play a vital role in improving the strength of reinforced concrete buildings when they are exposed to seismic loadings.

Comparison of analyzed models in term of stiffness

Tab. 6 - Stiffness of analyzed frames

Number of spans	Span length (3.00m)			Span length (4.50m)			Span length (6.00m)			Span length (7.50m)		
	Bare Frame	Fully Infilled	Ratio (%)	Bare Frame	Fully Infilled	Ratio (%)	Bare Frame	Fully Infilled	Ratio (%)	Bare Frame	Fully Infilled	Ratio (%)
2	63490	348824	*5.49*	81177	475040	*5.85*	99541	598909	*6.02*	117996	721909	*6.12*
4	117440	724729	*6.17*	150066	961867	*6.41*	183734	1200600	*6.53*	217288	1440452	*6.63*
6	170975	1099107	*6.43*	218558	1447250	*6.62*	267613	1801793	*6.73*	316207	2159438	*6.83*
Used unit is kN/m												

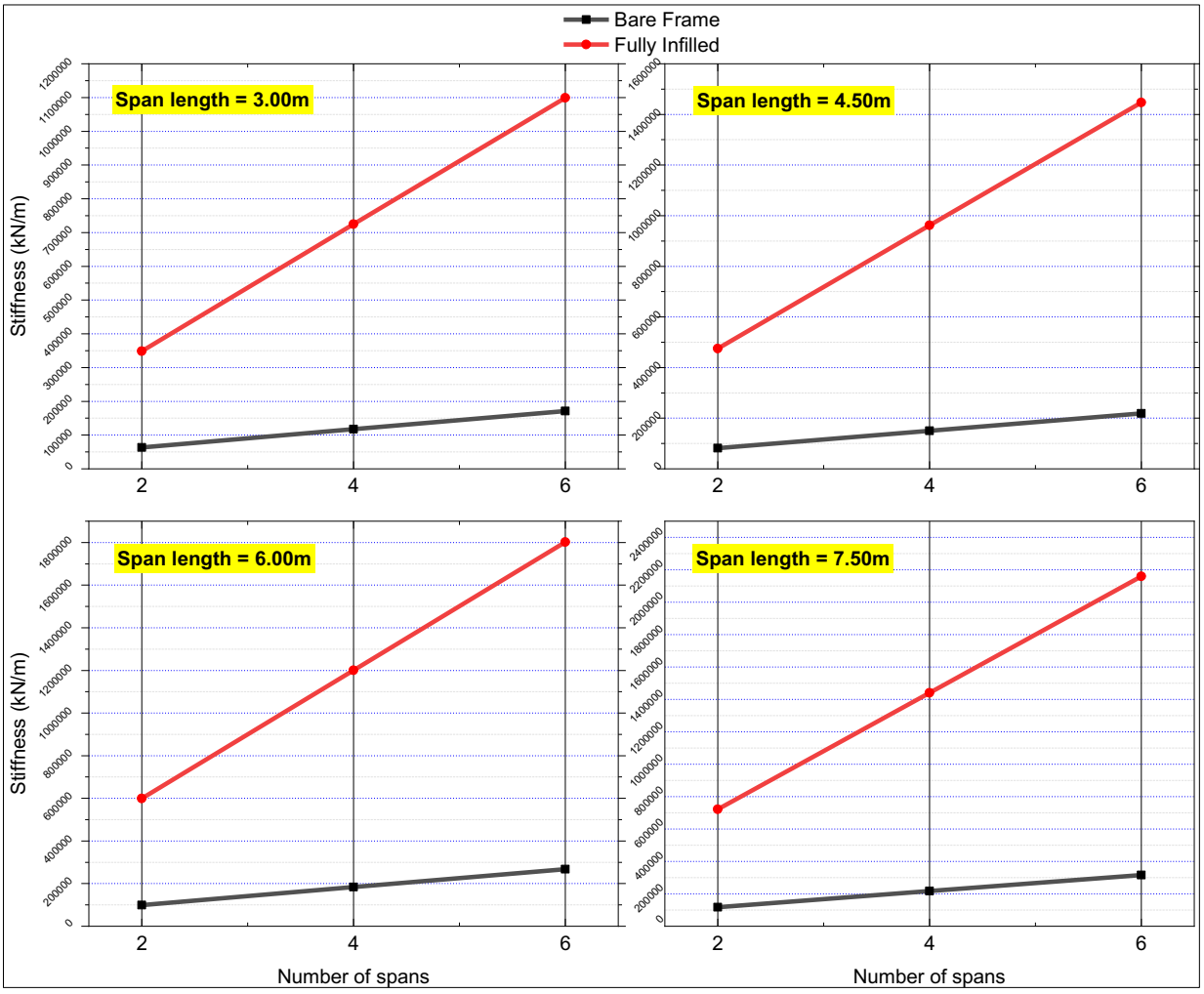

Fig. 6 – Stiffness of analyzed frames

From Figure 6 and also from Table 6, one can quite easily read the large values of the stiffness parameter recorded by all fully infilled frames, compared to fully bare frames, and this is mainly due to the presence of chained masonry infill walls, in the modeling process of reinforced concrete frames.

From the results presented in the table above, it is noted that all the fully infilled frames have stiffness values between 5 and 6 times compared to the values given by their fully bare counterparts.

The results obtained have proven to us beyond any reasonable doubt that the direct modeling of these chained masonry walls has greatly contributed to improving the seismic performance of reinforced concrete frames and significantly increased the strength of these frames when they are exposed to seismic loadings.

CONCLUSION

After completing the study of the proposed models, as well as the results and comparisons according to the parameters that we have previously identified, we can draw the following conclusions:

The direct introduction of chained masonry infill walls, like the main element in the modeling process of reinforced concrete frames, has greatly contributed to lowering the values of the period as well as the lateral displacement and increased the values of the base shear and stiffness. This

allows these frames to acquire better strength to seismic loadings and consequently improves the seismic performance of this type of buildings.

Through the previous results, we can see the essential impact that these walls left on the seismic response of reinforced concrete buildings.

The indirect inclusion of these walls, or their neglect in the process of modeling of reinforced concrete buildings, may lead to an inappropriate expression of the real behaviour of this type of buildings. We can therefore take advantage of the presence of these walls in the modeling process to increase the capacity of these buildings when they are exposed to seismic loadings.

Based on all of the above, we can say that these walls play a vital role in guiding the seismic behaviour of reinforced concrete buildings.

In general, it can be said that modeling infill walls by entering them directly into the design processes, can add additional strength and stiffness to the building that can reduce the losses caused by earthquakes. From there, we can take advantage of these walls to increase the efficiency of the building to dissipate the earthquake energy.

From this point of view, it has become imperative for all researchers, designers, as well as all those interested in this field, to unite their efforts to emerge a simulation better than what is available through a more accurate study based on experiments and as well as numerical analysis software.

We are in the process of using non-linear analysis methods for further study of this type of building, which has spread widely in various countries around the world.

We also try, in collaboration with many specialists in this field, to make contributions, albeit simple, within the framework of the preservation of urban heritage, in particular, what was carried out before the emergence of new simulation techniques, by studying its behaviour through innovative methods so that it can adapt to expected earthquakes and does not suffer significant damage, which can lead to its collapse.

Finally, all efforts must be focused on the linear and non-linear dynamic analysis, of the constituent elements of the masonry infill wall, being represented in a more precise and detailed way, so that specialists and researchers in this field can come closer to the real behaviour of these buildings to seismic loadings.

ACKNOWLEDGEMENTS

I would like to extend my sincere thanks to the people in charge of the Materials and Construction Processes Laboratory, Faculty of Sciences and Technology, University of Mostaganem, Algeria. Who with their help we have done many types of research. Through this laboratory, we were able to conduct many simulations and analyze results.

REFERENCES

[1] I. Fabio and D. Trapani, “Masonry infilled RC frames : Experimental results and development of Dottorato di Ricerca in Ingegneria delle Strutture - XXIV Ciclo Masonry infilled RC frames : Experimental results and development of predictive techniques for the assessment of seismic response Tesi di Dottorato di,” no. September, 2014.

[2] F. Christiana, N. Kyriakides, and E. Georgiou, “FINITE ELEMENT MODEL OF MASONRY-INFILLED RC FRAME FINITE ELEMENT MODEL OF MASONRY-INFILLED RC FRAME,” no. July, 2019.

[3] T. Nicola, C. Leandro, C. Guido, and S. Enrico, “Masonry infilled frame structures: State-of-the-art review of numerical modeling,” Earthq. Struct., vol. 8, no. 3, pp. 733–759, 2015.

[4] K. M. Dolatshahi and A. J. Aref, “Two-dimensional computational framework of meso-scale rigid and line interface elements for masonry structures,” Eng. Struct., vol. 33, no. 12, pp. 3657–3667, 2011.

[5] A. J. Aref and K. M. Dolatshahi, “A three-dimensional cyclic meso-scale numerical procedure for simulation of unreinforced masonry structures,” Comput. Struct., vol. 120, pp. 9–23, 2013.

[6] Q. P. G. Asteris, “Data in Brief The FP4026 Research Database on the fundamental period of RC in fi lled frame structures,” Data Br., vol. 54, pp. 2–7, 2016.
[7] C. Z. Chrysostomou and P. G. Asteris, “On the in-plane properties and capacities of infilled frames,” Eng. Struct., vol. 41, pp. 385–402, 2012.
[8] C. A. Filippou, N. C. Kyriakides, and C. Z. Chrysostomou, “The Open Construction & Building Numerical Modeling of Masonry-infilled RC Frame Abstract :,” pp. 135–148, 2019.
[9] C. A. Filippou, C. Z. Chrysostomou, and N. C. Kyriakides, “NUMERICAL MODELING OF MASONRY-INFILLED RC FRAME STRENGTHENED WITH TRM,” pp. 3114–3128, 2019.
[10] P. G. Asteris, D. M. Cotsovos, C. Z. Chrysostomou, A. Mohebkhah, and G. K. Al-Chaar, “Mathematical micromodeling of infilled frames: state of the art,” Eng. Struct., vol. 56, pp. 1905–1921, 2013.
[11] S. Engineering et al., “Modeling of the lateral stiffness of masonry infilled steel moment-resisting frames Modeling of the lateral stiffness of masonry infilled steel moment - resisting frames,” no. May, 2019.
[12] P. G. Asteris, “Finite element micro-modeling of infilled frames,” Electron. J. Struct. Eng., vol. 8, no. 8, pp. 1–11, 2008.
[13] L. Design, P. G. Asteris, C. C. Repapis, and E. V Repapi, “Fundamental period of infilled reinforced concrete frame structures,” vol. 2479, no. September, 2016.
[14] R. D. E. Conception, E. T. D. E. Calcul, and D. E. S. Maconneries, C 2.45 regles de conception et de calcul des maconneries. .
[15] F. Sap, “CSi Analysis Reference Manual CSI Anal y sis Reference Manual.”
[16] R. D. E. Conception, E. T. D. E. Calcul, D. E. S. Structures, and E. N. Beton, “Regles de conception et de calcul des structures en beton arme c.b.a.93.”
[17] A. Earthquake, R. Regulations, R. Parasismiques, A. Rpa, A. Earthquake, and R. Regulations, “l g e r i a,” pp. 1–39, 2008.
[18] “SeismoStruct User Manual 2018,” 2018.
[19] D. Concept, “Rapport de mission République Algérienne Démocratique et Populaire,” 2003.

CIVIL ENGINEERING JOURNAL

Article no. 34

THE CIVIL ENGINEERING JOURNAL 2-2021

SUSPEN DOME: AN EVALUATION WITH CFRP CABLES

IfeOlorun Olofin and Ronggui Liu

Jiangsu University, FacultyofCivil Engineering and Mechanics,Zhenjiang, No 301 Xuefu road, China; epher2002@yahoo.com

ABSTRACT

This study investigated the feasibility of using CFRP cable as tension cables in suspen domes in view of the fact that suspen domes have been made with steel cables as its cable-strut system for centuries due to its availability. Indisputably, CFRP cables have become the material of choice in the 21st century for its efficiency and innovative design in bridge works. However, the application of CFRP cables to other cable structures has been limited. The need for its application to other cable structures is required in order to acquire more knowledge about its behavioral patterns. This paper gives preliminary findings of a successfully designed and constructed suspen dome prototype which comprehensively deepens the understanding of CFRP cable performance as a cable-strut system in a suspen dome. Results show that with its high stiffness, low weight and high strength, CFRP has proven to be a technically efficient and adequately strengthening material for structurally improving the adequacy of a suspen dome.

KEYWORDS

Cable structures, Suspen dome, Cable-strut system, CFRP cable, Steel cable

INTRODUCTION

The trend for large span structures has become a preferred demand in the construction world today. New materials are searched for by Civil Engineers to construct lightweight structures with remarkable strength in the structure design of large span structures. Long span structures subjected to tension use cables for support. Some common cable structures include those illustrated in Figures. 1(a) and (b), to mention a few.

.

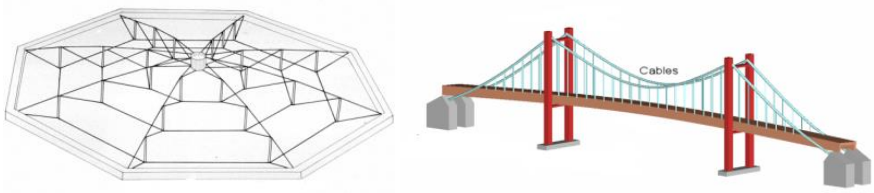

(a) Cable-stayed *(b) Suspension bridge*

Fig. 1- Cable-supported structures (Source: Google search)

An interconnected structure made up of a single reticulated shell and a tensegric system (strut and cable) as shown in Figures. 2(a) and (b) is known as a suspen dome. A cable-strut system is made up of tension and compressive member, where the radial and hoop are in tension and the strut in compression [1]. A Suspen-dome can be categorized as a cable stayed roof and also as a large span structure. The cable system within the suspen dome structure plays a key role in achieving longer span for the structure.

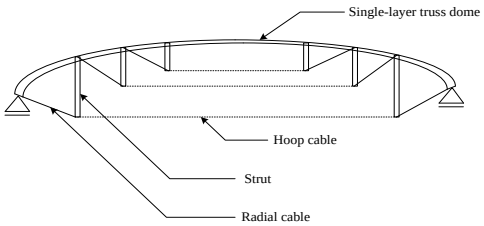

(a) Single reticulated shell and the cable-strut system [1]

Cable strut Radial cables Strut Hoop cables

(b) Details of a cable strut system [2]

Fig. 2- Suspen dome

It is known from literature that the cable-strut system of a suspen dome has only been constructed with steel cables [2]. Structural stability is a key problem in the design of steel structures. The high tensile strength of steel cables is an ideal structural element for long span structure but in situations where much longer distances are required one has to resort to applying a new material. For Civil engineering works composite materials are mostly used as replacement. A CFRP cable has properties of high strength, corrosion resistance, low maintenance requirement, light weight and low relaxation compared to steel cables. With the development and implementation of CFRP cables, researchers are becoming inclined in its use for bridge engineering [3].

This paper gives a general evaluation based on the findings on static behaviour of both steel and CFRP obtained from analysis of a successfully built prototype of a suspen dome with CFRP cables as the cable-strut system, despite its anchorage challenges, compared with analytical results of steel cables.

A REVIEW ON EXISTING ROOF STRUCTURES WITH CFRP CABLE

In today's world, new innovations are prominent for designing and constructing structures. As mentioned earlier, CFRP cables in real life architecture are mostly implemented in bridges [4-10]. Up till now, there are no existing cable structures other than bridges on large scale with CFRP cables. In reality, the studies of CFRP cables used in other cables structures are meagre. Hence, limited information can be gathered on such topic. However, Schlaich et al[11] researched on the utilization of CFRP tension members and their anchorage for a cable roof. Similarly, an orthogonally cable structure was constructed with CFRP cables by Brennd el al [12] and Yue et al.[13] though in a miniature scope to provide positive effect and elasticity of CFRP cables (Figure 3).

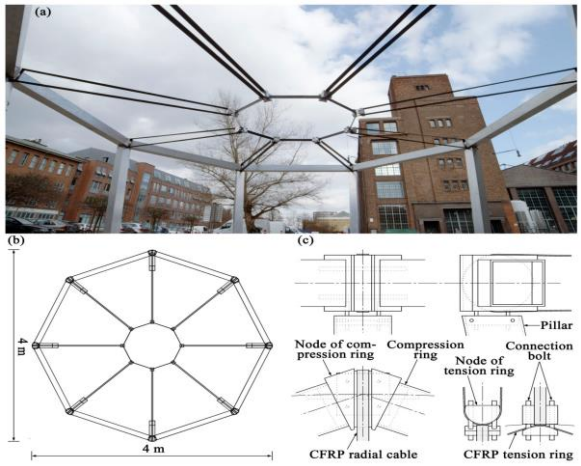

a) Plan view, compression and tension rings nodes of CFRP spoked wheel roof

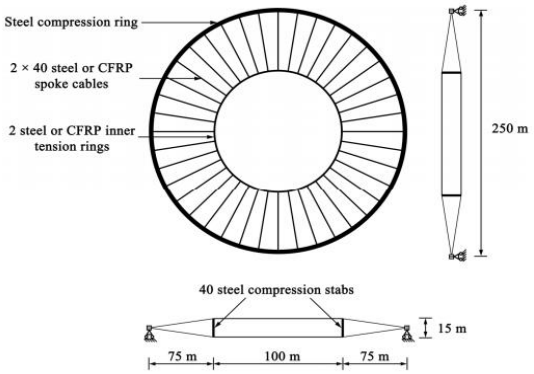

b) Design and restraint conditions for a spoked wheel cable roof

Fig 3. - Spoked wheel cable [13]

The researchers ascertained that CFRP cable can improve the economic efficiency of façade cable roof. In addition, increasing the structural stiffness can improve the stability of the spoked wheel cable roof. Analogously, Olofin and Liu. [14-16] verified the implementation of CFRP cables in lieu of steel in a suspen dome numerically to understand the behavioral pattern of the structure. In addition, a computational analysis on the peak bearing capacity of an existing suspen dome was analyzed to justify outcomes [17] (Figure 4).

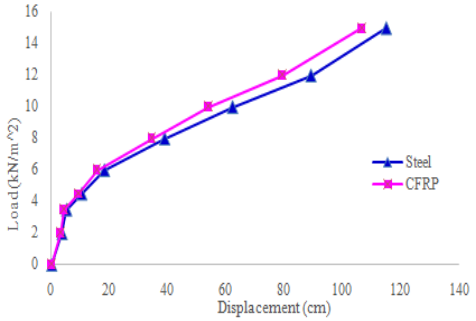

Fig 4. - Load-displacement comparison [17]

With the numerical results, experimentation on the static behavior of a prototype was investigated to verify the numerical findings [18]. The analyst concluded that CFRP gave outstanding performance which improved the structural efficiency of the cable-strut system as steel

cables. Hence using CFRP cables as a cable-strut system in a suspen dome is an important future development.

ANCHORAGE SYSTEM

Based on finite element analysis and bond theory, analysis and design of an anchor for CFRP was established. Due to the fact that anchoring of CFRP cable is one of the challenging factors for its utilization [19], the anchorage system was drafted to allow load transfer and minimal creep under a maximal cable prestressing strength.

LAYOUT OF THE ANCHORAGE

A conical hole of 24mm x16.5mm, a distance of 150mm made with Q235 steel was established for the outer sleeve cylinder steel. The interior surface of the hole was 8.1mm, in order to effect the motion due to friction between the exterior sleeve and interior wedge lubricant was added as exemplify in Figure 5.

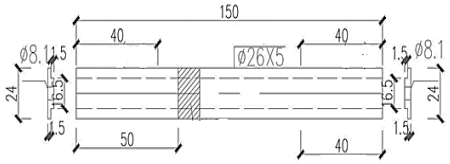

(a) Hoop cable anchorage

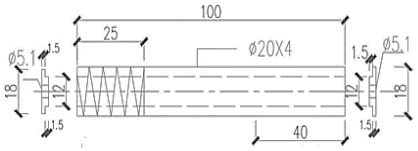

(b) Radial cable anchorage

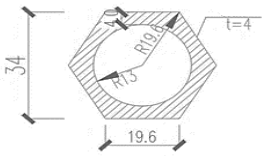

(c) Hexagonal nut

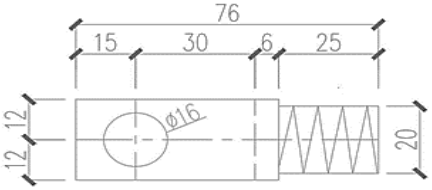

(d) Connector

Fig. 5 - Anchorage system

The CFRP anchor with connectors had a length of 151mm and width of 24mm. The connector length is 76mm and 24mm in width, spiralling though a hexagonal bolt of 25mm. The design criteria for the sleeve is 18mm x 12mm, with the interior thread as 18mm and exterior sleeve as25mm.

ANCHORAGE TEST

Using a tensile machine, a uni-axial tensile test was investigated on samples to determine the anchorage mechanism; results obtained was slip failure (Figure 6) and colloid interference.

Fig. 6 - Slip failure

Similarly, based on bond stress distribution, the mechanism of the loading process on the cable showed that the bending moment for CFRP was small when axial tensile force was measured which is acceptable for further investigation for the utilization of CFRP cables as tension members in tensegrity system for a suspen dome.

DESCRIPTION OF THE INVESTIGATED STRUCTURE

The design of the model was generally carried out in accordance with Chinese specification [20-21]. The model comprises of three interlacement, the beam, column and the single reticulated shell as illustrated in Figure 7(a) and detailed dimensions in Table 1.

Tab 1 - Model dimensions

Sections	Height (m)	Cross-sectional area(m)	Diameter(mm)
Reticulated system with steel bars	0.4	20 x 12	4
Columns	1.5	102 x 8	-
Circular beams	-	H200 x 200 x 8 x 12	4
Inner hoop	-	-	1.2
Outer hoop	-	-	2.6

The reliability, stiffness and strength of the joint was designed appropriately to avoid joint displacement due to brakeage not to affect the property mechanically. Figure 7(b). illustrates the joint connection for the proposed prototype.

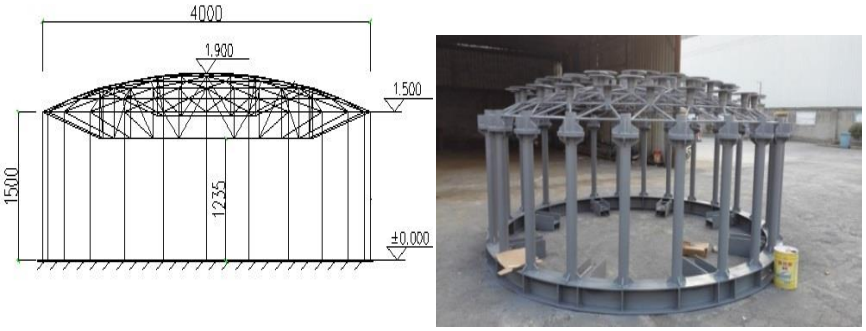

(a) Model

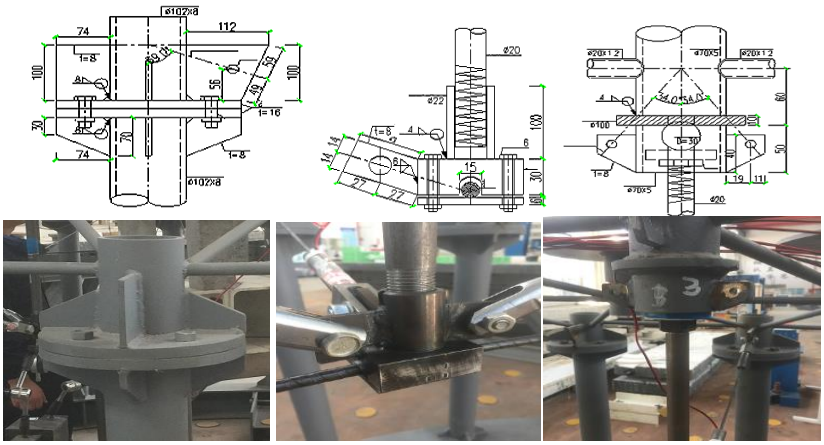

(b) Joint layout

Fig. 7 - Description of the prototype

An ideal elasto-plasticity Q235 steel was used for the reticulated single layer and column whereas the cables are elastic.

MATERIAL PARAMETER

Table 2 illustrates the material parameters used for the construction and simulation of the model.

Tab 2 - Material Parameters

Material	Density(kg/m^3)	Modulus of Elasticity(MPa)	Tensile tension(MPa)
Steel	7850	180	835
CFRP(Hoop cable)	1600	147	2550
CFRP(Radial cable)	1600	132	1528

INTERNAL FORCE MEASUREMENT IN CABLE MEMBERS

Tension sensor was used to measure the internal force produced in the hoop cable and strain gauge for the radial cable. The arrangement of the tension sensor on the hoop cable is illustrated in Figure 8(a) and the strain gauges were arranged as illustrated in Figure 8(b). The combination of tension sensor and strain gauge was used to measure tension in the cable. For the prestressed cables, thread sleeve method was employed with the scene layout illustrated in Figure 8(c) showing radial cable and hoop cable which was tensioned at 3kN.

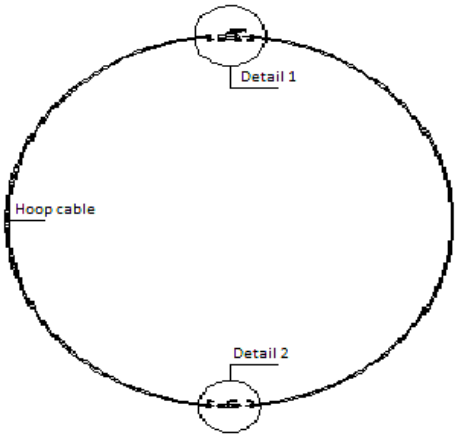

(a) Hoop cable overview

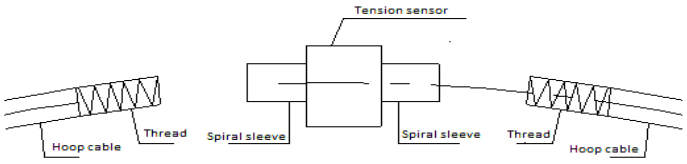

i) Detail 1

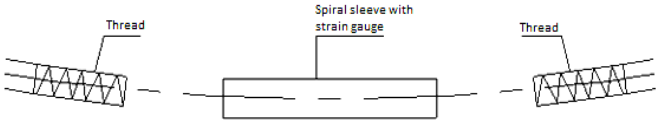

ii) Detail 2

(b) Detail layout

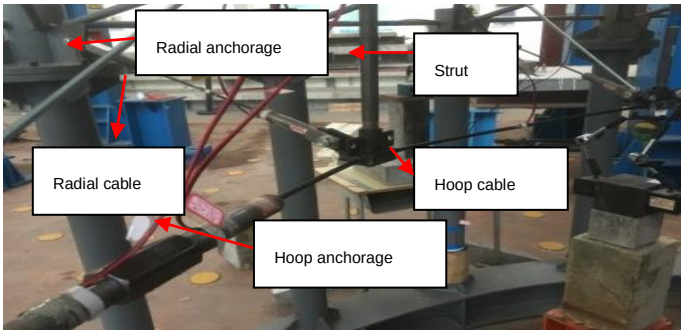

(c) Implementation of CFRP cables in the outer hoop and radial member

Fig. 8 - Outline of the cable members

Based on the findings of Kang et al. [22] which states that the maximum tension on the reticulated single layer are produced and intensive near the support of the hoop and radial cable, the experimentation CFRP cables were only applied for tension members which are the radial and hoop cable as illustrated in Figure 8. The hoop cables are 8mm in diameter and radial 5mm in diameter for CFRP.

LOADING AND BOUNDARY CONDITIONS

The dead, live, seismic and temperature are considered alongside with all pertinent load combinations as specified in Chinese standard codes for structures [20-21]. The single reticulated

shells are under uniform loads and joints are rigid. The degrees of freedom for the supporting joints are restricted and assumed as pin jointed.

NUMERICAL TECHNIQUE FOR THE MODEL

In this study, an FEM software namely ANSYS was used to investigate the model to gather numerical data in comparison to the experimental data for validation of the test model. Trusses and beams are the fundamental composite of a suspen dome; BEAM188 was implemented for the single reticulated shell while LINK 10 was for the cable members [23]. A mesh size of 1mm was adopted. Uniformly distributed load is equivalent to a vertical concentrated load based on the equivalent principle of static. (Figure 9).

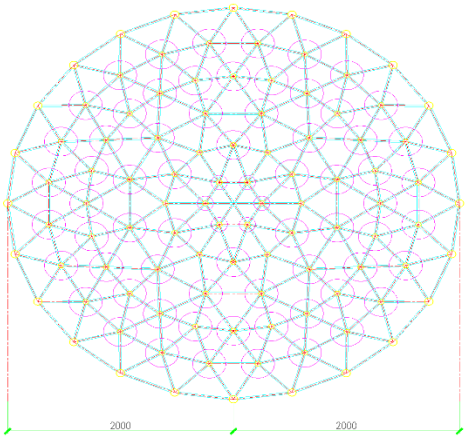

Fig. 9 - Numerical load setup for the single reticulated shell

Numerical simulation was investigated on CFRP and steel cables to make juxtaposition with the experimental data collected for CFRP cable. Full span loading was considered based on literature by Guo et al [24] to better understand the static behavior of the system**.**

EXPERIMENTAL PROCEDURE FOR THE MODEL

Three stages were involved for the test model setup which are i) installation i.e levelling, ii) geometric parameter measurement which entails measuring span, height, diameter to determine preliminary geometric imperfection of the prototype and iii) material limit dimension which entails test been carried out to determine tensile strength of the cables. The tests are specified into three categorizes i) deflection test, ii) strain test and (iii) the test of internal force produced in the cables. The measuring devices are i) displacement laser tracker and ii) TS3862 static resistance strain measurer (Figure 10 illustrates measuring points).

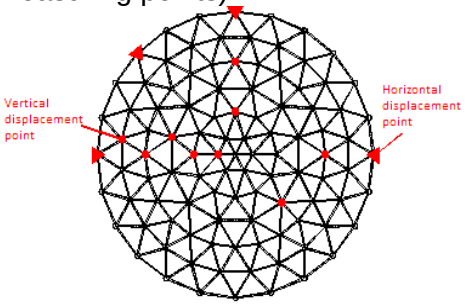

(a) Displacement measuring point

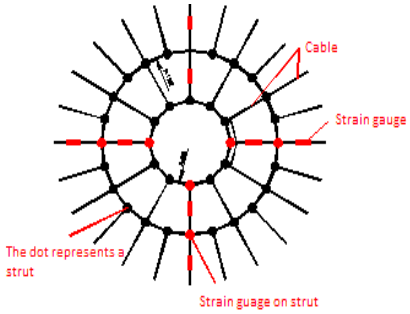

(b) Cable-strut system strain gauge layout

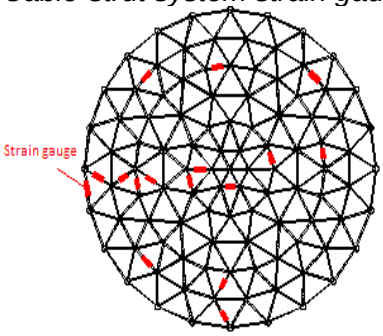

(c) Single reticulated shell strain gauge layout

Fig. 10 - Measuring points

SUSPEN-DOME WITH CFRP CABLES PROTOTYPE

Figure 11 illustrates the state of the art model with CFRP as the tensegrity system under full span loading. Based on Chinese specification, the test model was loaded symmetrically and unsymmetrically. Several loading processes were considered during the experimental measurement. The design requirements are specified in terms of the maximum load the structure must withstand.

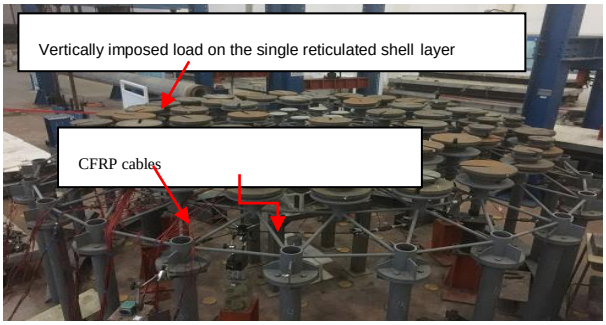

Fig. 11- Full span loading

Pretensioning of the cables were carried out by tightening the bolt at 180^{o} conservatively at intervals. Full span loading of10kg was considered in this study to justify that concentrated loads on CFRP cables has similar attributes as the traditional steel which can optimize the cable-strut system of a suspen dome.

RESULTS AND DISCUSSION

COMPARATIVE ANALYSIS OF MAXIMUM VERTICAL DISPLACEMENT

From Figure 12, it can be observed that the maximum displacement obtained for CFRP experimentally conforms to that of the numerical result of steel and CFRP. The little disparity, which is negligible, is believed to be the influence of the experiment surrounding.

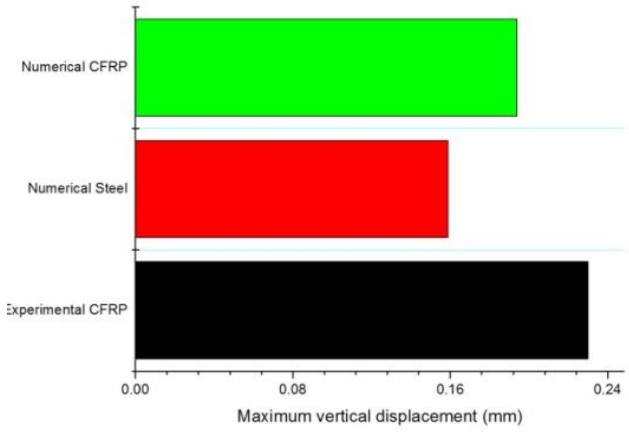

Fig. 12 - Maximum vertical displacement

Hence, it can be deduce that the measured displacement value of CFRP cable conforms to the allowable displacement specification for a tensegrity which should be l/400 (l is the span of the dome) [20].

COMPARATIVE ANALYSIS OF MAXIMUM STRESS GENERATED IN THE SINGLE RETICULATED SHELL

Under full span loading, the single reticulated shell bars were exposed to compressive stresses**.**

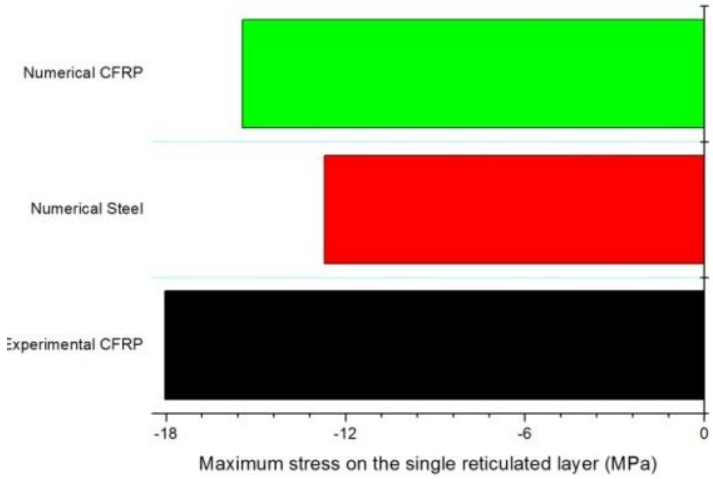

Fig. 13 - Maximum stress of the single reticulated shell

The trend of the stresses obtained from the experimentation with CFRP was similar to that of the FEM analysis as illustrated in Figure 13.

COMPARATIVE ANALYSIS OF INTERNAL FORCES GENERATED IN THE OUTER HOOP CABLE

The internal force generated for CFRP for the experimentation has about 50% percentage difference from the numerical results of steel and CFRP as illustrated in Figure 14.

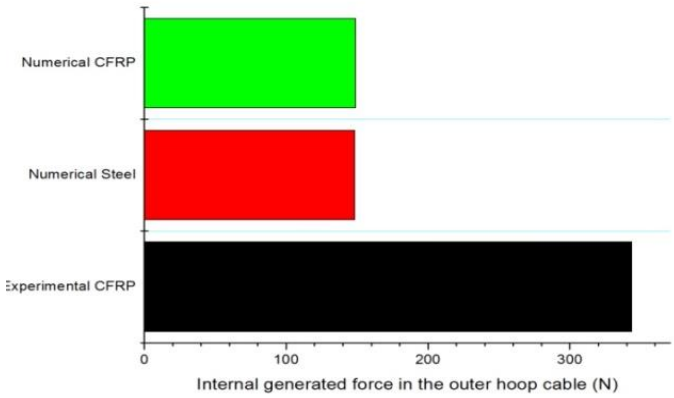

Fig. 14 - Comparison of internal generated force in the hoop cable

The possibility will be to adjust the pretension of the cables to lower the internal forces in the hoop cable or it could be as a result of the influence due to gauge position, shape of members and installing errors. Sometimes such errors may be compensated to produce accurate results.

COMPARATIVE ANALYSIS OF RADIAL CABLES NEAR THE OUTER HOOP

The pretensioning of the hoop cables directly produced the internal forces in the radial cables. Changes in the radial cable generated force is basically indistinguishable to that of the hoop cable.

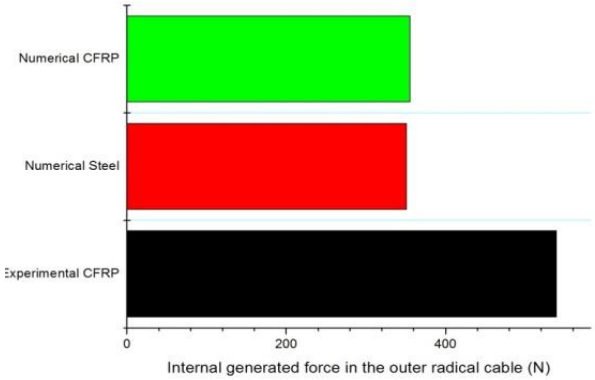

Fig. 15 - Internal generated force in the radial cables

Figure 15 illustrates the internal produced force in the radial cables. Due to the high internal force in the hoop cables, the radial cables have similar percentage difference. The difference in the measured and calculated forces could be also caused by little movement in the nodes of the actual structure.

ANALYSIS OF ANCHORAGE SYSTEM

The strain changes increase with rise in load. For the radial cable at initial loading the strain was 75*με* and increased to 630*με*. Similarly, the hoop cable had a value of -50*με* initially and increased to 37*με*.

HOOP AND RADIAL CABLE ANCHOR

Based on the ascribed loads, the strain changes in the anchor system for the radial and hoop cable conform to bond theory. The positioning of the strain gauge in the hoop cable for the anchor is exemplified in Figure 16, the strain gauge model is BX120-2AA.

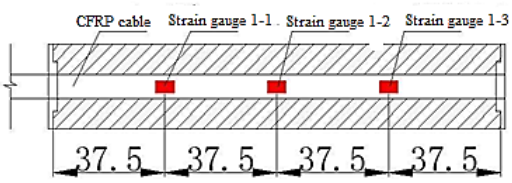

Fig. 16 - The hoop cable anchor with strain gauge (dimensions: mm)

The anchor consists of a three-piece strain gauge placed with adhesive and wired up to facilitate data collection. The radial cable is thinner since its diameter is 5mm, a smaller version of the strain gauge was used namely BX120-1AA. The three-piece strain gauge is enclosed firmly in the anchorage system as illustrated in Figure 17.

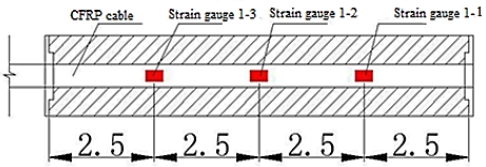

Fig. 17 - The radial cable anchor with strain gauge (dimensions: mm)

Table 3 illustrates the stresses generated in the anchorage system. Theoretically, the higher the prestressing force, the stress compression in the hoop cable approaches the anchoring node.

Tab 3 - Average stress generated in the anchorage system

Strain gauge position	Stress generated in hoop anchor(MPa)	Stress generated in radial anchor(MPa)
1-1,1-2,1-3	118.20	52.80

Based on bond stress distribution, the result in Table 3 shows that the performance of the cable is indistinguishable to the axial pull reflecting the impact on the hoop cable is minimal and does not influence the anchorage. Similarly, the stress distribution of the radial cable is analogous to the stress distribution due to axial tension. The anchoring for the radial cable has exceptional stress resisting capability under loading conditions.

CONCLUSION

First of all, CFRP cables as the tensegrity system for a suspen dome has been constructed though on a small scale despite the challenges of anchorage. The findings obtained gave some ideas about the structural static stability of CFRP cables as a cable-strut system in a suspen dome.

Secondly, the obtained simulated results validate the test model which gives a practical design for the suspen dome with CFRP cables. The stresses on the single reticulated shell layer, the internal forces of the hoop and radial cables and the overall displacements fall within the range of the defined code which entails that the bending moment is minute when carbon fibre reinforced polymer cable is subjected to axial tensile force. Based on the setup procedure and the results

gathered from the assembled prototype design, a real life large span suspen dome with CFRP cables as the cable-strut system can be erected in the future.

Finally, the information generated by the study could be used by researchers and engineers to upgrade and improve the design process of CFRP in cable structures for structural engineering works.

ACKNOWLEDGEMENT

The support of the National Science Foundation of China (Grant no: 51608234; 51478209) and Province Science of Jiangsu BK20160534 are acknowledged by the authors

REFERENCES

[1] Subramanian, N. 2006 “Space Structures: Principles and Practice”, Multi-Science Publishing Co Ltd, Brentwood, Essex, UK.
[2] Olofin, I. & Liu, R. 2012. “Suspen-dome System: A Fascinating space Structure”. The Open Journal of Civil Engineering. 11: 131-142
[3] Olofin, I. & Liu, R. 2015“The Application of CFRP (CFRP) Cables in Civil Engineering Structures”. SSRG International Journal of Civil Engineering 2: 1-5.
[4] Meier, U.2000 “Composite materials in bridge repair” . Applied Composite Material. 7: 75-94.
[5] Meier, U.1995 “Extending the life of cables by the use of carbon fibres” . International Association for Bridge and Structural Engineering.
[6] Wen, X., Cai, C. S., Yin, Z., Rucheng, X.2011 “Study of Super long Span cable stayed Bridges with CFRP components”. Engineering Structure. 33,330-343.
[7] Adanur, S., Gunaydin, M., Altunisik, A.C., Seuim, B. 2012“Dynamic behavior of a cable stayed bridge using CFRP cables” .Vienna Congress on Recent Advances in Earthquake Engineering and Structural Dynamics.
[8] Filiphbanck, O.R.A..2014 “Application of CFRP cables in super long span cable supported bridge: A feasibility study” . Chalmers University of Technology.
[9] Guoying, F., Ronggui ,L., Bei, C.” 2013Static Characteristics Analysis of cable-stayed bridges using CFRP cable”. IJCTT. 4: 861-866.
[10] Meier, U. 1992“Carbon Fibre-Reinforced Polymers: modern materials in bridge engineering”. Struct. Eng.Int .DOI :101686692780617020.
[11] Schlaich, M., Bernd, Z., Yue L., & Goller, R.2012“CFRP tension elements and their anchorages”. Bautechnik. 89. 841-849.
[12] Bernd, Z., Yue L., & Schlaich, M. 2014“Research on using CFRP Tension members in plane cables structures”. The 7th International Conference on FRP Composites in Civil Engineering, Vancouver, Canada.
[13] Yue, L., Bernd, Z., & Schlaich ,M. 2016 “Advantages of using CFRP cables in orthogonally loaded cable structures”. AIMS Material Science. 3. 862-880.
[14] Olofin, I., & Liu, R. 2016 “Numerical modal analysis of a suspen-dome with CFRP cable-strut system”. ASME Journals: Series Modelling A. 8. 13-24.
[15] Olofin, I., & Liu, R.2017 “Structural Optimization of Beijing Gymnasium Suspen-dome with CFRP (CFRP) cable”. Scientific Herald of the Voronezh State University of Architecture and Civil Engineering. 36.106-115.
[16] Olofin, I., & Liu, R. 2017 “Transient behavior of CFRP cable-strut system in a Suspen- dome”. Civil Engineering Journal. 8. 547-555.
[17] Olofin I, and Liu,R. 2019 A study on the ultimate bearing capacity of CFRP cable-strut system in a suspen dome ,The Civil Engineering Journal. 46. 555-565. DOI 10.14311/CEJ.2019.04.0046
[18] Olofin, I., & Liu, R.2020 “Research on the Static Behaviour of a Suspen Dome with CFRP (CFRP) Cable-strut System”. Iranian Journal of Science and Technology, Transactions of Civil Engineering. DOI 10.1007/s40996-020-00488-5(In press).
[19] Meier ,U.2012 “CFRP cables: Why? Why not? What if?” Arabian J.SCi.Eng. 37.399-411.
[20] GBJGJ7-2012. “Technical specification for space frame structure”. Chinese planning press, Beijing (In Chinese).
[21] GBJGJ257-2012. “Technical specification of cables structures”. Chinese planning press, Beijing (In Chinese).

[22] Kang, W., Chen, Z., Lam, H., & Zuo, C. 2003“Analysis and design of the general and outmost ring stiffened suspen-dome structure”. Engineering structures. 25. 1685-1695.
[23] ANSYS.2008 “Release 10.0 Documentation for Ansys”, USA.
[24] Guo, J. M., Dong, S. L., & Yuan, X. F. 2012“Research on static property of suspen-dome structure under heap load”. Advanced Steel Construction. 8.137-152.

CIVIL ENGINEERING JOURNAL

Article no. 35

THE CIVIL ENGINEERING JOURNAL 2-2021

MECHANICAL BEHAVIOR OF HORIZONTAL SWIVEL SYSTEM WITH UHPC SPHERICAL HINGE UNDER SEISMIC ACTION

Jiawei Wang, Bing Cao, Bo Huang and Yihan Du

Anhui Polytechnic University, School of Architecture and Civil Engineering, Department of Civil Engineering, Wuhu City, Beijing Middle Road, China; wjw526@126.com; caobing.0427@163.com; huangbo@ahpu.edu.cn; duyihan00@163.com

ABSTRACT

In the process of rotation, the total weight of the bridge structure is jointly supported by the spherical hinge and the supporting structure, and its lateral stability is poor. It is easy to lose stability under the action of dynamic loads such as seismic action effect. The present paper takes a 10,000-ton continuous rigid frame swivel bridge as the re-search object, analyzes the dynamic response of the seismic action to the horizontal swivel system and establishes several structure simulation models. Eighteen seismic waves in three directions that meet the calculation requirements are screened for time history analysis and compared with the response spectrum method. Finally, an optimization algorithm for the seismic response of the bridge under horizontal swivel system is proposed based on the mode superposition method. The UHPC spherical hinge bears all the vertical forces and 20% of the bending moment caused by the seismic action, the support structure bearing the remaining 80% of the bending moment. The optimization algorithm proposed in this paper features high accuracy.

KEYWORDS

Horizontal rotation, UHPC spherical hinge, Rotating process simulation, Seismic time history analysis, Optimization algorithm

INTRODUCTION

It is known that applying conventional construction methods for continuous rigid frame bridges is not advisable when crossing railways. The full framing method requires a railway protection shed; thus, it will affect the normal operation of the railway. While the cantilever pouring method requires symmetrical construction in sections, and it features a long construction period. Besides, the application of large cantilever poses safety hazard to the operation of the train. Under these circumstances, the rotating construction method becomes the most advantageous method, which could reduce the impact of bridge construction on railway operations. First, complete the construction of the bridge superstructure and rotating piers on both sides of the railway. Then, the horizontal traction equipment on the cap is used to rotate the bridge swivel system composed of the superstructure, the swivel pier and the spherical hinge to a certain angle (usually 90°) along the central axis. When the superstructure of bridge crosses the railway line, it is connected with the side pier, finally completing the structural system conversion [1-4].

In the process of bridge rotation, the spherical hinge structure is the most important part of the bridge rotation process. The swivel bridge constructed during 1980-1990 mainly used concrete spherical hinges [5-8], as shown in Figure 1-1a. Concrete spherical hinge features low cost but also poor bearing capacity, and is therefore mainly used in small tonnage bridges. With the continuous increase in tonnage of the swivel bridge and the rapid development of the manufacturing industry, the prefabricated steel structure spherical hinge in the factory has gradually become the first choice for the spherical hinge, which has the advantages of high bearing capacity and good contact surface

flatness, as shown in Figure 1-1b. However, the cost of steel spherical hinges is relatively high. A 20,000-ton spherical hinge can even cost several thousand dollars. In order to solve the shortcomings of the traditional spherical hinge structure, this paper applies Ultra-High Performance Concrete (UHPC) material to the spherical hinge structure [9-12]. The size of the UHPC spherical hinge greatly reduces the radius of the concrete spherical hinge, and at the same time reduces the manufacturing cost of the UHPC spherical hinge, all bringing high economic benefits.

During the rotation process of the horizontal swivel system, the spherical hinge and the supporting structure jointly establish the support system. When subjected to dynamic loads such as earthquakes effects, the bridge is prone to instability during the vibration process. Changjie Wang and Wei Hei analyzed the seismic response of a T-shaped rigid-frame rotating bridge in the completed state, and calculated the bending moment envelope diagram of the main girder and piers of the superstructure under seismic action by the response spectrum method. It is found that the structure is always in an elastic state, and the load-bearing capacity of the structure meets the design requirements [13]. However, the research is limited to the analysis of the completed bridge state, i.e., the two ends of the main beam are simply supported, and the pier positions are consolidated. The seismic response analysis of the maximum cantilever state during the rotation process is not performed. The constraint in the maximum cantilever state is poor, the frequency of the first three modes is small, and the swivel system is more prone to instability under dynamic loads. Although seismic action is a combination of accidental effects, it is necessary to carry out seismic calculation and isolation design for important bridges in earthquake-prone areas or bridges with poor stiffness. So, the rotating bridge therefore must be subjected to seismic calculations in the maximum cantilever state (in the process of rotation) and the completed bridge state (rotation completed).

Based on a 10,000-tonnage continuous rigid frame UHPC spherical hinged translation system bridge, this paper introduces the calculation method of seismic time history analysis of the system in the maximum cantilever state (in the process of rotation) and the bridge state (in the process of rotation completed) and mainly analyzes the influence of UHPC spherical hinge and the footing structure on structural stability under seismic action, proposing an optimization algorithm for the seismic response of the translation system and several structural measures to improve the seismic performance of bridges.

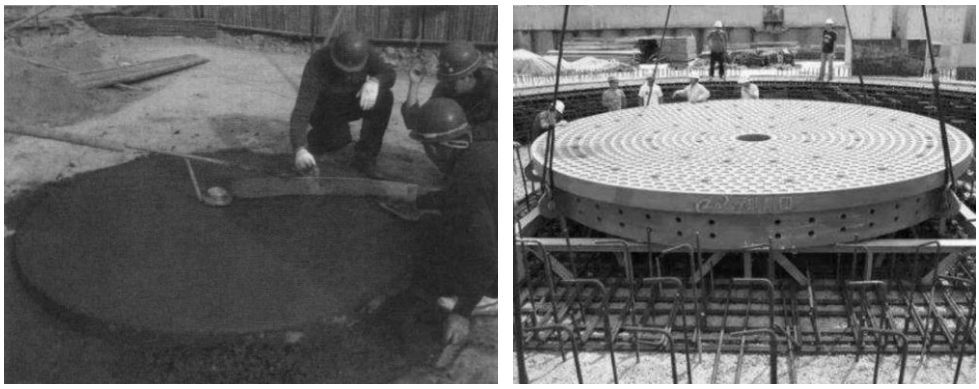

(a) Concrete spherical hinge *(b) Steel structure spherical hinge*

Fig.1 - Traditional spherical hinges

RESEARCH METHOD

Project overview

This paper takes a continuous rigid frame bridge with variable beam height as the research object, with a span of 2x62 m and a maximum cantilever length of 62m on one side. The main beam adopts C50 concrete single box three-chamber inclined web box section. The top plate of the box girder is 21.3 m wide, and the cantilever length of the flange plates on both sides is 3 m. The end thickness of the cantilever plate is 20 cm, the root thickness is 50 cm, the top plate thickness of the

middle fulcrum box beam is 70 cm, and the bottom plate thickness is 190 cm. The beam height of the fulcrum is 6m, the beam height of the side span straight section 2m, and the rotating weight is about 10,000t. The spherical hinge structure adopts UHPC spherical hinge. The dimensions of each part of the swivel system are shown in Figure 2.

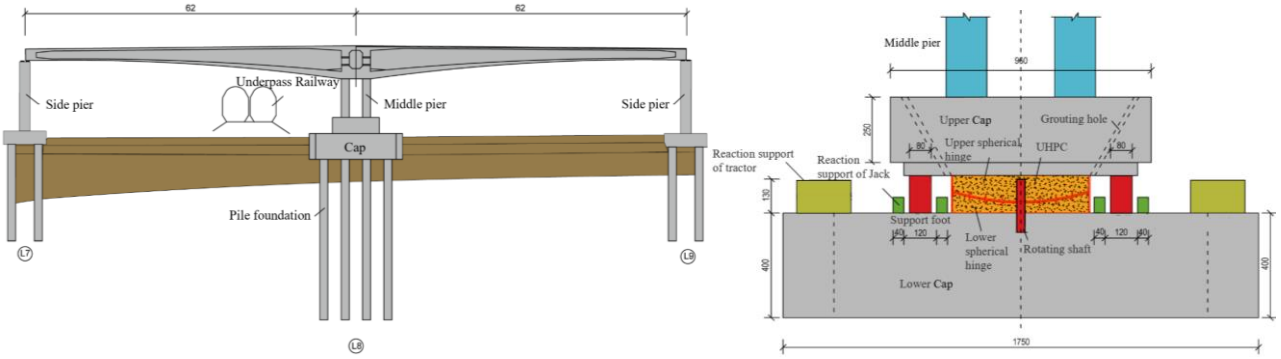

(a) Bridge elevation (unit: m) *(b) Structural of spherical hinge (unit: cm)*

Fig.2 - Dimensions of each part of the swivel system

Establishment of structural simulation model

This paper uses the application ANSYS for simulation analysis: in the swivel model, the pier and the main beam are consolidated together to form the maximum cantilever state; the two ends of the bridge are in an unconstrained state, the spherical hinges and the footing structure support the entire rotating structure. The model in the maximum cantilever state of the structure is Model 1, as shown in Figure 3-a. After rotating into a certain point, the cantilever ends are connected with the supports on the piers on both sides, the outer concrete of the spherical hinge is closed, and the joint transforms into a consolidated state. The structure of the bridge state model is Model 2, as shown in Figure 3-b. When the time history analysis method is used to calculate the response of the structure to the seismic action, the load step of a single seismic wave exceeds 10,000 steps. At the same time, geometric nonlinearity and material nonlinearity should be taken into consideration when analyzing the finite element simulation analysis. In order to simplify the calculation and improve the efficiency of analysis, this study adopts the overall model when calculating the internal force response of the structure, as shown in Figure 4-a. The local model analysis is used to calculate the influence of the spherical hinge and the footing structure on the stability of the system, as shown in Figure 4-b.

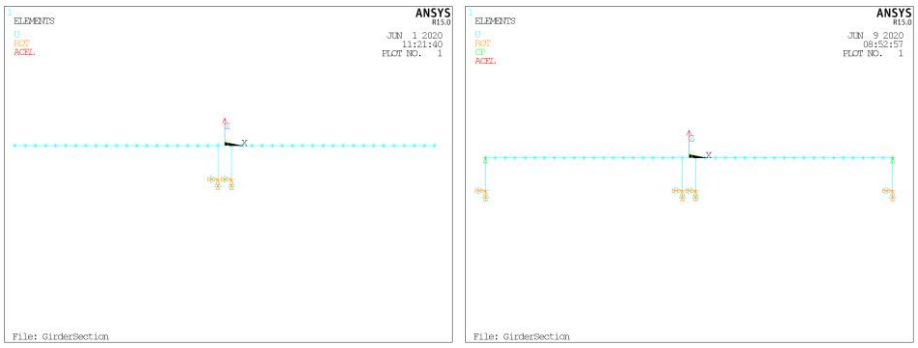

(a) Model 1 *(b) Model 2*

Fig.3 - Two analysis models

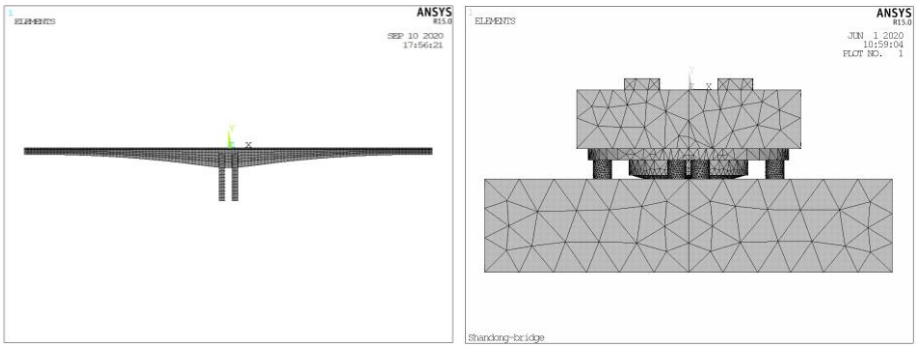

(a) Discrete graph of overall model (b) Discrete graph of local model

Fig.4 - Overall model and local model

The Beam 188 element is used for the main beam and bridge pier, and the element has a three-dimensional finite strain structure with two nodes. Each node has 6 degrees of freedom (3 translational degrees of freedom and 3 rotational degrees of freedom). In order to simulate the connection form between the bridge pier and the main girder, MPC184 unit was used for simulation. In the maximum cantilever state, the structure of the system is only restricted by the spherical hinge structure: the spherical hinge provides vertical force support, and the other footing structures provide lateral and longitudinal bending moment support, the overall structure in a balanced state. Finally, the Model 1 adopts a consolidation treatment at the bottom of the pier. In Model 2, the influence of side pier constraints on the structure is taken into consideration. Hence, we set vertical and horizontal general supports on the top of the pier and adopt Solid65 unit in the structure of the upper and lower spherical hinges and footing structures.

In structural dynamic time history analysis, how structural damping is defined is very important. structural damping is proportional to the speed of the structure. When the transient analysis is used in the ANSYS solver, the structural damping is Rayleigh damping [14], and its expression is shown in equation (1).

$$[C] = \alpha[M] + \beta[K] \quad (1)$$

In the above equation, [*C*] is the damping matrix, $[M]$ is the mass matrix, while $[K]$ is the stiffness matrix, α the mass damping coefficient, and β the stiffness matrix coefficient. The relationship between the coefficient α, β and the viscosity proportional coefficient ξ is shown below:

$$\alpha/(2 \times \omega) + \beta \times \omega/2 = \xi \quad (2)$$

In the formula: ω is the circular frequency, and f is the structure frequency, and $\omega=2\pi f$. Two equations are obtained through structural modal calculation:

$$\alpha/(2 \times \omega 1) + \beta \times \omega 1/2 = \xi$$
$$\alpha/(2 \times \omega 2) + \beta \times \omega 2/2 = \xi$$

Combine the above formulas, the following equation is obtained.

$$\alpha = 4 \times \pi \times f_1 \times f_2 \times \xi/(f_1 + f_2)$$
$$\beta = 2 \times \xi/(\omega_1 + \omega_2) = \xi/\pi/(f_1 + f_2) \quad (3)$$

Structural mode shape calculation

It is known that the dynamic characteristics of the structure are affected by the mass distribution and the boundary conditions of the structure. For the same order, Model 1 and Model 2 have different modal frequencies. The Lanczos method is used to calculate the first 10 modes of the structure, and the structure quality participation coefficient is over 95%. Vibration frequency and vibration form are shown in Table 1.

Tab.1 - Frequencies and modes of the first ten modes of the structure

Mode number	Frequency/Hz		Vibration form	
	Model 1	Model 2	Model 1	Model 2
1	0.390	1.826	the beam bent transversely, the 1st mode; the middle pier bent transversely, the 1st mode	middle pier bent longitudinally, the 1st mode
2	0.491	2.358	the beam bent longitudinally, the 1st mode	side piers bent transversely, the 1st mode
3	0.810	2.713	the beam bent longitudinally, the 2nd mode	the main beam bent longitudinally, the 1st mode
4	1.870	3.240	middle pier bent longitudinally, the 1st mode	side piers bent transversely, the 2nd mode
5	2.107	3.322	The beam bent transversely, the 2nd mode	beam bent longitudinally, the 2nd mode
6	3.905	6.340	the beam bent longitudinal, the 3rd mode	middle pier bent transversely, 1st mode; side pier bent horizontally, the 3rd mode
7	4.060	7.912	the beam twisted, the 1st mode; the middle pier bent transversely, the 2nd mode	the main beam twisted, the 1st mode
8	4.605	8.603	the main beam twisted, the 2nd mode	the main beam bent longitudinally, the 3rd mode
9	4.637	8.721	the main beam bent longitudinally, the 4th mode	the main beam bent longitudinally, the 2nd mode
10	7.340	9.340	the main beam twisted, the 3rd mode	side piers bent transversely, the 3rd mode

Earthquake input

The input process of earthquake is the main influencing factor of seismic response analysis. Time history analysis selects actual strong earthquake records or artificially simulated acceleration time history according to the type of site. At the same time, it is required that the actual seismic records should not be less than 2/3 of the total. The average value of the shear force at the bottom of the pier calculated by multiple seismic waves should not be less than 80% of the calculation result of response spectrum method [15-16]. In order to obtain the true response of the continuous rigid frame bridge under the maximum cantilever state, all seismic waves recorded by actual strong earthquakes are used in the study, and the maximum value is used as the calculation basis. The actual strong earthquake record is based on the seismic database of the Pacific Earthquake Engineering Research Center(PEER). By inputting the design response spectrum and the first three-order natural vibration period of the structure, multiple sets of suitable seismic waves are screened out. The actual response spectrum is obtained by Fourier transform, and the acceleration value under the first-order natural vibration period is compared with the designed response spectrum. The difference between the two should not be greater than 35%. Seismic waves are screened based on this principle. According to the screening results, it is found that the seismic records in three directions under the same set of ground motions: HMC180, HMC270, HMCDWN, are difficult to meet the requirement of less than 35% error at the same time under the first-order natural vibration period. Therefore, the seismic waves of Model 1 and 2 in the three directions are respectively different seismic data, and finally 18 seismic waves that meet the requirements are screened out of 50 strong earthquake records. This paper uses the acceleration response spectrum in the "Detailed Rules for Seismic Resistance of Highway Bridges" [16] as the comparative data for time history analysis, and the response spectrum is shown in equation (4).

$$s=\begin{cases} S_{A\max}\times(5.5T+0.45) & T<0.1s \\ S_{A\max} & 0.1s\le T\le T_g \\ S_{A\max}\times(T_g/T) & T>T_g \end{cases} \quad (4)$$

$S_{A\max}$ is the maximum seismic acceleration, while T_g is the characteristic period, T is the natural vibration period.

The actual seismic waves are screened through the characteristic period and the first three-order natural frequencies of the structure. All in all, there are two directions in the two models and a

total of 18 real seismic waves are screened. The acceleration time history curves of Model 1 and the seismic wave response spectrum after Fourier transformation are shown in Figure 5 and Figure 6.

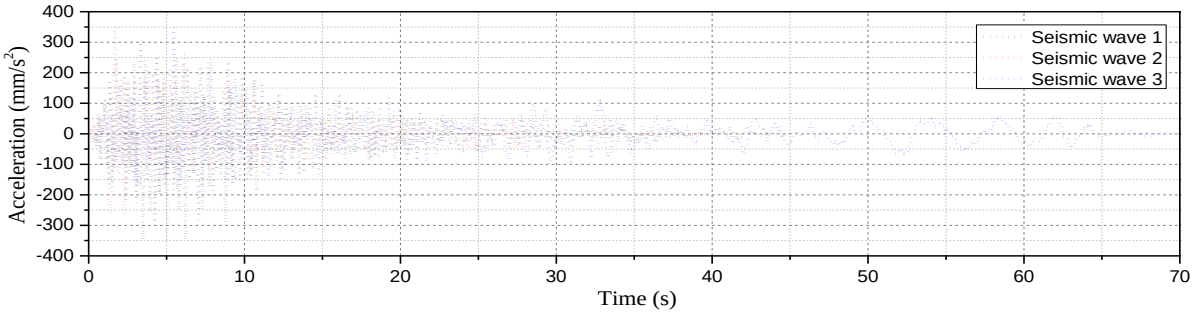

Fig.5 - Transerse seismic wave acceleration time history curve of Model 1

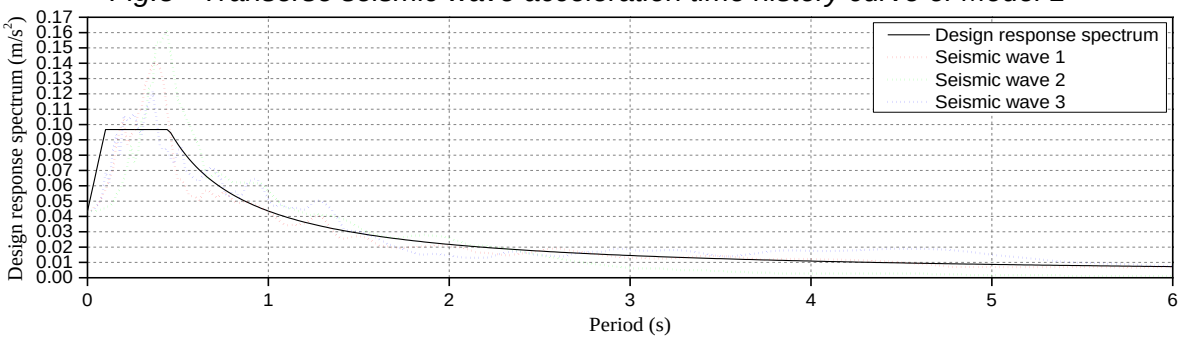

Fig.6 - Transverse seismic wave response spectrum of Model 1

It can be seen from the above figures (Figure 5 to Figure 6) that the seismic wave time history curve is relatively random, and the earthquake duration is different, ranging from 30s to 70s. What is for sure is that the duration of the earthquake is more than 5 times the basic period of the structure. The first-order natural vibration period of Model 1 is 2.56s; the corresponding design response spectrum acceleration is 0.017g, and the absolute value of the seismic wave error in the three directions is 11.8%-23.5%. The first-order natural vibration period of Model 2 is 0.55s; the corresponding design response spectrum acceleration value is 0.1 g, and the absolute value of the error in the three directions is 1.0%-23.7%; all meet the screening requirements.

RESULTS AND DISCUSSION

Simulation results

Seismic response analysis of Model 1

We performed nonlinear dynamic time history analysis on the two models, and compared the time history analysis results with the calculation results of the response spectrum method. It is necessary to consider the time integration function in ANSYS when calculating, otherwise the cumulative effect of seismic action cannot be considered. The time step of the seismic wave is 0.005s, and the calculation step should be consistent with the seismic wave record. The internal force response of Model 1 is shown in the following tables (Table 2 to Table 4).

Tab. 2 - Transverse seismic response of the bridge（force unit：kN，moment unit：kN·m）

Location	Internal force	Seismic wave 1	Seismic wave 2	Seismic wave 3	Max	Average	Response spectrum results
Pier top	shear force *Fy*	1820	3104	1747	3104	2224	3080
	bending moment *Mx*	15500	25540	15970	25540	19003	16269
Pier bottom	shear force *Fy*	1900	3204	1785	3204	2296	3065
	bending moment *Mx*	19000	33025	18736	33025	23587	19913
Cantilever root	shear force *Fy*	1712	2970	1536	2970	2073	2300
	bending moment *Mz*	68460	101477	62485	101477	77474	60736

Tab. 3 - Longitudinal bridge seismic response （force unit：kN，moment unit：kN·m）

Location	Internal force	Seismic wave 1	Seismic wave 2	Seismic wave 3	Max	Average	Response spectrum results
Pier top	axial force *Fz*	2432	1416	1383	2432	1744	1789
	shear force *Fx*	2700	1028	1413	2700	1714	1350
	bending moment *My*	13317	5045	7019	13317	8460	7930
Pier bottom	axial force *Fz*	2433	1417	1383	2433	1744	1800
	shear force *Fx*	2797	921	1400	2797	1706	2300
	bending moment *My*	14303	5425	7362	14303	9030	11760
Cantilever root	bending moment *My*	10641	4790	5210	10641	6880	6240

Tab. 4 - Vertical seismic response （force unit：kN，moment unit：kN·m）

Location	Internal force	Seismic wave 1	Seismic wave 2	Seismic wave 3	Max	Average	response spectrum results
pier top	axial force*Fz*	7610	9300	7610	9300	8173	6080
	shear force *Fx*	58	100	87	100	82	26
	bending moment *My*	419	673	587	673	560	215
pier bottom	axial force *Fz*	8370	9700	7710	9700	8593	7438
	shear force *Fx*	62	100	88	100	83	39
	bending moment *My*	200	321	280	321	267	147
cantilever root	shear force *Fz*	7190	9100	7550	9100	7947	6695
	bending moment*My*	21451	34483	30085	34483	28673	21744

From the above tables, we can see:

(1) Under lateral seismic input, the main response of the earthquake is the lateral bending moment from the pier bottom, the lateral shear force and the lateral bending moment of the main beam. The internal force at the top of the pier is less than that at the bottom of the pier, the axial force at the pier and the main girder are very small, and the transverse bending moment at the bottom of the pier is the controlling parameter. The calculation results of the three seismic waves are highly discrete, and their average results are close to the calculation results of the response spectrum.

(2) Under longitudinal seismic input, the main seismic response is the longitudinal bending moment at the bottom and top of the pier. Under this working condition, the longitudinal bending

moment of the bridge pier and the longitudinal bending moment of the cantilever root of the main beam are the control parameters. The calculation results of the three seismic waves are highly discrete. Among them, the calculation result of the first wave is about twice that of the other two waves, and the average result is close to the calculation result of the response spectrum.

(3) Under the vertical seismic input, the main seismic response is the axial force of the bridge pier and the longitudinal bending moment at the root of the main girder cantilever. The longitudinal bending moment has exceeded the seismic response in the longitudinal direction. The vertical axial force of the bridge pier and the longitudinal bending moment at the root of the main beam cantilever are the control parameters. The calculation results of the three seismic waves are relatively close, exceeding the calculation results of the response spectrum in the axial force response and the bending moment response.

In order to obtain the most unfavourable result of seismic action, this study selects the maximum value in the time history analysis as the calculation basis. According to the results, the internal force time history curve of each control section is shown in Figure 7 and 8.

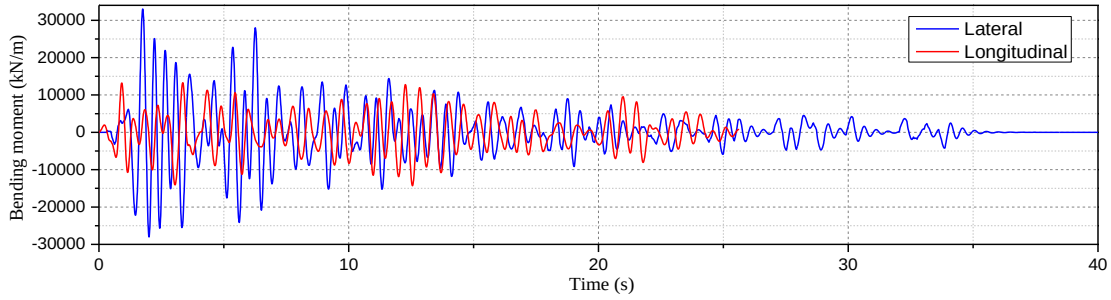

(a) Time history of bending moment

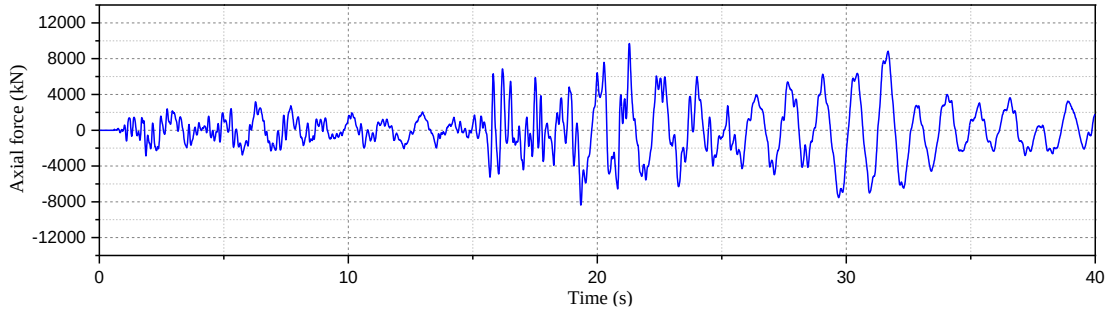

(b) Time history of axial force

Fig.7 - Internal force time history curve of the pier bottom

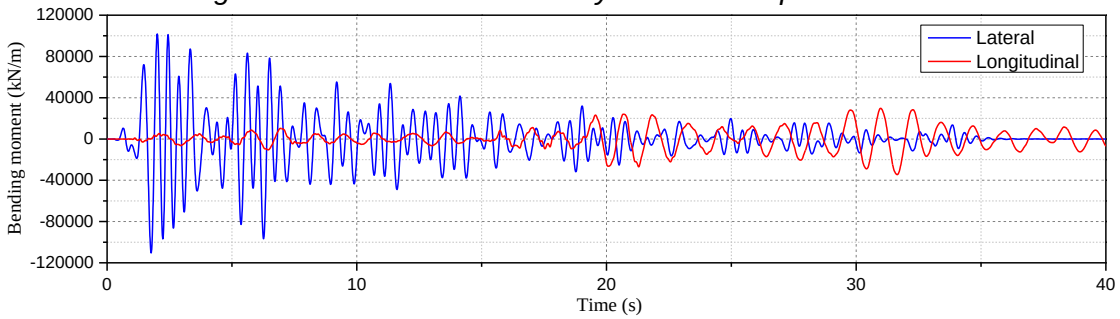

Fig.8 - Internal force time history curve of the beam

Under the action of three-dimensional earthquakes, the rotating structure will bend in the transverse and along the bridge direction and be compressed in the vertical direction. The axial force is borne by the UHPC spherical hinge, and the transverse as well as longitudinal bending moments are borne by the friction moment of the spherical hinge and the anti-overturning moment produced by the pressure between the footing structure and the slide way. Load the internal force of the pier

bottom into the local model, calculate the force of the UHPC spherical hinge and the footing structure, the UHPC spherical hinge compressive stress is shown in Figure 9 and Figure 10.

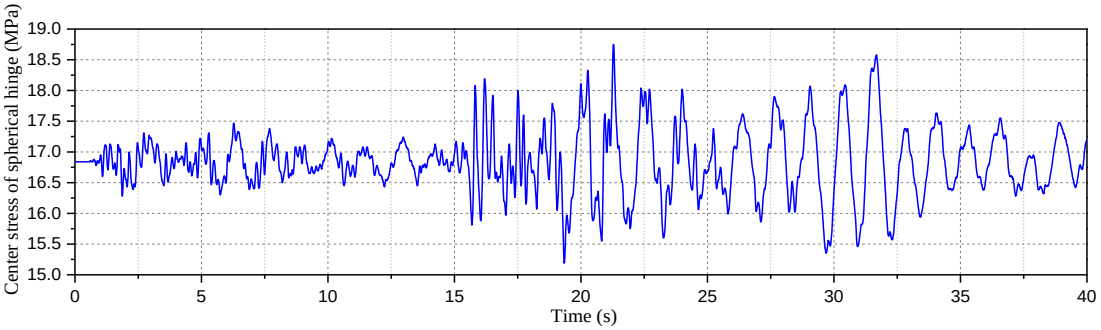

Fig.9 - Time history of central compressive stress of UHPC spherical hinge

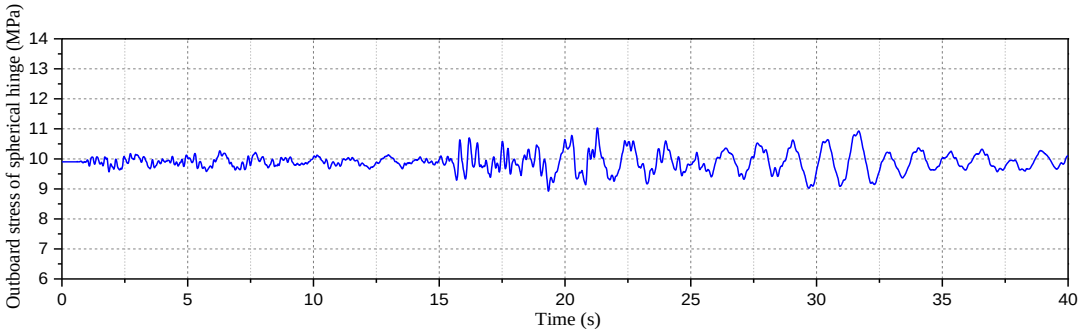

Fig.10 - Time history of the compressive stress on outer edge of UHPC spherical hinge

It can be seen from Figure 9 and Figure 10 that the compressive stress of the spherical hinge changes with the vertical seismic action: the central compressive stress of the spherical hinge floats on the straight line y=16.84 MPa from which it can be obtained that the maximum compressive stress is 18.75 MPa, and that the minimum compressive stress is 15.19 MPa. Among them, 16.84 MPa is the compressive stress value of the spherical hinge under its own weight load, and the range of change is -9.8% to 11.3%. The compressive stress of the outer edge of the spherical hinge fluctuates in the straight line y=9.9 MPa in which the maximum compressive stress is 11.03 MPa and the minimum compressive stress is 8.93 MPa, and the value of change ranges from -9.7% to 11.4%. The compressive stress of the spherical hinge under seismic action is about 11%. According to the research results of the literature [9,11], when the compressive strength of the UHPC spherical hinge is above 200 MPa, its compressive strength shall meet the seismic requirements of the bridge.

Under the action of vertical earthquake and its own weight, the pier is under axial compression, and its vertical compressive stress is all borne by the spherical hinge. At this time, the compressive stress of the supporting structure is basically zero. According to the results of the internal force time history of the pier, lateral bending is the most unfavourable response of the pier. The lateral bending moment at the bottom of the pier will be transmitted to the position of the spherical hinge through the cap, and the frictional resistance of the spherical hinge and the anti-overturning moment of the footing structure will be shared. The friction moment of UHPC spherical hinge is shown in Figure 11, and the stress is shown in Figure 12.

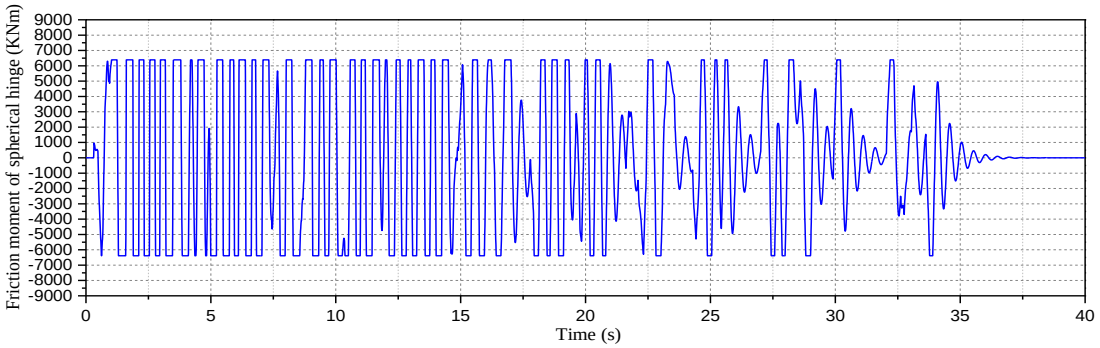

Fig.11 - Time history of friction moment of UHPC spherical hinge

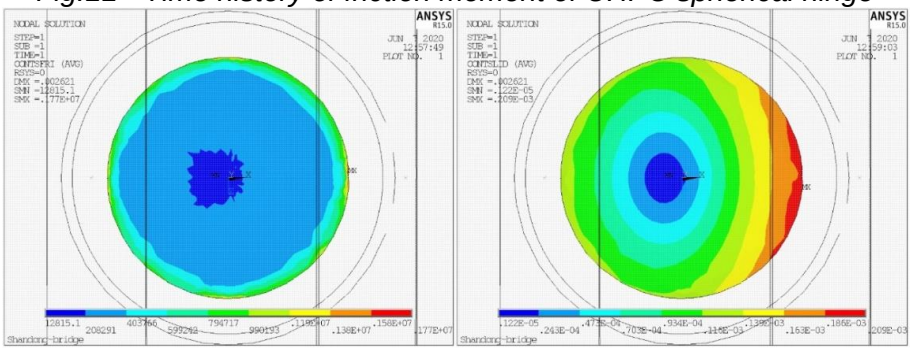

(a) Friction stress *(b) Sliding displacement*

Fig.12 - Stress of UHPC spherical hinge

Figure 11 shows that the friction moment curve of the spherical hinge has obvious "peak clipping". The maximum bending moment at the bottom of the pier is 33025kN·m, while the maximum friction moment of the spherical hinge fluctuates around 6300 kN·m. At this time, the spherical hinge reaches its limit state. Figure 12 is a diagram of the frictional stress and sliding displacement of the spherical hinge in the limit state. The contact surface of the spherical hinge slides along the bending moment, and the maximum sliding distance is 0.209 mm. At this time, the bending moment transferred from the pier will be transferred to the footing structure through the upper cap, and the footing structure will contact the slideway to generate axial stress. The compressive stress diagram in the axial direction of the footing structure is shown in Figure 13.

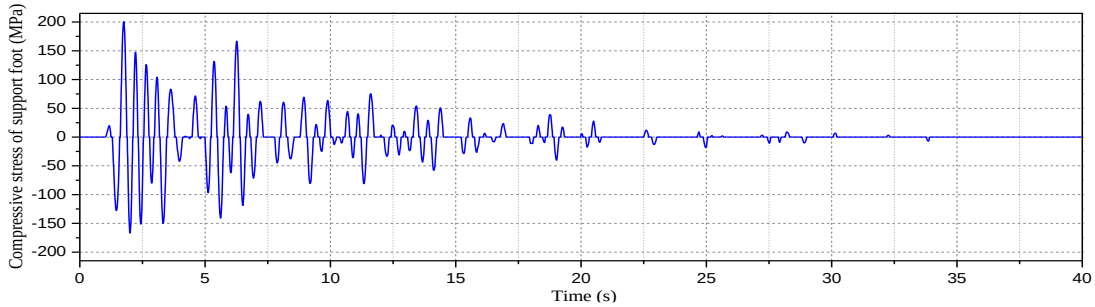

Fig.13- Pressure stress time history of the footing structure

When the compressive stress is positive, the compressive stress of the footing structures is calculated; when the stress value is negative, the calculated side compressive stress is 0, and it produces axial compressive stress on the opposite side of the supporting structures. It can be seen from Figure 13 that the calculated maximum compressive stress of the side brace is 200.6 MPa, and the maximum compressive stress of the opposite side is 166.9 MPa. At this time, the steel pipe of the section of the footing structures produces a large compressive stress under the action of the lateral earthquake. The footing structures are used as the safety reserve of the structure during the

design and construction of the rotating bridge; the structural stability of the supporting structure is thus usually ignored.

Seismic response analysis of Model 2

The internal force response of the key section under three-way seismic input of Model 2 is shown in the following tables (Table 5 to Table 7).

Tab. 5 - Transverse seismic response of the bridge(force Unit：kN, bending moment unit：kN·m)

Location	Internal force	Seismic wave 1	Seismic wave 2	Seismic wave 3	Max	Average	Response spectrum
Pier top	shear force *Fy*	2192	2445	2832	2832	2490	2983
	bending moment *Mx*	1763	2608	2295	2608	2222	2530
Pier bottom	shear force *Fy*	2243	2527	2940	2940	2570	3752
	bending moment *Mx*	21487	23913	26932	26932	24111	18075
Cantilever root	shear force *Fy*	2139	2374	2751	2751	2421	2552
	bending moment *Mz*	58946	59284	68845	68845	62358	55756

Tab. 6 - Response of the longitudinal bridge seismic

Location	Internal force	Seismic wave 1	Seismic wave 2	Seismic wave 3	Max	Average	Response spectrum
Pier top	Axial force *Fz*	5915	5423	6429	6429	5922	5550
	Shear force *Fx*	3675	2385	4238	4238	3433	3370
	Bending moment *My*	17725	11836	20553	20553	16705	15320
Pier bottom	Axial force *Fz*	5919	5428	6432	6432	5926	5152
	Shear force *Fx*	3788	2458	4391	4391	3546	3610
	Bending moment *My*	19809	12564	22805	22805	18393	16450
Cantilever root	Bending moment *My*	8830	11572	11114	11572	10505	11720

Tab. 7- Response of the vertical seismic（force Unit：kN，bending moment unit：kN·m）

Location	Internal force	Seismic wave 1	Seismic wave 2	Seismic wave 3	Max	Average	Response spectrum
Pier top	Axial force *Fz*	1410	1464	730	1464	1201	1230
	Shear force *Fx*	49	51	28	51	43	100
	Bending moment *My*	334	362	189	362	295	505
Pier bottom	Axial force *Fz*	1471	1504	739	1504	1238	1323
	Shear force *Fx*	50	55	28	55	44	112
	Bending moment *My*	103	174	91	174	123	215
Cantilever root	Shear force *Fz*	1375	1441	726	1441	1181	1235
	Bending moment *My*	17192	18621	9710	18621	15174	17300

The calculation results show that the seismic response of Model 1 at each control section is greater than that of Model 2. The bottom of the pier of Model 1 is consolidated, and the cantilever end of the main girder is a free end. As to Model 2, it applies vertical and lateral translational constraints at the cantilever end of the main girder through basin rubber bearings on both sides of

the pier. Under the action of lateral earthquake, the lateral restraint of the side pier limits the lateral displacement of the structure to a certain extent. Together with the bottom restraint of the middle pier, it limits the lateral bending moment of the bridge, thus reducing the lateral bending moment response of the middle pier section, which is transformed into lateral bending moment of the side pier. The maximum bending moment at the pier bottom section of Model 2 is 26932 kN·m, which reduces the seismic response by 18.4%; the maximum axial force of the pier bottom section 6432 kN is reduced by 29.3%; the maximum bending moment at the pier top is 20553 kN·m, which is reduced by 27.7%; The maximum axial force of the pier top is 6429 kN, which is reduced by 33.7%; the maximum bending moment value of the main beam is 18621 kN·m, which is reduced by 46%. The side pier greatly reduces the bending moment response of the main girder and the vertical seismic response of the middle pier through the vertical restraint, which is transformed into the vertical axial force of the side pier itself. In the longitudinal direction, the middle pier is mainly used to resist external forces, and the restraining capacity of the side piers is limited. Therefore, under a longitudinal earthquake, the effect of the bending moment on the top and bottom sections of the middle pier is basically the same. Through the above analysis, the seismic response of the bridge under the maximum cantilever state is the core of the seismic calculation of the rotating structure: in addition to the calculation of the main girder and pier structure, the force state of the spherical hinge and the footing structure should also be analyzed, for example, observing whether spherical hinge and the footing structure would reach the state of ultimate bearing capacity and whether the structure will undergo lateral instability.

This paper adopts the finite element calculation method, takes the maximum cantilever state as the research object, and selects real seismic waves as the external excitation for time history analysis. The calculation results are close to the real engineering situation. The time history analysis process has a large number of iterations, the total number exceeding 900,000 times, and the calculation time exceeds 3 days, which will bring more time costs to actual projects. Aiming at the characteristics of the swivel system, this paper proposes an optimization algorithm for seismic response, which shortens the calculation time of time history analysis on the premise of obtaining a certain calculation accuracy.

Optimization algorithm for seismic response of continuous rigid frame bridge

UHPC spherical hinge swivel system

Proposal of optimization algorithm

According to the vibration equation below:

$$[M]\{x''(t)\} + [C]\{x'(t)\} + [k]\{x(t)\} = -[M]\{I\}x''(t) \quad (5)$$

$[M]$: mass matrix; $[C]$: damping matrix; $[k]$: stiffness matrix; $x(t)$: displacement function of the structure. The first and second derivatives respectively represent the speed and acceleration functions of the structure. The mode number of the structural system is *n*, and the mode matrix can be expressed as:

$$[A] = [\{x\}_1\{x\}_2 \ldots \{x\}_n] \quad (6)$$

The displacement matrix expression is $\{x(t)\} = [\{x\}_1 q_1(t) + \{x\}_2 q_2(t) + \cdots + \{x\}_n q_n(t)] = [A]\{q\}$. Combine the displacement matrix with equation (5), the following formula is obtained:

$$M_j^* q_j'' + C_j^* q_j' + k_j^* q_j = -\{X\}_j^T [M]\{I\}x''(t) \quad (7)$$

$M_j^* = \{X\}_j^T [M]\{X\}_j^T$, $C_j^* = \{X\}_j^T [C]\{X\}_j^T$, $K_j^* = \{X\}_j^T [k]\{X\}_j^T$, after transformation, equation (7) can also be presented as the following equation:

$$q_j'' + 2\zeta_j\omega_j q_j' + \omega_j^2 q_j = -\gamma_j x''(t) \quad (8)$$

γ_j is the mode shape participation coefficient, its expression shown as follows:

$$\gamma_j = \frac{\{X\}_j^T[M]\{I\}}{\{X\}_j^T[M]\{X\}_j} = \frac{\sum_{i=1}^n m_i x_{ji}}{\sum_{i=1}^n m_i {x_{ji}}^2} \quad (9)$$

The mass point *i* is subjected to the unit mass $x_0''(t)$, and is assigned by γ_j to the mode *j*; then the following equation is obtained:

$$q_j(t) = -\frac{\gamma_j}{w_j}\int_0^t e^{-\rho_J w_j(t-\tau)} x_0''(\tau) sin\, w_j(t-\tau) d\tau = \Delta_j(t)\gamma_j \quad (10)$$

From the above formula, the displacement of the *j-th* mode shape is $x_{ji}\Delta_j(t)\gamma_j$. The expressions for all mode shape displacement and acceleration are:

$$x_i(t) = \sum_{j=1}^n \gamma_j \Delta_j(t)\gamma_j, \quad x_i''(t) = \sum_{j=1}^n \gamma_j \Delta_j''(t)\gamma_j \quad (11)$$

From the above formula, the expression of the inertial force at the mass point *i* in the structure is as the following:

$$F_i(t) = m_i[x_i''(t) + x_0''(t)] \quad (12)$$

According to the structure kinematics equation, the inertial force on the mass poin *i* is:

$$F_{ji}(t) = m_i\left[\gamma_j \Delta_j''(t) x_{ji}(t) + \gamma_j x_{ji} x_0''(t)\right] \quad (13)$$

Then the maximum inertial force is:

$$F_{(ji)max} = m_i\gamma_j x_{ji}\left|\left[\Delta_j''(t) + x_0''(t)\right]\right| \quad (14)$$

$\Delta_j''(t)$ is the seismic acceleration under the initial acceleration state $x_0''(t)$. The equation $\left|\left[\Delta_j''(t) + x_0''(t)\right]\right|$ can be obtained from the response spectrum according to the seismic fortification intensity and the characteristic period of the site. The above formula thus can be rewritten as the following:

$$F_{ji} = \gamma_j x_{ji}\alpha_j G_i \quad (15)$$

α_j is the horizontal seismic influence coefficient of mode *j*; x_{ji} is the horizontal relative displacement of mode *j* at the mass point *i*, γ_j the participation coefficient of mode *j*. According to the SRSS method, the total effect expression of seismic action is as follows:

$$S = \sqrt{\sum S_j^2} \quad (16)$$

Examples

The basic seismic acceleration of the translational system is 0.1g; the characteristic period of the site is 0.45 s, and the damping ratio of the structure is 0.05. The thrust stiffness of the pier is $k_1=k_2=3EI/H$, where E is the elastic modulus of the pier and I is the transverse bending moment of inertia of the pier; H is the height between the pier foundation and the main beam. The movement of the rotating structure can be equivalent to the movement of the elastic body with two degrees of freedom. Mass point 1 is the position of the centroid of the pier, and the mass is the mass of the pier itself, m_1=686 t. Mass point 2 is the position of the top of the pier, and the mass is the total mass of the main beam of the superstructure and the bridge paving load, m_2=9000t. According to the kinematic equations:

$$\left(\begin{bmatrix} k_{11} & k_{12} \\ k_{21} & k_{22} \end{bmatrix} - \omega^2 \begin{bmatrix} m_1 & 0 \\ 0 & m_2 \end{bmatrix}\right)\begin{pmatrix} x_1 \\ x_2 \end{pmatrix} = \begin{pmatrix} 0 \\ 0 \end{pmatrix}$$

The stiffness matrix is $k_{11}=k_1+k_2$, $k_{12}= k_{21}=- k_2$, $k_{22}= k_2$. The formula can be transformed as follows:

$$\left|\begin{bmatrix} k_{11} & k_{12} \\ k_{21} & k_{22} \end{bmatrix} - \omega^2 \begin{bmatrix} m_1 & 0 \\ 0 & m_2 \end{bmatrix}\right| = 0$$

Combined calculation of determinant: $\left|\begin{bmatrix} k_{11} - \omega^2 m_1 & k_{12} \\ k_{21} & k_{22} - \omega^2 m_2 \end{bmatrix}\right| = 0$

The angular frequency can be obtained from the above formula, and the mode diagrams at different natural frequencies can be obtained by continuing to solve the displacement matrix. By calculating the first few modes of the structure, the lateral main mode of the pier is drawn and solved. Through the previous finite element analysis, the first mode and the seventh mode in Model 1 are respectively the first and second lateral bending modes of the pier. The calculation results of the modal are directly used in the calculation. The frequency of the 7th mode is 4.06 Hz with a period of 0.246 s, and the frequency of the first mode is 4.06 Hz with a period of 2.564 s. Take the 7th mode in the finite element model as the first mode of calculation, i.e., T_1=0.246s. The first mode is used as the second mode of calculation, T_2=2.564s. The mode displacement is shown in Figure 14. The natural vibration displacement is normalized, and the natural vibration law of the elastic body with two degrees of freedom is obtained.

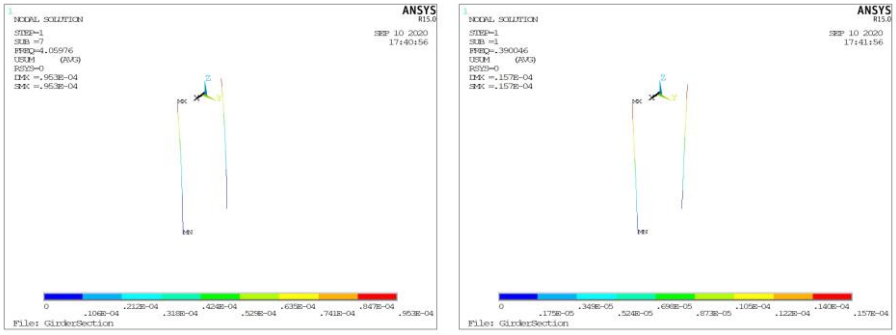

Fig.14 - First and second order transverse bending modes of bridge piers

The response of the first mode under horizontal seismic action will be discussed here. According to the design response spectrum, the seismic acceleration is 0.1g, and the influence coefficient of a horizontal earthquake is αmax=0.08. Since Tg=0.45s, and 0.1＜T1＜Tg, then α1=αmax=0.08, which can be obtained from equation (9):

$$\gamma_1 = \frac{\sum_{i=1}^{n} m_i x_{ji}}{\sum_{i=1}^{n} m_i {x_{ji}}^2} = \frac{1.0 \times 686 + 2.1 \times 9000}{1.0^2 \times 686 + 2.1^2 \times 9000} = 0.485$$

Combine it with equation (12), the horizontal seismic force on two mass points is obtained:

$$F_{11} = \gamma_1 x_{11} \alpha_1 G_1 = 0.485 \times 1.0 \times 0.08 \times 686 \times 10 = 266.2\text{kN}$$

$$F_{12} = \gamma_1 x_{12} \alpha_1 G_2 = 0.485 \times 2.1 \times 0.08 \times 9000 \times 10 = 7333\text{kN}$$

Similarly, the horizontal seismic action of the second-order mode is T2>5Tg, according to the design response spectrum, α_2=0.037, then

$$\gamma_2 = \frac{\sum_{i=1}^{n} m_i x_{ji}}{\sum_{i=1}^{n} m_i {x_{ji}}^2} = \frac{1.0 \times 686 + 1.7 \times 9000}{1.0^2 \times 686 + 1.7^2 \times 9000} = 0.60$$

Thus, the horizontal seismic action should be:

$$F_{21} = \gamma_1 x_{11} \alpha_1 G_1 = 0.6 \times 1.0 \times 0.037 \times 686 \times 10 = 152.3\text{kN}$$

$$F_{22} = \gamma_1 x_{12} \alpha_1 G_2 = 0.6 \times 1.7 \times 0.037 \times 9000 \times 10 = 3397\text{kN}$$

According to the SRSS method, after the two modes are superimposed, *F1*=306 kN, *F2*=8081 kN, then the bending moment of the pier bottom *Mx*'=306(10-2.9)/2+8081(10-2.9)=58462 kN·m . The finite element result is Mx=233025=66050 kN·m, and the optimization algorithm is 90% of the finite element calculation result, which is close to the finite element calculation result.

CONCLUSIONS

In this paper, the mechanical behaviour of continuous rigid frame bridge UHPC spherical hinge translation system under seismic action is studied, and the following conclusions are obtained:

(1) Based on the seismic data of the Pacific Earthquake Engineering Research Center (PEER), 18 seismic waves of Model 1 and Model 2 in the three directions are screened to meet the calculation requirements. The calculation results of real seismic waves are highly discrete, but the average value is close to the calculation results of the response spectrum method.

(2) The main seismic response of Model 1 is the lateral bending and vertical axial force at the bottom of the pier, also, the longitudinal and lateral bending of the main girder. The turntable structure bears the internal force of the pier and the UHPC spherical hinge bears all the axial pressure and 20% of the lateral bending moment, the footing structure bearing the remaining 80% of the lateral bending moment. As to Model 2, the lateral bending moment and vertical axial force at the bottom of the pier reduce by 18.4% and 29.3%, respectively, and the maximum bending moment of the main beam at the root of the cantilever reduces by 46%. The side pier bears part of the internal force of the middle pier and the main beam, so the stress analysis during the horizontal rotation is the focus of the bridge seismic analysis.

(3) An optimization algorithm for the seismic response of a continuous rigid frame bridge in the horizontal rotation process is proposed, which has higher accuracy compared with the calculation results of time history analysis and response spectrum method. Post-evaluation of the seismic performance of the bridge has been carried out for the built project. The compressive stress of the footing structure is reduced by increasing the distance between the footing structure and the center of rotation, increasing the number of the footing structure, increasing the wall thickness of the footing structure, and adopting a steel tube concrete structure. Thereby improving the seismic performance of the bridge horizontal swivel system.

AFFILIATION

Supported by “The Initial Scientific Research Funds of Anhui polytechnic University”, and the project number is 2021YQQ021

REFERENCES

[1] Deng Renbin, Tang Weijun. Current situation and development prospect of highway and bridge construction in China [J]. Heilongjiang transportation science and technology, 2017, 40 (07): 139 + 141.

[2] J. Zhang, T. E. El-Diraby, Constructability analysis of the bridge superstructure rotation construction method in China [J]. 132(2006),353-360.

[3] Siwowski, Tomasz, Wysocki, Artur, Horizontal rotation via floatation as an accelerated bridge construction for long-span footbridge erection: Case study[J]. Journal of Bridge Engineering,20(2015),124-126.

[4] Wu Yuyong. Key points of construction technology for transit bridge in bridge engineering [J]. Highway transportation technology (Application Technology Edition), 2019, 15 (08): 105-107.

[5] Liu Haiqi, Overview of main bridge swivel system of dulaying Bridge[J]. Transportation world, 03(2016):80-81.

[6] Wang Shuwang, Design of curved swivel T-shaped rigid frame for Beijing Shanghai Railway[J]. Railway Construction Technology, S2(2010):24-26+52.

[7] Lu Jinhua, Study on construction control and stability of large tonnage continuous rigid frame bridge[D]. Lanzhou Jiaotong University, 2016.

[8] Wei Qing, Research on the construction technology of super wide asymmetric T-frame swivel over Zheng Wan high speed railway[J]. Railway Construction Technology, 04(2020):69-72.

[9] Wang, Jiawei; Sun, Quansheng. Experimental Study on Improving the Compressive Strength of UHPC Turntable. Advances in Materials Science and Engineering [J], Vol.2020, WOS: 000556811300003.

[10] Wang, Jiawei; Sun, Quansheng. Dynamic analysis of swivel construction method under multi-variable coupling effects. International Journal of Structural Integrity[J], 2019, Vol.10, No.4, pp:580-598. Accession number:20192507063782.

[11] Wang, Jiawei; Sun, Quansheng. Experimental research on compressive strength of UHPC spherical hinge. International Journal of Structural Integrity [J], 2019, Vol.10, No.6, pp: 518-537. Accession number: 20194607674167.
[12] Wang, Jiawei; Sun, Quansheng. Parameter sensitivity analysis of stability of T-shaped rigid frame bridge by adopting swivel construction method. Multidiscipline Modeling in Materials and Structures [J], 2020. Accession number: 20201808588847.
[13] Wang Changjie. Integral stress analysis and pier optimization design of T-shaped rigid frame bridge with Swivel Construction[D]. Southwest Jiaotong University, 2017.
[14] Wang Xinmin. Numerical analysis of ANSYS engineering structure[M]. Bei Jing: People's Communications Press, 2020.
[15] National standards of the people Republic of China. Code for seismic design of buildings (GB 50011-2010) [S]. China Construction Industry Press, 2016.
[16] National standards of the people's Republic of China. Detailed rules for earthquake resistance of Highway Bridges (GBT50152-2012) [S]. People's Communications Press, 2012.

CIVIL ENGINEERING JOURNAL

Article no. 36

THE CIVIL ENGINEERING JOURNAL 2-2021

EXPERIMENTAL STUDY ON THE RATE OF ABSORPTION OF WATER OF BASALT, POLYPROPYLENE AND STEEL FIBERS REINFORCED CONCRETE

Mustapha Abdulhadi[1] and S.I. Haruna[*]

1. *School of mechanic, Civil Engineering and Archtichture Northwestern Polytechnic University Xi'an 710071 P.R. China*
2. *Department of Civil Engineering, Bayero University, Kano P.M.B. 3011, Nigeria, siharuna.civ@buk.edu.ng*

ABSTRACT

Good durability of concrete is an essential part of the design process, and durability designs are carried out by specifying material requirements and the exposure conditions in which the structure is in contact. The main feature of durable concrete is low water absorption. Almost all forms of deterioration in reinforced concrete involve harmful fluid ingress through the concretes pore structure. In wet concrete, the water ingress rate or other liquids is mainly controlled by absorption due to capillary rise. This study examines the effect of basalt, polypropylene, and steel fiber in different volume fractions (V_f) of 0.3%, 0.6%, and 0.9% for absorption tests. A total of 8 specimens for different fiber volume fractions were examined based on the rate of water absorption test recommended by ASTM C1585-04. A result obtained has been analyzed and compared with the control specimen. A relationship between absorption rate and the square root of time for both concrete mixtures was represented graphically and linearly. Result data showed a precise decrease in absorption due to incorporating both types of fiber. Also, basalt and polypropylene showed greater uptake than steel fiber and enhanced water transport into concrete specimens from the result data. However, steel fiber showed high resistance to absorption rater than the control specimen and other fiber.

KEYWORDS

Basalt fiber, Water absorption, Polypropylene fiber, Steel fiber

INTRODUCTION

The durability of concrete mostly depends on how fluids penetrate the concrete matrix. For instance, damage caused due to the present chloride ions in de-icing salts or seawater. The durability of concrete is affected by pore structure. The porosity and connectivity of the pore play a vital role in the permeability of concrete. The experimental test results are widely used as a factor for concrete durability has been adopted in the past study [1,2].

0.05% by volume fraction of Polypropylene fiber is considered the optimum amount of polypropylene fibers to be added to concretes mixture due to its excellent performance at elevated temperature [3]. Improving the hardened property, the mainly compressive strength of concrete does not enhance its behavior, especially tensile strength and strains. [4]. The behavior of self fiber compacting concrete was affected by incorporating silica fume [5]. Steel fiber showed the best resistance to the damaging effect of NaCl than other types of fiber and control specimens as its compressive strength increased by 0.6% and 0.9% by 4.6% and 16.4%, respectively. That might result from relatively high bonding, which blocked water and NaCl solution from traveling between fiber and hardened concrete [6]. The basalt aggregate was used in slurry infiltrated fiber concrete

[7]. The anti-cracking behavior of steel fiber in steel fiber ceramic concrete was enhanced with fiber content [8]. Niveditha and Srikanth [17] study the effect of mineral admixture on the hardened properties, water absorption rate, and permeability in geopolymer concrete. They reported that the addition of ultra-fine slag enhances the durability properties.[9]

The investigating parameters such as permeability, diffusivity, and rate of water absorption behavior are vital for the durability of concrete [10]. Sorptivity, the rate of water absorption, is a rapid and simple test that can indicate the transport properties of cover concrete and its tendency to absorb and transmit water by capillarity [11]. The water absorption varies mainly depending on the cement paste aggregate in the concrete mixture [12]. Four requirements must be met for the water absorption vs. $\sqrt{t}$ Law to hold, [13]: (I) homogeneous material is required on the penetration distance scale, (II) The capillary absorption flow, (III) the availability of water to flow at the inflow surface of the reservoir, and (IV) Gravitational effects. The $\sqrt{Time}$ law translate the kinetics of capillary absorption (sorptivity). Other factors that can affect the sorptivity values of concrete are the sorptivity properties of the individual components of the mix, such as the cement paste matrix and its physical arrangement, for example, the aggregate distribution [13]. In this study, the absorption rate of water of concrete mixtures incoprated with basalt, polypropylene, and steel fiber were evaluated. And the method involved in determine the increase in the mass of a specimens that results from the absorption of water as a function of time when only one surface of specimens is under water.

EXPERIMENTAL PROGRAM

Material

Ordinary cement (42.5N) was used to prepare concrete mixtures; Table 1 shows the properties of aggregates used in the study, following the international standard [14]. Natural river sand with a specific gravity of 2.60 was used as fine aggregate. A natural stone with a nominal size of 15–20 mm was used as a coarse aggregate. The cement, sand, coarse aggregate, and water content were 407, 535, 1245, and 203.7 kg/m^3, respectively, prepare to achieved C30 concrete according to [15]. The three specific fibers, namely: basalt, polypropylene, and straight steel fiber, as shown in Figure 1, were used in the study.

Tab. 1 - Properties aggregates used

Materials	Apparent density (kg/cm^3)	Apparent density (kg/cm^3)	Fineness modulus	Moisture content (%)
Coarse aggregate	2665	1450	-	-
Fine aggregate	2670	1554	2.46	3.1

Tables 2 and 3 present the fibers' performance behavior to fabricate the fiber-reinforced concrete mixture. The average compressive strength of the reference sample and fiber reinforced concrete specimens were also presented in Table 3.

Tab. 2 - performance Properties of fibers used

Property	Basalt	Polypropylene	Steel fiber
Length (mm)	18	12	13
Diameter (mm)	0.013	0.021	0.2
Aspect ratio (l/d)	1384	544	65
Tensile strength (MPa)	3000~3500	365~600	2900
Ultimate elongation (%)	3.2	25~60	4
Density (g/cm^3)	2.65	0.9	7.8
Modulus of Elasticity (GPa)	90~110	2.4~3.2	210

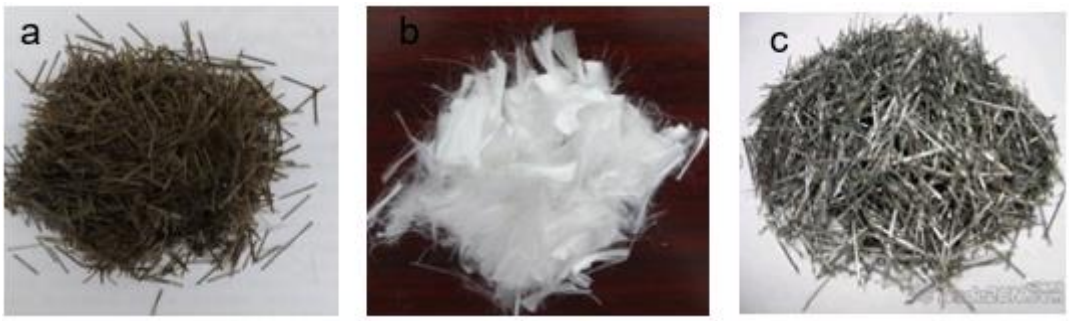

Fig.1- Fiber type: (a) Basalt fiber (b) PP fiber, (c) Steel fiber

Mixing and sample preparation

The mixing of non-fibrous and fiber reinforced concrete was described as follows: first, the constituent materials, including coarse aggregate, fine aggregate, and cement, were mixed dry in a concrete mixer for about 2 minutes. Subsequently, water was added gently to the mixture, while mixing was continued for the next 1 minute. The fibers were scattered into the concrete mixture to prevent the fiber clotting., the mixing was continued for another 3 minutes to obtain homogeneous concrete mixtures. For absorption test, eight 185 × 150 mm cylinder specimens were produced with fiber volume fraction of 0.0%, 0.3%, 0.6%, and 0.9%, respectively. While for the compressive strength test, three 150× 150× 150 mm Cubic specimens were cast for each fiber volume fraction. The average of samples from each mixing condition was taken as the compressive strength as shown in Tab. 4. After 24 hours, all the samples were removed and cured at the standard curing room for 28 days. The cylinder specimens were prepared for the water absorption test.

Tab. 3: The compressive strength results of fiber reinforced concrete mixtures.

Specimen	Type of Fiber	Fiber volume fraction V_f (%)	Number of specimens	Average Compressive strength (MPa)
Plain/Control	-	0.0	3	35.55
BFRC	Basalt	0.3	3	32.02
		0.6	3	33.24
		0.9	3	35.86
PFRC	Polypropylene	0.3	3	33.44
		0.6	3	33.27
		0.9	3	29.92
SFRC	Steel	0.3	3	37.95
		0.6	3	43.82
		0.9	3	45.55

Compressive strength for concrete cube specimen with 0%, 0.3%, 0.6%, and 0.9% of Basalt, Polypropylene, and Steel Fibers are shown in Table 3.

As seen from the table, the addition of 0.3% and a 0.6% volume of Basalt fiber resulted in decreased compressive strength relative to plain concrete by 9.9% and 6.5. At the same time, 0.9% volume of Basalt fiber indicates a slight increase in compressive strength (i.e., 0.9%). Similarly, the addition of 0.3%, 0.6%, and 0.9% volume of polypropylene fiber resulted in a decrease of compressive strength relative to plain concrete by 5.9%, 6.4%, and 15.8%, respectively. For steel fiber, addition of 0.3%, 0.6% and 0.9% resulted in an increase in compressive strength by 6.8%, 23.3% and 28.1% respectively. The addition of polypropylene and basalt fibers in the concrete mixture has different degrees of reducing compressive strength. Several factors affect the strength of concrete, such as cement strength, water-cement ratio, and the size of the concrete aggregates [14]. The incorporation of the fibers within the concrete matrix changes the phase of each component. As seen from the test results analysis, with the same series of fiber concrete, the strength decreases with the increase of fiber mixing ratio increases; also, with the same volume of fiber, different series of fiber results in different compressive strength of concrete.

Testing procedure

The water absorption rate of fiber reinforced concrete mixtures was conducted according to [16] ASTM C1585-04. The influence of fiber volume fraction and fiber type were evaluated accordingly. The water intake led to an increase in the mass of a specimen due to the capillary action of water expressed as a function of time, subjecting only one surface of the sample to water, and the top surface was sealed (candle wax). The water absorption is calculated using Eq. 1. For this study, the temperature variation was considered constant, and 0.001 g/mm^3 is taken as water density.

$$I = \frac{mt}{A \times \rho_w} \quad (1)$$

Where *I, mt,* ρ_w *A*nd A are the water absorption in (mm), change in specimen mass (g) at a time t, density of water (g/mm^3*),* and exposed area of the specimen (mm^2), respectively.

The square root of time relationship controls the water transport into the concrete by capillarity. The initial rate of absorption (mm/s^{-2}) was defined as the slope of the line that is the best fit to I plotted against the square root of time (S^{-2}). This slope is obtained using the least-squares, linear regression method of the plot of I versus time S^{-2}. A schematic setup of the capillary suction

test is shown in Figure 2. A cylindrical specimen was placed on the support device at the bottom of the pan, filled with tap water, then the water level was maintained 1 to 3mm above the top of the support device. The absorbed water quantity was recorded at different time intervals as indicated in Tab.le4 through 6. Any surface water was blotted off with a dampened paper towel for each mass determination.

Linear regression was used to determine the slope. The experimental setup of the capillary action test is depicted in Figure 2. The test specimens were put on the pan filled with water and supported by a device. The water level was kept at a height ranging from 1 to 3mm above the top of the support device. The absorbed water quantity was monitored at different time interval indicated in Table 4.

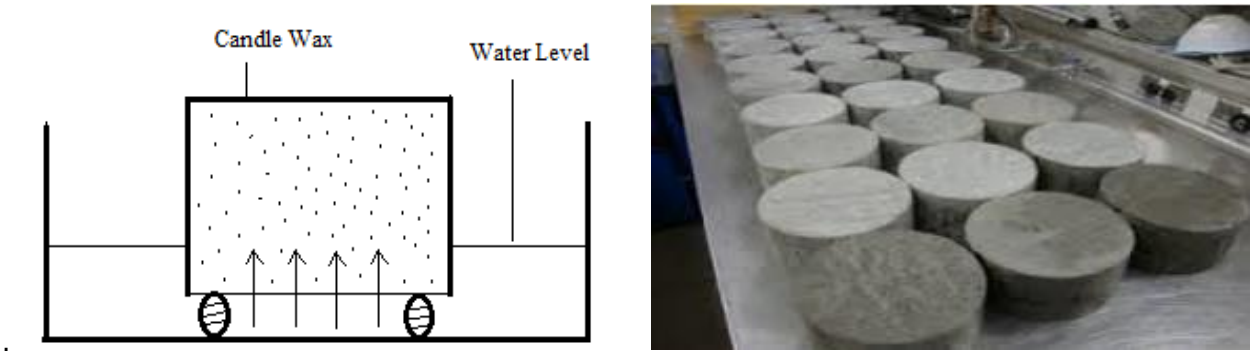

A schematic setup *Cylindrical specimens*

Fig. 2- Experimental Setup

RESULT AND DISCUSSION

Water absorption

The result of the water absorption test of non-fibrous and fiber reinforced concrete cylinder specimens incorporated with 0%, 0.3%, 0.6%, and 0.9% of basalt, polypropylene, and steel fibers are summarized and given in Tables 4 – 6. The square root of time relationship monitors the water absorption in concrete specimens by capillarity action. The initial rate of water absorption (mm/$s^{1/2}$) described the slope of the line drawn on the graph of absorption versus the square time ($s^{1/2}$). Slop was obtained by using least–square linear regression analysis from the plot of I versus the square root of time 1, 5, 10, 20, 30, and 60 minutes using all the points within this range. The secondary rate of water absorption (mm/$S^{1/2}$) is described as the slope of the line that is the best fit to the water absorption graph plotted against the square root of time ($S^{1/2}$) 1, 2, 3, 4, 5, 6 and 7 days using all the points from1*d* to 7*d* [16].

Tab. 4 - water absorption of BFRC

Observed time		Water absorption (mm)			
Time (s)	$\sqrt{time}$ $(s^{1/2})$	0% Fiber	0.3% Fiber	0.6% Fiber	0.9% Fiber
0	0	0.0000	0.0000	0.0000	0.0000
60	8	0.3348	0.3348	0.5580	0.5580
300	17	0.1860	0.5208	0.5580	0.5580
600	24	0.1860	0.7068	0.7440	0.7440
1200	35	0.3720	0.7068	0.9301	0.7440
1800	42	0.3720	0.7068	0.9301	0.9301
3600	60	0.5580	1.0788	1.3021	1.1161
7200	85	0.5580	1.2649	1.4881	1.1161
10800	104	0.7440	1.4509	1.6741	1.4881
14400	120	0.9300	1.4509	1.8601	1.4881
18000	134	1.1161	1.4509	1.8601	1.4881
21600	147	1.3021	1.6369	2.0461	1.6741
99420	315	1.4881	2.1949	2.7901	2.0461
196620	443	1.6741	2.3801	2.9762	2.2321
272220	522	1.6741	2.5670	2.9762	2.2321
355020	596	1.4881	2.7530	3.1622	2.4181
529980	728	1.6742	2.7530	3.3482	2.4181
6223580	790	1.6742	2.7530	3.3482	2.6041

Tab. 5 - water absorption of PFRC

Observed time		Water absorption I (mm)			
Time (s)	$\sqrt{time}$ $(s^{1/2})$	0% Fiber	0.3% Fiber	0.6% Fiber	0.9% Fiber
0	0	0.0000	0.0000	0.0000	0.0000
60	8	0.3348	0.5580	0.7440	0.1860
300	17	0.1860	0.5580	0.7440	0.1860
600	24	0.1860	0.7440	0.9301	0.5580
1200	35	0.3720	0.7440	0.1161	0.5580
1800	42	0.3720	0.7440	0.1161	0.7440
3600	60	0.5580	0.9301	1.3021	0.9301
7200	85	0.5580	1.4881	1.4881	0.9301
10800	104	0.7440	1.4881	1.8601	0.9301
14400	120	0.9300	1.4881	1.8601	0.1161
18000	134	1.1161	1.4881	2.0461	0.1161

21600	147	1.3021	1.6741	2.0461	1.3021
99420	315	1.4881	2.7902	2.4181	1.6741
196620	443	1.6741	2.7962	2.6041	1.6741
272220	522	1.6741	2.7902	2.4181	1.6742
355020	596	1.4881	2.9762	2.6041	1.6742
529980	728	1.6742	2.9762	2.6041	1.6742
623580	790	1.6742	3.1622	2.6041	1.8601
717180	847	1.8601	3.1622	2.6041	1.8601

Tab. 6 - water absorption of SFRC

Observed time		Water absorption I (mm)			
Time (s)	$\sqrt{time}$ $(s^{1/2})$	0% Fiber	0.3% Fiber	0.6% Fiber	0.9% Fiber
0	0	0.0000	0.0000	0.0000	0.0000
60	8	0.3348	0.1860	0.3720	0.0000
300	17	0.1860	0.3720	0.3720	0.0000
600	24	0.1860	0.3720	0.3720	0.1860
1200	35	0.3720	0.3720	0.5580	0.3720
1800	42	0.3720	0.3720	0.5580	0.3720
3600	60	0.5580	0.5580	0.5580	0.3720
7200	85	0.5580	0.7440	0.5580	0.3720
10800	104	0.7440	0.7440	0.5580	0.7440
14400	120	0.9300	0.9301	0.5580	0.7440
18000	134	1.1161	0.9301	0.7440	0.7440
21600	147	1.3021	0.1161	0.7440	0.9301
99420	315	1.4881	1.4881	0.7440	0.1161
196620	443	1.6741	1.4881	0.9301	1.3021
272220	522	1.6741	1.4881	0.9301	1.3021
355020	596	1.4881	1.4881	0.9301	1.3021
529980	728	1.6742	1.4881	1.3021	1.3021
623580	790	1.6742	1.6742	1.3021	1.3021
717180	847	1.8601	1.6742	1.3021	1.3021

The concrete mixture absorption rates incorporated with different fibers at various intervals were proportional to the square root of time linearly at the initial stage. Among the fiber type, steel fiber is more resistant to capillary suction in various mixtures than basalt fiber. However, polypropylene for both mix ratios indicates the fastest absorption rate for the initial period. The basalt showed an accelerated degree of absorption for secondary absorption compared to steel fiber and control.

As shown in Figure 3, the absorption rate of BFRC specimens is higher than non-fibrous samples. The inclusion of basalt fiber at 0.6% volume fraction shows the highest absorption at the initial and secondary stage of absorption with values 2 mm and 3.6 mm, respectively. The absorption rate of specimens containing 0.9% basalt fiber was lower than the absorption of samples incorporated with 0.3% basalt fiber. The case is different in PFRC specimens, whereby specimen with 0.3% polypropylene fiber exhibits the highest absorption rate. The absorption rate decreases with an increase in polypropylene fiber, as shown in Figure 4. The steel fiber reinforced concrete revealed that the control sample has the highest absorption rate, and the specimen containing 0.9% steel fiber had the lowest absorption capacity, as depicted in Figure 5.

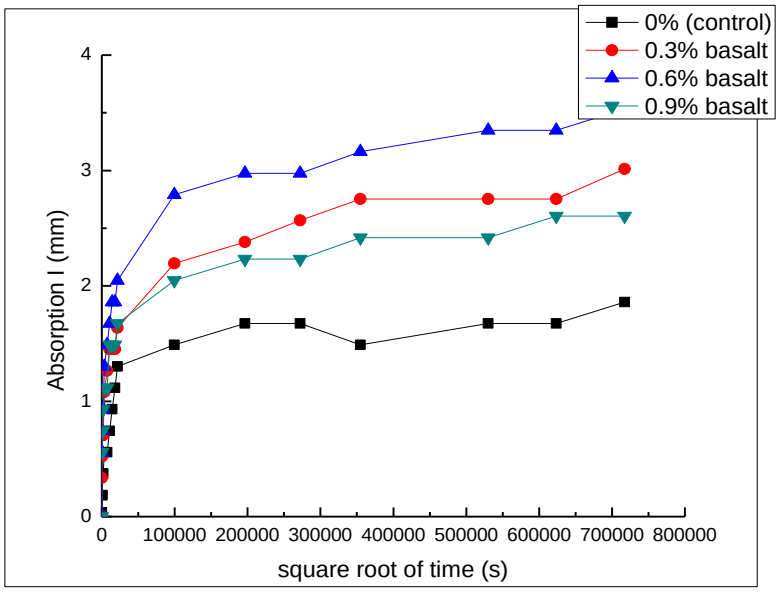

Fig. 3- Rate of absorption against the square root of time for BFRC

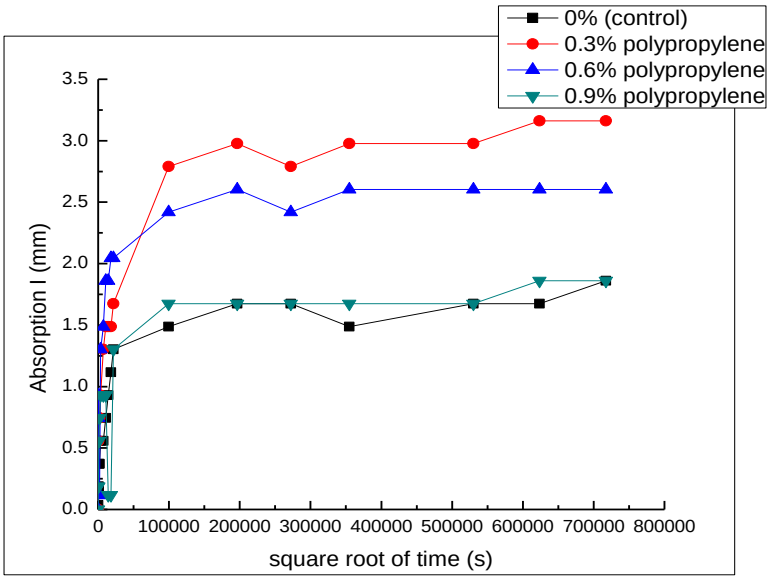

Fig. 4- Rate of absorption against the square root of time for PFRC

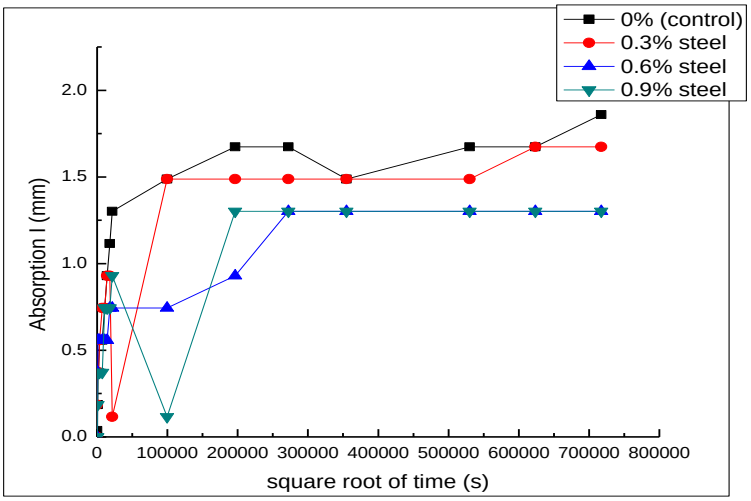

Fig. 5- Rate of absorption against the square root of time for SFRC

Effect of Fibers on the rate of absorption at initial and final stages

Figures 6 and 7 show the comparison of initial and secondary absorption for non-fibrous and fiber reinforced concrete. Generally, incorporating fibers into the concrete mixtures compared to the reference specimens leads to a significant decrease in water absorption rate regardless of the fiber type at an initial stage. It can be seen, at 0.3 and 0.6% of polypropylene fiber, the amount of water absorption remains the same and further reduce at 0.9% volume fraction. A nearly constant reduction of the absorption rate was revealed at the three different volume fractions of basalt fiber at an early absorption stage. However, in SFRC, the water absorption decreases with an increase in steel fiber. At the secondary stage, the absorption rate of plain, BFRC, PFRC, and SFRC specimens demonstrate similar behavior. However, the steel fiber reinforced concrete specimens revealed a significant decrease in the absorption rate at all levels of increment of steel fiber, presumably attributed to steel fiber's metallic nature.

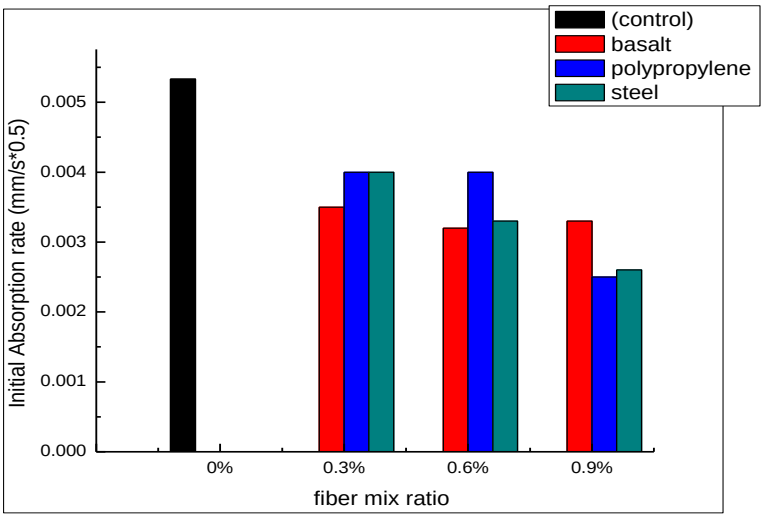

Fig. 6- Initial absorption vs. fiber mix ratio for Plain, BFRC, PFRC, and SFRC.

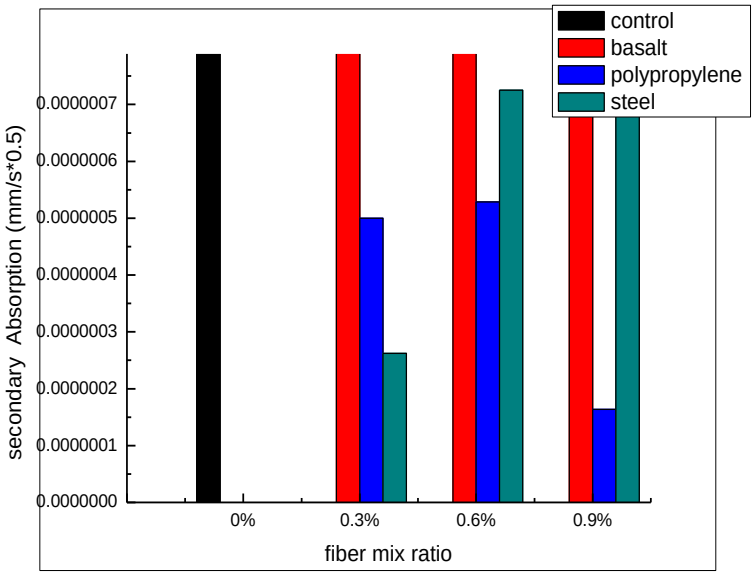

Fig. 7- Secondary absorption vs. fiber mix ratio for Plain, BFRC, PFRC, and SFRC

CONCLUSION

In this study, the effect of fiber volume fraction and fiber types was experimentally investigated to determine the water absorption rate in the concrete mixtures. The need to overcome the problem of degradation of concrete by the mass movement of water into concrete structures. The following conclusions can be drawn:

- The absorption rate for each type and each volume of fiber were linearly proportional to the square root of time.
- The addition of basalt, polypropylene, and steel fiber in different volume ratios showed a significant decrease in the initial absorption rate. However, basalt showed no notable change with secondary absorption, while steel and polypropylene showed little secondary absorption.
- Among the fiber reinforced concrete specimens, SFRC showed the highest resistance to the capillary action compare to reference samples, which might result from relatively stable bonding, which blocked water from traveling between fiber and hardened cement paste. However, BFRC and PRFC revealed a high absorption rate than SFRC because PRFC significantly accelerated water transport into concrete; this is presumably due to interfacial transition zone resulting from incorporating polypropylene fiber in the mixture, thin and long hydrophobic behavior.

REFERENCES

[1] M. Abdulhadi, A comparative Study of Basalt and Polypropylene Fibers Reinforced Concrete on Compressive and Tensile Behavior, Int. J. Eng. Trends Technol. 9 (2014) 295–300. https://doi.org/10.14445/22315381/ijett-v9p258.

[2] R. Punyamurthy, D. Sampathkumar, R.P.G. Ranganagowda, B. Bennehalli, C. V Srinivasa, Mechanical properties of abaca fiber reinforced polypropylene composites: Effect of chemical treatment by benzene diazonium chloride, J. King Saud Univ. - Eng. Sci. 29 (2017) 289–294. https://doi.org/https://doi.org/10.1016/j.jksues.2015.10.004.

[3] A.N.S. Al-Qadi, S.M. Al-Zaidyeen, Effect of fiber content and specimen shape on the residual strength of polypropylene fiber self-compacting concrete exposed to elevated temperatures, J. King Saud Univ. - Eng. Sci. 26 (2014) 33–39. https://doi.org/https://doi.org/10.1016/j.jksues.2012.12.002.

[4] M.I. Khan, Y.M. Abbas, G. Fares, Review of high and ultrahigh performance cementitious composites incorporating various combinations of fibers and ultrafine, J. King Saud Univ. - Eng. Sci. 29 (2017) 339–347. https://doi.org/https://doi.org/10.1016/j.jksues.2017.03.006.
[5] H. Prayuda, F. Monika, M. Dwi Cahyati, F. Saleh, Self Fiber Compacting Concrete (SFCC) Properties Incorporated With Silica Fume and Fiber, Stavební Obz. - Civ. Eng. J. 29 (2020) 52–60. https://doi.org/10.14311/cej.2020.01.0005.
[6] M. Abdulhadi, M.S. Labbo, Comparative Study on the Effect of Sodium Chloride NaCl Solution as Curing Medium of Basalt, Polypropylene and Steel Fiber Reinforced Concrete on Compressive Strength, 6 (2016) 4750–4756. https://doi.org/10.4010/2016.1180.
[7] M. İpek, Examination of the Usability of Basalt Aggregate in Sifcon, Stavební Obz. - Civ. Eng. J. 27 (2018) 500–512. https://doi.org/10.14311/cej.2018.04.0040.
[8] Y. Zhang, Study on Anti-Cracking Performance Evaluation Method of Steel Fiber Reinforced Ceramsite Concrete (Sfrcc) Based on Partly-Restrained Shrinkage Ring, Stavební Obz. - Civ. Eng. J. 26 (2017) 394–403. https://doi.org/10.14311/cej.2017.04.0033.
[9] B. Bhushan Jindal, P. Jangra, A. Garg, 2020. Effects of ultrafine slag as mineral admixture on the compressive strength, water absorption, and permeability of rice husk ash-based geopolymer concrete, Mater. Today Proc. vol. 32 871–877. doi.org/10.1016/j.matpr.2020.04.219.
[10] J. a. Kropp, Performance criteria for concrete durability, n RILEM Report 12., London: E&FN Spon., 1995.
[11] B.B. Sabir, S. Wild, M. O'Farrell, A water sorptivity test for mortar and concrete, Mater. Struct. 31 (1998) 568. https://doi.org/10.1007/BF02481540.
[12] J. Castro, D. Bentz, J. Weiss, Effect of sample conditioning on the water absorption of concrete, Cem. Concr. Compos. 33 (2011) 805–813. https://doi.org/https://doi.org/10.1016/j.cemconcomp.2011.05.007.
[13] R.J. Gummerson, C. Hall, W.D. Hoff, Water movement in porous building materials—II. Hydraulic suction and sorptivity of brick and other masonry materials, Build. Environ. 15 (1980) 101–108. https://doi.org/https://doi.org/10.1016/0360-1323(80)90015-3.
[14] JGJ52-2006, Chinese National Standards, for technical requirements and test method of sand and crushed stone for ordinary concrete, n.d.
[15] 2011. JGJ55, Chinese National Standards. Specification for mix proportion design of Ordinary concrete, n.d.
[16] A. C1585-04, Standard Test Method for Measurement of Rate of Absorption of Water by Hydraulic-Cement Concretes, ASTM Int. (2004).
[17] Niveditha, M. and Srikanth, K. Effect of Durability properties on Geopolymer concrete – A Review E3S Web of Conference 184, 01092 (2020), ICMED 2020. https://doi.org/10.1051.e3sconf/202018401092

CIVIL ENGINEERING JOURNAL

Article no. 37

THE CIVIL ENGINEERING JOURNAL 2-2021

MECHANICAL PROPERTIES OF STEEL-POLYPROPYLENE HYBRID FIBER REINFORCED CONCRETE IN BUILDING STRUCTURE

Tao Zhang[1] and Deng Pan[2]

1. *Architectural Engineering Department, Henan College of Transportation, Zhengzhou, Henan 450000, China; taodu9527@126.com*
2. *Highway College, Henan College of Transportation, Zhengzhou, Henan 450000, China*

ABSTRACT

This study mainly analyzed the effect of steel fiber (SF) mixed with polypropylene fiber (PF) on the performance optimization of concrete. Firstly, the steel fiber reinforced concrete (SFRC), polypropylene fiber reinforced concrete (PFRC) and steel-polypropylene hybrid fiber reinforced concrete (SP-HFRC) specimens were designed. Then, the slump experiment, compressive strength experiment, and tensile strength experiment were carried out. The results demonstrated that the increase of fibers reduced the slump, and the influence of PF on the slump was the largest, followed by SF and SP; when the content of SF was 1% and the content of PF was 0.1%, the compressive strength and tensile strength of the concrete were 73.16 MPa and 6.33 MPa, which was superior to the concrete mixed with single fiber. In the perspective of the seismic performance, the ultimate load of the SP-HFRC specimen was 6.25% higher than that of the plain concrete (PC) specimen, and its energy consumption was 126% higher than the PC specimen. The experimental results demonstrate that SP-HFRC has a superiority in mechanical property and can be further promoted and applied in building structure.

KEYWORDS

Hybrid fiber reinforced concrete, Steel fiber, Polypropylene fiber, Mechanical property

INTRODUCTION

As a kind of building material, concrete has been widely used in buildings, bridges, roads and tunnels because of advantages such as low price, convenient construction and good durability. But concrete also has some defects, such as low tensile strength, poor ductility and multiple cracks [1]. The existence of cracks will accelerate steel corrosion and affect the mechanical properties of the structure. With the development of society, the performance of ordinary concrete has not been able to meet people's needs. How to improve the performance of concrete has attracted more and more attention of researchers. It has been found that the addition of fibers in concrete is beneficial to reduce the occurrence of cracks and improve the tensile and crack resistance of concrete [2], while the performance optimization effect of two or more fibers is better than that of single fiber. Yang et al. [3] studied hooked steel fibers with various aspect ratios and volume fractions and found that the aspect ratio of the fibers increased from 65 to 80 and the reduction of 0.25% of the volume fraction of the fibers would not affect the optimization effect. Sadiqul Islam et al. [4] studied polypropylene fibers in different proportions (0.10%, 0.15%, 0.2%, 0.25% and 0.3%) and found that the plastic

shrinkage cracks of concrete which was added with fibers decreased by 50-99%, but the permeability coefficient of water and gas increased. Hay et al. [5] studied the role of steel and polyvinyl alcohol (PVA) fibers in concrete and found that 1.65% volume fraction of composite fibers was beneficial to improve the applicability and durability of concrete structures. Song and Yin [6] studied the mixing of 0.5%, 1%, 1.5% steel fibers and 0.1% carbon fibers and found that the addition of fibers could improve the compressive strength and compressive toughness of concrete. In this study, through the design of steel fiber reinforced concrete (SFRC), polypropylene fiber reinforced concrete (PFRC) and steel-polypropylene hybrid fiber reinforced concrete (SP-HFRC) specimens, the performance optimization effect of hybrid fiber was studied. It was found that the best performance optimization effect was obtained when the content of steel fiber (SF) is 1%, and the content of polypropylene fiber (PF) was 0.1%. This study makes some contributions to the further application of SP-HFRC in practical engineering.

CONCRETE MATERIAL WITH HYBRID FIBERS

At present, steel fibers (SF) [7], polypropylene fibers (PF) [8], basalt fibers (BF) [9] and carbon fibers (CF) [10] are fibers which are frequently used in concrete. It is found that the addition of fibers can prevent the expansion of cracks in concrete, improve the tensile and bending resistance, and enhance the corrosion resistance of steel bars [11], which has a good development prospect. Hybrid Fiber Reinforced Concrete (HFRC) refers to the concrete which is added with two or more kinds of fibers in concrete to optimize the performance of concrete in many aspects. At present, the mixing of fibers mainly includes the following forms:

(1) the mixing of main fibers and minor fibers;

(2) the mixing of one fiber in different sizes;

(3) the mixing of different kinds of fibers with similar sizes;

(4) the mixing of fibers with different sizes and types.

It is found that the mixing of metal fibers and non-metal fibers plays an excellent role in optimizing the performance of concrete. Therefore, the performance of SP-HFRC was analyzed in this study.

MATERIALS AND METHODS

Materials

Cement: 42.5R ordinary Portland cement, Dalian Xiaoyetian Cement Plant.

Coarse aggregate: gravel with particle size between 5 mm and 20 mm and 1.3% mud content.

Fine aggregate: river sand with 2.48 fineness modulus.

Water reducer: polycarboxylic acid water reducing agent, Beijing Muhu Admixture Co., Ltd.

Water: ordinary tap water.

SF: Hengshui Guangjun Rubber and Plastic Products Co., Ltd. (Figure 1), and its performance indicators are shown in Table 1.

PF: Wanfeng Building Materials Chemical Co., Ltd. (Figure 2), and its performance indicators is shown in Table 1.

Tab. 1 - Performance indicators of fibers

	SF	PF
Length/mm	35	12
Diameter/mm	0.8	0.035
Density/(g/m^3)	7.8	0.91
Tensile strength/MPa	≥ 800	≥ 350
Elasticity modulus/GPa	210	3.5

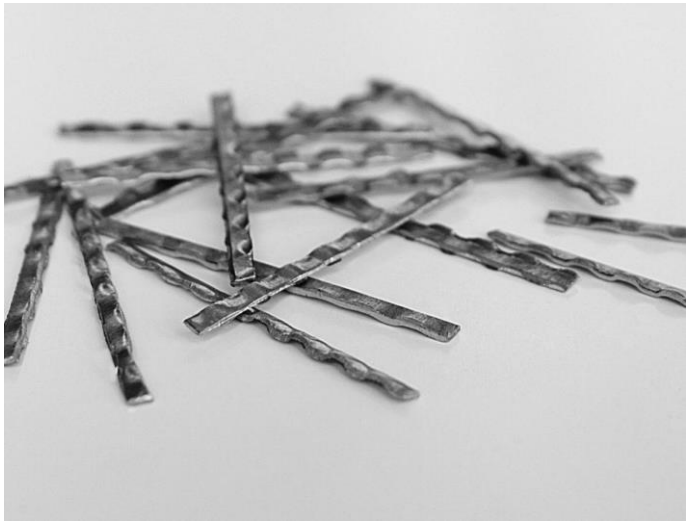

Fig. 1 – Steel fibers

Fig. 2 – Polypropylene fibers

Preparation of specimen

The proportion of cement, coarse aggregate, water and water reducing agent of the concrete was 1:2.2:1.8:0.012. The amount of cement in 1 m^3 concrete was 450 kg/m^3. Fiber content of different specimens is shown in Table 2. PC is plain concrete, SF5 means that the volume of SF in concrete is 0.5%, PF1 means that the volume of PF in concrete is 0.1%, S10P1 means that the content of SF in concrete is 1% and the content of PF is 0.1%, and so on.

Mixing was done by a forced mixer. Firstly, the coarse aggregate was mixed. During mixing, the fibers were evenly added. Sixty seconds later, cement was added, followed by water reducer and water. The test specimen is shown in Figure 3.

Tab. 2 - Experimental groups

Specimen number	SF volume fraction/%	PF volume fraction/%
PC	0	0
SF5	0.5	0
SF10	1	0
SF15	1.5	0
PF1	0	0.1
PF2	0	0.2
PF3	0	0.3
S10P1	1	0.1
S10P2	1	0.2
S10P3	1	0.3

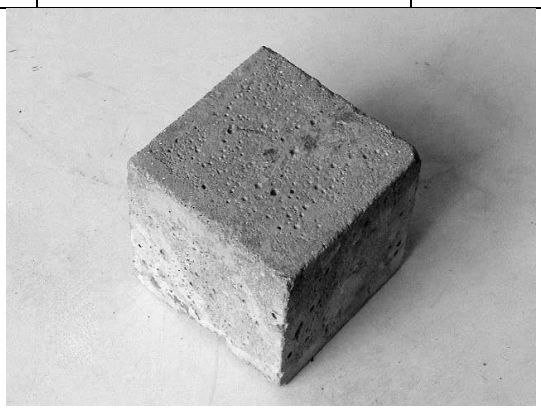

Fig. 3 – The test specimen of concrete

Experimental methods

(1) Slump test: To ensure that the slump cylinder (Figure 4) was horizontally fixed, the concrete was evenly placed into the cylinder in three layers. After clearing the concrete on the bottom plate of the cylinder, the cylinder was lifted vertically and smoothly between 5 and 10 s. The whole experiment process was controlled within 150 s. The height difference between the height of the

cylinder and the highest point of the slump concrete was measured, which was regarded the slump value of the concrete.

Fig. 4 – Slump cylinder

(2) Compression test: A specimen in a size of 150 mm × 150 mm × 150 mm × 150 mm was loaded by JES-2000A pressure tester (Figure 5). The specimen was placed in the middle of the lower pressure plate, and the bearing surface was perpendicular to the top surface to ensure the balanced contact between the upper pressure plate and specimen. The loading speed was between 11.25 kN/s and 18 kN/s. The loading continued until the specimen was destroyed. Compressive strength $f = \frac{F}{A}$, where F stands for the failure load of the specimen and A stands for the bearing area of the specimen.

Fig. 5 – JES-2000A Pressure Testing Machine

(3) Tensile test: A specimen in a size of 150 mm × 150 mm × 150 mm × 150 mm was loaded by WE-600C hydraulic universal testing machine (Figure 6). Firstly, the center line was drawn on the specimen, and then the cushion block, cushion strip and specimen were placed in turn. All the centers were aligned with the center line of the pressure plate of the testing machine, and the loading speed was between 0.05 Mpa/s and 0.08 Mpa/s. The loading continued until the specimen was destroyed. Tensile strength $f = 0.637\frac{F}{A}$, where F stands for the failure load of the specimen and A stands for the split area of the specimen.

Fig. 6 – WE-600C Hydraulic Universal Testing Machine

RESULTS

Slump

The slump values of different specimens are shown in Figure 7.

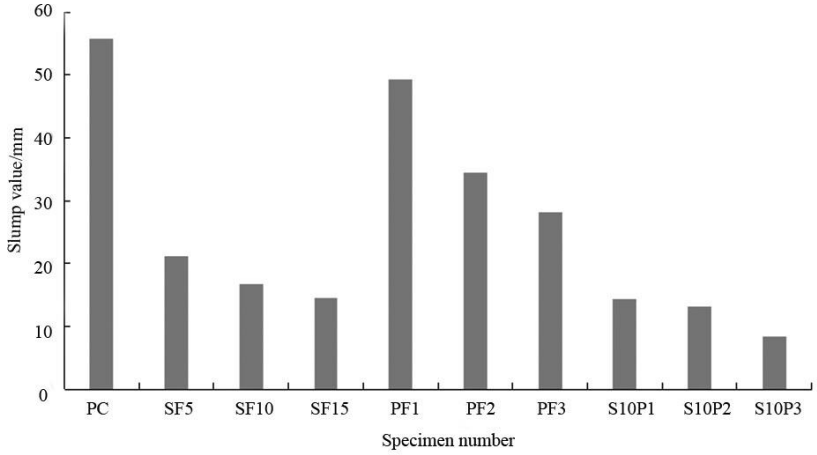

Fig. 7 – Slump values of different specimens

It was found from Figure 7 that the type and content of fibers had a significant impact on slump. The slump value of PC was the highest. In SFRC and PFRC, with the increase of fiber content, the slump decreased gradually; the impact of SF on slump was greater. In HFRC, the increase of fiber content also reduced the slump. High slump indicates that concrete has good fluidity and cohesion. Considering slump, the fiber content in HFRC should be as low as possible.

Compressive strength

The compressive strength of different specimens is shown in Figure 8.

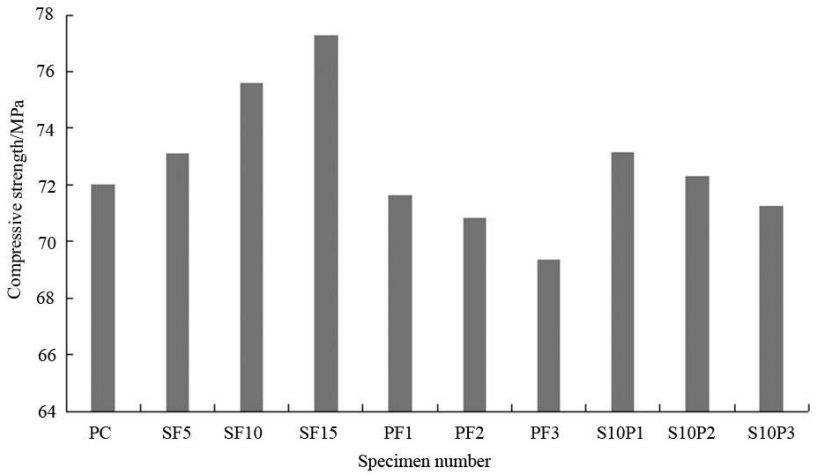

Fig. 8 – Compressive strength of different specimens

It was found from Figure 8 that the compressive strength of SFRC was higher than that PC, while PFRC was slightly lower than PC. When the content of SF content was 1.5%, the compressive strength of concrete reached 77.27 MPa, the highest, 7.3% higher than PC. When the content of PF was 0.3%, the compressive strength of concrete is 69.36%, 3.7% lower than PC. The change of compressive strength of HFRC was between SFRC and PFRC; HFRC had slight improvement compared to PC. When the content of SF was 1% and the content of PF was 0.1%, the compressive strength of concrete reached 73.16 MPa, the highest, 1.6% higher than PC.

Tensile strength

The tensile strength of different specimens is shown in Figure 9.

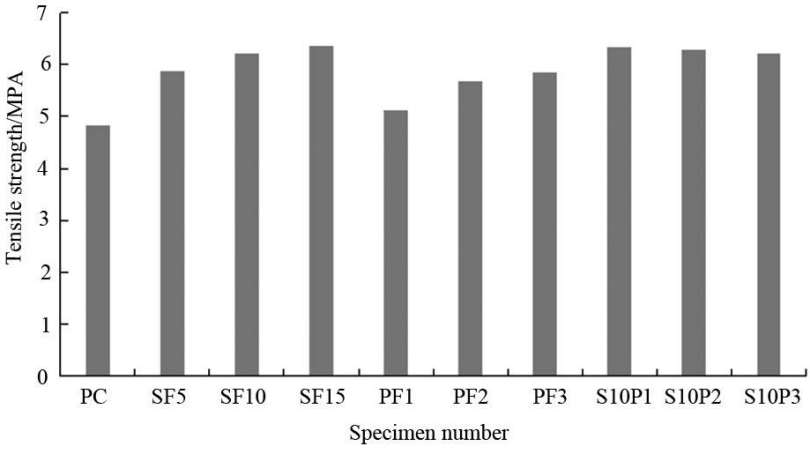

Fig. 9 – Tensile strength of different specimens

It was found from Figure 9 that the addition of SF could significantly enhance the tensile strength of concrete. When the content of SF was 1.5%, the tensile strength of SFRC was 31.68% higher than that of PC. When the content of PF was 0.3%, the tensile strength of PFRC was 20.91%

higher than that of PC. When the content of SF was 1% and the content of PF was 0.1%, the tensile strength of HFRC was higher than that of single-fiber concrete, 1.9% higher than SF10 and 23.6% higher than PF1.

SEISMIC PERFORMANCE

It was found from the comprehensive experimental results that when the content of SF was 1% and the content of PF was 0.1%, the performance optimization effect of the SP-HFRC specimen was obvious. To analyze the seismic performance of the specimen, concrete columns were prepared using PC and concrete containing 1% SF and 0.1% PF. The cross-section size of the column was 250 × 250 mm. The concrete base was 400 × 400 × 900 mm. The longitudinal steel bar was HRB400. The stirrup was HPB300. The parameters of steel bars are shown in Table 3. The reinforcement ratio was 1.62%. The stirrup ratio was 0.62%, and the ratio of axial compression stress to strength was 0.35. The structure of the test specimen is shown in Figure 10.

Tab. 3 - Parameters of steel bars

	HRB400	HPB300
Diameter/mm	14	8
Yield strength/MPa	552.98	330.76
Ultimate strength/MPa	670.29	437.15

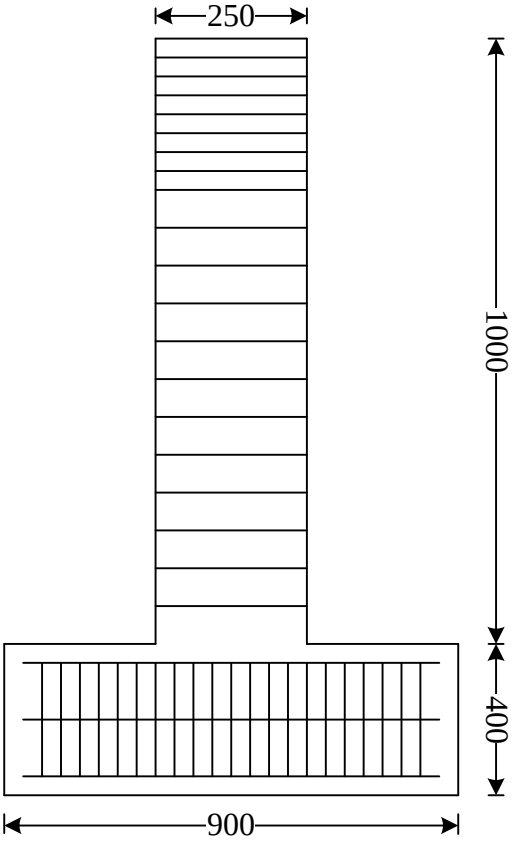

Fig. 10 – The structure of the test specimen

The seismic performance of the test specimen was tested by the pseudo static test. The axial load was loaded using an oil jack. The repeated load was applied at the beam end using a hydraulic servo actuator at a loading rate of 0.4 mm/s, and the loading continued until the load of the beam end significantly reduced. The layout of measuring points is shown in Figure 11 and 12.

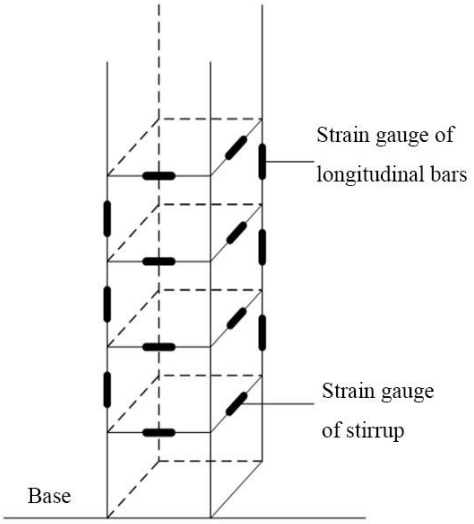

Fig. 11 – The layout of strain gauges

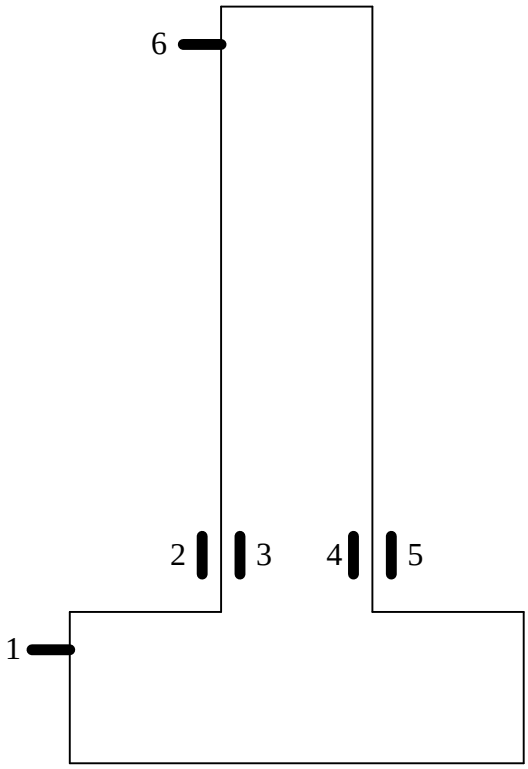

Fig. 12 – The layout of displacement meters

The loading of the two test specimens is shown in Table 4.

Tab. 4 - Comparison of load

	PC	SP-HFRC
Cracking load/kN	19.87	24.78
Yield load/kN	39.68	45.32
Ultimate load/kN	46.76	48.69
Final load/kN	39.87	42.36

It was seen from Table 4 that the loads of the SP-HFRC specimen were significantly larger than those of the PC specimen, indicating that the strength of the SP-HFRC column had more significant improvement than the PC column; the final load of the SP-HFRC specimen was 6.25% larger than that of the PC specimen. It was found that the addition of fibers was beneficial to the seismic performance of the structure.

The energy consumption of the test specimens was compared, and the results are shown in Figure 13.

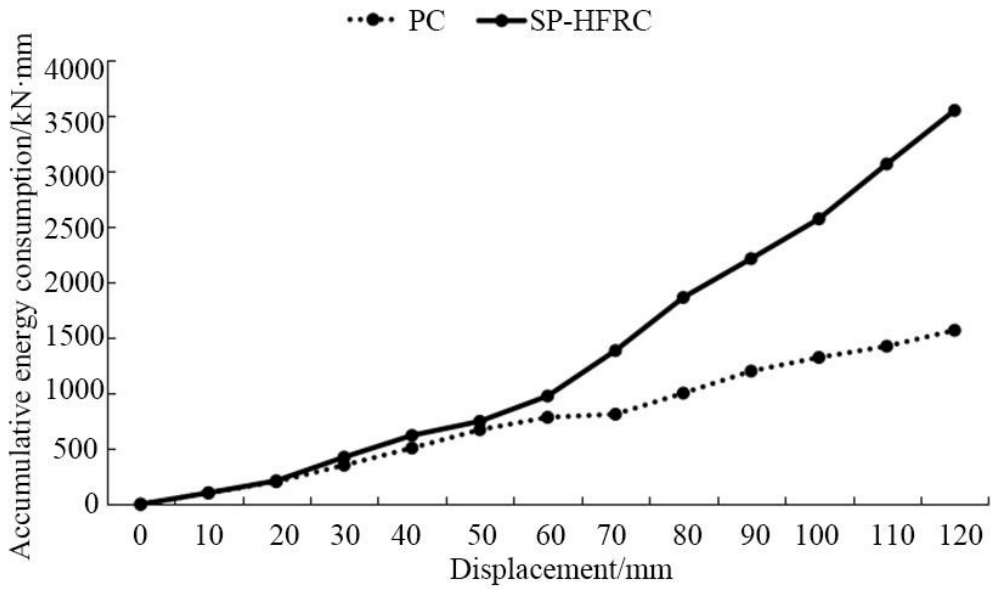

Fig. 13 – Comparison of energy consumption

It was found that the energy consumption of the two test specimens was similar under small displacements, but the difference became larger and the energy consumption of the SP-HFRC specimen was significantly larger with the increase of the displacement. It demonstrated that the addition of fibers significantly improved the energy consumption ability of the structure. Taking 120 mm displacement as an example, the energy consumption of the SP-HFRC specimen was 126% higher than that of the PC specimen.

DISCUSSION

Concrete is one of the most important building materials, and the research on performance optimization of concrete plays an important role in social and economic development. It is found that fibers plays an important role in optimizing the performance of concrete and they can improve the

compressive strength of concrete [12], restrain cracks, delay corrosion [13], and enhance the bonding strength between concrete and steel bars [14]. HFRC composed of two or more mixed fibers can give full play to the advantages of multiple fibers and has high practical application values in building structure.

This study mainly focused on the optimization effect of SF and PF on concrete performance, designed SFRC, PFRC and SP-HFRC specimens, and tested their performance. Firstly, it was found from the slump measurement results (Figure 7) that the addition of fibers reduced the slump, and the higher the content of fibers, the lower the slump. It might be because that the addition of fibers adsorbed more moisture, which reduced the water content in concrete, and moreover SF and PF also increased the viscosity of concrete, resulting in the decline of slump and the decrease of concrete fluidity. The experimental results of compressive strength (Figure 8) demonstrated that the addition of SF increased the compressive strength of specimens, and the addition of PF decreased the compressive strength of specimens. In S P-HFRC, the change of compressive strength was between the specimens with single SF and PF. When the content of SF was 1% and the content of PF was 0.1%, the maximum compressive strength was 73.16 MPa, which was 1.6% higher than that of PC. It was found from Figure 8 that the tensile strength of SFRC was significantly higher than that of PC, and the higher the content of SF, the larger the improvement. When the content of SF was 1.5%, the tensile strength of SP-HFRC was 31.68% higher than that of PC. The tensile strength of SP-HFRC was also higher than that of PC and higher than that of the concrete added with the same content of single fiber. The comparison of the load and energy consumption between the two concrete columns in the analysis of the seismic performance of the test specimens showed that the addition of mixed fibers was effective in enhancing the seismic performance of the building structure. Firstly, fibers could improve the strength of the concrete column. It was seen from Table 4 that the SP-HFRC specimen had high load, indicating that it had high strength. Then, in the perspective of energy consumption, with the increase of the displacement, the accumulative energy consumption of the SP-HFRC specimen was significantly larger than that of PC, showing that the SP-HFRC specimen had better energy consumption ability.

It was concluded from the experimental results that the incorporation of fibers could reduce the collapse degree of concrete, was not conducive to the fluidity of concrete, and had an inconspicuous optimization effect on compressive strength, but it had a good strengthening effect on the tensile strength. When the content of SF was 1% and the content of PF was 0.1%, the concrete had improved compressive and tensile strength and good strength and energy consumption ability.

Although some achievements on research of SP-HFRC have been obtained in this study, there are still many shortcomings, which need to be improved in further work.

(1) This study only considers the content of fiber, but does not consider the influence of fiber length, shape, etc.

(2) The properties of concrete such as high temperature resistance, low temperature resistance, seismic resistance and impermeability need further study.

(3) Study on the blending of more than two kinds of fibers is needed.

(4) The influence of additives such as water reducing agent was not taken into account.

CONCLUSION

In this study, the mechanical property of SP-HFRC in building structure was analyzed through experimental design, and the properties of SFRC, PFRC, and SP-HFRC with different content of fibers were compared. It was found that:

(1) the increase of fibers reduced the slump of the concrete;
(2) the increase of fibers improved the compressive and tensile strength of the concrete;
(3) compared with SFRC and PFRC, SP-HFRC presented better mechanical properties; when the content of SF and PF was 1% and 0.1% respectively, the performance of SP-HFRC was optimal.
(4) compared with the PC column, the SP-HFRC column had better strength and energy consumption ability, i.e., better seismic performance.

REFERENCES

[1] Mazzoli A., Monosi S., Plescia E.S., 2015. Evaluation of the early-age-shrinkage of Fiber Reinforced Concrete (FRC) using image analysis methods. Construction & Building Materials, vol. 101: 596-601.
[2] Köroğlu M.A., Özdöner N., 2016. Behavioural study of steel fiber and polypropylene fibre reinforced concrete. Key Engineering Materials, vol. 708: 59-63.
[3] Yang J.M., Yoo D.Y., Kim Y.C., Yoon Y.S., 2017. Mechanical properties of steam cured high-strength steel fiber-reinforced concrete with high-volume blast furnace slag. International Journal of Concrete Structures and Materials, vol. 11: 391-401.
[4] Sadiqul Islam G.M., Gupta S.D., 2016. Evaluating plastic shrinkage and permeability of polypropylene fiber reinforced concrete. International Journal of Sustainable Built Environment, S2212609015300789.
[5] Hay R., Ostertag C., 2014. Development and application of high performance green hybrid fiber-reinforced concrete (HP-G-HyFRC) for sustainable and energy-efficient buildings. Key Engineering Materials, vol. 629-630: 299-305.
[6] Song W., Yin J., 2016. Hybrid effect evaluation of steel fiber and carbon fiber on the performance of the fiber reinforced concrete. Materials, vol. 9: 704-.
[7] Soufeiani L., Raman S.N., Jumaat M.Z.B., Alengaram U.J., Ghadyani G., Mendis P., 2016. Influences of the volume fraction and shape of steel fibers on fiber-reinforced concrete subjected to dynamic loading - A review. Engineering Structures, vol. 124: 405-417.
[8] Huang L., Xu L., Chi Y., Xu H., 2015. Experimental investigation on the seismic performance of steel-polypropylene hybrid fiber reinforced concrete columns. Construction and Building Materials, vol. 87: 16-27.
[9] Kizilkanat A.B., Kabay N., Akyüncü V., Chowdhury S., Akca A.H., 2015. Mechanical properties and fracture behavior of basalt and glass fiber reinforced concrete: An experimental study. Construction & Building Materials, vol. 100: 218-224.
[10] Dundar C., Erturkmen D., Tokgoz S., 2015. Studies on carbon fiber polymer confined slender plain and steel fiber reinforced concrete columns. Engineering Structures, vol. 102: 31-39.
[11] Blunt J., Jen G., Ostertag C.P., 2015. Enhancing corrosion resistance of reinforced concrete structures with hybrid fiber reinforced concrete. Corrosion Science, vol. 92: 182-191.
[12] Düğenci O., Haktanir T., Altun F., 2015. Experimental research for the effect of high temperature on the mechanical properties of steel fiber-reinforced concrete. Construction and Building Materials, vol. 75: 82-88.
[13] Nguyen W., Duncan J.F., Monteiro P.J.M., Ostertag C.P., 2016. Multi-scale characterization of corrosion initiation of preloaded hybrid fiber-reinforced concrete composites. Key Engineering Materials, vol. 711: 195-202.
[14] Garcia-Taengua E., Martí-Vargas J.R., Serna P., 2016. Bond of reinforcing bars to steel fiber reinforced concrete. Construction and Building Materials, vol. 105: 275-284.

CIVIL ENGINEERING JOURNAL

Article no. 38

THE CIVIL ENGINEERING JOURNAL 2-2021

STRENGTH, DURABILITY AND MICROSTRUCTURE INVESTIGATIONS OF CONCRETE CONTAINING EMPTY PALM OIL FRUIT BUNCH ASH (EPO-FBA)

Christopher Ajiboye Fapohunda[1], Ayotunde Olumide Babatola[1] and Olawale Blessing Oluwasegunota[1]

Federal University, Oye-Ekiti, Faculty of Engineering, Department of Civil Engineering, Nigeria; christopher.fapohunda@fuoye.edu.ng

ABSTRACT

Understanding of the internal arrangement of the constituents of structural concrete, at the microscopic level, and its strength behavior, as well as its ability to result in durable concrete, are necessary in order to enhance its innovative and sustainable application. This paper presents the results of investigation conducted to ascertain the strength characteristics, microstructure configuration and durability traits of concrete with its ordinary Portland cement (OPC) fraction replaced partially with empty palm oil fruit bunch ash (EPO-FBA). The compressive strength properties were assessed with 150 x 150 x 150 cube specimens while 100 x 100 x 100 cube specimens were used to assess the durability properties. An insight into the morphology and the microstructure of samples with EPO-FBA was obtained through Scanning Electron Microscopy (SEM). The results showed that EPO-FBA is a good supplementary cementing material up to 10% replacement level, however, the samples with EPO-FBA showed a significantly improved compressive strengths development and good durability characteristics at latter ages, at the replacement level beyond 10%.

KEYWORDS

Compressive strength, Microstructure**,** Sorptivity, Water absorption

INTRODUCTION

Sustainable design and practices in structural concrete require that: (i) usage of materials be optimized, (ii) unsuitable materials be made fit, (iii) new materials be developed to minimize and conserve the consumption of non-renewable materials used in the production of structural concrete, and (iv) materials be used innovatively. Thus, understanding of the internal arrangement of the constituents of structural concrete, at the microscopic level, and its strength behavior, as well as its ability to result in durable concrete, are necessary in order to enhance its innovative and sustainable application. The relative lack of success in developing microstructure/property relationships for concrete is due to the apparent lack of good microstructural characterization. It is well-known that concrete has a heterogeneous and complex microstructure, which has made it difficult to construct realistic models of its microstructure [1]. Knowledge of its microstructure would have enabled the behavior of the material to be reliably predicted [2]. The heterogeneity of concrete, according to [1], can be considered on several levels, with the simplest level, consisting of aggregate particles, distributed in a matrix of cement paste. On a more detailed level, says [1] the paste itself is a mixture of unreacted cement, hydration products, pores, and water and at a still finer level these phases themselves have complex microstructures. While it is known that the hydration products control the strength and mechanical properties of concrete, the pores (sizes, distribution, continuity/discontinuity), on the other hand governs the durability characteristics of concrete. Thus,

understanding the microstructure and properties of the individual components of concrete and their relationship to one another can serve as a means of re-constructing and re-configuring its properties for innovative application. This is because microstructure of a material determines many of its physical and mechanical properties [3]; in this case, the strength and durability characteristics of structural concrete. This is particularly important for materials sourced from agricultural wastes that are being discovered as potential structural material for enhancement of sustainability in structural concrete in developing countries. For many of these materials, a complete structural response is yet to be captured. For example, there is paucity of literature on the microstructure of concrete with the ordinary Portland cement portion partly replaced with the empty palm oil fruit bunch ash (EPO-FBA). The earlier work by [4] on the possible use of EPO-FBA as partial replacement of ordinary Portland cement (OPC) in concrete covers little area. For example, only the latter ages (60, 75, and 90 days) were considered. According to [5], without 28 days' strength, the results seemed to lack any constructional and structural value. This is because the 28 days' strength is what is used in the design of structural concrete in codes and standards, and many other properties of concrete for construction purposes are linked to the 28-day strength. However, their work yielded a useful insight into the levels of replacement of OPC with EPO-FBA in concrete that will not affect the compressive strength of the concrete. The value was 15% by weight of the OPC. Subsequent work by [6] tried to address this shortcoming. But their work, though with expanded scope, did not however extend to microstructure and durability investigations of concrete with EPO-FBA. Also, the work of (7) dealing with the use of the ashes of oil palm empty fruit bunch was limited to mortar only. In all these investigations, durability and microstructural studies were conspicuously absent. Thus, the aim of this investigation is to assess the compressive strength, microstructure and durability characteristics of concrete with EPO-FBA as partial substitute of its OPC fractions. Specific objectives to be achieved for the concrete samples with EPO-FBA as partial replacement of cement are (i) determination of compressive strength development, (ii) assessment of durability properties through water absorption and sorptivity, and (iii) morphological investigations using scanning electron microscopy (SEM).

MATERIALS AND METHODS

Materials

Investigations in this work were carried out by using the following materials.

The Binder.

Ordinary Portland Cement (OPC), produced to satisfy the requirements of [8, 9], and classified as grade 42.5.was used as the binder for this work.

Fine Aggregates

A sand deposit at Ootunja, a settlement near Ikole Ekiti, Nigeria, served as the source of the fine aggregate used for this work. In order to ensure the fitness of the sand for use in structural concrete as per [10], the sand was dried and sieved through sieve 2.36 mm. All forms of debris and other deleterious materials were also removed.

Coarse Aggregates

An active quarry, located in Ikole town in Ekiti State, Nigeria, serves as the source of the coarse aggregates used for this work. The size of the aggregates ranged from 4.75mm to 20mm as per the recommendation of [11] in relation to aggregate for structural concrete.

Empty Palm Oil Fruit Bunch Ash (EPO-FBA).

The empty palm oil fruit bunch ash (EPO-FBA) used to partially replace the OPC was obtained from empty palm oil fruit bunches, which were collected from palm oil industries in Ikole-Ekiti, Nigeria. Thebunches were sun-dried (Figure 1) and then pulverized.

In order to obtain the ash, the pulverized empty palm oil fruit bunches were burnt through open field burning as described by [12]. The ash samples passing through 45 μm test sieve were collected,

bagged and stored in a cool place.

Water

For the execution of this research work, potable water that satisfied the requirement of [13] was used.

Fig. 1 - Drying of Empty Palm Oil Fruit Bunches

Mix Proportion, Design and Concreting

In order to model Nigerian field situations as much as possible, a mix proportion of 1:2:4 and water/cement ratio were chosen. These values were chosen to align with practice in Nigeria. The cement fraction in the mix was partially replaced with EPO-FBA up to 15% at interval of 5% by weight. Observations by [4] had showed that, beyond 15% replacement values, the strength development was very low. The mix proportion is presented in Table 1.

Tab. 1: The Mix Proportion used for the Investigation

% EPO-FBA in the Mix	Mix Designation	Binder (kg/m^3)		Fine Aggregate (kg/ m^3)	Coarse Aggregate (kg/ m^3)	Water (kg/ m^3)
		Cement	EPO-FBA			
0	M_0	343	0.00	686	1372	172
5	M_5	325.85	17.15	686	1372	172
10	M_{10}	308.70	34.30	686	1372	172
15	M_{15}	291.55	51.45	686	1372	172

Concreting was carried out by measuring out the concrete ingredients by weight, thoroughly mixed and cast into moulds. Two types of moulds were used during the investigation. The 150 x 150 x 150 mm cubes were used for compressive test specimens and 100 x 100 x 100 mm cube moulds were used for durability tests specimens. The cast concrete specimens were then properly compacted by tamping. The specimens were left in the moulds for 24 hours, after which they were de-moulded, and then placed in curing tank for curing process. All the concrete specimens were moist cured in a curing tank, until the day of testing. The testing days were 7, 14, 28, 60 and 90 days for compressive test specimens. The durability test specimens were tested at 28 and 90 days of curing. The 28-day samples were used for microscopic investigations. The specimens without EPO-FBA served as the control. A total of 60 numbers 150 x 150 x 150 mm cube specimens and 48 numbers of 100 x 100 x 100 mm cube specimens were cast.

Experimental procedures

Determination of Physical and Chemical Properties of the Materials

Preliminary investigation was carried out to characterized the materials used by determining some of their properties. Physical properties like: specific gravity, moisture content, water absorption, dry density, bulk density and sieve analysis, were carried out on the aggregates. Chemical and physical tests were also performed on samples of EPO-FBA to determine its oxide composition and some physical properties like fineness (dry-sieving on 45μm) and specific gravity.

The Compressive Strength Test

The compressive strength of concrete specimens containing EPO-FBA were assessed using 150 x 150 x 150 mm cube specimens. This was carried out in accordance to the provisions of [14]. A 2000KN WAW-2000B computerized electrohydraulic servo universal testing machine with accuracy of ± 1% of test force, was used to determine the compressive strength. Three specimens were tested at the testing date, and the average used to evaluate the mean strength.

Water Absorption Test

According to [15], absorption is a measure of the volume of pore space in concrete. A method suggested by [16, 17] is used to assess this property. To conduct this experiment, 100mm x 100mm x 100mm concrete cubes specimens were cast and were moist-cured in a curing tank for 28 and 90 days. At each of the testing day, the cube specimens were taken out of the curing tank and oven-dried at temperature of 105^0 C until a constant weight was reached. The specimens were then sealed, and then allowed to cool in a container for three days. Silicone sealant was then used to coat the sides of the concrete samples so that flow is constrained to flow in one direction. Then the samples were positioned in a vertical position and partially immersed in water to a depth of 5 mm at one end. The rest of the portions were kept exposed to the laboratory air as shown in Figure 2 as adapted from [16].

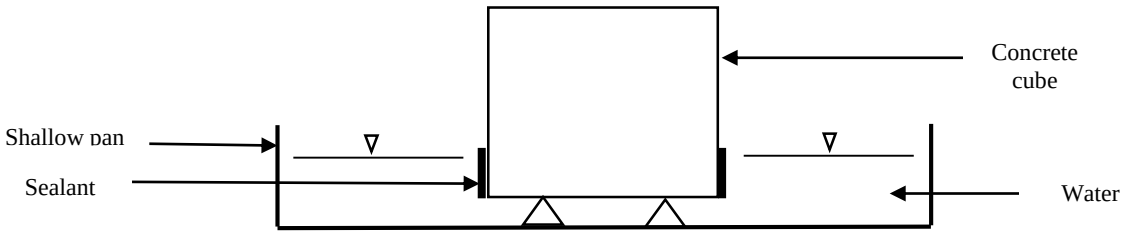

Fig - 2. Set up for the measurement of Coefficient of water absorption and Sorptivity of Concrete specimens (adaptation from [16]).

During the first 60 minutes, the quantity of water absorbed was calculated. This is done by measuring the increase in mass (gained over a period of 60 minutes) as a percentage of dry mass. Then, the coefficient of water absorption of concrete specimens containing EPO-FBA, after 28 and 90 days of moisture curing were determined using the formula used by [16].

$$K_a = (\frac{Q}{A})^2 \times \frac{1}{t} \quad (1)$$

where K_a is the coefficient of water absorption (m^2/s), Q is the quantity of water absorbed (m^3) by the oven dry specimen in time (t), t is 3600 seconds and A is the surface area (m^2) of concrete specimen through which water penetrates.

Sorptivity Test

According to [15], sorptivity measures the rate of absorption of water by capillary suction of unsaturated concrete placed in contact with water, where no head of water exists, thus determining the rate of capillary-rise absorption by concrete specimens. This is a reflection of the capillary forces exerted by the pore structure causing fluids to be drawn into the body of the material [16, 18]. A

method suggested by [21] was used to assess the sorptivity of concrete specimens with EPO-FBA as partial replacement of ordinary Portland cement. The test is similar to that of absorption test described above, but with little difference. The difference is that after the initial mass measurement of the cube samples was taken, subsequent mass measurement was taken at 4, 8, 10, 20, 30, 60, 90 and 120 minutes, and the gain in mass per unit area over the density of water was obtained. The gain in mass was then plotted against the square root of the elapsed time. The slope of the line of best fit of these points was taken as the sorptivity value. The formula (equation 2) suggested by [18] was then used to calculate the sorptivity of the specimens.

$$i = \frac{S}{\sqrt{t}} \quad (2)$$

Where *i* = the cumulative water absorption per unit area of the surface (m^3/m^2); S is the sorptivity ($mm/min^{0.5}$) and t is the elapsed time (s). The sorptivity of the concrete cube specimens containing EPO-FBA as partial replacement of ordinary Portland cement were determined after 28 and 90 days of water curing. The setup for the measurement of sorptivity values of the concrete cubes is shown in Figure 2 [16].

Microstructural and Morphology Investigation

Scanning electron microscopy (SEM) equipment (ASPEX 3020) with energy dispersive spectrometry capabilities was used for microstructural investigations. SEM investigations were carried out on broken sample of 28 days concrete specimens containing EPO–FBA as partial replacement of ordinary Portland cement, in order to examine their morphological structures.

RESULTS

Physical and Chemical Properties of Materials

The results of some physical properties of aggregates and that of the chemical properties of EPO-FBA are respectively presented in Tables 2 and 3.

Tab. 2: Some Physical Properties of Aggregates Used

Properties	Coarse Aggregates	Sand
Bulk Density (kg/m^3)	1779.02	1387.79
Dry Density (kg/m^3)	1702.89	1501.60
Specific Gravity	2.64	2.60
Moisture Content (%)	3.87	6.07
Water Absorption Capacity (%)	3.75	3.59
Coefficient of Curvature (C_c)	1.72	1.14
Coefficient of Uniformity (C_u)	4.75	6.70
Fineness Modulus	-	2.62

With coefficient of curvature or gradation ($C_c = \frac{D_{30}\, x\, D_{30}}{D_{60}D_{10}}$) and the coefficient of uniformity ($C_u = \frac{D_{60}}{D_{10}}$) calculated from the results of mechanical analysis for coarse aggregates to be 1.72 and 4.75, and for the sand to be 1.14 and 6.70, as can be seen from Table 2, suggested well graded aggregate that will guaranty adequate compaction [20]. Also, the fineness modulus obtained for the sand is 2.62. This value satisfies [21] specifications for fine aggregates of between 2.3 and 3.1 for use for structural concrete. Though the combined total of SiO_2+Al_2O_3+Fe_2O_3 in EPO-FBA (Table 3) is not up to the value that could allow classification into the categories of fly ash as per [21]. From Table 3, it can be seen that EPO-FBA has a higher loss on ignition (LOI) than that of cement and also greater than the limits of 5.0% set by [9]. The loss on ignition, a measure of the extent of carbonation and hydration of free lime and free magnesia is due to atmospheric exposure [15]. The higher value, according to [13], is actually advantageous as hydrated free lime is innocuous. The overall chemical composition of EPO-FBA as presented in Table 3, resembles bauxite (found in Ghana) and natural cement (found in UK) in the work of [24] which were found to have cementitious properties.

Tab. 3: Chemical and Physical Properties of Empty Palm Oil Fruit Bunch Ash (EPO-FBA)

Oxide	EPO-FBA	OPC
CaO (%)	19.01	64.37
SiO_2 (%)	6.42	20.68
Fe_2O_3 (%)	6.64	3.62
MgO (%)	4.10	1.81
Al_2O_3 (%)	12.70	5.41
SO_3 (%)	1.42	1.03
Na_2O (%)	7.25	0.51
K_2O (%)	1.86	0.47
LOI (%)	40.60	0.39
Specific Gravity	2.55	3.12

But the high alkali (K_2O and Na_2O) value (9.11%) raises concerns about possible alkali-aggregate reaction if used in concrete without mitigating measures.

Compressive Strength

The compressive strength development of concrete samples containing EPO-FBA as partial replacement of cement is shown in Figure 3.

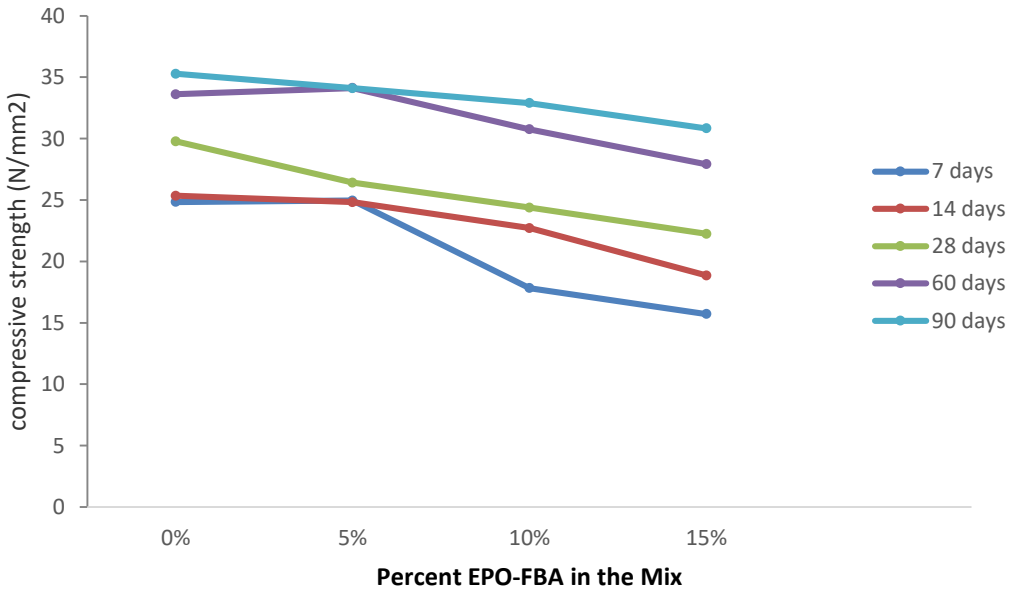

Fig. 3 - Compressive Strength Development of Concrete Samples with EPO-FBA

It can be observed that compressive strengths increased with increasing curing ages at all replacement values. This is a well-established trend. Continuous hydration produces the strength-formation C-S-H gel, and the more its quantity, the greater the strength that will be developed. However, the compressive strength of the samples decreased with increase in the content of EPO-FBA in the mix. This can be observed in Table 4 through the perfomance criterion of strength activation index (SAI). However, this decrease, in relation to the control samples, was at a decreasing rate with curing ages. For example, in the concrete samples designated as M_{15}, the decreased were 68.69, 74.39, 74.68, 81.85, and 87.42% respectively at 7, 14, 28, 60 and 90 days of curing. This pattern was the same for concrete samples in other replacement values. According to [23], the strength activation index (SAI) can be used to assess the pozolanicity of any material. A compressive strength of the blended concrete sample at 7-day or/and 28-day that is higher than 75% of the compressive strength of the control specimens suggests a material with pozzolanic

characteristics. It can be observed from Table 4 that the specimens with 10% EPO-FBA developed compressive strength that are higher than 75% of the control at both 7 and 28 days of curing. At higher curing ages of 60 and 90 days however, it can be observed that the SAI increased significantly to over 90% of the control.

Tab. 4: Compressive Strength Development of Concrete Samples with EPO-FBA

Mix Designation	Compressive Strength, CS (N/mm^2) and Strength Activation Index, SAI									
	Curing Age (days)									
	7		14		28		60		90	
	CS	SAI (%)	CS	SAI (%)	CS	SAI (%)	CS	SAI (%)	CS	SAI
M_0	24.84	100.00	25.34	100.00	29.78	100.00	33.61	100.00	35.28	100.00
M_5	24.96	100.48	24.82	97.95	26.42	88.72	34.12	101.52	34.11	96.68
M_{10}	19.82	79.79	22.71	89.62	24.38	81.87	30.75	91.49	32.90	93.25
M_{15}	15.82	63.69	18.85	74.39	22.24	74.68	27.51	81.85	30.84	87.42

It is thus obvious that on the basis of the data presented in Table 4, that concrete samples with up to 10% EPO-FBA content meet the performance index criterion for pozzolanicity.

Durability

The durability properties of concrete samples containing EPO-FBA were assessed through water absorption and sorptivity tests; and the results are presented in Figures 4. Though both measured different things - water absorption measuring volume of pore space in the concrete and sorptivity measuring the rate of capillary-rise absorption - they were in agreement in relation to the durability properties of concrete specimens containing EPO-FBA. From figure 4(a), it can be observed that the water absorption of concrete specimens containing EPO-FBA was lower at 90 days than at 28 days. This is suggestive of reduction in the volume of pore space in the concrete specimens at longer curing ages. Sorptivity reflects the capillary porosity on which the permeability of hardened cement paste is dependent [15]. Permeability on the other hand, is a reflection of the interconnectivity of pores in the paste. From Figure 4(b), it can be observed that the 90 days sorptivity of samples were lower than that of 28 days samples. This means 90 days samples are less porous or less permeable than 28 days samples.

The results of durability characteristics of specimens with EPO-FBA presented in Figure 4, can be explained in relation to the pore structure of the hydrated paste phase. With the progress of hydration, the hydration products (the C-S-H gel) fill the originally water-filled void [15]. This not only reduces the volume of pore space in the samples, but also results in discontinuity of pores. This results in reduced permeability with time, observed for 90 days specimens, as more hydration products continue to fill the available pores. The results of the durability test also agree with the pattern of strength development of concrete samples with EPO-FBA, in which strength development improved with curing age, as discussed in section 3.2.

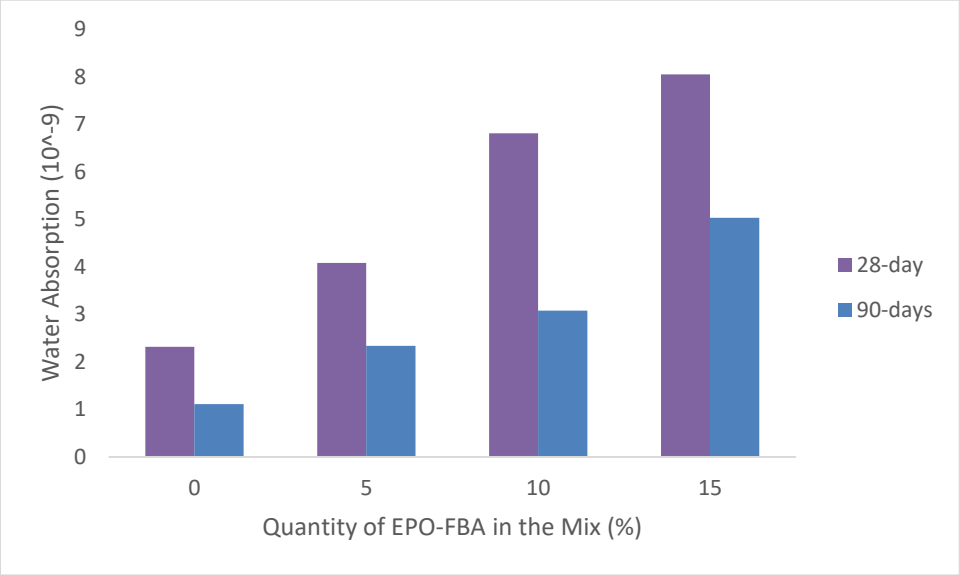

a) Water Absorption of Concrete Samples with EPO-FBA

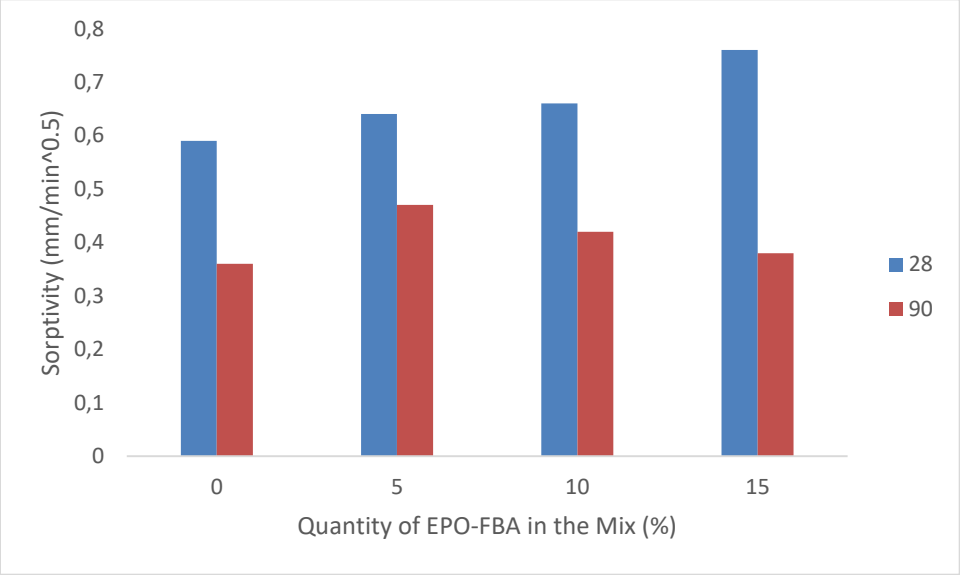

b) Sorptivity of Concrete Samples with EPO-FBA

Fig. - 4 Durability Properties of Concrete Samples with EPO-FBA

According to [15], there is a relationship between the relative volume of hydrated products gel in the space available to it (permeability) and strength. As hydration continues unhindered, hydration products are formed with the double effect of increased strength and reduced permeability in the concrete samples, as witnessed in this work.

Microstructure

The SEM micrographs of concrete samples with EPO-FBA at replacement levels of 0%, 5%, 10% and 15% cured for 28 days are shown in Figures 5 and 6, for a glimpse into the structure of the hydrated paste samples. In relation to the control, the microstructure appears to be progressively less dense or of increased porosity due to reduced formation of C-S-H gel.

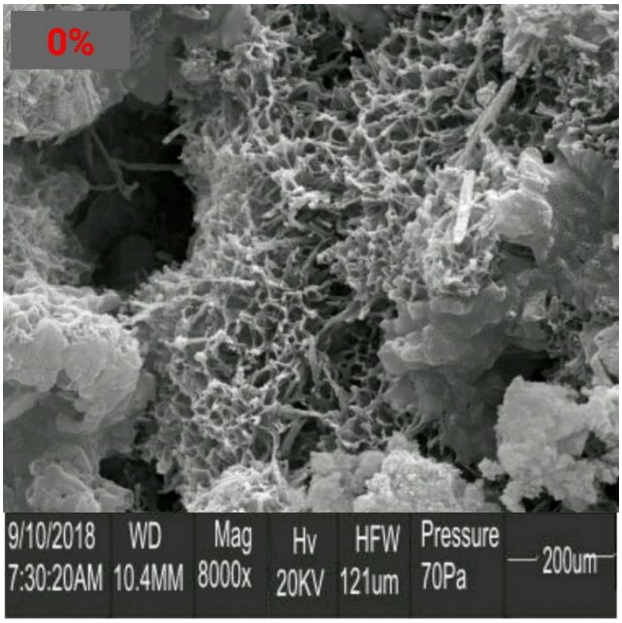

Fig. 5 - SEM Images for Concrete samples with EPO-FBA (Control)

It appears that higher EPO-FBA replacement percentage has relatively lighter structure. The SEM images of the control samples show a well-developed aggregate–cement paste interface and the hydration product C-S-H (Calcium Silicate Hydrate) can be seen as honeycombs structure with some surrounding few pores but no crack. On the other hand, the 5% replacement level with EPO-FBA shared similar characteristics with that of the control sample. The strength forming product of hydration C-S-H can be seen surrounding the whole aggregate structure with many pores compared to that of 0% replacement. The SEM micrograph for 10% and 15% of EPO-FBA show pores that are large and the structure becomes relatively porous, thus less densely-packed. This can be connected to the fact that there is reduction in the quantity of strength forming hydration product C-S-H as the quantity of EPO-FBA increases. The EDX spectrum of the concrete samples are shown in figure 7.

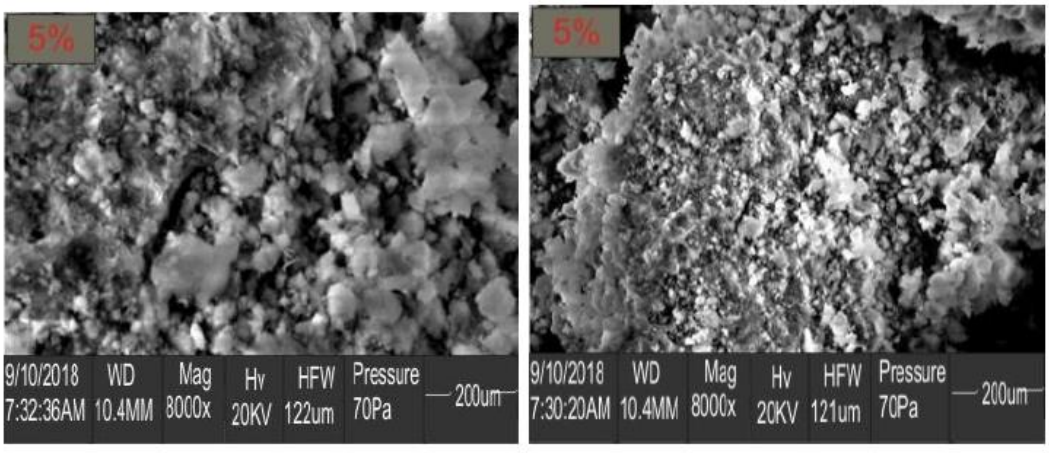

Fig. 6 - SEM Images for Concrete Samples with EPO-FBA (5, 10, & 15%)

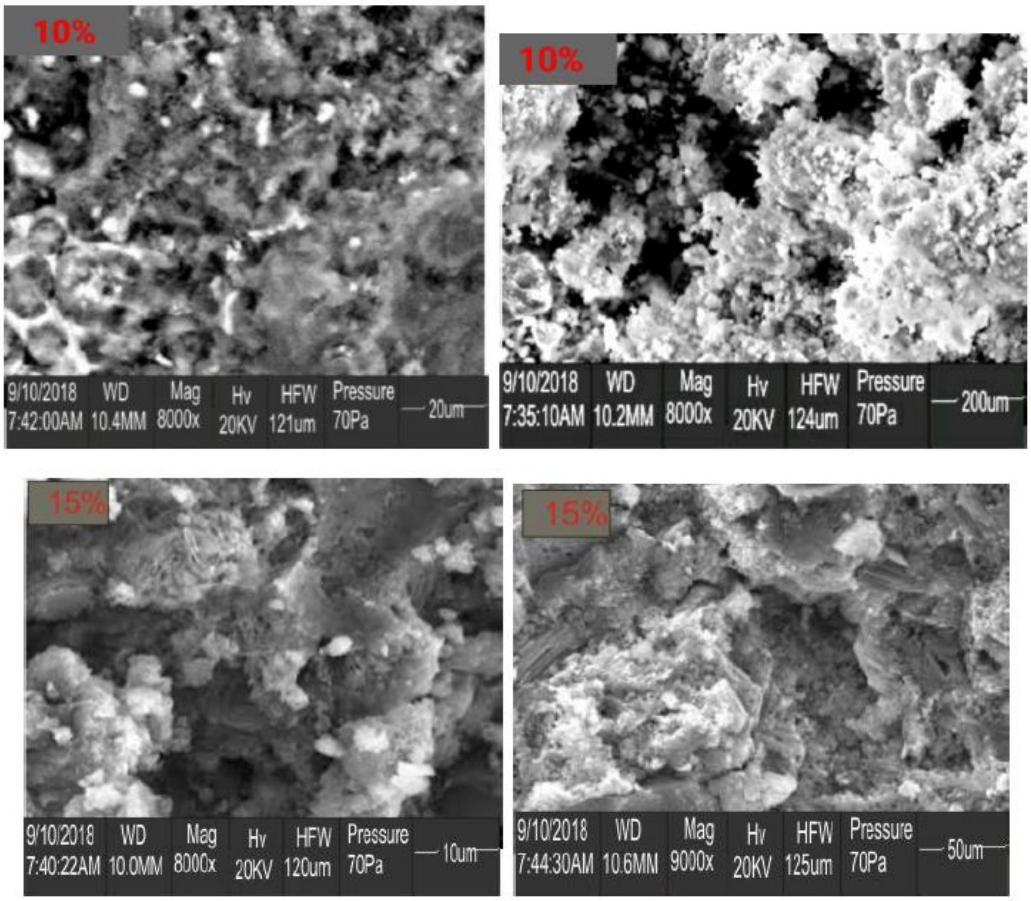

Fig. 6 - SEM Images for Concrete Samples with EPO-FBA (5, 10, & 15%)

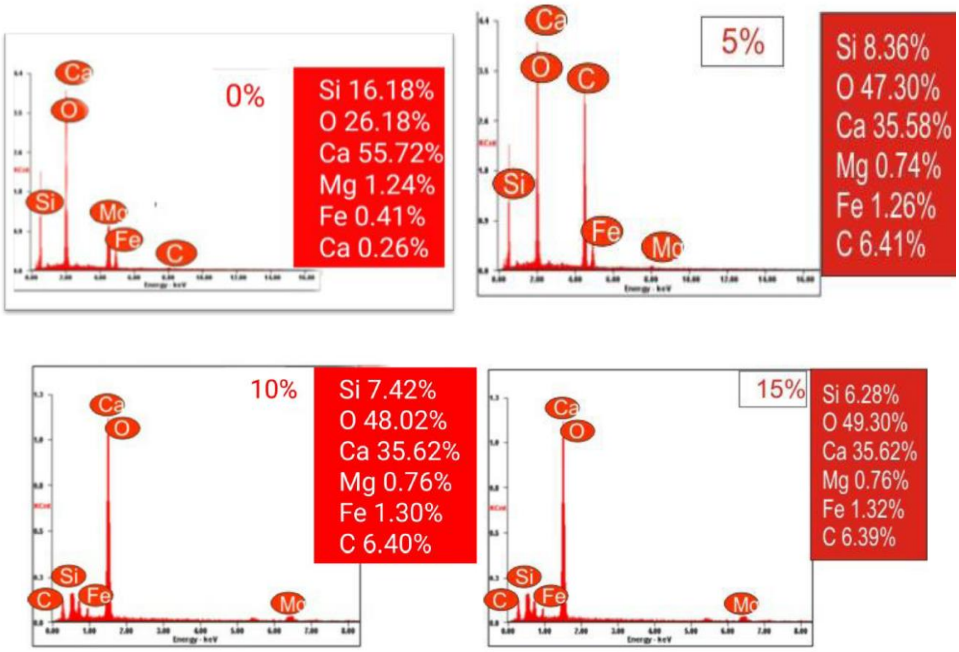

Fig 7 - The EDX Spectrum of Samples with EPO-FBA (0, 5, 10 & 15%)

It can be seen that the count of Silicon and Calcium which are the main element responsible for the strength forming and bonding of concrete structure declines with increasing EPO-FBA (Table 5).

Tab. 5 - The C/S Ratio of Mixes with EPO-FBA

Mix Designation	Ca (C)	Si (S)	$\frac{C}{S}$
M_0	55.72	16.18	3.44
M_5	35.58	8.36	4.26
M_{10}	35.62	7.42	4.80
M_{15}	35.62	6.28	5.67

This contributes to the reason why there is decrease in the compressive strength of concrete with increasing EPO-FBA. The ratio of silicon and carbon however increased with increase in the quantity of EPO-FBA in the mix. According to [26], increasing ratio means increasing pozzolanic activities. But this would not be felt until later ages, as can be seen from the result of the compressive strength and sorptivity. This is characteristic of SCM, with well-known latent pozzolanic properties.

CONCLUSIONS AND RECOMMENDATION

From the analysis of the results of this investigation, the following conclusions can be made:

1. Partly replacing the cement fraction of concrete mix with empty palm oil fruit bunch ash (EPO-FBA) led to reduction in compressive strength. However, replacement at 10% of the cement by weight will develop strength comparable to the control.
2. The compressive strengths of concrete samples with EPO-FBA continued to improve with curing ages at all the replacement level considered in this investigation.
3. Concrete specimens with EPO-FBA developed improved durability characteristics with age.
4. The microstructure of 28-day concrete specimens with EPO-FBA showed porous microstructure, but with latent pozzolanic activities.

It is obvious from the analysis of the results of this investigation that a relationship exists between the compressive strength, durability properties and morphological structures of the concrete samples containing EPO-FBA as partial replacement of cement. Although this investigation can be considered as preliminary, that the concrete samples have heterogeneous microstructure, with the pores (sizes and distribution) playing a significant role in the quality of the concrete samples, is not in doubt. For innovative application of EPO-FBA in structural concrete, more research works aimed at finding ways to reduce the pores, not only at latter ages, but at earlier ages, is necessary. Research works in this area are thus recommended.

ACKNOWLDGEMENT

Sincere appreciations to Ms. Blessing Adigo for reading through this manuscript.

REFERENCES

[1] Scrivener K. R., 2018. The Microstructure of Concrete. Materials Science of Concrete, 18 pp. Retrieved from www.comisiru.uct.ac.za/../The_Microstructure_of_Concrete.pdf .

[2] Mehta P. K., Monteiro P. J. M., 2014. Concrete: Microstructure Properties and Materials. McGraw Hill Education, New York, USA, 239 pp.

[3] Boccaccini A. R. 2005. Ceramics. Biomaterials, Artificial Organs and Tissue Engineering. Woodhead Publishing Series in Biomaterials. Retrieved from https//doi.org/10.1533/9781845690861.1.26.

[4] Fapohunda C. A., Shittu A. O., 2017. Some Later Ages Structural Characteristics of Concrete Containing Empty Palm Oil Fruit Bunch Ash (EPO-FBA) as Partial Replacement of Ordinary Portland Cement. FUOYE Journal of Engineering and Technology, vol. *2, nos.* 1: 42–46.

[5] Bamforth P., Chisholm D., Gibbs J., Harrison T. 2008. Properties of Concrete for use in Eurocode 2 – How to optimise the engineering properties of concrete in design to Eurocode 2. *A Cement and Concrete Industry Publication.* Retrieved from www.concretecentre.com.

[6] Fapohunda, C. A. and Oluwasegunota, O. B. (2019). Evaluation of Structural Performance of Concrete With OPC Fraction Partly Replaced By Empty Palm Oil Bunch Ash (Epo-Fba). FUW Trends in Science & Technology Journal, vol. 4, Nos. 1: 202 – 208

[7] Coelho, V. A., Guimaraes, C. C., Doutto, G. G. And Pedra, P. M. (2019). Evaluation Of Mortar Properties Obtained Through Partial Substitution Of Portland Cement By Ashes Of Oil Palm Empty Fruit Bunch. Cerâmica vol. 65, 375. https://doi.org/10.1590/0366-69132019653752575

[8] NIS 444-1, 2014. *Cement* – Part I: Composition and Conformity Criteria for Common Cements. Standard Organization of Nigeria, Abuja, Nigeria.

[9] BS EN 197-1, 2000. Cement, Composition, Specification and Conformity Criteria for Common Cements. British Standard Institution, London, U.K.

[10] BS EN 12620:2002, 2008**.** Specification for Aggregates from Natural Sources for Concrete. British Standard Institution, London, U.K.

[11] BS 8110, 1997. Structural Use of Concrete – Code of Practice for Design and Construction. British Standard Institution, London, U.K.

[12] Oyekan G. L., Kamiyo, O. M., 2011. A study on the engineering Properties of Sandcrete Blocks produced with Rice Husk Ash Blended Cement. Journal of Engineering and Technology Research, vol. 3, nos. 3: 88-98.

[13] ASTM C 1602, 2012. Standard Specification for Mixing Water Used in the production of Hydraulic Cement Concrete. ASTM International, Philadelphia, USA.

[14] BS EN 12390-3, 2009. Testing Hardened Concrete: Compressive Strength of Test Specimens. British Standard Institution, London, U.K.

[15] Neville A. M., 2011. Properties of Concrete. Pearson Educational Publishers, London, U. K. 779 pp.

[16] Ganesan K., Rajagopal K., Thangavel K., 2008. Rice husk ash blended cement: assessment of optimal level of replacement for strength and permeability properties of concrete. Construction and Building Materials, vol. 22, nos. 8:1675–1683.

[17] Giannotti-da-Silva F., Liborio J. B. L., Helene P. 2008. Improvement of physical and chemical properties of concrete with Brazilian silica rice husk (SRH). Revista Ingeniería de Construcción, vol. 23, nos. 1:18-25.

[18] Hall C., 1989. Water sorptivity of mortars and concretes: A review. Magazine of Concrete Research, vol. 41, nos. 14: 51–61.

[19] ASTM C 1585, 2004. Standard Test Method for Measurement of Rate of Absorption of Water by Hydraulic Cement Concrete. ASTM International, Philadelphia, USA.

[20] Stanish K. D., Hooton R. D., Thomas M. D. A., 1997. Testing the chloride penetration resistance of concrete: a literature review, FHWA contract DTFH61. Department of Civil Engineering, University of Toronto, Toronto.

[21] Terzaghi K., Peck R. B., Mesri G., 1996. Soil Mechanics in Engineering Practice. John Wiley, New York, USA. 549 pp.

[22] ASTM C 33 (1997). *Concrete and Aggregates - ASTM Standards, Concrete and Aggregates*. ASTM International, Philadelphia, USA.

[23] ASTM C 618 (2005) *Standard Specification for Coal Fly Ash and Raw or Calcined Natural Pozzolan for Use in Concrete.* ASTM International, Philadelphia, USA.

[24] Day R. L., 1990. Pozzolans for Use in Low-Cost Housing – A State of the Art Report for the International Development Research Centre, Ottawa. Department of Civil Engineering, University of Calgary, Canada.

[25] Malhotra V. M., Mehta P. K., 1996. Pozzolanic and Cementitious Materials - Advances in Concrete Technology. Volume 1. Edited by V.M. Malhotra. Gordon and Breach Publishers, Ottawa, Canada.

[26] Nazari A., Rafieipour M. H., Riahi S., 2011. The Effects of CuO Nanoparticles on Properties of Self Compacting Concrete with GGBFS as Binde*r*. Materials Research, vol. 14, nos. 3: 307–316.

CIVIL ENGINEERING JOURNAL

Article no. 39

THE CIVIL ENGINEERING JOURNAL 2-2021

STUDY ON ARRANGEMENT OF COOLING WATER PIPE TO CONTROL HYDRATION HEAT OF CONCRETE IN BEAM OF CABLE-STAYED BRIDGE

Long Liu, Saisai Yu, Wentao Xu and Zhilong Wang

Anyang Institute of Technology, the west end of Huanghe Avenue, Anyang 455000, China; 20160913@ayit.edu.cn

ABSTRACT

The box girder joint section of the Yangtze River Highway Bridge is taken as the research background, and the finite element software MIDAS/FEA is used to simulate the hydration heat of concrete to the layout of cooling water pipe in building mass concrete. The correlation between the finite element calculation results and the measured data is more than 0.976, which is in good agreement. On this basis, the influence of changing the diameter and distance of the cooling water pipe, the inlet temperature and the flow rate on the temperature of hydration heat is studied. The results show diameter of the cooling water pipe and inlet temperature have a significant effect on the temperature of hydration heat. The change of water flow rate has little effect on the temperature of hydration heat. It provides a reference for the layout of the same concrete cooling water pipe arrangement.

KEYWORDS

Cooling water pipe, Water temperature, Hydration heat, Test, Simulation analysis

INTRODUCTION

Concrete is a building material mainly composed of cement and aggregate. In the pouring of mass concrete, the internal temperature is much higher than the external temperature, and improper treatment after pouring will produce cracks in the later curing and affect the performance [1-3]. The commonly used measure to reduce the temperature difference between inside and outside the project is to arrange cooling water pipes. Academician Zhu Bofang [4] studied the simplified calculation of polyethylene water pipes in dam cooling. Ding Baoying [5] studied the relationship between concrete and water pipe temperature difference by combining finite element and break mechanics theory. Liu Yaodong [6] studied the influence of different cooling water temperature, flow rate and water pipe spacing on the cooling and crack prevention of the cap, taking the concrete construction of the Yellow River highway and railway bridge in Zhengzhou as the background. Guo Sanyuan [7] determined the appropriate parameters such as the distance, flow rate and cooling water pipes for the bridge through finite element analysis of hydration heat of concrete in the cap of a continuous rigid frame bridge. Taking Chongqing Zhaiziping Bridge as the engineering background, Tang Yang [8] studied the influence of cooling water pipe arrangement, water inlet and temperature on the hydration heat of the cap.

Because of the large volume and serious hydration heat of dam, raft foundation, bridge pier, cap and other parts, more scholars have studied these structures. Liu Guangyan [9] put forward the late heat release model of fly ash with double E curve, which provides guidance for the late pouring of the dam, through monitoring the Shimao Project (under construction). Chen Zhijun [10] used ANSYS software to simulate the temperature effect of hydration heat in the construction of 178m tall blocks and gained the hydration heat effect different from the ordinary mass concrete, which

provided reference for designers and builders. Zhang Yongjian [11] used the finite element software MIDAS/CIVIL to simulate the temperature and stress of three auxiliary hole caps of Dongting Lake Bridge with different cement types. The measured results were in well agreement with the calculated results, and the temperature appreciation and average temperature rise rate during the hydration of low-heat cement were significantly reduced. Wang Jianqun [12] settled a rigid frame beam part model by using finite element software, studied the law of temperature field and stress field of hydration heat of concrete in beam part, and determined the reasonable demolish time of concrete.

Therefore, this paper takes the concrete pouring construction recording of a Yangtze River highway bridge as the background and uses the finite element software MIDAS/FEA to settle a three-dimensional simulation model to analyze the temperature field variation of concrete hydration heat. Through studying the influence of changing the cooling water pipe and the related parameters of cooling water on the hydration heat, the most suitable diameter and distance of cooling water pipe during concrete pouring and the factors that have great influence on the hydration heat are gained. The correctness of the model is verified by comparing with the measured data, which provides a reference for the ideal layout of cooling water pipes in the control of hydration heat of the same concrete.

BASIC PRINCIPLE

(1) Transient heat conduction equation

The essence of calculation of temperature field inside concrete is the solution of heat conduction equation under specific boundary conditions and initial conditions. The three-dimensional transient heat conduction equation is shown in formula (1) and formula (2) [13-14]:

$$\frac{\partial T}{\partial \tau}=\alpha\left(\frac{\partial^2 T}{\partial x^2}+\frac{\partial^2 T}{\partial y^2}+\frac{\partial^2 T}{\partial t^2}\right)+\frac{\partial \theta}{\partial t} \quad (1)$$

$$\alpha=\frac{\lambda}{c\rho} \quad (2)$$

Where,α is the thermal conductivity (m^2 /h), λ is the thermal conductivity (W/(m·K)), c is the specific heat capacity of the material (J/(kg·°C)), ρ is the material density (kg·m^3), θ is the adiabatic temperature rise of concrete (°C), T is the time (h).

(2) Initial conditions and boundary conditions

The heat conduction equation shows the relationship between temperature of an object and time, space, but there are many kinds of situations satisfying the solution of the equation. To determine the unique temperature field, the initial conditions and boundary conditions must be determined.

The initial conditions can be divided into two categories: first, the temperature field is a known function of coordinates; second, the initial temperature distribution is constant. The research content of this paper belongs to the second initial conditions, as shown in formula 3:

$$T(x,y,z,0)=T_0(x,y,z)=const \quad (3)$$

The boundary conditions can be divided into three categories: first, the boundary temperature of the object is a known temperature; second, the surface heat rate is a known of time; third, when the surface of an object is in contact with air, the rate of heat on the surface of the object is proportional to the temperature. The content of this paper belongs to the third boundary conditions, as shown in formula 4:

$$-\lambda\frac{\partial T}{\partial n}=\beta(T-T_a) \quad (4)$$

Where, β is the surface heat release coefficient (kJ/(m^2·h·°C)), and T_a is the ambient temperature (°C).

(3) Heat source function

Heat source function is to simulate the process of adiabatic temperature rise in the process of concrete hydration, and its common expressions include exponent, hyperbolic, and so on. The exponential formula is used in this paper, as shown in formula 5:

$$\theta(t) = \theta_0\left(1 - e^{mt}\right) \quad (5)$$

Where, θ_0 is the maximum value of concrete adiabatic temperature rise (°C), m is a constant which is related to cement varieties, casting temperature, and so on.

BACKGROUND

The main bridge of a Yangtze River Highway Bridge adopts the form of mixed beam, the span composition is (70+75+84+818+233.5+124.5) m. The layout of the bridge facade is shown in Figure1. In this paper, the concrete in the joint section of the mixed beam is taken as the research object. The width of the box girder at this position is 38.90m, the height of the girder at the center is 3.60m, and the height of the side and side girders is (1.981+1.25) m. The height of the access hole is 1.60m, the radius of the chamfered arc is R=0.40m, the diameter of the set in steel pipe is 0.80m, and it is 1.25m away from the top surface of the box girder and 0.75m away from the bottom of the box girder.

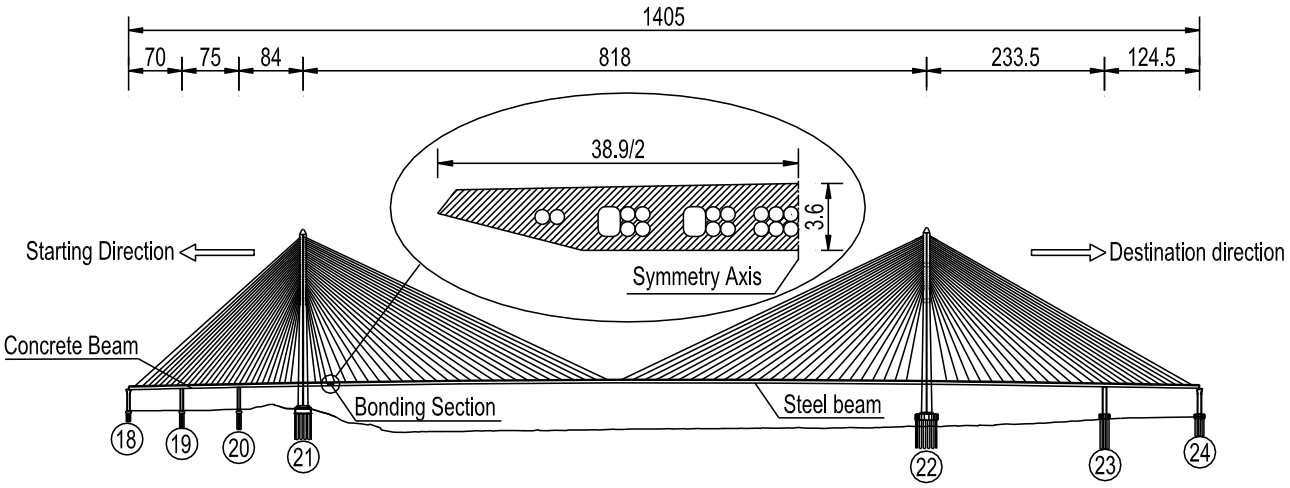

Fig. 1 – Bridge Layout (unit: m)

The concrete box girder adopts horizontal layering method combined with indirect advancing method, and the layering thickness is about 40 ~ 50cm. The order of casting is bottom plate, web and roof. The concrete fit of the project is shown in Table 1. The physical and thermal parameters of the concrete are shown in Table 2. To reduce the influence of hydration heat, the cooling water pipe is arranged to cool the temperature. The cooling water pipe is arranged in three layers from bottom to top. The distance between the first layer and the second layer is 100cm, and the distance between the second layer and the bottom layer is 120cm. The water inlet is arranged on the riverside, and the water outlet is arranged on the bankside. The temperature test points of box girder and the layout of cooling water pipes are shown in Figure2. The measuring range of JMT-36C type resistance sensor is -20°C to 120°C, and the sensitivity is 0.1°C. It has the advantages of high precision, strong stability, and insulation, and can cope with long-term temperature recording and automatic recording

on various occasions. The measured data is the resistance value, and the transformation between temperature and resistance is shown in formula 6:

$$T = \frac{1}{(0.003132398 + 0.003155718 \times \ln R_t + 0.0000048255 \times \ln^2 R_t) - 273.2} \quad (6)$$

Where T(unit: ℃) is the temperature value and R_T (unit:Ω) is the measured resistance value.

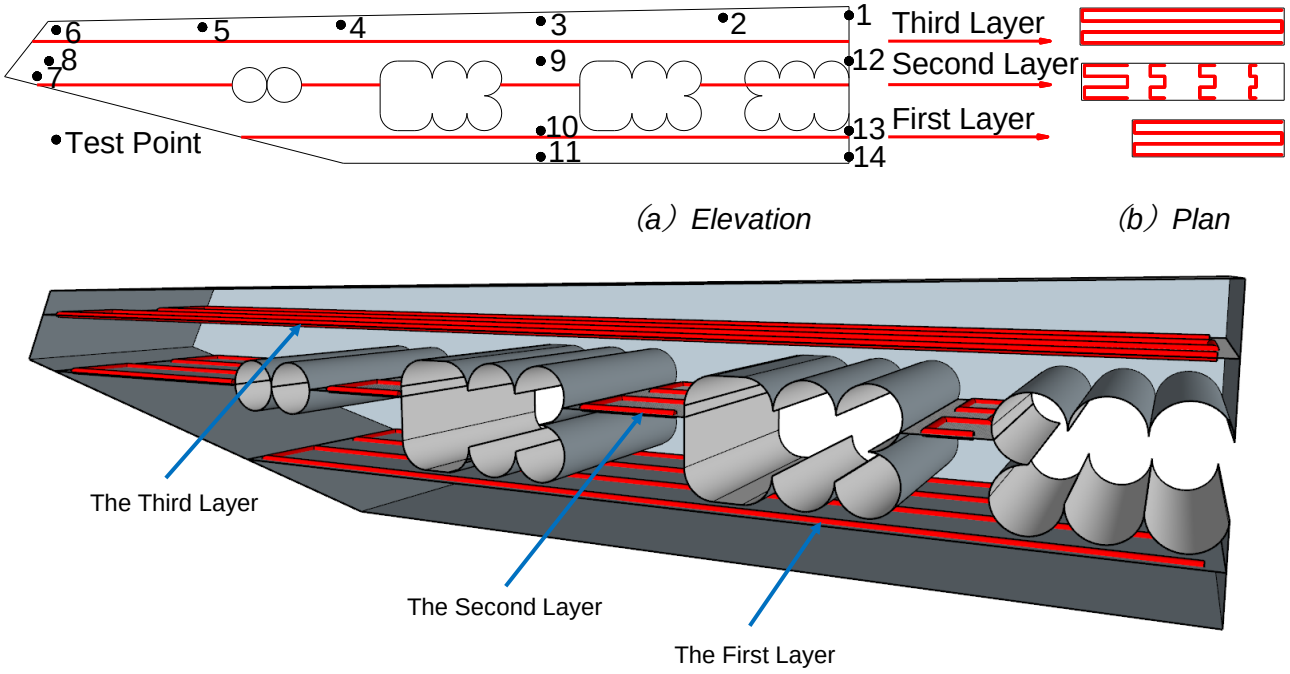

(a) Elevation (b) Plan

(c) Schematic diagram of cooling water pipe layout

Fig. 2 – Schematic diagram of arranging cooling water pipes and temperature test points in 1/2 beam section

Tab. 1 – Concrete batching table (unit: kg/m³)

Cement	Gravel (4.75-9.5mm)	Gravel (9.5-19mm)	Sand	Fly ash	Water reducing agent	Water
372	337	792	724	125	5.97	150

Tab. 2 – Thermal parameters of concrete

Strength (MPa)	Poisson's ratio	Coefficient of linear expansion (1/°C)	Bulk density (kN/m³)	Specific heat capacity kJ/(kN·T)	Thermal conductivity kJ/(m·h·T)
55	0.2	1.00E-05	25	62.9	10

FINITE ELEMENT MODEL

Finite element analysis software MIDAS/FEA is used to settle the three-dimensional model and calculation, because the box girder section and boundary conditions are symmetric, so half of the model is settled. The model has 12,650 nodes and 30,363 elements. The concrete is simulated by hexahedral and wedge elements. The finite element model is shown in Figure 3.

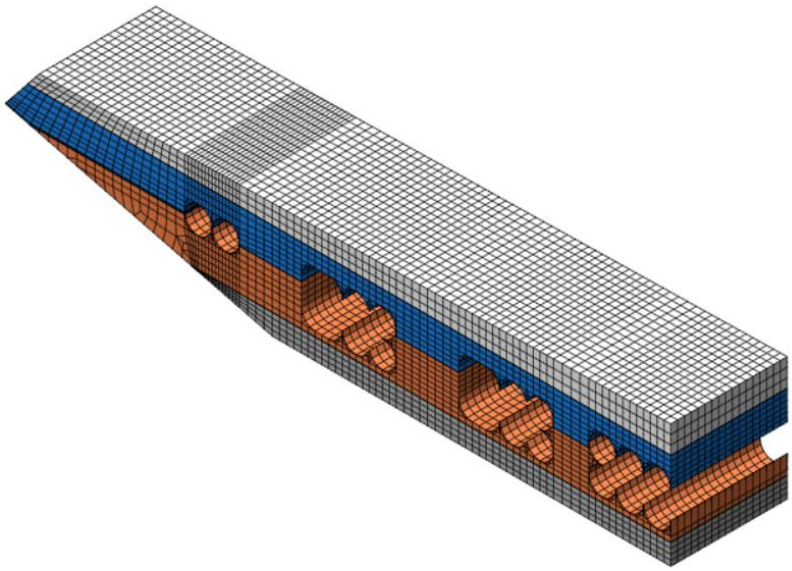

Fig. 3 – Finite element model diagram of box girder

To verify the accuracy of finite element software MIDAS/FEA in the simulation of hydration heat, the calculated values of the model at test point 1 at the top of the roof, test point 3 at the top of the roof and test point 8 at the center of the air nozzle are compared with the measured data, and the results are shown in Figure 4. Figure5 shows the temperature cloud map of finite element calculation at 35h.

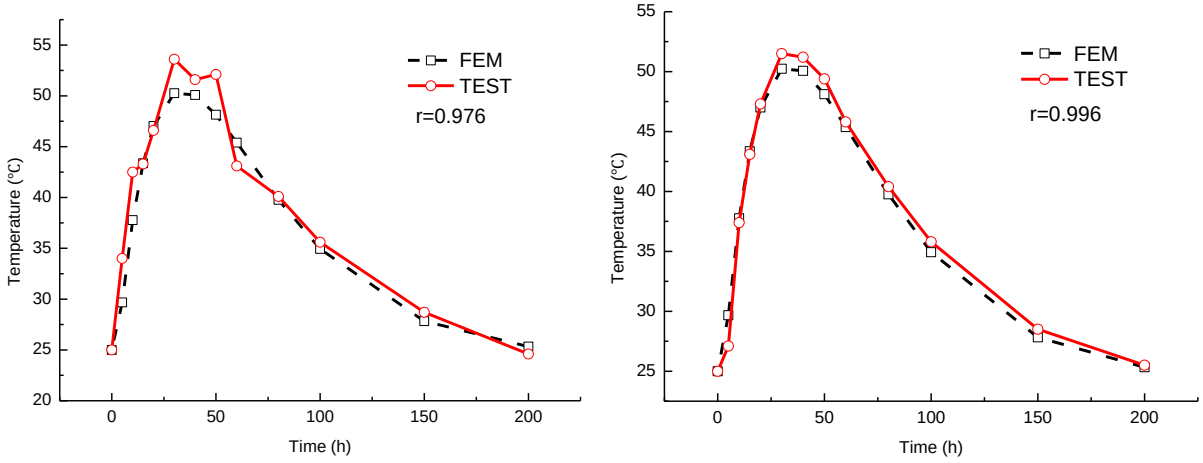

(a) Test point 1 *(b) Test point 3*

Fig. 4 – Comparison between FEM and test values of temperature

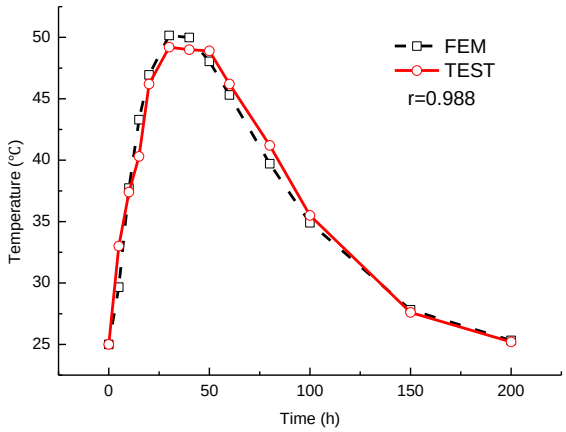

(c) Test point 8

Fig. 4 – Comparison between FEM and test values of temperature

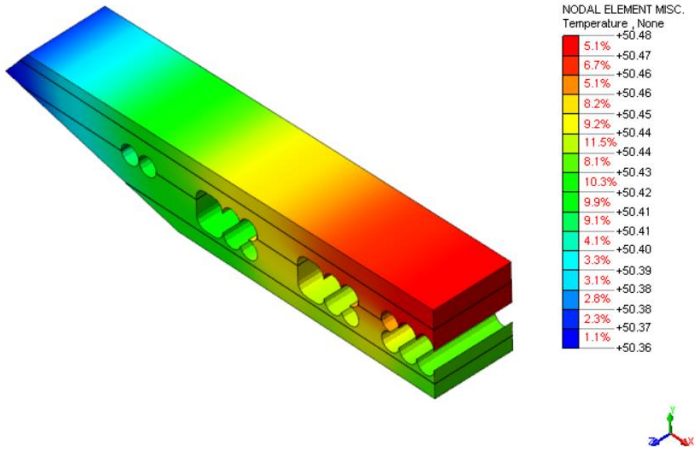

Fig. 5 – Temperature stress nephogram of box girder at 35h

It can be seen from Figure 4 that the measured temperature at the top of the roof at the central axis is significantly different from the calculated temperature at the temperature rise stage. In the concrete pouring, the superstructure of the set in steel pipe is poured in the later period, there is a time interval, and the hydration heat is late. Because of the large size of the test point on the upper part of the set in steel pipe, the measured temperature rise rate of hydration heat is faster than the calculated value, and the peak value of hydration heat is greater than the calculated value. The test point at the upper part of the central axis reaches the peak time later than the calculated value, because the lower part is first poured and then the upper part is poured, so there is a certain delay in time. The outbursts in the measured curves are caused by environmental factors and are measured at a time of day when the temperature is high. The cooling rate of the late is slower than the calculated value, which is determined by the position of the test points.

According to the comparison between Figure 4 (a) and Figure 4 (b), the duration of high temperature in the center of the roof at the axis is longer than in other parts of the roof. The measured data and calculated values at the center of the roof test point 3 fit well in the temperature rise stage. Figure 4 (c) shows the measured value curve of test point 8 at the center of the air nozzle fits well with the calculated value curve. In the temperature rising stage, the maximum error between measured and calculated values is about 3°C. There are several abrupt changes of temperature in the time history curve of measured temperature value, which are obviously different from the calculated value. This is caused by the influence of external factors such as sunshine, air humidity

and wind speed, which are not considered in the calculation. Considering comprehensively, the difference between the measured value and the calculated value is within the allowable range, and the model can be used for the next stage of parameter analysis.

PARAMETER STUDY

During the construction, the change of diameter, spacing and flow rate of cooling water pipes will lead to the change of temperature field in concrete. To reduce the hydration heat at the maximum efficiency and the capital cost at the same time, the relevant parameters of cooling water pipes are analyzed.

(1) Diameter of cooling water pipe

The diameter of cooling water pipe decides the area of contact between cold water and concrete. To study the diameter of the cooling water pipe when the cooling effect is ideal under the condition of changing the diameter of the cooling water pipe, this paper calculates the temperature value of the test point when the diameter is 9mm, 15mm, 21mm, 27mm, 33mm, 39mm and 45mm respectively. Figure 6 (a) shows the temperature change of test point 1 with different cooling water pipe diameters.

As seen in Figure 6 (a), the temperature variation trend is the same under different cooling water pipe diameters. Concrete reaches its peak temperature about 35 hours after casting, and then the concrete temperature decreases rapidly at first and then slowly. When the diameter of cooling water pipe is 9mm, the maximum instantaneous temperature rise rate of test point is 1.662°C/h, and the maximum instantaneous temperature drop rate is 0.293°C/h. When the diameter of cooling water pipe is 21mm, the maximum instantaneous temperature rise rate of the test point is 1.616°C/h, and the maximum instantaneous temperature drop rate is 0.296°C/h. When the diameter of cooling water pipe is 33mm, the maximum instantaneous temperature rise rate of test point is 1.572°C/h, and the maximum instantaneous temperature drop rate is 0.294°C/h. When the diameter of cooling water pipe is 45mm, the maximum instantaneous temperature rise rate of the test point is 1.530°C/h, and the maximum instantaneous temperature drop rate is 0.290°C/h. According to the function fitted by the maximum instantaneous temperature drop rate, as shown in formula (7), the diameter of the water pipe is 25mm when the maximum instantaneous temperature drop rate is achieved.

$$y = e^{-5.867\times10^{-5}x^2+0.00281x-1.248} \quad (7)$$

(2) Spacing of cooling water pipes

The distance between cooling water pipes decides the influence of different water pipes on the same concrete. In this paper, the temperature values of test points are calculated when the horizontal spacing of water pipes is 0.5m, 1.0m and 1.5m respectively. Figure6 (b) shows the temperature change of test point 1 under different horizontal spacing of cooling water pipes.

According to Figure 6 (b), when the horizontal spacing of cooling water pipes is 0.5m, the maximum instantaneous temperature rise rate is 1.571°C/h, and the maximum instantaneous temperature drop rate is 0.294°C/h. When the horizontal distance between water pipes is 1.0m, the maximum instantaneous temperature rise rate is 1.620°C/h, and the maximum instantaneous temperature drop rate is 0.296°C/h. When the horizontal spacing of water pipes is 1.5m, the maximum instantaneous temperature rise rate is 1.637°C/h, and the maximum instantaneous temperature drop rate is 0.295°C/h. According to the fitting function of the maximum instantaneous temperature drop rate, as shown in formula (8), it can be known when the maximum instantaneous temperature drop rate is achieved, the horizontal spacing of water pipes is 1.0m.

$$y = 0.29467 + 0.0015\sin\left(\pi\frac{x-0.625}{0.75}\right) \quad (8)$$

(3) Temperature of inlet water

Temperature of inlet water is a factor that has a great influence on the cooling effect. This paper calculates the temperature values of test points when the water inlet temperature is 5°C, 10°C, 15°C, 20°C and there is no cooling water pipe. Figure 6 (c) shows the temperature change of test point 1 at different water inlet temperatures.

As seen in Figure 6 (c), when there is no cooling water pipe, concrete reaches its peak temperature about 40 hours after casting. When cold water is injected, concrete reaches its peak temperature about 5 hours earlier, and the peak temperature decreases by more than 3°C. When the water inlet temperature is 5°C, the maximum instantaneous temperature rise rate is 1.538°C/h, and the maximum instantaneous temperature drop rate is 0.305°C/h. When the water inlet temperature is 15°C, the maximum instantaneous temperature rise rate is 1.590°C/h, and the maximum instantaneous temperature drop rate is 0.299°C/h. When there is no cooling water pipe, the maximum instantaneous temperature rise rate is 1.698°C/h, and the maximum instantaneous temperature drop rate is 0.288°C/h. It can be seen from Fig.6 (c) the change of water inlet temperature has a significant influence on the temperature produced by hydration heat.

(4) Flow rate of water

In this paper, the temperature values of test points are calculated when the flow rate is 0.4m³/h, 1.2m³/h, 1.6m³/h, 2.0m³/h, 2.4m³/h, 2.8m³/h, 3.2m³/h. Figure 6 (d) shows the temperature change of test point 1 at different water flow rates.

According to Figure 6 (d), when the flow rate is 0.4m³/h, the maximum instantaneous temperature rise rate is 1.614°C/h, and the maximum instantaneous temperature drop rate is 0.296°C/h. When the flow rate is 1.6m³/h, the maximum instantaneous temperature rise rate is 1.614°C/h, and the maximum instantaneous temperature drop rate is 0.296°C/h. When the flow rate is 2.4m³/h, the maximum instantaneous temperature rise rate is 1.614°C/h, and the maximum instantaneous temperature drop rate is 0.296°C/h. When the flow rate is 3.2m³/h, the maximum instantaneous temperature rise rate is 1.614°C/h, and the maximum instantaneous temperature drop rate is 0.296°C/h. According to Figure 6 (d), the change of water flow rate has little influence on the temperature produced by hydration heat.

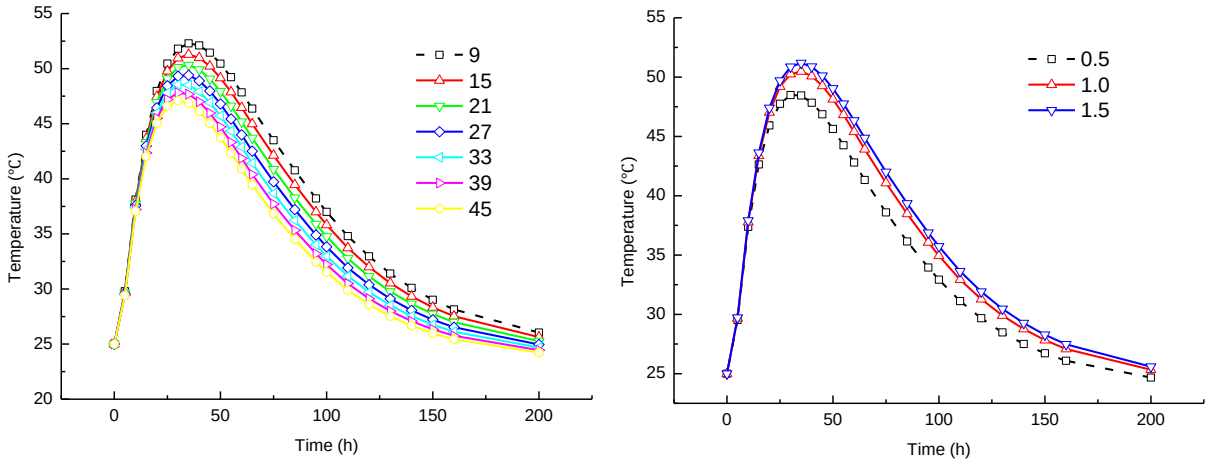

(a) Different diameters of cooling water pipes (b) Different spacing of cooling water pipes

Fig. 6 – Temperature changes of test point 1 under different parameters

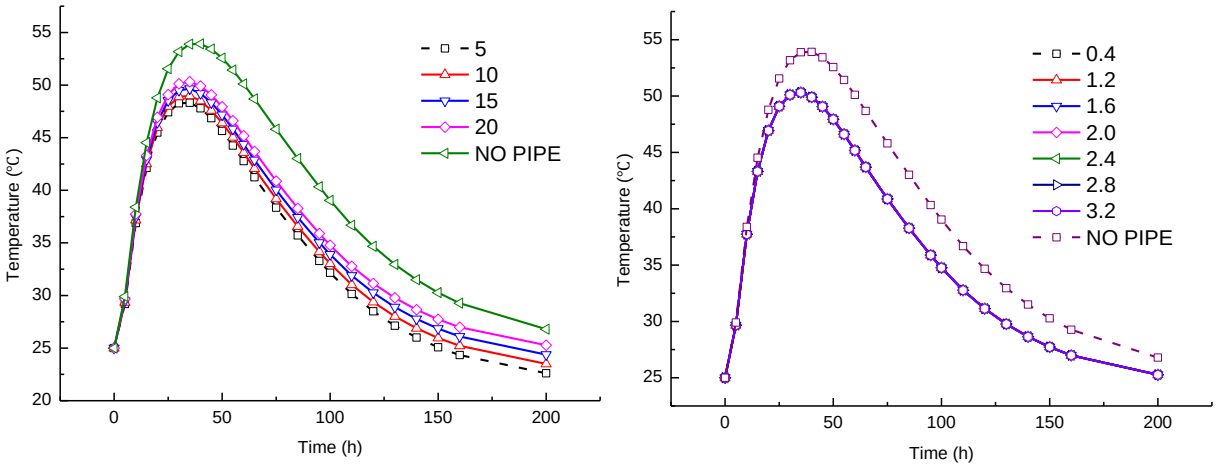

(c) Different temperatures of inlet water (d) Different flow rates of water

Fig. 6 – Temperature changes of test point 1 under different parameters

The influence of different parameters changes on the temperature of measurement point 1 are compared, as shown in Figure 7. As can be seen from the figure, the change of diameter of the water pipe and temperature of inlet water have a great influence on the Temperature, while water inlet rate has a small influence.

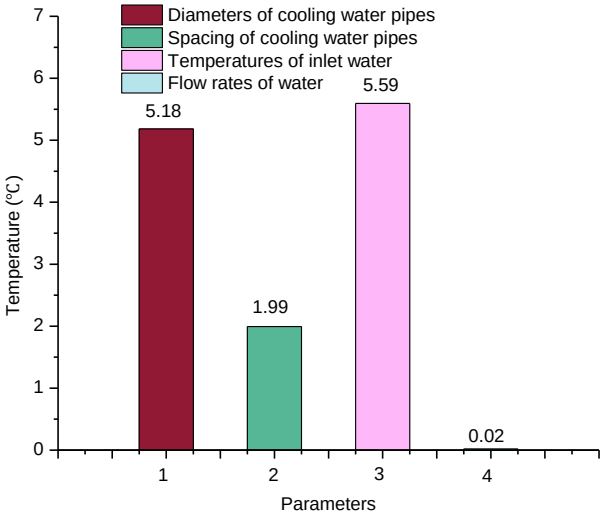

Fig. 7 –Different parameters influence comparison

CONCLUSION

In this paper, the cooling water pipe layout and field measurement of the mass concrete in the joint section of box girder of a cable-stayed bridge are carried out, and the finite element software is used for simulation calculation. The influence of the change of relevant parameters of cooling water pipe on the temperature field of concrete is systematically analyzed. The research conclusions are as follows:

(1) Between 30~45h after concrete pouring, the temperature reaches the highest value, and the concrete temperature rises sharply first and drops slowly.

(2) The calculated value of finite element is in well agreement with the field measured data.

(3) Among the parameters related to the cooling water pipe, the change of water inlet temperature and water pipe diameter has a greater impact on the concrete temperature, while the change of water inlet rate has a smaller impact on the temperature.
(4) When only the diameter of the water pipe is changed, the fitting function can be gained by considering the instantaneous temperature drop rate. Based on this, the ideal effect can be gained when the diameter of the water pipe is 25mm.
(5) When only the horizontal spacing of water pipes is changed, the fitting function can be gained by considering the instantaneous temperature drop rate. Based on this, the horizontal spacing of water pipes is 1.0m.

ACKNOWLEDGEMENTS

This paper is supported by the Anyang Science and Technology Plan Project (2020) (grant number: 251) and Anyang Institute of Technology Research and Cultivation Fund (grant number: YPY2020021).

REFERENCES

[1] Wang Xiushan, Hou Ning, 2019. Influence Research of Water Pipe Cooling on Temperature Stress of Mass Concrete (China Concrete and Cement Products), 15-18.
[2] Song Fuchun, Liu Ce, 2015. Analysis on Hydration Heat of Massive Concrete with Pipe Water Cooling (Journal of Shenyang Jianzhu University(Natural Science)) , 95-101.
[3] Zhang Yiduo, Guo Yiquan, Zhang Guoyun, 2015. Numerical Analysis on Hydration Heat Temperature Field of Prestressed Concrete Box Girder(China Concrete and Cement Products), 44-47.
[4] Zhu Bofang, 1999. Temperature stress and temperature control of mass concrete (Beijing: China Electric Power Press), 1-7 pp.
[5] Ding Baoying, 1997. Determination of temperature difference of water pipe between mass concrete and cooling water pipe(Water Resources and Hydropower Engineering), 12-16.
[6] Liu Yaodong, Bai Yinghua. et al., 2009. Optimization research on cooling pipe of mass concrete pier cap based on MIDAS(Concrete), 110-112.
[7] Sanyuan Guo, Caiping Huang, Henglin Xiao, 2016. Control and Optimization of After Rirer's Mass Concrete Pile Cap Cooling Tube(Highway Engineering),136-139.
[8] Tang Yang, Cao Haiyang, 2019. Effects of Layout Line of Cooling water pipes and Setting Parameters on Hydration Heat of the Caps(China Concrete and Cement Products), 86-91.
[9] Liu Guangting, Hu Yu, 2002. Analysis and measurement of the temperature field in the Shimenzi RCC arch dam[J]. (Journal of Tsinghua University(Science and Technology)), 539-542.
[10] Chen Zhijun, Kang Wenjing, Li Li, 2007. Study of the temperature effect caused by heat of hydration in hollow-thin pier (Journal of Huazhong University of Science and Technology(Natural Science Edition)) ,105-108.
[11] Zhang Yongjian, Li Ou, 2016. Test Study of Temperature Control of Mass Concrete for Pile Caps of Dongting Lake Bridge (Bridge Construction), 45-50.
[12] Wang Jianqun, Wei Guiliang, 2020. Measurement and Analysis of Hydration Heat in Massive Concrete Pile Cap of a Sea-Crossing Bridge (Bridge Construction),25-31.
[13] Liu Yi, Chen Bing, 2010. Numerical Simulation of Hydrated Heat Temperature Field of Massive Concrete (China Concrete and Cement Products), 15-18+27.
[14] Liu Guoxing, Huang Yonghui, Wan Yang, 2018. Experimental Research and Numerical Simulation on Hydration Heat of Bridge Mass Concrete(China Concrete and Cement Products), 94-97.

CIVIL ENGINEERING JOURNAL

Article no. 40

THE CIVIL ENGINEERING JOURNAL 2-2021

APPLICATION OF BIM TECHNOLOGY COMBINED WITH GENETIC ALGORITHM IN CONSTRUCTION MANAGEMENT

Guoan Wei

Department of Engineering Management, Henan Technical College of Construction, Zhengzhou, Henan 450000, China; beiwei6065420@163.com

ABSTRACT

The construction industry includes multiple projects. The management in the construction process is an important factor in ensuring construction quality. This paper briefly introduced the relevant content of building information modeling (BIM) and the application of BIM combined with the genetic algorithm (GA) in optimizing the processing scheme in the cutting process of steel structure buildings. A grid-shaped steel shed in Zhengzhou, Henan, was taken as an example to compare the traditional scheme, particle swarm optimization (PSO) combined BIM optimization scheme, and GA combined BIM optimization scheme. The results showed that the GA combined BIM optimization scheme made the best use of raw materials with different specifications and had the highest economic benefits because of the highest utilization rate, the least number of processors, and the shortest working hours.

KEYWORDS

Building information modeling, Construction management, Genetic algorithm, Layout optimization

INTRODUCTION

People's life is inseparable from clothing, food, housing, and transportation. The construction industry has always been very important. With the progress of various technologies, the production technology of the construction industry has also been improved [1]. However, in any case, the construction is a big project. The construction process involves a lot of related industries and departments. For example, before construction, it is necessary to do planning for the construction, coordinate the cost of building materials, and reduce the cost as much as possible under the premise of ensuring the quality; in the construction process, it is necessary to pay attention to the work allocation among various departments and the safety management of the construction site; after construction, it is necessary to monitor and maintain the building structure [2]. The works mentioned above are usually completed by workforce in the traditional method, but the diverse work items affect efficiency and consume a lot of workforce. The construction industry is different from the conventional industry. There is room for repeated modification of the design scheme in the architectural design process, but it will be difficult to modify the design scheme after the construction project starts, and the management costs involved will become additional costs [3]. Nowadays, the emergence of technologies such as the Internet of things, big data, and artificial intelligence makes construction management more intelligent and efficient. Building information modeling (BIM) technology is an auxiliary tool for construction management. BIM can establish a three-dimensional construction model and quickly count the building information to provide effective information for construction personnel. BIM cannot only use the model design scheme but also combine with artificial intelligence technology to optimize the project scheme at different stages in the construction process [4]. Liu et al. [5] proposed a genetic algorithm (GA) for resource constrained project scheduling problems and verified that the algorithm was effective through the simulation experiment.

Azadeh et al. [6] introduced a flexible GA-fuzzy regression method to predict future asphalt consumption. The experimental results showed that the algorithm was better than the traditional method as it had flexibility in the amount and uncertainty of input data and could be easily applied to the prediction of other materials and different construction projects. When faced with the resource balance problem (RLP) in construction management, Benjaoran et al. [7] proposed a new concept of RLP with relationship options and used the GA to optimize the solution. The simulation results showed that the model could calculate and arrange project schedules for all selected alternative relationship types, reducing resource demand fluctuation and the maximum resource demand level. Song et al. [8] studied a BIM-based structural framework optimization and simulation system for construction planning and schedule management. With this system, the construction process could be dynamically visualized. In addition, when inputting more than one construction schemes into the system, its simulation function could compare the advantages and disadvantages of construction schemes. In order to analyze the carbon performance of the building life cycle, Eleftheriadis et al. [9] established an embedded BIM method by using specific carbon indicators and the results of heuristic structural optimization. The experimental results verified that the structural optimization design could affect the life cycle of buildings. In this study, BIM and GA were combined to optimize the cutting processing scheme of steel structure buildings. Although GA alone can also optimize the cutting scheme, detailed building information needs to be collected, and the information cannot directly present the structure of the building. Therefore, in the BIM combined GA scheme used in this study, the importance of BIM is that BIM can intuitively present the structural information of the building, and it can also collect the structural information of the building more quickly and accurately, reducing the labour cost. Finally, an instance analysis was carried out by taking a grid-shaped steel shed in Zhengzhou city of Henan Province as an example to compare the traditional and BIM optimized schemes. The comparison results showed that the BIM and GA optimized scheme was more economical.

INTRODUCTION OF BIM

BIM is an information management platform that integrates different design types by specifying the same data specification based on 3D modeling technology. In the actual construction process, since BIM contains all the basic information of the construction project, the main units participating in the construction can communicate with the basic content of BIM through the Internet [10].

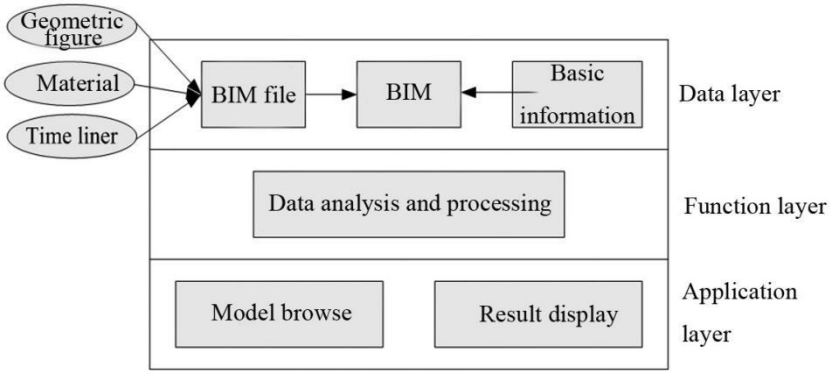

Fig. 1 – The basic framework of BIM

As a building information management platform, BIM has been widely used in the construction field, such as building effect display, construction process simulation, construction scheme optimization [11], etc. The basic framework of BIM is shown in Figure 1, divided into the data layer, function layer, and application layer [12]. The data layer is the bottom layer of the whole BIM framework, and its main function is to provide data support for the data analysis and processing of the function layer. The main data type in the framework is the BIM file, which contains related data,

such as the geometry, material properties, and Timeliner. BIM is constructed according to BIM files and basic information. The content of basic information is determined by the content that BIM needs to process. For example, if the safety of building structures is monitored by BIM, then the basic input information includes building monitoring information. If the building scheme is planned or optimized by BIM, then the input basic information includes various constraints, budget, material allowance, etc.

The function layer is the middle layer of the system, and it is also the key structure layer of BIM to realize various construction project management optimization functions. The data analysis and processing module is the main component to realize the above functions. It calls the BIM model and basic information data in the data layer and then processes the data called. The algorithm used in the analysis and processing will change according to the application project of BIM.

The application layer is the top layer of the system, through which users can interact with the system. The application layer is divided into the result display module and model browsing module. The result display module displays the target result of BIM by calling the data of the data analysis and processing module in the function layer. The model browsing module uses NavisWorks and API encapsulation functions to visualize the BIM model, calls the data of the result display module, and marks the relevant processing information in the visualized BIM model. In this module, users can access the images of different positions in the BIM model and corresponding information [13].

APPLICATION OF ARTIFICIAL INTELLIGENCE IN BIM

The construction industry is an industry with many divisions of labour. There are many departments or projects in the construction industry. In project implementation, although the division of labour and cooperation can improve efficiency, it is easy to form an "information island" between various implementation projects, which will reduce the construction efficiency and the quality of construction. The emergence of BIM makes labour division have a referable standard building model information [14]. There are many kinds of construction projects, and different projects adopt different strategies when using BIM for management. Limited by the length of the paper, it is impossible to cover all aspects. Therefore, this paper mainly focuses on "artificial intelligence + BIM" for construction material cutting in construction management.

In recent years, the application of steel structure building is more and more extensive. Compared with the traditional concrete building, the steel structure building is relatively simple in the main structure construction. It does not need the operation of concrete mixing, steel bar erection, and bricklaying but only needs to connect and build the steel after processing. In the construction management of steel structure buildings, the optimization of the processing scheme for building materials (mainly steel) is also a kind of construction management. The traditional building materials processing scheme is to process as many raw materials as needed and to cut bars at will, which will produce a lot of surplus materials and waste. After using BIM, facing the cutting scheme of steel bars in steel structure building, firstly, according to the building scheme (including steel structure building information, such as the number and type of steel structure bar frame, welding ball joint connection, and bar welding), a three-dimensional model consistent with that after the completion of construction is rapidly generated [15], and then the material information of bars and parts required for the construction of steel structure buildings are input through BIM. The material information with the specified format can facilitate the staff in the workshop and construction site to find and process the bar and be used to quickly optimize the scheme of processing raw material to obtain bars [16].

When the processing scheme of raw materials in construction management is optimized by BIM, the data processing and analysis module in the functional layer will be applied. The optimization of processing schemes by BIM is usually carried out by artificial intelligence, and the GA and particle swarm optimization (PSO) algorithm are commonly used. In this paper, the scheme is optimized by a GA. GA is an imitation of the rule of survival of the fittest in nature. The optimization principle of GA for the problem to be optimized is as follows. The factors that can affect the solution of the problem to be optimized are regarded as gene fragments of chromosomes, and a chromosome is

the factor set of a solution. Different chromosomes are generated in a random way. Through crossover and mutation, the chromosomes are iterated. Chromosomes are screened using the adaptive function that can reflect the excellent degree of chromosomes, making the population composed of chromosomes evolve in a better direction. Finally, the optimal chromosome is selected from the optimal population as the final scheme of the problem to be solved.

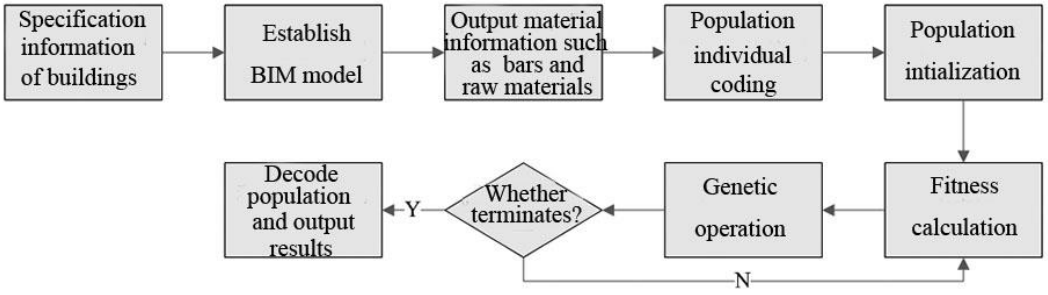

Fig. 2 – The optimization flow of the processing of steel structure building materials based on BIM combined with GA

Conventionally, steel structure bars are usually randomly taken from the raw materials before processing. For example, there are several five-meter long steel bars, and five four-meter long steel bars are needed in the construction project. In the traditional scheme, five steel bars are often taken for cutting for convenience, and the five one-meter long steel bars left will be wasted. However, if it is adjusted to the weldable form, only four five-meter long steel bars are needed, and there is no waste. Figure 2 shows the optimization flow of BIM combined with a GA to process steel structure building materials.

① Firstly, the BIM model of the steel structure building is established rapidly according to the design scheme. The design information includes project name, workpiece number, workpiece internal force, workpiece specification, node number, node coordinates, etc., which will be imported into BIM software in the form of "*. log". BIM software establishes the spatial coordinates of steel structure nodes by reading the "*. log" file and determines the relative position of bars in space according to the connection information of bars and nodes and the geometric parameters of bars. Due to a large number of bars and nodes in steel structure buildings and the complex modeling, the collision of bars cannot be predicted directly by simple space parameters. If bars are installed directly according to the design parameters, once the bars overlap, the construction process will be seriously affected. Therefore, after the preliminary construction of a BIM model, it is necessary to adjust using the Boolean operation, and the bar list will be generated and exported after the adjustment.

② According to the given material information, individuals in the population in the genetic algorithm are coded. Chromosome coding was used in the steel bar processing scheme using $I \times J$ character encoding [17]. I refers to the serial number of steel component to be processed, and J refers to the serial number of steel used for manufacturing components. For example, $A_1, A_2, A_3, \cdots A_I, B_1, B_2, B_3, \cdots B_J$ refers to processing $A_1 \sim A_I$ components on $B_1 \sim B_I$ materials in order. Genetic loci such as A_I and B_J contain the basic information of component and raw material, respectively. The genetic loci of components include the project name, serial number, specification, material, length, node name, and internal force of components. The genetic loci of raw materials include the project name, serial number, specification, material, length, processing sequence number, and whether there is surplus material. The genetic locus information of the above components and raw materials comes from the building material information obtained after establishing BIM.

③ Population chromosomes are initialized. The function of population initialization in this paper is to provide various steel bar material processing schemes. The initialization method is as follows.

Firstly, according to the information of steel bars and raw materials given by BIM, they are sorted according to the length, from large to small, and given the initial codes. Then, two genetic loci are randomly selected in the component coding area to exchange. The raw material coding area is in the same way. The population initialization finishes after multiple times of random exchanges [18].

④ The fitness of chromosomes (processing scheme) in the population is calculated, but chromosomes in the population cannot be directly used for the fitness calculation. Before fitness calculation, it is necessary to decode the chromosome according to the set layout strategy [19] (i.e., the cutting rules to be followed when raw materials are used to manufacture steel bars). The fitness is calculated according to the decoded scheme. The calculation formula is:

$$f = \sum_{i=1}^{n} C_i \cdot L_i + \sum_{h=1}^{m} C_h \cdot L_h \qquad (1)$$

where f is the bar production cost under the individual chromosome scheme, C_i is the value of residual waste after raw material cutting, which depends on the specification and type of raw materials, C_h is the welding cost of a single welding line of steel bars, which depends on the specification and type of bar to be welded, and L_i and L_h are the residual length of the i-th raw material and the length of the h-th welding line respectively. The fitness calculation formula is the objective function of the layout optimization problem, and the ultimate goal is to minimize it. The layout strategy is the limiting condition, including: (1) only one welding seam is allowed for bars; (2) the number of bars with welding seams cannot exceed 20% of the total number of bars; (3) the bars connected by nodes cannot all be bars with welding seams; (4) the length of bars to be welded should be at least 300 mm. The above restricted conditions are converted to mathematical version, as follows.

Condition ①: whether it is a draw bar is determined according to the numerical value of the internal force of bar A_i in the generated chromosome coding. If the numerical value of the internal force is positive, then it is a draw bar, and welding seams are not allowed; if it is negative, then it is a compression bar or bending bar, and only one welding seam is allowed. If meet seams then jump to the next raw material B_{i+1}.

Condition ②: when $s > 0.2I$ (s is the total number of bars with welding seams, and I is the total number of bars), according to the number of welding seams on the bar at the node of the steel structure building, the bars are sorted in order. If meet bars with welding seams at the node then jump to the next bar during layout.

Condition ③: the number of bars with welding seams at the node where bar A_i is located is recorded. If the number exceeds 20% of the total number of bars at the node, then jump to the next raw material during layout.

Condition ④: when $L_{B_j} - L_{A_i} < 300mm$, the layout of A_{i+1} needs to be conducted on B_{j+1}.

⑤ Genetic operations, including selection, crossover and mutation, are carried out on chromosomes in the population. The single-point crossover is used in both the component coding region and the raw material coding region of chromosomes. As shown in Figure 3, two chromosomes are randomly selected, and a crossover position is randomly selected (the intersection position of two chromosomes is the same). The coding sequence before the position keeps the same. After being added to the region to be exchanged, it is also regarded as the region to be exchanged, and then the genetic codes of the regions to be exchanged of the two chromosomes are exchanged. Finally, the same genetic codes in the exchange region and the non-exchange region are removed.

Mutation operation adopted the single-point position exchange. One chromosome is randomly selected, and then two positions are randomly selected in the component coding region to exchange genetic code. The treatment for the material coding region is the same. To enhance the convergence of the algorithm, the “excellent chromosome reservation” strategy is implemented for both operations. Before crossover and mutation, the best and worst chromosomes are selected from

the parent chromosome. Suppose the optimal chromosome is selected for crossover or mutation. In that case, the excellence of the filial generation is compared with that of the parental generation, and the more excellent one is reserved. The worst chromosome must be crossed or mutated and replaced by the filial generation, and the other chromosomes were crossed or mutated according to conventional crossover and mutation operations.

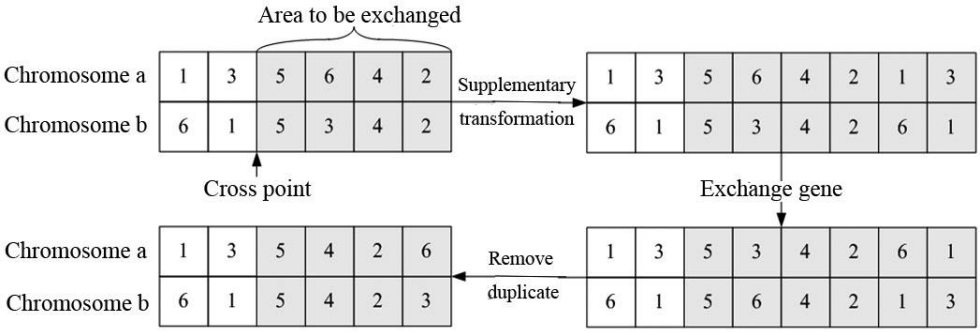

Fig. 3 – The flow of single-point crossover operation

⑥ Whether the algorithm terminates is determined. The termination conditions include the maximum number of iterations and population fitness convergence. If the termination condition is satisfied, the optimal solution is output and decoded according to the layout strategy. If the termination condition is not reached, it returns to step ④.

CASE ANALYSIS

Case overview

The construction management subject for case analysis in this study is a grid-shaped steel shed in Zhengzhou City, Henan, China, and its structure diagram is shown in Figure 4. The whole steel shed is composed of steel. The grid structure is adopted to ensure the strength of the roof. The grid structure which can be assembled and welded can reduce the construction difficulty. The distance between the supporting columns is 10 m, the height and diameter of the columns is 5 m, and the height of the roof is 1.5 m. To ensure the stability of the roof, the double-layer structure is adopted, and the staggered steel pipe structure is used between the upper and lower layers, and stable triangles are formed between the steel pipes. The diameter of the staggered steel pipe is 0.11 m. The diameter of vertical steel pipes used for supporting the roof on the roof beams and beams is 0.09 m. After modelling the steel shed with BIM, it was found that 535 steel joints and 3845 steel bars were needed in the construction process. The BIM software used in this study was Navisworks, and the GA needed by the layout scheme optimization was written in the VB language.

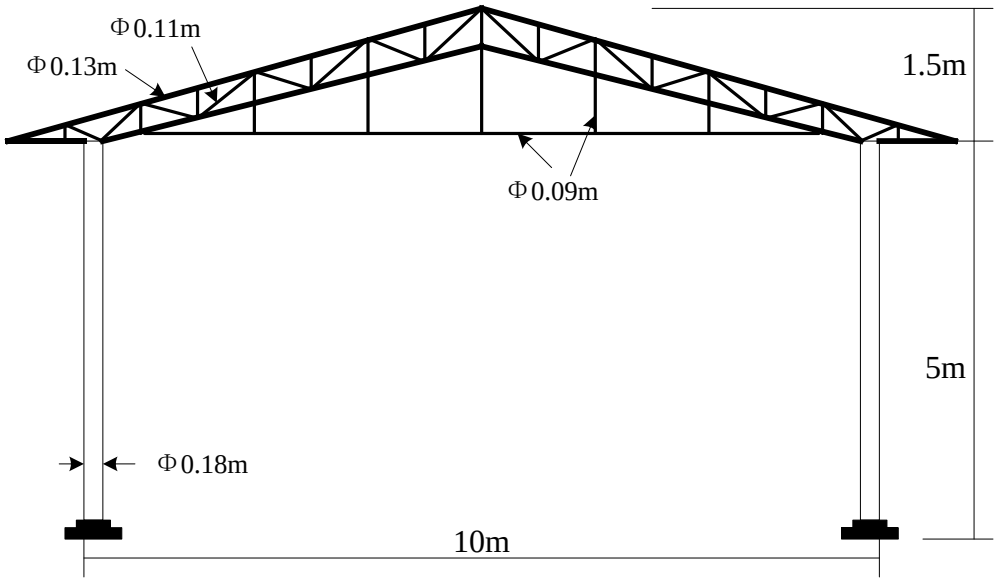

Fig. 4 – The structural diagram of the grid-shaped steel shed

Experimental setup

During the construction of the grid-shaped steel shed, it is an important construction management project to count the specification and number of steel bars and raw materials required for construction. In this construction management project, the scheme optimization of processing raw materials into steel bars was also included. Table 1 shows the basic parameters of steel members and raw materials required in the construction process of grid-shaped steel shed. It was seen from Table 1 that there were four specifications of steel bars, and the quantity required for each specification is described in Table 1. The basic specifications of raw materials used for making steel bars were also consistent with those of steel bars. Q235 steel was used as the material of steel bars [20]. The length of the bar was smaller than that of the raw material in Table 1.

Tab. 1 - Basic parameters of steel bars and raw materials needed in the construction of the grid-shaped steel shed

	Specification/mm	Number	Material	Length/mm
Steel bar	$\phi 180\times 6$	986	Q235	1200~4300
	$\phi 130\times 4$	887		100~4500
	$\phi 110\times 4$	1011		1100~4800
	$\phi 90\times 3$	961		1000~4300
Raw material	$\phi 180\times 6$	15		8000~12000
	$\phi 130\times 4$	10		7000~10000
	$\phi 110\times 4$	12		6000~11000
	$\phi 90\times 3$	10		5000~9000

In this study, the processing scheme of raw materials was optimized by the genetic algorithm. The parameters of the genetic algorithm are set as follows: population size: 70; maximum times of iteration: 500; crossover probability: 0.8; mutation probability: 0.2. When the genetic algorithm was used for optimization, the layout strategy adopted followed the following principles: 1) if welding was required for steel bars during manufacturing, only one weld was allowed; 2) steel bars without welding joints shall not be less than 80% of the total quantity; 3) at least one bar connected to any node had no weld; 4) the length of the bar to be welded shall not be less than 300 mm.

In addition to the GA, this study also used the PSO algorithm for comparison. In the PSO algorithm, the size of the population was 70, the maximum number of iterations was set as 500, two

learning factors were both set as 1.5, and the inertia weight was set as 0.8. The coding and decoding modes of the population particles in the PSO algorithm were the same as the GA.

Experimental results

In the construction process of the grid-shaped steel shed, when using raw materials to make steel bars, it was necessary to select the corresponding specifications of raw materials according to the specifications of the bars. Therefore, in the design of the optimal scheme, the overall optimal result could be obtained as long as the optimal schemes under different specimens were considered. The utilization rate of raw materials in the traditional scheme and the scheme of BIM combined with the genetic algorithm is shown in Table 2 and Figure 5. It was seen from Table 2 that the utilization rate of the traditional scheme, the PSO combined BIM optimization scheme, and the GA combined BIM optimization scheme was 92.3%, 94.5%, and 99.7% under the specification of $\phi 180 \times 6$, 93.1%, 95.1%, and 99.6% under the specification of $\phi 130 \times 4$, 92.1%, 94.6%, and 99.5% under the specification of $\phi 110 \times 4$, and 91.4%, 94.8%, and 99.4% under the specification of $\phi 90 \times 3$. The overall utilization rate of the traditional scheme, the PSO combined BIM optimization scheme, and the GA combined BIM optimization scheme was 92.2%, 94.7%, and 99.6%, respectively. Figure 5 clearly shows that no matter what the specification was, the GA combined BIM optimization scheme had the highest utilization rate.

Tab. 2 - Utilization rates of raw materials in the traditional scheme and BIM optimized schemes

Material specification/mm	Traditional scheme	PSO combined BIM optimization scheme	GA combined BIM optimization scheme
$\phi 180 \times 6$	92.3%	94.5%	99.7%
$\phi 130 \times 4$	93.1%	95.1%	99.6%
$\phi 110 \times 4$	92.1%	94.6%	95.5%
$\phi 90 \times 3$	91.4%	94.8%	99.4%

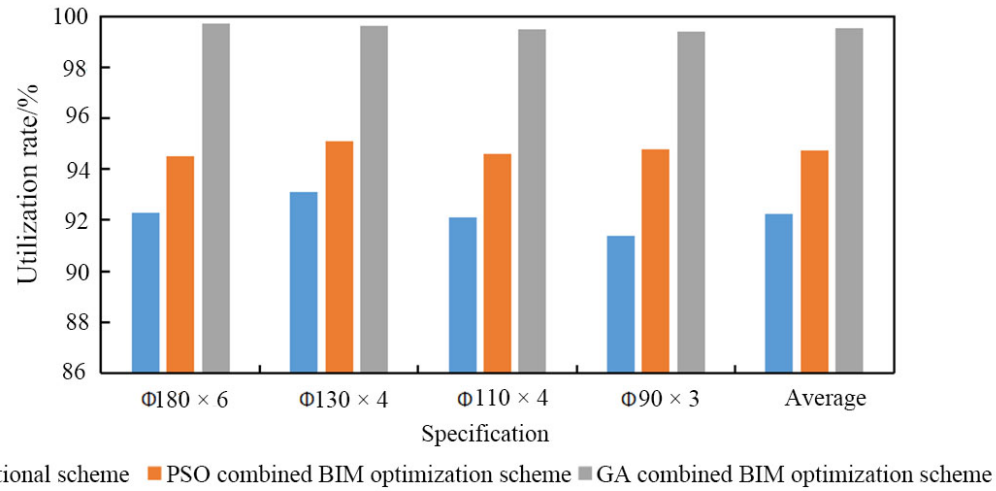

Fig. 5 – The utilization rate of raw materials with different specifications under the traditional scheme and the BIM optimization scheme

The economic comparison between the BIM optimized processing schemes and the traditional scheme is shown in Table 2, which indicates the total amount, unit price, and utilization rate of processing materials, construction drawing design, numerical control programming, and processing labour costs. The total amount of materials and unit price came from the pre-designed construction scheme. The salary of staff referred to the average salary of relevant works. The number of project participators in the traditional scheme referred to the number of participators originally involved in the construction project. The number of participators in the optimization

schemes referred to the case study of the project. As the GA combined BIM optimization scheme had a higher utilization rate for materials, the waste was less; the reduced part was the saved cost, 49950 yuan. In the traditional scheme, more people were needed to design the plane drawing, and communication between people was also needed to avoid the description error of the same component in different drawings. In the BIM optimization schemes, the standard model could be obtained by inputting relevant data, and the description on the same component was more consistent, which saved the communication time; thus, the workforce and time consumption was less, and 27300 yuan was saved for the design of the construction drawing. In the traditional scheme, the numerical control programmers needed to write the control program of the processing instrument according to the drawing, while the BIM optimization schemes only needed to transform relevant data into the unified format that the numerical control instrument could recognize, which greatly reduced the workforce and time consumption and saved a numerical control programming cost of 3640 yuan. In the traditional scheme, the cutting and welding of materials were fresh, which did not take the waste and the reduction of welding work amount into account, while the BIM optimization schemes reduced the number of materials that needed to be cut and welded, which reduced the processing time and the number of workers and saved a cost of 15000 yuan. The GA combined BIM optimization scheme saved 95890 yuan and 30 days compared to the traditional scheme. The comparison between the PSO combined BIM optimization scheme and the traditional scheme is also shown in Table 3. The utilization rate of raw materials of the PSO combined BIM optimization scheme was 94.8%, and it saved 17500 yuan compared to the traditional scheme. The labour cost of the PSO combined BIM optimization scheme was consistent with that of the GA combined BIM optimization scheme. Although there was a difference in time between the two schemes because of the complex design of the steel structure, the difference was insignificant compared to the whole construction period. The labour cost of the above two schemes was lower than that of the traditional layout scheme, which was because BIM was used as an auxiliary. Finally, it was seen from Table 3 that the final cost saving of the GA combined BIM optimization scheme was more excellent than the PSO combined BIM optimization scheme.

Tab. 3:- Comparison of economic benefits between schemes

	Traditional scheme	PSO + BIM optimization scheme	GA + BIM optimization scheme	The saved cost of the PSO + BIM optimization scheme/yuan	The saved cost of the GA + BIM optimization scheme/yuan	The total saved cost of the PSO + BIM optimization scheme/yuan	The total saved cost of the GA + BIM optimization scheme/yuan	The total saved construction time of the PSO + BIM optimization scheme/day	The total saved construction time of the GA + BIM optimization scheme/day
The utilization rate of materials/%	92.2%	94.8%	99.6%	17500	49950	63440	95890	30	30
The total amount of materials/t	150								
Material unit price (yuan/t)	4500								
Number of people designing the construction drawing/n	10	3	3	27300	27300				
Design time of construction drawing/time	15	2	2						
Salary of construction drawing designer (yuan/day)	300								
Time of numerical control programming/day	8	1	1	3640	3640				
Number of numerical control programmers/n	4	2	2						
Salary of numerical control programmer (yuan/day)	260								
Processing time/day	10	10	10	15000	15000				
Number of processors/n	12	6	6						
Salary of processor (yuan/day)	250								

CONCLUSION

This paper briefly introduced the relevant content of BIM and the application of BIM combined with the genetic algorithm in optimizing the processing scheme in the cutting process of steel structure buildings. Finally, taking a grid-shaped steel shed in Zhengzhou, Henan, China, as an example, the study compared the traditional scheme, the PSO combined BIM optimization scheme, and the GA combined BIM optimization scheme. The results are as follows: (1) the construction of the grid-shaped steel shed needed four specifications of steel bars, including $\phi 180 \times 6$, $\phi 130 \times 4$, $\phi 110 \times 4$, and $\phi 90 \times 3$, and no matter which specification was, the GA combined BIM optimization scheme had the highest utilization rate of raw materials; (2) in terms of economic benefits, the GA combined BIM optimization scheme saved 9589 yuan and 30 days compared with the traditional scheme, which was more excellent than the PSO combined BIM optimization scheme. One of the limitations of this paper is that it only studied one artificial intelligence algorithm, i.e., the GA. Although the GA was compared with the PSO algorithm, research on the combination of BIM and intelligent algorithms was seldom. The other limitation is that the application of BIM combined with artificial intelligence in construction management was only applied to steel structure buildings. The future research direction is to combine more intelligent algorithms with BIM and expand its application in construction management to more kinds of buildings.

REFERENCES

[1] Dore C, Murphy M, Mccarthy S, Brechin F, Casidy C, Dirix, E., 2015. Structural Simulations and Conservation Analysis-Historic Building Information Model (HBIM). ISPRS - International Archives of the Photogrammetry, Remote Sensing and Spatial Information Sciences, vol. XL-5/W4: 351-357, DOI: 10.5194/isprsarchives-XL-5-W4-351-2015.

[2] Sánchez A R, Meli R, Chávez M M., 2016. Structural Monitoring of the Mexico City Cathedral (1990–2014). International Journal of Architectural Heritage, vol. 10: 254-268, DOI: 10.1080/15583058.2015.1113332.

[3] Riaz Z, Edwards D J, Parn E A, Edwards DJ, Arslan M, Shen C, Pena-Mora F., 2017. BIM and sensor-based data management system for construction safety monitoring. Journal of Engineering, Design and Technology, vol. 15: 738-753, DOI: 10.1108/jedt-03-2017-0017.

[4] Nguyen L H, Goulet J A., 2018. Anomaly detection with the Switching Kalman Filter for structural health monitoring. Structural Control & Health Monitoring, vol. 25: e2136.

[5] Liu J, Liu Y, Shi Y, Li J., 2020. Solving Resource-Constrained Project Scheduling Problem via Genetic Algorithm. Journal of Computing in Civil Engineering, vol. 34: 04019055.1-04019055.10.

[6] Azadeh A, Kalantari M, Ahmadi G, Eslami H., 2019. A flexible genetic algorithm-fuzzy regression approach for forecasting. Construction Innovation, vol. 19: 71-88.

[7] Benjaoran V, Tabyang W, Sooksil N., 2015. Precedence relationship options for the resource levelling problem using a genetic algorithm. Construction Management & Economics, vol. 33: 711-723.

[8] Song S, Yang J, Kim N., 2012. Development of a BIM-based structural framework optimization and simulation system for building construction. Computers in Industry, vol. 63: 895-912, DOI: 10.1016/j.compind.2012.08.013.

[9] Eleftheriadis S, Duffour P, Mumovic D., 2018. BIM-embedded life cycle carbon assessment of RC buildings using optimised structural design alternatives. Energy & Buildings vol. 173: 587-600, DOI: 10.1016/j.enbuild.2018.05.042.

[10] Almeida N M, Sousa V, Dias L A, Branco F.A., 2015. Engineering risk management in performance-based building environments. Statyba, vol. 21: 218-230.

[11] Han K K, Golparvar-Fard M., 2015. Appearance-based material classification for monitoring of operation-level construction progress using 4D BIM and site photologs. Automation in Construction, vol. 53: 44-57, DOI: 10.1016/j.autcon.2015.02.007.

[12] Zhao D, Yao Y., 2018. Research on 3D Simulation of Fabricated Building Structure Based on BIM. 3D Research, vol. 9: 57.

[13] Henke K, Pawlowski R, Schregle P, Winter S., 2015. Use of digital image processing in the monitoring of deformations in building structures. Journal of Civil Structural Health Monitoring, vol. 5: 141-152, DOI: 10.1007/s13349-014-0091-6.

[14] Eleftheriadis S, Duffour P, Stephenson B, Mumovic D., 2018. Automated specification of steel reinforcement to support the optimisation of RC floors. Automation in Construction, vol. 96: 366-377, DOI: 10.1016/j.autcon.2018.10.005.

[15] Eleftheriadis S, Duffour P, Greening P, James J, Stephenson B, Mumovic D., 2018. Investigating relationships between cost and CO2 emissions in reinforced concrete structures using a BIM-based design optimisation approach, Energy and Buildings, vol. 166: 330-346.

[16] Ghosh A, Parrish K, Chasey A D., 2015. Implementing a Vertically Integrated BIM Curriculum in an Undergraduate Construction Management Program. International Journal of Construction Education & Research, vol. 11: 121-139.

[17] Ghaffarianhoseini A, Zhang T, Naismith N, Ghaffarianhoseini A, Doan D, Rehman AU, Nwadigo O, Tookey J., 2018. ND BIM-integrated knowledge-based building management: Inspecting post-construction energy efficiency. Automation in Construction, vol. 97: 13-28, DOI：10.1016/j.autcon.2018.10.003.

[18] Nguyen T H, Vu A T, Building Information Modeling Based Optimization of Steel Single-Plate Shear Connections Using Differential Evolution Algorithm. Proceedings of the 5th International Conference on Geotechnics, Civil Engineering Works and Structures, Ha Noi, Vietnam, 1199-1204.

[19] Ji Q, Chen W., 2020. The Application of BIM Technology in the Cost Management of the Whole Process of Construction Projects. Journal of Physics: Conference Series, vol. 1648: 032016 (6pp), DOI：10.1088/1742-6596/1648/3/032016.

[20] Li X, Xu J, Zhang Q., 2017. Research on Construction Schedule Management Based on BIM Technology. Procedia Engineering, vol. 174: 657-667.

CIVIL ENGINEERING JOURNAL

Article no. 41

THE CIVIL ENGINEERING JOURNAL 2-2021

MACHINE LEARNING BASED MODELLING FOR ESTIMATION OF THE FUNDAMENTAL TIME PERIOD OF PRECAST CONCRETE STRUCTURES USING COMPUTER PROGRAMMING

Nitin Dahiya, Babita Saini and H.D. Chalak

Dept. of Civil Engineering, National Institute of Technology Kurukshetra, Haryana, India;nitindahiya17@gmail.com ; bsaini@nitkkr.ac.in; chalakhd@nitkkr.ac.in

ABSTRACT

This research investigated the capability of machine learning approaches using computer programming to evaluate the fundamental time period (F_{TP}) of precast concrete structures. A data set consisting of 288 models with configuration including shear wall and beam-column frame were used in the present study. The 288 models were analysed using Etabs software and Rstudio. Input parameters for the present study consisted of the height of the building, number of bays, length and breadth of the building, cracked or uncracked section, number of storeys and frame type on the F_{TP} of precast concrete structures. Out of the 288 models, 108 arbitrary selected models were used for testing and the remaining 180 models were used for training. Linear (LRF), polynomial (PLF) and radial basis (RBF) kernel functions were used for machine learning approach i.e support vector machines (SVM) and gaussian process (GPR). A correlation coefficient of 0.9832 was achieved by linear function-based support vector machines (SVM-LRF) as compared to 0.9284 by gaussian process regression, indicating that SVM-LRF has improved efficiency in predicting the F_{TP}. The accuracy of the machine learning approaches was verified through comparison with the available equations to evaluate the F_{TP} in literature.

KEYWORDS

Fundamental time period, Precast concrete, Machine learning, Support vector machines, Gaussian process

INTRODUCTION

A pre-cast concrete structure is a complex assembly of the shear wall, beams, column, slab, vertical and horizontal connections. The F_{TP} is a crucial variable for the analysis of precast concrete structures. The majority of proposal available in the literature are based on codal equations which do not take into consideration the cracking of members, storey height variation and material property. This leads to a change in the F_{TP} of a building.

Apart from the height, the two-elements on which the F_{TP} of precast concrete structures rely on are the distribution of mass and stiffness. Thus, any component with rigidity/mass or perhaps both has an impact on the F_{TP} of a pre-cast concrete structure. Mostly due to earthquake amplitude and location of dynamic forces there is a considerable variability with respect to time that causing significant inertia effects on buildings. Under the dynamic characteristics of a building, a building behaves under the influence of dynamic forces which is controlled by its mass and stiffness properties. Furthermore, the sturdiness along with deformability of constituent members are the factors affecting the performance of a building.

With ever-evolving technology and with high-speed precision computers, the F_{TP} of the structure can be analysed either by an exact eigenvalue analysis or by a logical approach. However, during an earthquake, the codal guidelines offer imperial equation based on the inspection of the F_{TP} of original structures. However, the codal equation is used to determine the dissimilarities in the F_{TP} of structures. Codes and research work provide various formulae and results. In many cases, the analytical approaches and formulae depend on one parameter, i.e height of the building. Probably the most typical expression for the computation of the F_{TP} is [2]:

$$T = C_t . h^{3/4} \quad (1)$$

where, h is the height and C_t is the coefficient, which is determined by the typology of a structure. Equation 1 was first adopted in 1978 by the ATC [2] for RC frames. The C_t coefficient was determined based on the measurement of the fundamental time period during the San Fernando earthquake (1971). A regression analysis of the data gives a C_t value of 0.075. IS 1893[20], Eurocode 8[14] and UBC [28] adopt a similar expression assigning the different value of C_t.

The UBC proposed formulation has been updated in FEMA-450 [17] based on the research carried out by Goel and Chopra [18]. On the basis of the data presented by Goel and Chopra [18], FEMA proposed an expression:

$$T = C_r H_n^x \quad (2)$$

where H_n is the height, C_r is 0.0466 and x is 0.9.

Numerous investigators have suggested expression for F_{TP} of RC frame structures based on the height of the structure (Table 1). Crowley and Pinho [11] proposed an equation for the fundamental time period based on displacement design. Various old buildings were analysed in accordance with previous codes. Crowley and Pinho [12] in 2006 studied the elastic period of various RC frame building and proposed a simplified expression for the fundamental time period using eigenvalue analysis. The analytical results depicted that the presence of shear walls and partition walls reduces the fundamental time period of a building. Guler et al. [19] proposed an equation for the fundamental period of vibration derived from elastic numerical analysis. Asteris et al. [3] in 2015 studied the parameters affecting the fundamental period of frame structures that include the numbers of span, infill wall panels, location of soft storey and soil structure interaction. Asteris et al. [5] in 2016 proposed a equation using statistical regression for fundamental period. Again in 2016, Asteris et al. [4] predicted the fundamental time period using artificial neural networks using two hidden layer back propogation neural network (BPNN). The results showed that the BPNN model was accurate and reliable. In 2019, Asteris et al.[7] predicted the fundamental period using metaheuristic algorithm based neural network. They used artificial bee colony algorithm for the optimization of neural network. The results show that the ABC algorithm was a powerful tool for optimization.

The lack of dependable and robust computer programming modelling for predicting the fundamental time period of precast concrete systems can be attributed to an ‘n’ numbers of input parameters affecting the behaviour of the structure. The available literature depict variation [5,6,9,11] in predicting the fundamental time period. As the deterministic techniques did not provide reliable estimates of output parameters as visible from the literature from last two decades, machine learning techniques such as SVM, ANN have significantly gained populairity and helped in the estimation of various output parameters. Pal and Deswal [20] used SVR on deep beams to predict the shear strength. Omran et al. [1] used SVM and GP to predict the compressive strength of concrete. Asteris et al.[7] used artificial bee colony algorithm for the optimization of neural network for predicting the fundamental period. In the present study, computer programming based on Rstudio [25] was developed for SVM and GP regression modelling to predict the F_{TP} of precast building.

Support Vector Machines

Support Vector machines (SVM) is out of the box classifier used for non linear class boundaries. SVM is an extension of support vector classifier which uses kernels to create non linear boundaries. Support vector classifier is a soft margin classifier.

Tab. 1 - Fundamental time period equation for various codes and research

Fundamental time period Expression	Code/Author
$T = 0.09\ h / D^{0.5}$	IS 1893:2016
$T = 0.075\ h^{0.75}$	EC 8
$T = 0.01\ N$	NBCC 2005
$T = 0.075\ h^{0.75}$	UBC 97
$T = 0.053\ h^{0.9}$	Goel and Chopra [17]
$T = 0.1\ h$	Crowley and Pinho [10]
$T = 0.055\ h$	Crowley and Pinho [11]
$T = 0.026\ h^{0.9}$	Guler et al. [18]

Vapnik in 1995 proposed ε SVR by applying a ε - insensitive loss function [29] which allows the problem to be solved using the concept of margin. For training data with k number of models defined as $\{x_i, y_i\}$, i = 1, ……, k, where x_i is input vector and y_i is the target value, a linear decision function can be given by:

$$f(x) = (w, x) + b \tag{3}$$

where vector *w* regulates the direction of a perceptive plane, while scalar *b* regulates the offset of the perceptive plane from the origin. A miniature value of *w* designates the flatness of Eq (3), which can be attained by reducing the Euclidean norm defined by $\|w\|^2$. Consequently, a problem of regression was written for optimisation.

$$\text{Minimise} \quad \frac{1}{2}\|w\|^2 \tag{4}$$

$$\text{Subject to} \begin{cases} y_i - (w, x_i) - b \leq \varepsilon \\ (w, x_i) + b - y_i \leq \varepsilon \end{cases}$$

The problem in Eq. (3) can be expressed in the form of:

$$f(x) = \sum_{i=1}^{k} (\lambda'_i - \lambda_i)(x_i . x) + b \tag{5}$$

The approach analysed above can be expanded to allow for non-linear support regression by introducing the concept of the kernel function [30].

Support vector machines function in Eq. (5) are now written as:

$$f(x) = \sum_{i=1}^{k} (\lambda'_i - \lambda_i)\boldsymbol{K}(\boldsymbol{x_i}.\boldsymbol{x_j}) + b \tag{6}$$

Where:

$$\boldsymbol{K}(\boldsymbol{x_i}.\boldsymbol{x}) \equiv \boldsymbol{\Phi}(\boldsymbol{x_i}).\boldsymbol{\Phi}(\boldsymbol{x_j}) \tag{7}$$

This relation is known as kernel function since $\boldsymbol{\Phi}(\boldsymbol{x})$ cannot be mapped in the featured space. Support vector machines function in Eq. (5) are now optimised as:

$$f(x) = \sum_{i=1}^{k} (\lambda'_i - \lambda_i)\boldsymbol{K}(\boldsymbol{x_i}.\boldsymbol{x}) + b \tag{8}$$

In the optimization problem, the functions used are for the computational price of working with a higher-dimensional space alternative. A reference " Nature of statistical learning theory" [30] is made for an extensive analysis of SVM and gaussian process regression has been described in detail in a journal article "gaussian process regression" [8].

METHODOLOGY AND DATABASE

Descriptions of analytical models

In the present research, the 288 models of the pre-cast building were analysed with different Ground floor height, material property, the number of bays and section cracking were considered (table 2). The preferred input parameters were fed in the machine learning model that include the building height, building length, building width, number of bays, number of storeys, type of sections and type of frames.

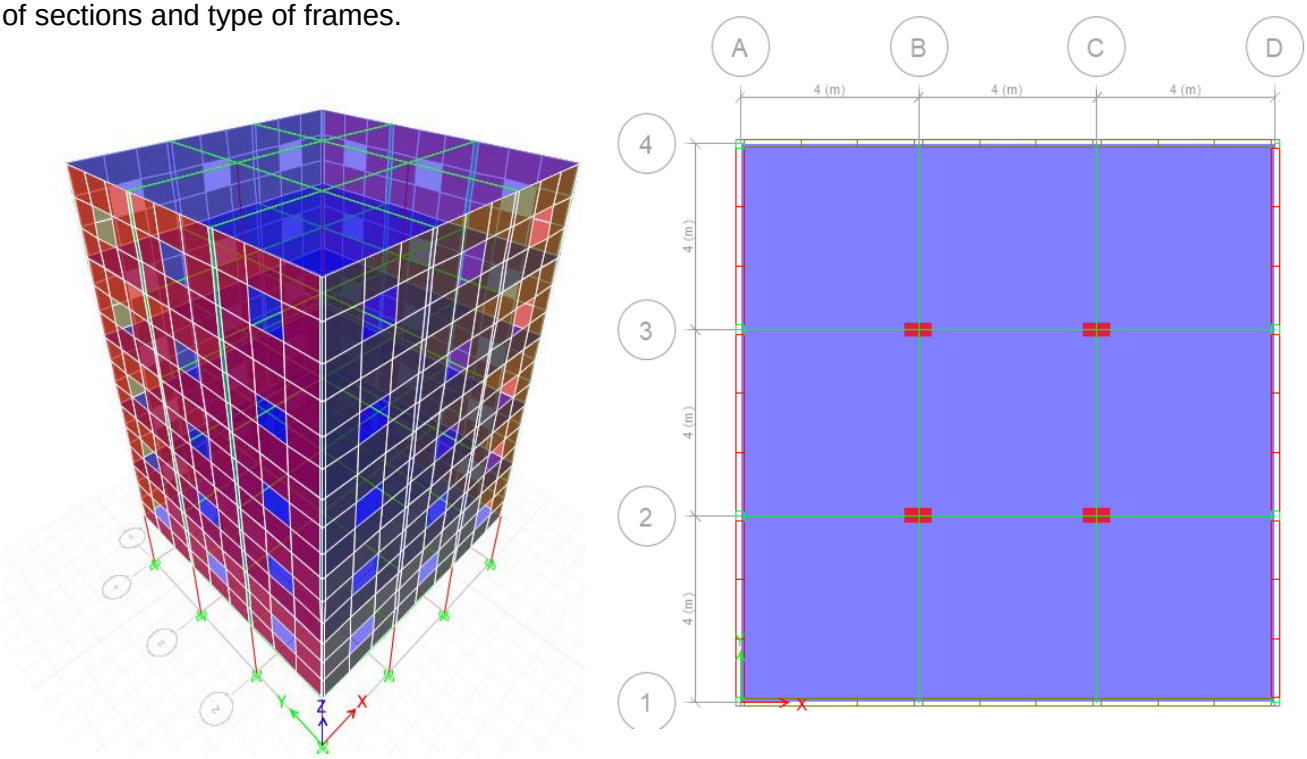

Fig. 1 - Typical Plan & 3D view of a computer model of 6 storey building

To assess the impact of input parameters on the F_{TP} of structures, 288 number of computer models were prepared. The storey height was assumed as 3 m for all storeys and for some models 4 m storey height was considered for the ground floor. The dimensions of slabs were 4 m x 3 m x 0.15 m, 4 m x 4 m x 0.15 m and cross-section of shear walls were 3 m x 0.15 m, 4 m x 0.15 m and 4 m x 0.20 m. The dimensions of the longitudinal and transverse beams were 450 mm deep and 300 mm wide. The size of the columns adopted was 300 mm wide and 600 mm deep. A live load of 3 kN/m^2 and SDL of 1 kN/m^2 was considered for analysis. M30/M40 grade concrete and also Fe 500 grade steel was utilised for design. The structure was modelled and analysed in ETABS 2015 [13] software. The ETABS software was used to analyse the burj khalifa [32]. Hence, the ETABS software is a reliable tool to be used for structural analysis and design. Seismic analysis is performed using the equivalent static and dynamic method given in IS 1893:2016. The plan and 3D modelling of the typical 6 storey structure are shown in Figure 1. To explore the outcome of each input parameters on the F_{TP} of structure, a sensitivity analysis was also carried out.

PERFORMANCE AND ANALYSIS OF SVM AND GPR

Out of a total of 288 models, 67 per cent of the arbitrarily split data have been utilized in training data set using Rstudio [25]. In the current research, 180 randomly split data were used as training data set and 108 random samples were utilized as testing data. Input variable was the

building height, building length, building width, number of bays, number of storeys, type of sections and type of frames for both SVM and GPR. The summary of training and testing data is provided in table 3 with different analytical approaches.

In SVM and GPR, various kernel functions are used for regression. Linear kernel, RBF kernel and polynomial kernel function have positive performance as suggested by numerous studies. In the present study, three kernel functions were considered - *LRF* ($K(x,x') = (x.x')$, *PLF* ($K(x,x') = \left((x.x') + 1\right)^d$) and *RBF* ($K(x,x') = e^{-\gamma|x-x'|^2}$), where *d* and γ are the hyper tuning parameters of *PLF* and *RBF* respectively. Size of error-insensitive zone ε and regularisation parameter C (Cost) optimum value and setting up of kernel function where required. Noise parameter is required in GPR and a trial-and-error was carried out to find the optimum value.

To select optimum values of hyper tuning parameters of SVM and GPR, a number of trails were conducted and grid search was performed. The hyper tuning parameter for SVM and GPR is given in Table 4 for which the data is working well. *LRF*, *PLF* and *RBF* with same hyper tuning parameters were used in the regression. The performance of regression approaches and their function was verified by correlation coefficient (CC) and root mean square error (RMSE).

Tab. 2 - Building input parameters

Model	**Parameters**	**Parameters Values**
Base Model	No of storeys (N_s)	3 m,6 m,9 m,12 m,15 m,18 m
	No of bays (N_b)	2 bay,3 bay,4 bay,5 bay
	Frame Type (F_t)	Shear wall with and without opening
	Building Length (L)	8 m,12 m,16 m,20 m
	Building Breadth (B)	8 m,12 m,16 m,20 m,3 m,6 m, 9 m,12 m
	Building Height (H)	9 m, 18 m, 27 m, 36 m, 45 m, 54 m,
	Section Cracking (S_c)	Uncracked and Cracked
	Column Size	300 mm x 600 mm
	Beam Size	300 mm x 450 mm
	Shear Wall thickness	200 mm and 150 mm
	Concrete Grade	M 40
Base Model with ground floor height changed	Building Height changed	10 m, 19 m, 28 m, 37 m, 46m, 55 m
Base Model with concrete grade changed	Concrete Grade	M 30

Tab. 3 - Summary of the training and testing data

Input parameters	Training Data					Testing Data				
	Min.	Max.	Mean	Median	SDV	Min.	Max.	Mean	Median	SDV
No of storeys	3	18	10.8	12	5.12	3	18	10	9	5.12
No of bays	2	5	3.26	3	1.12	2	5	3.89	4	0.99
Frame Type	0	1	0.5	0.5	0.50	0	1	0.5	0.5	0.50
Building Length	8	20	13.07	12	4.51	8	20	15.56	16	3.99
Building Breadth	6	20	11.43	12	4.31	6	20	13.61	13.5	4.03
Building Height	9	55	32.73	36	15.39	9	55	30.33	28	15.37
Section Cracking	0	1	0.5	0.5	0.50	0	1	0.5	0.5	0.50

Tab. 4 - Hyper tuning parameters used in SVM and GP

Machine learning Function	*LRF*	*RBF*	*PLF*
SVM	Cost =20	Cost =20, Sigma = 0.1	Cost = 20, Degree = 1
GPR	Initial Noise = 1	Initial Noise = 1, Sigma = 0.1	Initial Noise = 1, Degree= 1

RESULTS AND DISCUSSION

Figure 2 and Figure 3 provide the plot between the actual and predicted fundamental time period by *LRF*, *PLF* as well as *RBF* according to GPR and SVM utilizing test data set. Outcomes from both SVM and GPR are within line with analysis. The optimum value of cost =20 for SVM and intitail noise=1 for GPR, a hyper-parameter was obtained by trial-and-error method. Table 5 suggests that the SVM linear kernel function perform much better compared to any kernel function in both SVM and GPR. SVM linear kernel function has a correlation coefficient of 0.9832 and RMSE of 0.0530 seconds in comparison to GPR linear kernel function which has a correlation coefficient of 0.9284 and RMSE of 0.1084 seconds. A graph between fundamental time period obtained from analysis and predicted fundamental time period by SVM and GPR versus the number of test data on the x-axis was plotted; from this plotted graph, the SVM linear kernel function predicted value is in close immediacy of fundamental time period obtained from the analysis. As linear kernel function works well with both modelling techniques, another line chart between 108 test samples and fundamental time period is plotted (Figure 4) to check whether the SVM linear kernel function works well in predicting the time period.

Tab. 5 - Evaluation of SVM and GP performance on training and testing data

Machine Learning Technique	Training Data		Testing Data	
	CC	RMSE (Second)	CC	RMSE (Second)
SVM - *LRF*	0.9804	0.0619	0.9832	0.0530
SVM - *PLF*	0.9577	0.0905	0.9632	0.0778
SVM - *RBF*	0.9300	0.1148	0.9452	0.1008
GPR - *LRF*	0.8862	0.1296	0.9284	0.1084
GPR - *PLF*	0.8862	0.1295	0.9284	0.1084
GPR - *RBF*	0.8708	0.1407	0.9090	0.1241

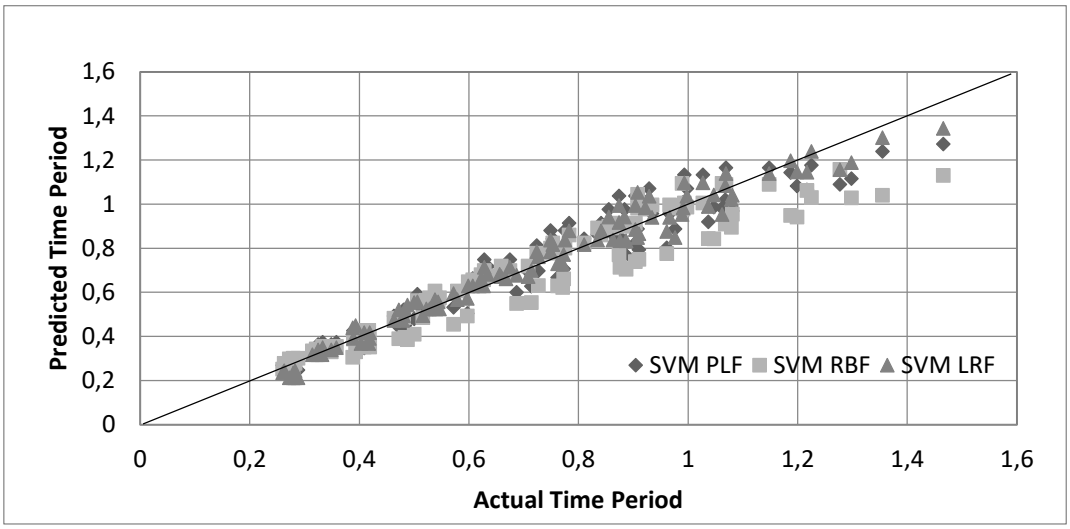

Fig. 2 - Actual time period vs predicted time period on testing data for SVM

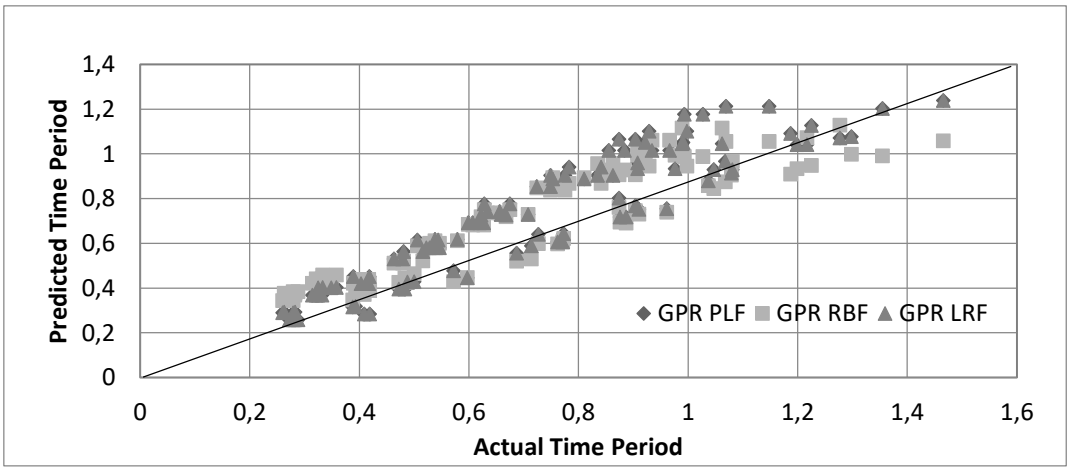

Fig. 3 - Actual time period vs predicted time period on testing data for GPR

SENSITIVITY ANALYSIS

Sensitivity analysis was performed to identify the significance of all the input variables in predicting the fundamental time period. The best kernel function is used with the training data for the analysis. SVM-LRF is used on a different set of training data by removing each input parameter:

- In first iteration all input parameters were used;
- In second iteration, frame type (F_t) was removed,
- In third iteration, building height (H) and frame type (F_t) is removed,
- In fourth iteration, number of storeys (N_s) and frame type (F_t) is removed,
- In fifth iteration, number of bays (N_b) and frame type (F_t) is removed,
- In sixth iteration, building length (L) and frame type (F_t) is removed,
- In seventh iteration, building breadth (B) and frame type (F_t) is removed,
- In eighth iteration, section cracking (S_c) and frame type (F_t) is removed and

- In the ninth iteration number of bays (N_b), building length (L) and frame type (F_t) is removed and results were obtained and analysed in form of CC and RMSE with the test data set for all the nine iterations as shown in Table 6.

Table 6 implies that number of bays (N_b), building length (L) and frame type (F_t) has least impact in predicting the F_{TP}, while building height (H), number of storeys (N_s), building breadth (B) and section cracking (S_c) have a major role in predicting the F_{TP}.

Tab. 6 - Sensitivity analysis

Input Parameter	CC	RMSE (Seconds)
N_s, N_b, F_t, L, B, H, S_c	0.9832	0.0530
N_s, N_b, L, B, H, S_c	0.9831	0.0532
N_s, N_b, L, B, S_c	0.9110	0.1247
N_b, L, B, H, S_c	0.9219	0.1157
N_s, L, B, H, S_c	0.9830	0.0532
N_s, N_b, B, H, S_c	0.9830	0.0532
N_s, N_b, L, H, S_c	0.9807	0.0568
N_s, N_b, L, B, H	0.9588	0.0823
N_s, B, H, S_c	0.9814	0.0557

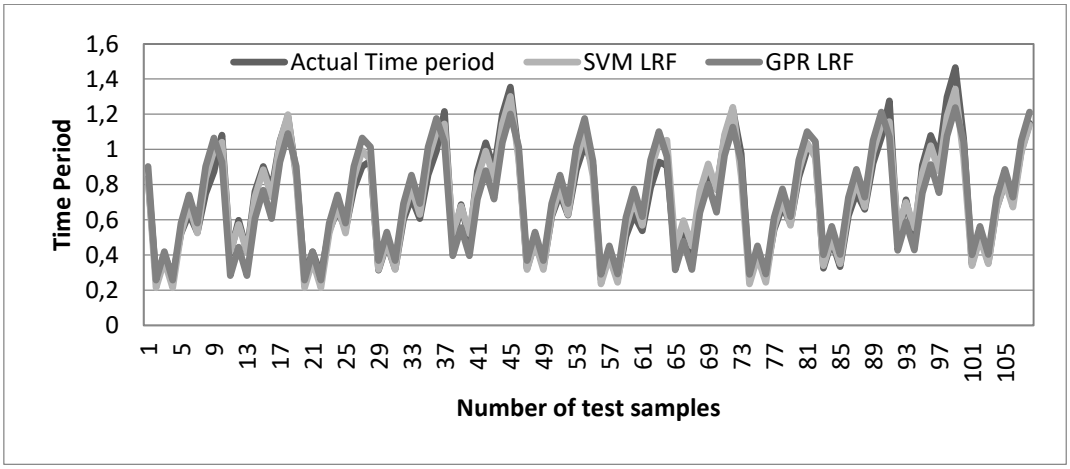

Fig. 4 - Variation in predicted values of Time period using SVM-linear and GPR-linear to the actual time period.

MODEL VALIDATION

The correlation coefficient (CC) and root mean square error (RMSE) were calculated for the machine learning technique SVM-LRF as well as for the formulae available in the literature as shown in Table 7. The lower value of RMSE indicates the more accurate predicting result and higher value of correlation coefficient indicating a heightened match in between analytical and machine learning approach values.

The advantage of SVM-LRF compared to codal equations and other literature formulae for 288 model data are given in Table 7. The highest CC value obtained is 0.9829 using SVM-LRF, whereas the lowest value obtained is 0.8609 for IS 1893. It is certainly apparent from the Table 7 that the SVM-LRF has a high correlation coefficient and low RMSE in comparison to the predicted F_{TP} and the actual F_{TP} (periods obtained from analysis).The CC and RMSE value of SVM-LRF model has the best fit of values than the formulae given in the literature.

In Figure 5, the result of actual F_{TP} (time period calculated from analysis) has been compared with the predicted result from SVM linear kernel function. In Figure 6, 7, 8 and 9 the result of the actual fundamental time period has been compared with the empirical formula of IS 1893:2016, NBCC 2005, EC 8 and Goel and Chopra. These outcomes demonstrate that the value of the F_{TP} predicted from SVM linear kernel function offers a better fit than the values of F_{TP} from empirical formulae.

Tab. 7 - Statistical results of SVM-Linear Kernel and literature formulae for all data

Method	Mean	Std Dev	CC	RMSE (seconds)
SVM-LRF	0.7344	0.2876	0.9829	0.0561
IS 1893:2016	0.7992	0.4162	0.8609	0.2272
NBCC 2005	0.105	0.0512	0.8957	0.6847
EC8	0.9804	0.3743	0.9031	0.2914
Goel and Chopra	1.179	0.5237	0.9053	0.5223

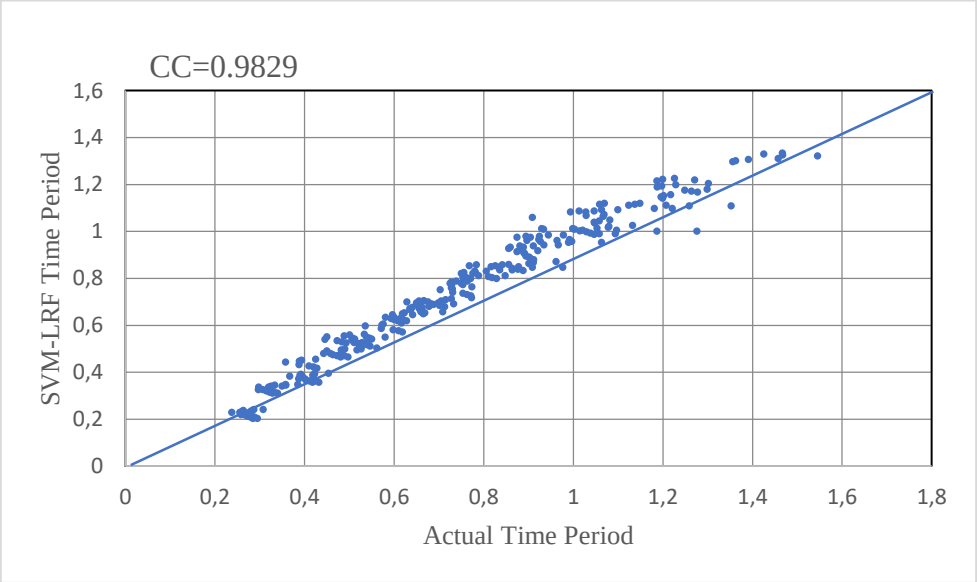

Fig. 5 - Actual Time period vs predicted time period on all data for SVM-LRF

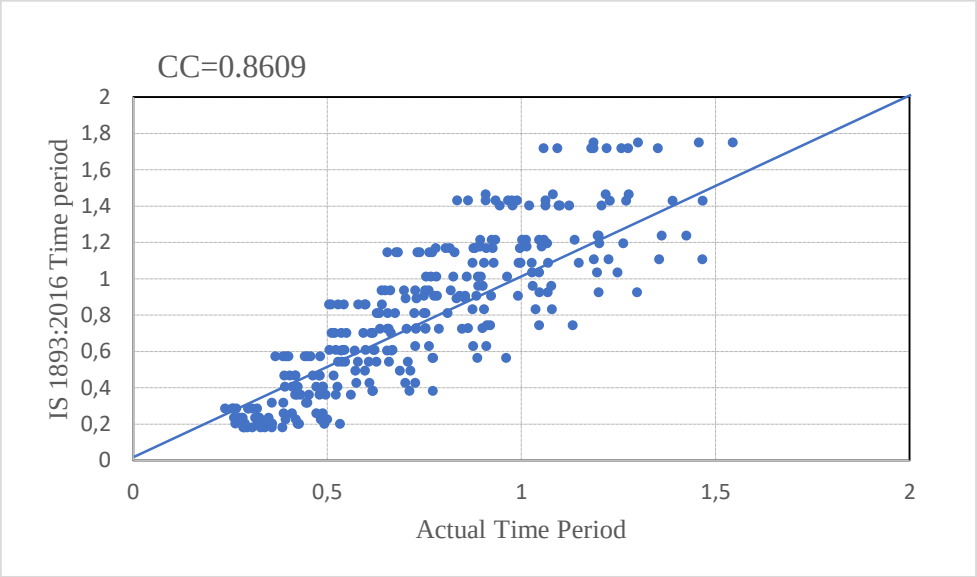

Fig. 6 - Actual Time period vs predicted time period on all data for IS 1893:2016

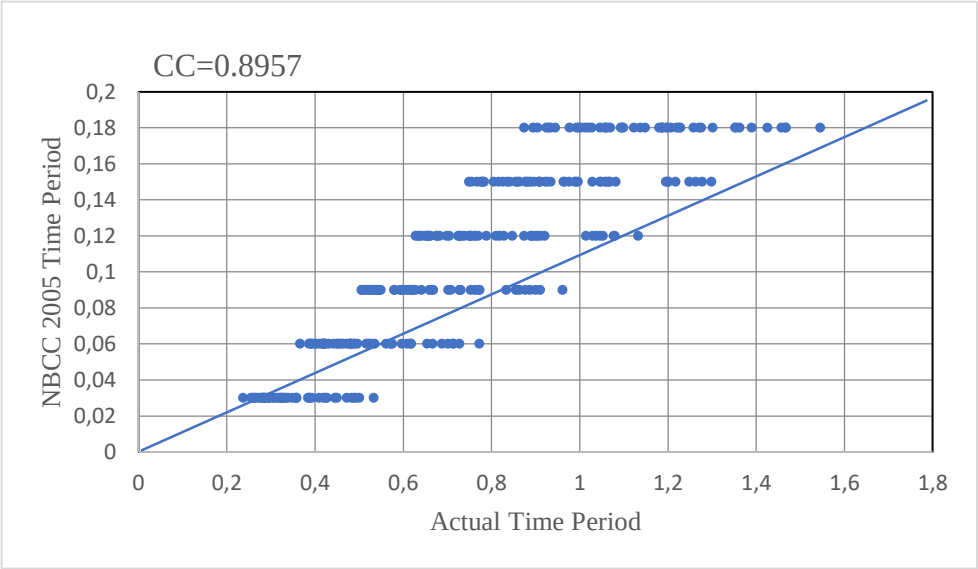

Fig. 7 - Actual Time period vs predicted time period on all data for NBCC 2005

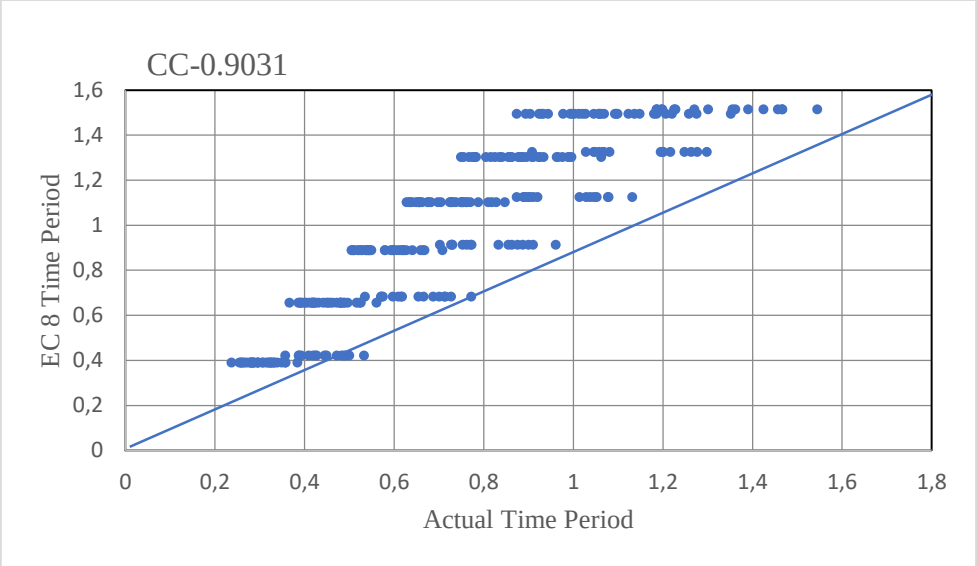

Fig. 8 - Actual Time period vs predicted time period on all data for EC 8

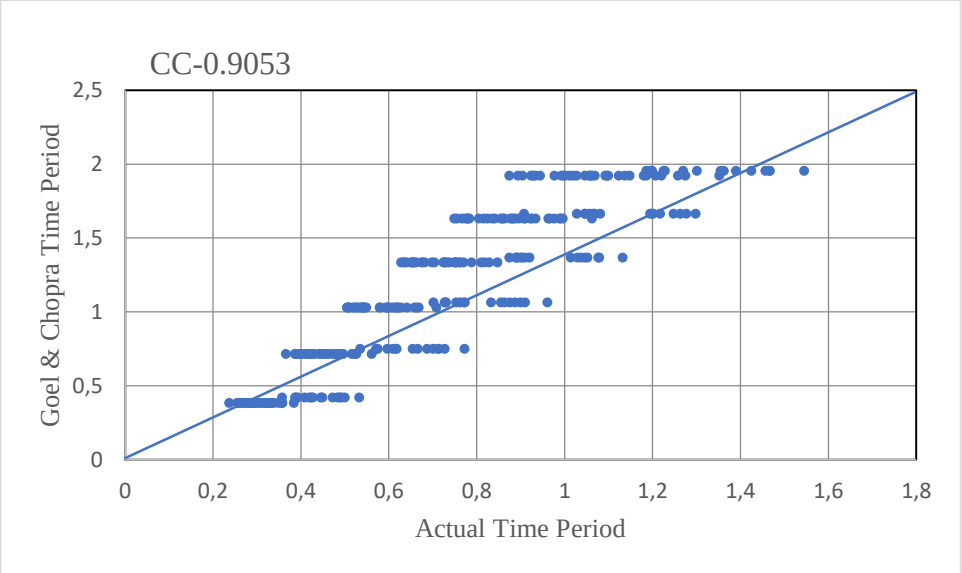

Fig 9 - Actual Time period vs predicted time period on all data for Geol & Chopra

PRACTICAL APPLICABILITY OF THE PROPOSED METHOD

In this study, the F_{TP} of precast concrete structures is predicted using computer programming. In research, practical application of proposed method is vital and important. To check the efficiency and limitation of proposed method, two models of 9 storey (total height = 27 m) with slab size of 4 m x 3 m x 0.15 m, beam size of 450 mm deep and 300 mm wide and column size of 300 mm wide and 600 mm deep were used. A LL of 3 kN/m^2 and SDL of 1 kN/m^2 was considered for analysis. M40 grade concrete and also Fe 500 grade steel was utilised for design. The F_{TP} is calculated based on proposed method and IS 1893: 2016 is shown in Table 8.

Tab. 8 - Fundamental time period of proposed method and IS code method

Fundamental Time Period	Proposed Method	IS 1893:2016
	0.511 second	0.888 second

Column forces and beam forces for various load combinations were calculated and compared for both the models. Column forces (Axial, shear and moment) for the proposed method was around 20% lesser than the IS code and 15 % lesser in case of beam forces. The reduction in forces suggest that while designing the members using proposed method will be economical, but it has a limitation – the proposed method can be used only for buildings up to 60 metres in height.

CONCLUSION

In this study, computer programming based on Rstudio was developed for support vector machines and gaussian processes regression to predict the F_{TP} of precast concrete structures. The obtained result shows that SVM works good in comparison to GPR for the data set, specifically the SVM linear kernel function provides the very best outcomes in term of CC and RMSE (CC = 0.9832 and RMSE = 0.0530 seconds) for predicting the F_{TP} of precast concrete structures. Moreover, the SVM linear kernel function appeared to fit the data better than the codal equations and other literature formulae on all data set by providing high CC and minimal RMSE. The present study also concludes that the number of bays do not have significant effect on the F_{TP}. There is a linear relationship between the length/ breadth with the F_{TP}. *Cracked section is having about 13.4 % more* F_{TP} as compared to uncracked section. The height of the building has significant influence of the F_{TP}. It can also be concluded from this study that SVM is a robust and accurate modelling approach and need to be used further in structural and civil engineering problems. Present study explored the use of cost as a hyper tuning parameter to create the model, but metaheuristic algorithm can also be used for optimization of hyper tuning parameter SVM.

REFERENCES

[1] Abounia Omran, Behzad & Chen, Q. & Jin, Ruoyu. (2016). Comparison of Data Mining Techniques for Predicting Compressive Strength of Environmentally Friendly Concrete. Journal of Computing in Civil Engineering. 30. 04016029. 10.1061/(ASCE)CP.1943-5487.0000596.

[2] Applied Technology Council (ATC) (1978) Tentative provision for the development of seismic regulations for buildings. Report No. ATC3-06. Applied Technology Council, Redwood.

[3] Asteris PG, Repapis CC, Tsaris AK, Di Trapani F, Cavaleri L(2015) Parameters affecting the fundamental period of infilled RC frame structures. Earthq Struct 9(5):999-1028.

[4] Asteris PG, Tsaris AK, Cavaleri L, Repapis CC, Papalou A, Di Trapani F, Karypidis DF (2016) Prediction of the fundamental period of RC frame structures using artificial neural net-works. Comput Intell Neurosci 016:5104907

[5] Asteris PG, Repapis CC, Repapi EV, Cavaleri L (2017) Fundamental period of infilled reinforced concrete frame struct Infrastruct Eng 13(7):929-941

[6] Asteris PG, Repapis CC, Foskolos F, Fotos A, Tsaris AK(2017) Fundamental period of infilled RC frame structures with vertical irregularity. Struct Eng Mech 61(5):663-674

[7] Asteris, P.G., Nikoo, M. Artificial bee colony-based neural network for the prediction of the fundamental period of infilled frame structures. Neural Comput & Applic 31, 4837–4847 (2019). https://doi.org/10.1007/s00521-018-03965-1

[8] Chen T, Morris J, Martin E(2007) Gaussian process regression for multivariate spectroscopic calibration, Chemometr Intell lab Syst 87(1):59-71. https://doi.org/10.1016/j. chemolab.2006.09.004

[9] Chiauzzi L, Masi A, Mucciarelli M, Cassidy JF, Kutyn K, Traber J, Ventura C, Yao F (2012) Estimate of fundamental period of reinforced concrete buildings: code provisions vs. experimental measures in Victoria and Vancouver (BC, Canada). In: Proceedings of 15th world conference on earthquake engineering 2012 (15WCEE), Lisbon

[10] Cortes C, Vapnik VN. Support vector networks. Mach Learn 1995;20(3):273-97.

[11] Crowley H, Pinho R (2004) Period-height relationship for existing European reinforced concrete buildings. J Earthq Eng 8(1):93-119, https://doi.org/10.1080/13632460409350522
[12] Crowley H, Pinho R (2006) Simplified equations for estimating the period of vibration of existing buildings. In: Proceedings of seismology, Geneva, 3-8 sept, Paper Number1122
[13] E-Tabs (2015)- Integrated software for structural analysis and design. Version 15.0. Berkeley. Computer & Structures, Inc 2015.
[14] Eurocode 2: Design of concrete structured-Part 1-1: general rules and rules for buildings (2004) EN 1992-1-1, Comite Europeen de Normalisation
[15] Eurocode 8: Design of structures for earthquake resistance. Part pp 1-1998. European Standard EN Brussels
[16] European Committee for Standardization CEN (2004) Eurocode 8: design of structures for earthquake resistance -part 1: general rules, seismic actions and rules for buildings. European Standard EN 1998-1
[17] FEMA-450 (2003) NEHRP recommended provisions for seismic regulations for new buildings and other structures. Part 1: provisions. Federal Emergency Management Agency, Washington
[18] Goel RK, Chopra AK (1997) periods formulas for moment resisting frame buildings. ASCE J Struct Eng123(11):1454-1461. http://doi.org/10.1061/(ASCE)0733-9445(1997)123:11(1454)
[19] Guler K, Yuksel E, Kocak A (2008) Estimation of the fundamental period of existing RC buildings in Turkey utilizing ambient vibration records. J Earthq Eng 12(S2):140-150. http://doi.org/10.1080/13632460802013909.
[20] IS 1893 (Part 1)- 2016: Indian standard criteria for Earthquake Resistant Design of Structures, Part 1- General Provisions and Buildings (Sixth Revision), Bereau of Indian Standards, New Delhi.
[21] Pal M, Deswal S (2008) Modeling pile capacity using support vector machines and generalized regression neural network. J Geotech Geoenviron Eng 134(7):1021-1024. https://doi.org/10.1061/(ASCE)1090-0241(2008)134:7(1021)
[22] Pal M, Deswal S (2010) Modelling pile capacity using Gaussian process regression. Comput Geotech 37(7):942-947. https://doi.org/10.1061/j.compgeo.2010.07.012
[23] Pal M, Deswal S (2011) Support Vector regression based shear strength modelling of deep beams, computer and structures 89 (2011):1430-1439.
[24] Platt JC. Fast training of support vector machines using sequential minimal optimization. In: Scholkopf B, Burges C, Smola A, editors. Advances in kernels methods: support vector machines . Cambridge, MA: MIT Press:1999.
[25] RStudio Team (2015). RStudio: Integrated Development for R. RStudio, Inc., Boston, MA. http://www.rstudio.com/.
[26] Sung AH, Mukkamala S. Identifying important features for intrusion detection using support vector machines and neural networks. In: Workshop on statistical and machine learning techniques in computer intrusion detection, June 11-13, Johns Hopkins University, US: 2002.
[27] S Varadharajan, V.K. Sehgal, B. Saini, Fundamental time period of RC setback Buildings, Concrete Research Letters, vol.5, pp. 901-935, 2014b.
[28] UBC (1997). International conference of building officials (ICBO), Uniform Building Code. Whittier, California, 1997
[29] Vapnik VN. Statistical learning theory, New York: John Wiley and Sons; 1988.
[30] Vapnik VN. The nature of statistical learning theory. New York: Springer- Verlag: 1995.
[31] Witten IH, Frank E. Data mining: practical machine learning tools and techniques. 2nd ed. San Franciso: Morgan Kaulmann; 2005.
[32] William F. Baker et al. The Challenges in Designing the World's Tallest Structure: The Burj Dubai Tower, Structures 2009: Don't Mess with Structural Engineers American Society of Civil Engineers, 2012

CIVIL ENGINEERING JOURNAL

Article no. 42

THE CIVIL ENGINEERING JOURNAL 2-2021

STUDY ON THE PROPERTIES OF POLYURETHANE-CEMENT COMPOSITE (PUC)

Kexin Zhang[1,2], Dachao Li[2], Tianyu Qi [2], Yanfeng Li [2] and Xingwei Xue[2]

1. *MOE Key Lab of Disaster Forecast and Control in Engineering, Jinan University, No.601 Huangpu Dadao West, Guangzhou, Guangdong Province, China; jt_zkx@sjzu.edu.cn*
2. *School of Traffic Engineering, Shenyang Jianzhu University, No.25 Hunnan Zhong Road,Shengyang, Liaoning Province, China*

ABSTRACT

In order to study the properties of polyurethane cement composite (PUC) material, this paper has carried out the tests of compressive resistance, flexural resistance, axial tension, bonding and acid and alkali corrosion resistance of the material. The average compressive strength of the material is 59.3 MPa, the average flexural strength is 41.5 MPa, and the average axial tensile strength is 31.0 MPa. The bonding strength between the material and concrete in axial tension is 3.56 MPa, and that between the material and concrete in bending is 3.16 MPa. The failure interface of the two bond tests is not on the bond surface, indicating that the polyurethane cement composite (PUC) material has good bonding property. The chemical corrosion resistance test of polyurethane cement material showed no visible change on the surface of the material, indicating good chemical corrosion resistance.

KEYWORDS

Polyurethane cement, Mechanical property, Acid and alkali resistance, Adhesive property

INTRODUCTION

Bridge is an important part of highway transportation and plays an important role in highway transportation. With the continuous development of social economy and increasingly busy transportation, bridge as the throat of highway traffic plays an irreplaceable role [1-3]. With the development of social economy, the transportation industry is unprecedentedly prosperous. As the carrier of transportation, the vehicle has undergone great changes compared to the past, with the increase of vehicle load and flow being the most obvious. Due to the rapid increase of vehicle load, coupled with the influence of acid rain, air and temperature and other natural conditions, the bridge structure has produced a series of diseases such as stress crack, concrete deterioration, steel corrosion and so on [4-6]. These man-made and natural factors affect the bridge to varying degrees, mainly reflected in the safety, applicability and durability of the structure, and finally reduce the bearing capacity of the bridge, endangering the long-term operation of the bridge [7-11].

Bridge superstructure reinforcement methods include section enlargement method, bonding high-strength composite fiber material, bonding steel plate method, reinforcement method of external unbonded prestressed steel strand [12-15]. The section enlargement method is a traditional reinforcement method, which has the advantages of simple construction and strong adaptability, but the wet work workload is large, the construction maintenance period is long, the dead weight increases greatly, and the traffic is greatly affected. The reinforcement method of sticking steel plate can give full play to the tensile performance of steel and the compressive performance of masonry materials. The construction is simple, the construction period is short, and the influence on traffic is

small. However, the steel plate is difficult to adapt to the uneven concrete surface, and it is easy to rust in the natural environment. The bonded fiber material method is simple in construction and has little influence on the original structure as a whole. In the microscopic aspect, the physical and chemical properties of the carbon fiber composite are stable and can resist the harsh environment. However, the carbon fiber cloth/board is relatively thin, which does not significantly improve the structural stiffness and the material cost is high. Prestressed steel strand reinforcement method can make the bearing capacity and stiffness increase more obviously, but it has the disadvantage of being greatly affected by the site and component conditions, and the construction is very troublesome.

Polyurethane cement composite (PUC) material has the characteristics of early strength and convenient construction, which is used for structural reinforcement by scholars. Yang Yongqing [16] studied the bridge performance after the reinforcement of pouring polyurethane concrete, and the results showed that the transverse load distribution influence line of the reinforced hollow slab bridge was gentler than that before the reinforcement, and the overall transverse mechanical performance of the bridge was significantly improved. Guiwei et al. [17] obtained polyurethane concrete composite material through material preparation, and reinforced Zhejiang Baixi Bridge with PUC material. The results show that polyurethane concrete material can better improve the bearing capacity of the structure and can carry out construction operations without the traffic being stopped. Zhang Hongxiang et al. [18] took Zhongxing Bridge as an example to carry out an experimental study on the bearing capacity of bridges reinforced with polyurethane concrete, showing that the bearing capacity and stiffness of bridges reinforced with polyurethane concrete have been greatly improved. Gao Feng [19] carried out bending reinforcement test of PUC material for 13 m hollow slab beams, and no slip between PUC material and concrete section appeared in the whole test process. Formulas for calculating the strain and flexural capacity of hollow slab beams reinforced by PUC are established. Gu Dandan et al. [20, 21] carried out load tests on the reinforced hollow slab girder bridge, and the test results showed that the strength and stiffness of the reinforced structure were significantly improved. Haleem K et al. [22-24] used polyurethane cement (PUC) composites to carry out flexural reinforcement tests on 7 T-section beams with different damage degrees, and the results showed that the ultimate bearing capacity of the beams strengthened with PUC could be significantly improved and the cracks of the beams could be significantly reduced.

At present, the research on PUC mainly focuses on the reinforcement of bridge structures, the study of polyurethane cement composite is not comprehensive enough. In order to make PUC get better application, the mechanical properties and acid and alkali corrosion resistance of polyurethane cement material were systematically studied in this paper.

METHODS PUC RAW MATERIALS AND RATIO

Polyurethane (PU)

Polyurethane cement is a kind of polymer concrete material, its main component is polyurethane. Polyurethane is a polymer with excellent performance, mainly from the polymerization of isocyanates and polyols, the main raw material components are shown in Table 1.

The hardness range of polyurethane materials is 10-100 (IRHD), where 0 (IRHD) represents a modulus of elasticity of 0, and 100 (IRHD) represents an infinite modulus of elasticity. Polyurethane material has good wear resistance, chemical corrosion resistance, fluidity, bonding and molding properties. A series of polyurethane cement materials were developed by measuring the density of the new material.

Tab. 1 - Main chemical composition of polyurethane

Chemical Constitution		Percentage（%）
polyhydric alcohols	Polyether	49
	Silicone oil	1
	water	0-1
isocyanate		50-51

Polyurethane cement composite (PUC)

Polyurethane cement composite (PUC) raw materials in accordance with the quality ratio of mixing and polymerization reaction, polyol: isocyanate: cement =1:1:2 (mass ratio). High density polyurethane cement material was prepared, as shown in Table 2. Polyol, isocyanate and cement were the main raw materials in the mixture ratio. The polyurethane cement material was cured in dry environment for 7 d. The production process of PUC is shown in Figure 1 and Figure 2.

Tab. 2 - Composition of PUC

PUC	Percentage（%）
Polyether polyol	25
Isocyanate	25
Cement	50

Fig.1- PUC material mixing diagram

Fig. 2- Pouring drawing of PUC

MATERIAL CHARACTERISTIC TEST

Test content

In this paper, starting from the properties of PUC material, the corresponding stress-strain curve is obtained through compressive test, flexural test and axial tensile test. The bonding strength and failure mode under different stress forms are obtained through axial tensile bonding test and bending bonding test. Finally, the PUC material was placed in different concentrations of acid and alkali solutions, and the acid and alkali corrosion resistance of the material was analyzed by testing the mass loss and apparent appearance of the specimen

Compression and bending test

Compression and flexural strength

In order to study the mechanical properties of PUC, 1550 kg/m^3 PUC material with high compressive strength and flexural strength was selected as the research object in this paper. The polyurethane cement material with a density of 1550 kg/m^3 is expressed as PUC-1550, with the matching as shown in Table 3. The compressive strength test adopts the cube test with the size of 70mm×70mm×70mm, and the bending strength adopts the rectangular test with the size of 450mm×100mm×100mm. Resistance strain gauges are pasted on the surface of the cube block along the horizontal and vertical sides respectively to measure the horizontal and vertical strain changes of the cube block in the process of compression. In the middle position of the cuboid,

resistance strain gauges are arranged on the top surface, the bottom surface and the middle position respectively along the horizontal direction to test the strain changes at the top edge and bottom edge of the specimen during the bending resistance process.

Firstly, the polyurethane raw material and cement are poured into the container according to the mass proportion, and the material is mixed evenly with an electric stirring rod for 3 min. Then the material is poured into the steel test mold and cured for 7 d under dry conditions. Compressive strength and flexural strength tests of PUC were carried out according to specification JTG E30-2005. Figure 3 and Figure 4 are the test drawings of the compressive strength and flexural strength of cubes. The resistance strain gauge is attached to the surface of the cube block and the prism block to measure the strain value during the loading process. The compressive strength and flexural strength tests of PUC-1550 material are shown below.

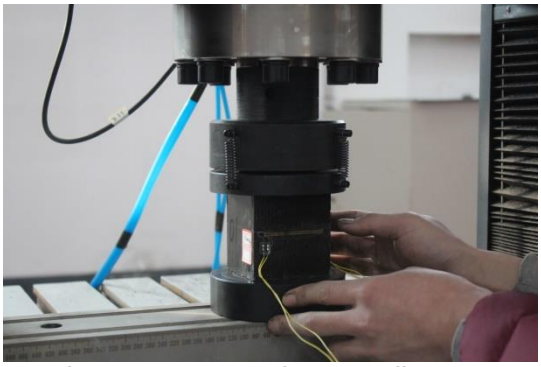

Fig. 3 - Compression test diagram

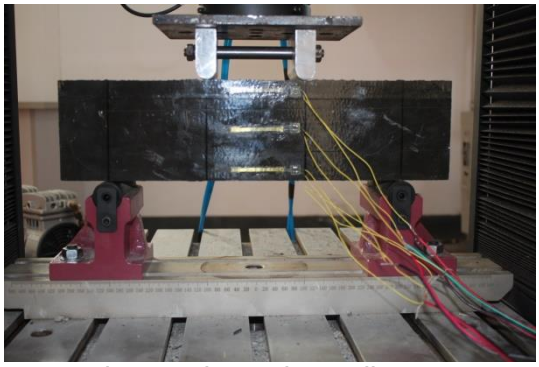

Fig. 4 - Flexural test diagram

The compressive strength and flexural strength of PUC-1550 are shown in Table 4 and Table 5. As can be seen from Table 3, the compressive strength of PUC with a density of 1507 kg/m^3~1588 kg/m^3 is 57.8 MPa ~ 60.6 MPa, with an average density of 1552 kg/m^3 and an average compressive strength of 59.3 MPa. According to Table 4, the flexural strength of PUC with a density of 1524 kg/m^3~1584 kg/m^3 is 39.6 MPa ~ 43.3 MPa, with an average density of 1548 kg/m^3 and an average flexural strength of 41.5 MPa.

Tab. 3 - Compressive strength values of PUC-1550

Number	F01	F02	F03	F04	F05	F06	Average Value
Density (kg/m^3)	1507	1524	1544	1568	1579	1588	1552
Strength (MPa)	60.6	57.8	59.3	59.6	59.5	59.0	59.3

Tab. 4 - Bending strength values of PUC-1550

Number	C01	C02	C03	C04	C05	C06	Average Value
Density (kg/m^3)	1524	1533	1546	1560	1577	1584	1548
Strength (MPa)	42.2	39.6	40.8	41.1	43.3	41.9	41.5

Compressive stress-strain curve

The test was loaded by the universal testing machine, and the number of compressive specimens was six. The dynamic strain acquisition instrument was used for the collection. According to the measurement results of each test block, the compressive average stress-strain curve is obtained, as shown in Figure 6. At the initial loading stage, the stress-strain curve shows a linear relationship, the average compressive strength is 59.3 MPa, and the strain is 27956 με. In the late loading stage, the stress-strain curve is nonlinear, and the strain at failure is 34612 με.

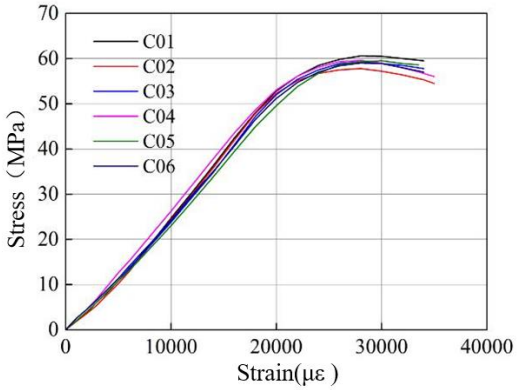

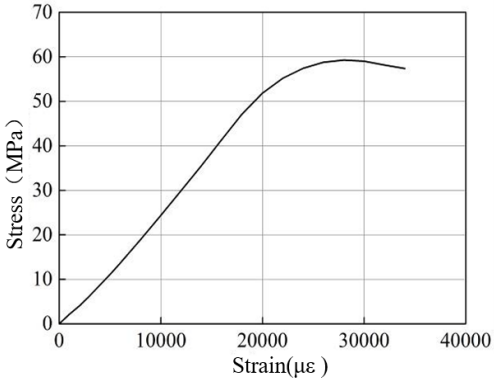

Fig. 5 - Compressive stress-strain curve *Fig. 6 - Compressive stress-strain curve (average)*

Blending stress-strain curve

The flexural specimens were prismatic blocks, with a number of six, and were cured for 7 d under dry conditions. The dynamic strain acquisition instrument was used for data acquisition. The resistance strain gauges were pasted on the top surface, bottom surface and middle position of the test block, and the top surface was used to measure the compressive strain of the specimen in the bending process. The bottom surface measures the tensile strain of the specimen in the bending process, and the strain value is the average value of the measured values of the two resistance strain gauges in each test block. The bending stress-strain curve of each test block is shown in Figure 7. According to the tensile measurement results of each test block, the average stress-strain curve of tension is obtained, as shown in Figure 8. The average tensile strength is 41.5 MPa. According to the stress-strain curve, the elastic modulus of bending and tension was calculated to be 4300-5200 MPa.

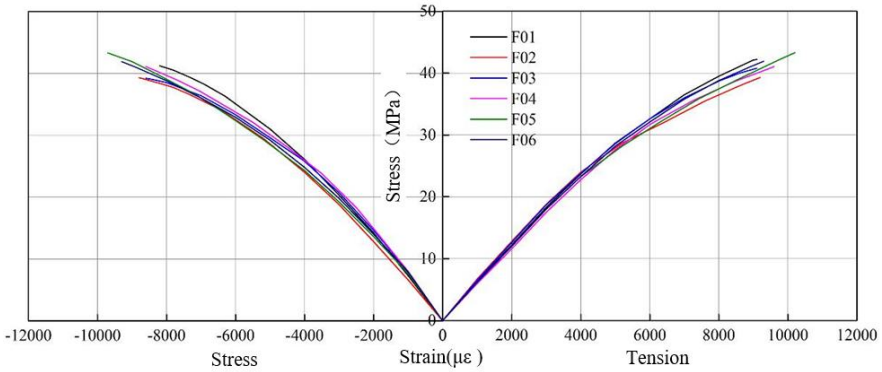

Fig. 7 - Flexural stress-strain curve

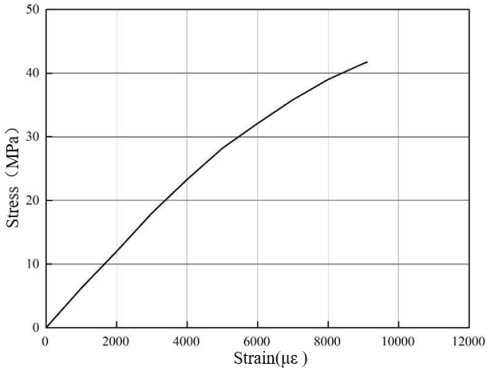

Fig. 8 - Tensile stress-strain curve (average)

According to the stress and strain relationship points of the tensile side of the flexural specimen, the stress-strain relationship curve is fitted, as shown in Figure 9. The fitting formula is as follows:

$$\sigma\text{=-}268870.3\varepsilon^2\text{+}6954.1\varepsilon\text{-}0.237 \quad R^2 = 0.999 \tag{1}$$

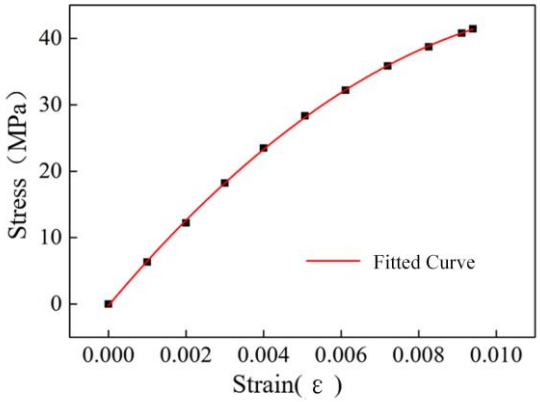

Fig. 9 - Stress-strain relationship fitting curve

Poisson of polyurethane cement material is shown in Figure 10, the average value of Poisson's ratio is a constant value v=0.27.

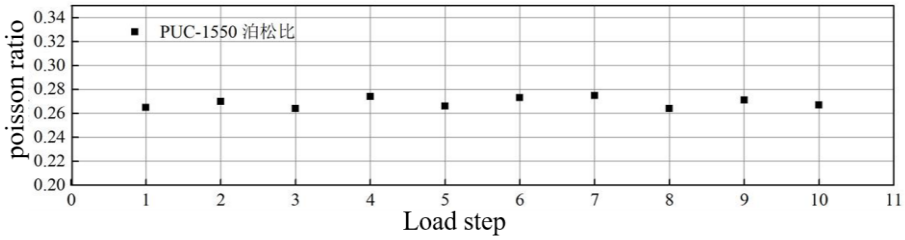

Fig. 10 - Poisson's ratio diagram of PUC

Direct tensile test of material

Specimen making

The specimen in this test is a dumbbell type sheet specimen with a thickness of 10mm, a middle width of 25mm and a width of 40mm on both sides, as shown in Figure 11. The mold test in the pouring process is self-designed, as shown in Figure 12. The tensile test was carried out 7 d after the PUC material was cast. The tensile test was carried out on the small-range tester, and the loading speed was 50 N/s. The resistance strain gauge was pasted in the middle of the specimen and pasted symmetrically on both sides along the stretching direction to measure the strain change in the stretching process. The dynamic strain acquisition instrument was used for data acquisition.

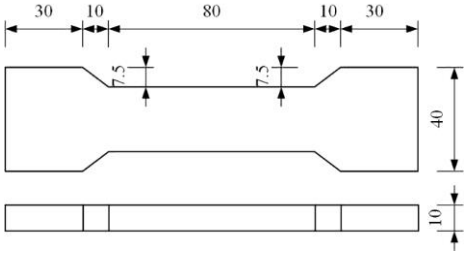

Fig. 11- Dimensions of PUC axial tensile specimen (unit: mm)

Measurement results

Tab. 5- PUC material axial tensile strength

Number	ZL01	ZL02	ZL03	ZL04	ZL05	ZL06	Average Value
Strength（MPa）	30.5	31.8	31	32.1	31.6	28.9	31.0

According to the data in Table 5, the average axial tensile strength of polyurethane cement material is 31.0 MPa, and the straight-tension elastic modulus is calculated to be 4200-5700 MPa according to the stress-strain curve.

According to the tensile force and the corresponding strain data collected during the test, the stress-strain relationship curves of the six specimens in straight tension were drawn, as shown in Figure 12. According to the straight-tension measurement results of the test block, the average stress-strain curve of axial tension is obtained, as shown in Figure 13.

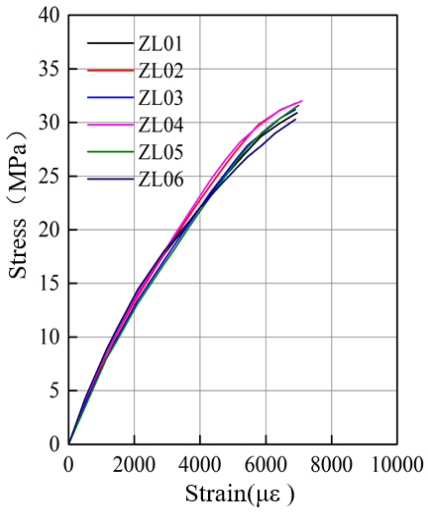

Fig. 12 - Direct tensile stress-strain curve

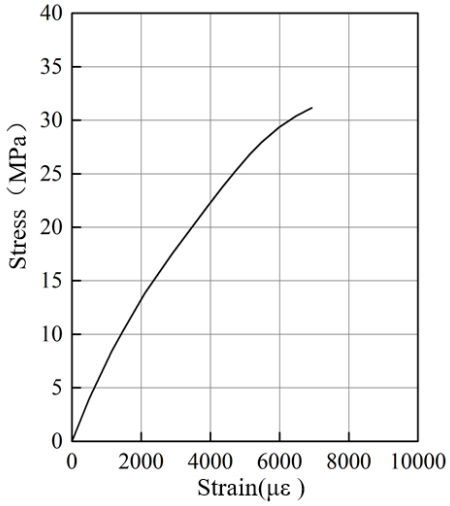

Fig. 13 - Stress-strain curve (average)

According to the stress and strain relationship points of axial tensile specimens, the stress-strain relationship curve is fitted, as shown in Figure 14. The fitting formula is as follows:

$$\sigma = 0.496 + 6977.3\varepsilon - 365682.2\varepsilon^2 \quad R^2 = 0.999 \tag{2}$$

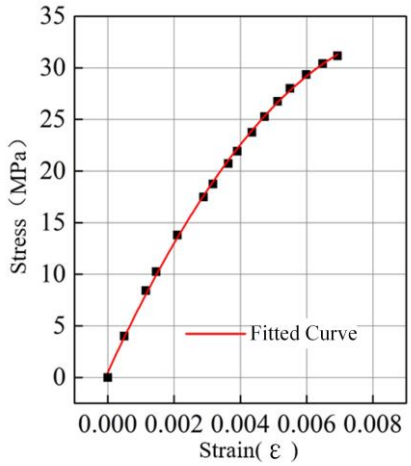

Fig. 14 - Fitting curve of axial tensile stress-strain relationship

Bonding test between material and concrete

Direct tensile bonding test

First of all, the concrete is cut into 100mm×100mm×100mm cube blocks with the concrete cutting machine to expose the aggregate of concrete and remove the floating ash on the surface of concrete. Then a 50mm×50mm×50mm template with an inner cavity is made and placed on the concrete block so that the template is perpendicular to the concrete surface to avoid excess stress. Then place the 80mm length bolt into the formwork so that the bolt center corresponds to the center of the concrete test block, as shown in Figure 16b. Finally, polyurethane cement material was poured into the formwork, and the wood formwork was removed after 7 d. The number of the same test blocks is three. The size diagram of the test blocks is shown in Figure 15. The concrete block of the specimen is inserted into the custom fixture, the fixture tie rod is upward, and the specimen screw is downward. The fixture with the specimen is placed on the tension test machine, the fixture tie rod is placed in the upper jaw, and the specimen screw is placed in the lower jaw, as shown in Figure16a. In the process of tensile test, the ultimate tensile force of the specimen was tested.

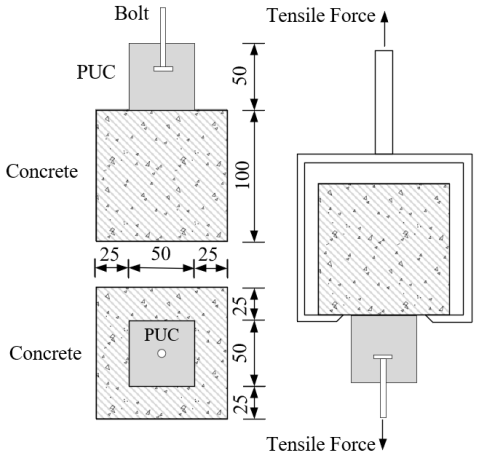

Fig. 15 - Schematic diagram of tensile bonding specimen size (unit: mm)

Calculate the axial tensile bond strength of polyurethane cement and concrete according to formula (2-3) :

$$\sigma = \frac{F}{ab} \tag{3}$$

F —Ultimate Tensile Force of the Specimen；

a — length of the contact surface between PUC and concrete；

b —Width of the contact surface between PUC and concrete.

Tab. 6 - PUC material bonding strength table

Number	ZN01	ZN02	ZN03	Average value
Strength (MPa)	3.35	3.58	3.75	3.56

The direct tensile bonding test results of PUC materials are shown in Table 6. The bonding force between PUC material and concrete is larger than that of concrete material itself, and the average bonding stress is 3.56 MPa. In the tensile process, the concrete material itself will suffer bond failure, as shown in Figure 16c and Figure 16d. The failure interface does not occur on the bonding surface between concrete and PUC material, indicating that PUC material has good bonding property.

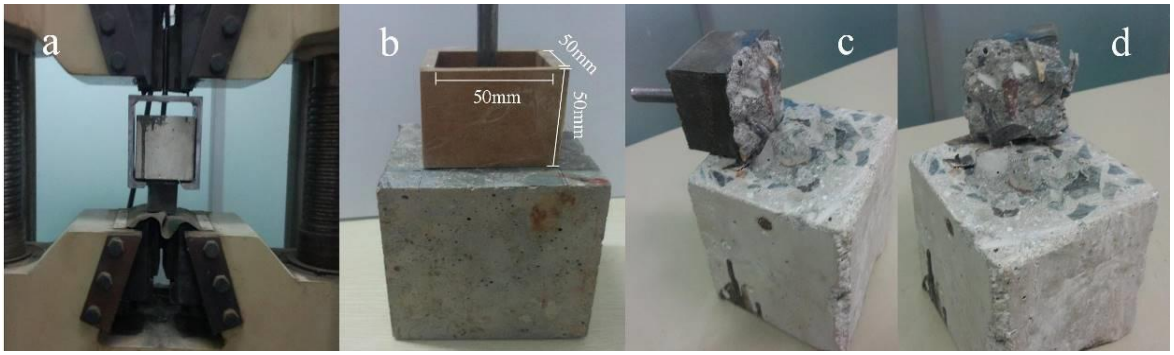

Fig. 16 - Test diagram of direct drawing bonding (Unit: mm)

Bending bond test

According to the method of bonding between polymer concrete and concrete tested by the Romanian National Institute of Building Research and Development [25], the bond test of PUC material was conducted. The casting of the bonding test blocks was completed in the 70mm×70mm×70mm concrete triplet die. The cut 70mm×70mm×70mm concrete test blocks were placed in both ends of the triplet die, and the PUC material was poured in the spare position in the middle, and the casting height was 60 mm. The number of the same specimen is three, and the size of the specimen is shown in Figure 17 and Figure 18b. The universal testing machine was used for three-point loading, and the distance between the two fulcrum points was 160mm, so as to obtain the flexural strength of the specimen in the loading process, as shown in Figure 18a.

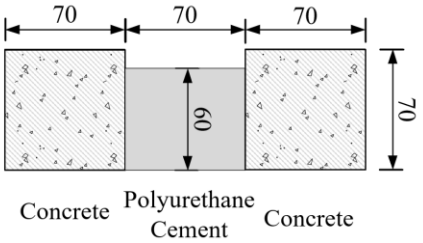

Fig. 17 - Schematic diagram of bonding test block size (unit: mm)

Calculate the axial tensile bond strength of polyurethane cement and concrete according to formula (4) :

$$\sigma = \frac{3F\left(l\text{-}a\right)}{bh^2} \tag{4}$$

F — Bending destructive force of the specimen;
l — Distance between two fulcrum points during loading;
a — Longitudinal length of PUC in the specimen;
b — Transverse width of PUC in the specimen;
h — Height of PUC in the specimen.

Tab. 7 - PUC material bonding strength table

Number	WN01	WN02	WN03	Average value
Strength (MPa)	3.15	3.08	3.25	3.16

The bonding test results of polyurethane cement materials are shown in Table 7. The bonding force between polyurethane cement material and concrete is higher than the bonding force of concrete material itself, and the average bonding stress is 3.16 MPa. In the process of bending, the

bond failure of concrete material itself occurs, as shown in Figure 18c. The failure interface does not occur on the bonding surface between concrete and PUC material, indicating that PUC material has good bonding property.

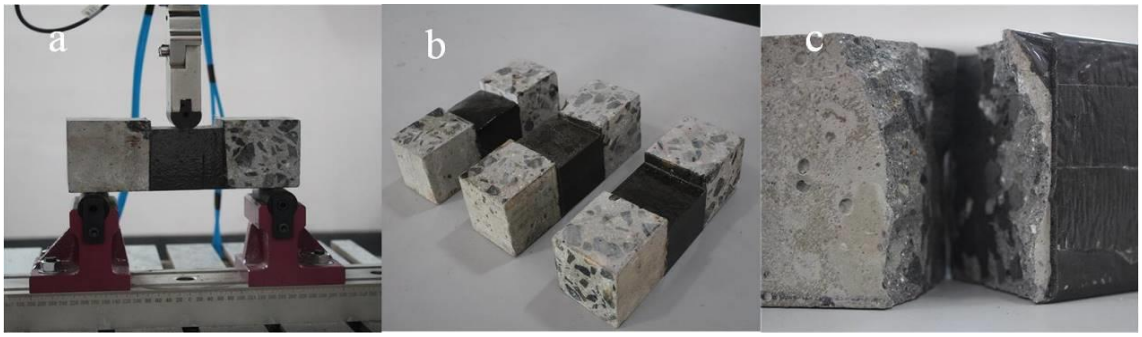

Fig. 18 - Bending bond test diagram

Acid and alkali resistance test

Two 40mm×40mm×160mm test blocks were taken, both in the middle of the test blocks, for the chemical corrosion resistance determination of PUC-1550. Low-concentration and high-concentration acid-base solutions are configured, as follows:

3% hydrochloric acid solution (volume fraction), 30g/L potassium hydroxide solution, 18% hydrochloric acid solution (volume fraction) and 100g/L potassium hydroxide solution.

The samples were put into an oven at 110℃±5℃ to dry. The difference value of weighing the test block for two consecutive times is no more than 0.1g, and then the test piece is cooled to the room temperature. The samples were then immersed in the test solution at a depth of 25 mm in each solution. The lid of the vessel is covered, and the soaked test samples are placed in the ambient temperature of 20℃± 2℃, as shown in Figure 19. After immersed in the solution for 12 d, the samples were taken out and washed with running water for 5 d. Then, the samples were completely immersed in boiling water and boiled for 30 min. After that, they were taken out and gently wiped with wring-out but still wet suede, and then dried in a drying oven at 110℃±5℃.

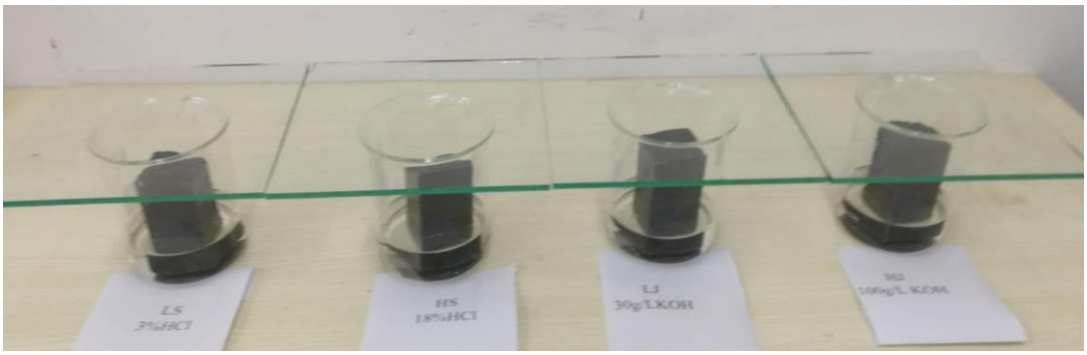

Fig. 19 - Chemical corrosion resistance determination

Tab. 8 - Chemical corrosion resistance determination

Number	Solution	Initial mass	Pre-test quality	Post-test quality	Quality loss	Mass loss rate（%）	Corrosion resistance grade
LS	3% HCl	94.76	94.59	94.47	0.12	0.127	ULA
HS	18% HCl	82.85	82.71	82.54	0.17	0.206	UHA
LJ	30g/L KOH	95.32	95.21	94.95	0.26	0.274	ULA
HJ	100g/L KOH	77.18	77.05	76.73	0.32	0.417	UHA

The test results of chemical corrosion resistance are shown in Table 8. There is no visible change on the surface after immersion in solution of different concentrations.

CONCLUSION

In this paper, through the compression, bending, axial tensile, tensile bonding, bending bonding and chemical corrosion resistance tests of PUC material (PUC-1550) with a density of 1550 kg/m^3, the research results can provide material theory basis for bridge reinforcement and new structure bridge, the conclusions are as follows:

The mean compressive strength of PUC-1550 is 59.3 MPa, the mean flexural strength is 41.5 MPa, the mean axial tensile strength is 31 MPa, and the Poisson's ratio of the material is 0.27. The bending tension stress-strain curve and the axial tension stress-strain curve were obtained by fitting.

The average bond strength between PUC-1550 material and concrete is 3.56 MPa through the axial tensile bond test, and 3.16 MPa through the bending bond test. The failure interface of the two bonding tests did not occur on the bonding surface between concrete and PUC material, indicating that polyurethane cement material has good bonding property.

Chemical corrosion resistance test was carried out in different concentrations of acid and alkali solution. The results show that the PUC surface has no visible change and it has good chemical corrosion resistance.

ACKNOWLEDGEMENTS

Thank You for the Open Fund project of key Laboratory of Ministry of Education for Disaster and Control of Major Engineering, Jinan University (20200904012)

REFERENCES

[1] Wang, E. L. ,2018. Construction monitoring on steel truss bridge's maintenance and reinforcement. Applied Mechanics and Materials, 878, 89-94.

[2] Liu, J.,2015. The detection evaluation and reinforcement research of kankan river bridge. Engineering, 07(7), 462-468.

[3] Yeh, C. K. , & Lin, H. T., 2016. Automatic bridge bidding using deep reinforcement learning. Journal of Lightwave Technology.

[4] Fang R, Yang X.,2015. Cause and Countermeasure of Structure Disease of Bridge[C]// International Conference on Transportation Information & Safety.

[5] Diao, Yan.,2014. Stone Arch Bridge Disease Detection and Evaluation[J]. Applied Mechanics & Materials, 501-504:1332-1335.

[6] Zhongqiu F, Guyu S , Tong S , et al.,2017. Research on Fatigue Diseases Evation of Steel Bridge Deck Based on Fuzzy Comprehensive Method [J]. Industrial Construction.

[7] Hui M C H , Wong C K P.,2009. Stonecutters Bridge–Durability, Maintenance and Safety Considerations[J]. Structure & Infrastructure Engineering, 5(3):229-243.

[8] Cheng, Kang.,2002. Modeling and Simulation of Bridge Stability Based on Deep Learning[C]// 2018.

[9] Gui, C. , Zhang, J. , Lei, J. , Hou, Y. , & Qian, Z. . (2021). A comprehensive evaluation algorithm for project-level bridge maintenance decision-making. Journal of Cleaner Production, 289, 125713.

[10] Lee W F , Chen C H , Chang C F , et al.,2010. Bridge Monitoring and Safety Evaluation Method Using a Vibration Thchnique [J].

[11] Utsunomiya T., 2004. Bridge Maintenance, Safety, Management and Cost[J].

[12] Wang Y , Zhu X , Hao H , et al.,2009. Corrosion-induced Cracking of Reinforced Concrete Beam : Experimental Study[J]. Applied Mechanics & Materials, 256-259(12):1148-1153.

[13] Sonoda K , Okino M , Hayashi H , et al.,2010. Reliability of Epoxy Bonded Steel Plate Method for Repairing Damaged RC Slabs of Bridge[J]. Proceedings of the Japan Society of Civil Engineers (398):245-254.

[14] Zhao S W , Qiao X P.,2011. Experimental Study on Reinforced Hollow Beam with Carbon Fiber Reinforced Polymer and External Prestressed Strand[J]. Applied Mechanics & Materials, 94-96:495-499.

[15] Zhishen G, Wei, et al.,2014. Flexural strengthening of RC beams using distributed prestressed high strength steel wire rope: theoretical analysis[J]. Structure & Infrastructure Engineering: Maintenance, Management, Life-Cycl.
[16] Yongqing Y, Meng Y, Xiaobin L.,2014. Theoretical and Experimental Study of Load Transverse Distribution of Hollow Slab Bridge Strengthened by Modified Polymer Concrete[J]. Bridge Construction , 44(6): 63-68.
[17] Jianlin W, Guiwei L, Lishui Y.,2013. Research on the application technology of strengthening hollow slab bridge with MPC composite material[J]. Highway, 8: 39-43.
[18] Hongxiang Z, Chao C , Tianlai Y.,2015. The application of simply supported T beam strengthended by MPC [J]. Low Temperature Architecture Technology, 3: 59-61.
[19] Feng G. An experimental study on strengthening reinforced concrete hollow-slab girder using new material polymethane-cement (PUC) [D]. Harbin Institute of Technology, 2016.
[20] Dandan G, Quansheng S.,2015. Study of Static Tests for Using MPC Composite Material to Strengthen Void Plate Girder Bridge[J]. World Bridges, 43(6): 88-92.
[21] Jiancai G, Yanqun Z, Bingjun C, Guiwei L., 2017. Reinforced concrete solid slab girder bridge reinforced with MPC composite materials[J]. Highway, 3: 126-130.
[22] Haleem K. H, Lianzhen Z, Guiwei., 2013. An experimental study on strengthening reinforced concrete T-beams using new material poly-urethane-cement (PUC)[J]. Construction and Building Materails, 40: 104-117.
[23] Haleem K. H, Guiwei L, Yuwen Y., 2014. Experimental study to investigate mechanical properties of new material polyurethane-cement composite (PUC)[J]. Construction and Building materials, 50: 200-208.
[24] Liu G, Otsuka H, Mizuta Y, Shimitsu A., 2006. A Foundational Study on Static Mechanical Characteristics of the Super Lightweight and High Strength Material Using Fly-ash[J]. Journal of the Society of Material Science Japan, 55(8):738-745.
[25] Leon Agavriloaie, Stefan Oprea, Marinela Barbuta, Florentina Luca. Characterisation of polymer concrete with epoxy polyurethane acryl matrix[J]. Construction and building materials, 2012, 37: 190-196.

CIVIL ENGINEERING JOURNAL

Article no. 43

THE CIVIL ENGINEERING JOURNAL 2-2021

ANALYSIS OF DYNAMIC AND STATIC CHARACTERISTICS OF SUSPENSION BRIDGE WITH WIND CABLES

Long Liu[1], Wenqi Li[2]

1. *Anyang Institute of Technology, the west end of Huanghe Avenue, Anyang 455000, China;20160913@ayit.edu.cn*
2. *China Construction Second Bureau Second Construction Engineering Co., Ltd., No.0169, Qianhai Road, Shenzhen, 518000,China; 2107596884@qq.com*

ABSTRACT

In this paper, a suspension bridge carrying oil pipelines is taken as the research object. A spatial finite element analysis model of the bridge is established for the bridge by using MIDAS/CIVIL finite element analysis software, and the structural analysis of static and dynamic characteristics is carried out. The analysis of dynamic characteristics shows that the wind cable can greatly improve the natural vibration characteristics of the suspension bridge. The analysis of static characteristics shows that the internal forces of the suspender are evenly distributed and the vertical displacement of the main girder of the steel truss is distributed in a parabola, besides, the strength of each main component can meet the safety needs.

KEYWORDS

Pipeline, Suspension bridge, Wind cable, Dynamic, Static

INTRODUCTION

In addition to being used by people and vehicles, the bridge also has an important function. It can also undertake the crossing obstacles such as oil and gas pipelines. Due to the requirement of crossing rivers and valleys, it is necessary to build some special bridges with large span during the transportation of oil and gas pipelines. Suspension bridges have advantages such as large span capacity, light deadweight, small damping and large flexibility, which make them more competitive in the selection of long-span bridge types. Suspension bridges have strong adaptability to complex terrain and climate. Many suspension span structures have been applied in the transportation process of oil and gas in China. These suspension bridges usually have long spans and are located in complex terrain and climate.

On pipeline, pipe accessories and supporting components, according to the environment, erection forms and working conditions, considering the combination of gravity, variable loading and accidental loading, design and check calculations are carried out. If necessary, wind resistance and seismic dynamic performance analysis should be carried out according to the environment of the pipeline project. As early as 1979, static and dynamic load test research on a 720m span suspension bridge was carried out by Deyin Li over the Dnieper River [1]. In 2018, Chong Chen and others made researches on deformation and stress change of long-span suspension bridge under wind load the with the method of finite element analysis [2]. In 2020, Lei Wang and others made analyses of the stress and deformation of suspension bridge under various working conditions [3]. In 2021, Yongzhen Wang and others conducted an experimental study on the structural safety of suspension bridge through scaling test [4].

In this paper, the structure of a suspension bridge with wind cables is analyzed, the spatial finite element model of the suspension bridge is settled by using MIDAS/CIVIL software. The influence of wind cable setting on the dynamic characteristics of the bridge is studied, and the

static structure of the whole bridge is analyzed, which can provide a necessary reference for the design and construction of similar bridges.

BACKGROUND

The span layout of a suspension bridge for a crude oil pipeline is (29+270+29) m, and the elevation of the bridge is shown in Figure1 (a). The vector height of the middle span main cable is f=22.5m, the vector to span ratio is f/1=1/12, the suspender spacing is 5m, and no suspender is set for the side span main cable. The main girder is in the form of steel truss, and every 5m is a section. The diameter of crude oil pipeline is D610×12.7mm. The shape of the main cable is catenary, and the curve cable arrangement is adopted for the wind cable. Its layout is shown in Figure1(b). Parallel wire bundles of φ7mm are used for the main cables and the main cables of the wind cables; parallel wire bundles of φ5mm are used for the hanger rod of the main cables and the stay cable of the wind cables. The tower is made of A-shaped steel tower, and the main limbs and transverse belly bars are made of seamless steel tubes. The tower height H =29.1m, the transverse center spacing at the top of the tower B= 1.5m, and the transverse center spacing at the bottom B=4.5m.

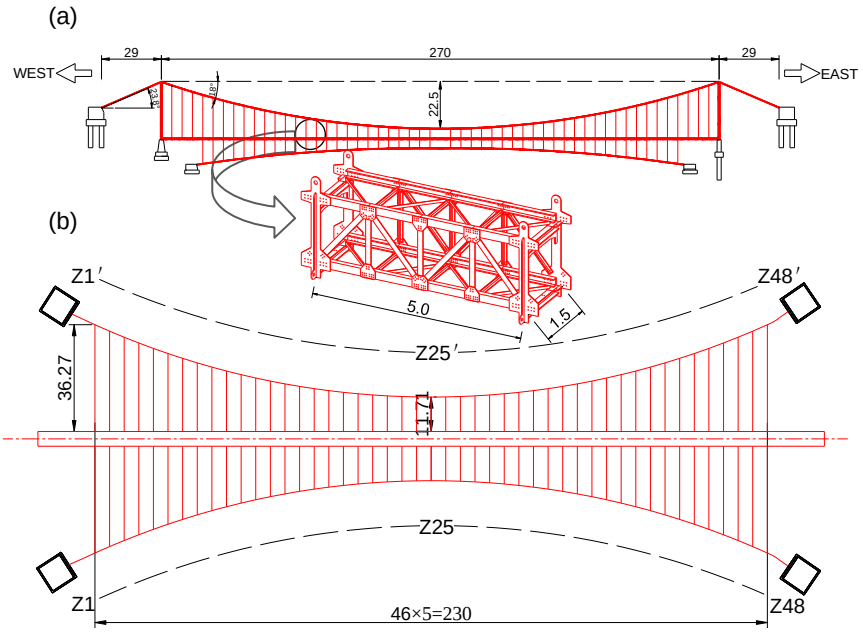

Fig. 1 – Bridge Layout (unit: m) (a) Elevation; (b) Wind cable plan

FINITE ELEMENT MODEL

MIDAS/CIVIL analysis software is adopted to analyse the suspension bridge with wind cables. Considering the stress characteristics of each component, two types of elements are applied in the finite element analysis of the model: tension-only truss element and beam element.

Tensile only truss units: main cables, main cable derricks, wind cables, and wind cable stays are all used as tension-only truss elements, serving only to transmit the axial tension between the components. This element is a three-dimensional spatial element, and the two nodes of the element have 6 degrees of freedom. There are 408 tension only truss elements in the model.

Beam element: beam element is similar to truss element, since MIDAS/CIVIL carries out spatial three-dimensional calculation, beam element is a spatial element. Each node of the element has 3 translational degrees of freedom and 3 rotational degrees of freedom. Beam element is adopted in the model of steel tower and steel truss beam. There are 2756 beam elements in the model.

The boundary conditions adopted by the model are as follows: hinge constraints at both ends of the steel truss girder and the bottom of the steel tower (ball hinge structure), fixed constraints at both ends of the main cable and wind cable. For the steel truss girder, which is the hinged connection mode to simulate its joints, the method of releasing beam end hinge constraints is adopted. The gravity of the main cable is taken into account, and the equivalent elastic modulus method proposed by German engineer Ernst in 1932 is adopted to modify the elastic modulus of the main cable.

In order to study the influence of wind cables on the dynamic characteristics of the suspension bridge with wind cables, two different finite element models were established, as shown in Figure 2.

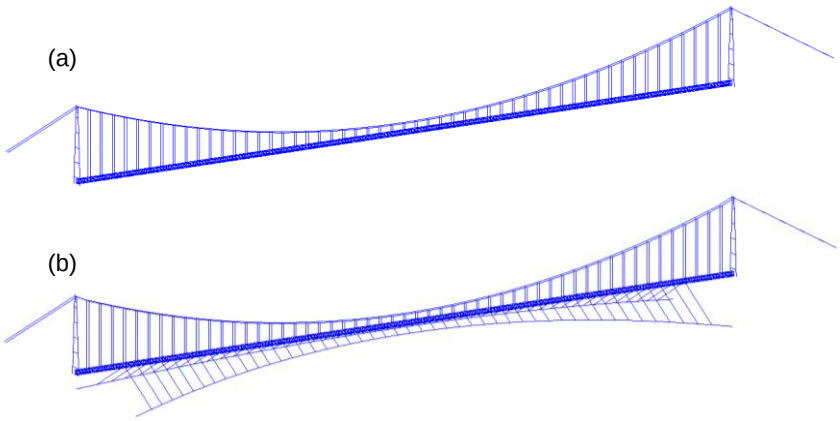

Fig. 2 – Finite element model (a) Without wind cable; (b) With wind cable

DYNAMIC CHARACTERISTICS ANALYSIS

In this paper, the influence of wind cables on the dynamic characteristics of suspension bridge with wind cables is analyzed.

(1) Dynamic characteristics without wind cables

First, natural vibration characteristics are analyzed according to the general suspension cable structure without setting wind cable. The Lanczos method is used to calculate the natural vibration characteristics of the bridge, namely, all the loads are converted into mass firstly, and then the structure is discretized through the method of the finite element. The calculated natural frequencies of the first four orders are shown in Table1:

Tab. 1 - Frequency and period of the first fourth order natural vibration (without wind cable)

Mode number	Frequency (cycle/sec)	Period (sec)	Allowable error
1	0.067	14.912	0
2	0.184	5.435	0
3	0.184	5.426	0
4	0.317	3.150	0

Main modes are shown in Figure3:

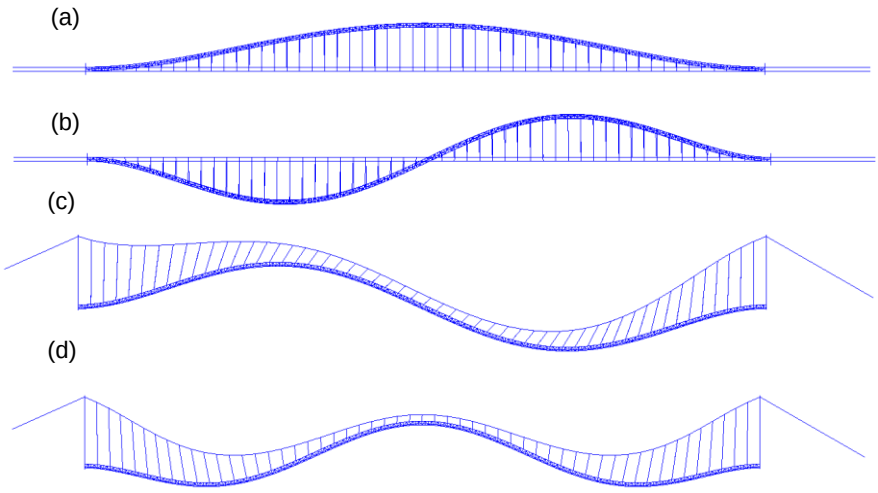

Fig. 3 - Modal diagram of mode shapes without wind cable (a) Mode 1; (b) Mode 2; (c) Mode 3; (d) Mode 4

Table1 lists the first four order natural vibration frequencies and periods of the suspension bridge in the absence of wind cables. The first-order natural vibration period is 14.912s and the frequency is 0.067Hz, indicating that the first-order natural vibration period is relatively long, and the suspension bridge belongs to a long-period without wind cables. Figure 3 shows the first four modes of the suspension bridge in the absence of wind cables, the first-order natural vibration mode characterized by symmetrical transverse bending girder 1 order, second- order natural vibration modal expression is antisymmetric transverse bending girder 1 order, 3 order natural vibration modal of girder antisymmetric order vertical bending, 4 order natural vibration modal of antisymmetric vertical bending girder 2 order. It can be seen that without wind cables, the structural natural vibration is first manifested as transverse bending, indicating that the suspension bridge is more affected by transverse wind load or transverse seismic force, while the vertical bending appears later [5-7].

(2) Dynamic properties with wind cables

Since the main girder with small size and greater flexibility is usually used in the suspension bridge, wind cables can be installed in this type of bridges. As shown in Figure 1 and Figure 2 (b), wind cables are also installed in the suspension bridge. The main cable of the wind cable is curved in space, and the plane where the wind cable stays is at an angle of 30 degrees from the horizontal plane. The natural vibration characteristics of the suspension bridge are calculated when wind cables are set, and the obtained first four natural vibration frequencies and periods are shown in Table 2:

Tab. 2 - Frequency and period of the first fourth order natural vibration (with wind cable)

Mode number	Frequency (cycle/sec)	Period (sec)	Allowable error
1	0.338	2.955	0.00E+00
2	0.431	2.322	0.00E+00
3	0.745	1.342	5.23E-83
4	0.795	1.258	5.28E-76

Main modes are shown in Figure 4:

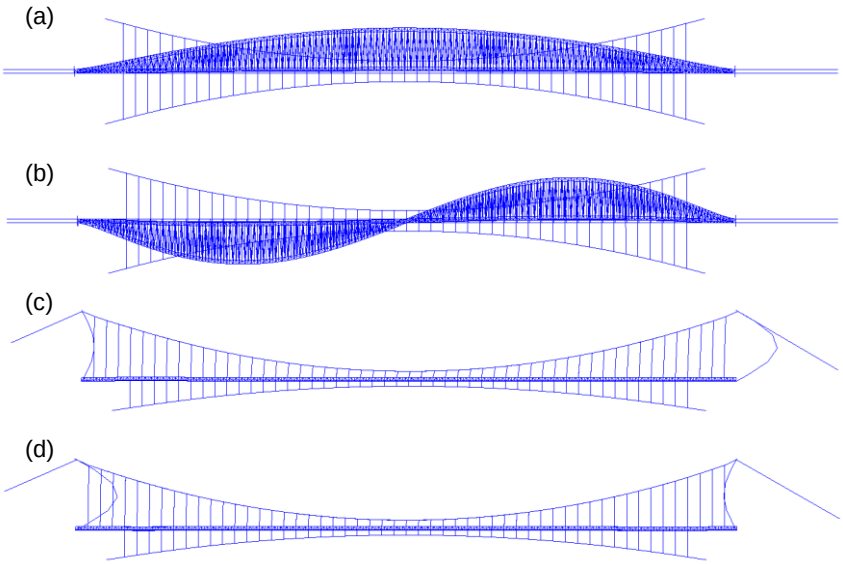

Fig. 4 - Modal diagram of mode shapes with wind cable (a) Mode 1; (b) Mode 2; (c) Mode 3; (d) Mode 4

After considering the influence of wind cables, the first four order natural vibration frequencies and periods are given in Table 2. The first-order natural vibration period is 2.955s, and the frequency is 0.338Hz. Compared with the condition in the absence of wind cables, the natural vibration period is reduced greatly, while the natural vibration frequency is increased greatly. Figure4 shows the first four modes of the suspension bridge with wind cables installed, and their modal characteristics are different from those in the case of no wind cables. The main girder of the first-order natural mode still shows symmetrical transverse bending, but its vibration amplitude is limited by the wind cables, and the amplitude is obviously reduced. Similarly, the second-order natural vibration mode also shows similar characteristics, and the third and fourth- order vibration modes are mainly tower deformation. It can be seen that the installation of wind cables plays an obvious role in suppressing the vibration of the main girder, especially in the transverse direction, the vibration of the main girder is greatly suppressed. It can be predicted that if the angle between the plane where the wind cable is located and the horizontal plane is further reduced, the wind cable will play a greater role in improving the natural vibration characteristics of the main girder.

STATIC CHARACTERISTICS ANALYSIS

(1) Force analysis of main cable

The suspension bridge has two main cables side by side, with a transverse spacing of 1.5m. After the bridge is completed and in operation, the main cable will act as the core bearing component under acting gravity and the live load of oil transmission. Under various load conditions, the internal forces of each unit of the main cables are shown in Figure 5:

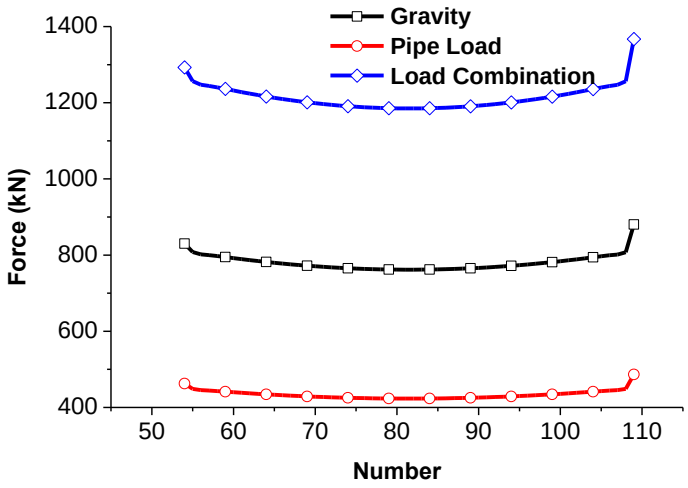

Fig. 5 - Force of main cable

According to Figure 5, during the operation of the bridge, the force of the main cables gradually decreases from the fulcrum to the middle of the span, and the force of Unit 54 and Unit 109 near the fulcrum receive greater internal forces. Under the acting load combination, the internal forces of No. 54 side main cable and No. 109 side main cable are respectively 1293kN and 1367kN, and the different internal forces of the two elements are caused by the different horizontal angles. Among them, the horizontal Angle of Unit 54 is 23.8 degrees, and that of Unit 109 is 29.6 degrees, that is, the greater the degree of inclination, the greater the force. The maximum stress of the main cable is 294MPa, less than the allowable stress σ =1670/3=557MPa, which can meet the strength requirements.

(2) Force analysis of main cable derrick

The suspension bridge has a total of 53 pairs of hanger rods, and the spacing between the hanger rods is 5m. After the completion of the bridge, the tension of the derrick under various load conditions is shown in Figure 6:

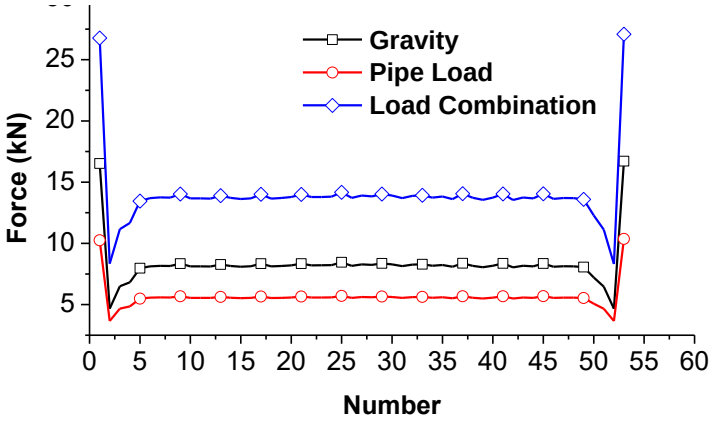

Fig. 6 - Force of derrick

As can be seen from Figure 6, except for the internal forces of No. 1, No. 2, No. 52, and No. 53 derricks on both sides, the internal forces of No. 3 to 51 derricks are relatively uniform. Under the action of load combination, the maximum internal force of the derrick is 27.08kN, and the stress of the derrick is 105MPa, which can meet the strength requirements. In the load combination, the contribution of the structure's dead weight to the internal force of the derrick is 60%, while the crude oil load during operation is only 40%.

(3) Displacement analysis of main girder

The displacing the main beam of the steel truss under the action of gravity, crude oil load and load combination is solved, and the vertical displacement of the lower edge node of the main beam of the steel truss is extracted, as shown in Figure 7:

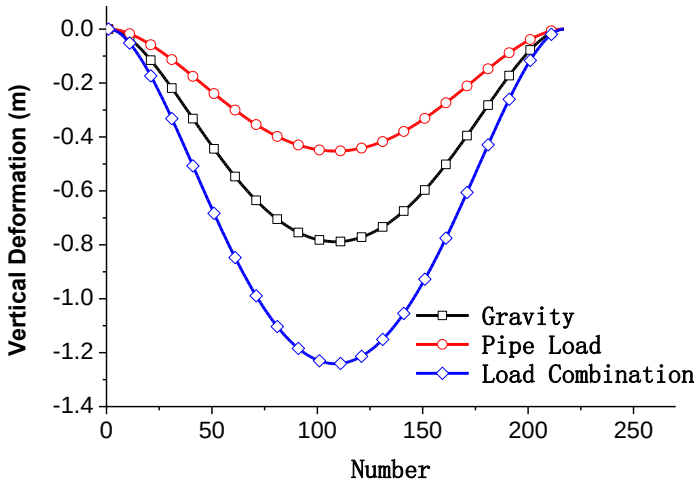

Fig. 7 - Vertical displacement of main girder

It can be seen from Figure 7 the vertical displacement of the main girder under the action of gravity and crude oil is in the form of a parabola. The maximum vertical displacement of the main girder in the middle span under the action of gravity is 0.79m, the maximum vertical displacement under the action of crude oil is 0.45m, and the maximum vertical displacement of the main girder is 1.24m under the load combination. The allowable displacement value of the suspension bridge is L/150=1.8m, and the deformation value of the suspension bridge can meet the requirements.

(4) Strength check of component

The suspension bridge adopts the form of steel structure, which has the advantages of light weight, fast construction and convenient standardization construction. The strength of the main components of the bridge is checked, and the maximum stress of each component is shown in Table 3:

Tab. - 3 Strength check of main components

Component	Stress(MPa)	Allowable strength(MPa)	Check result
Main cable	294	557	Satisfy
Main cable derrick	105	557	Satisfy
Wind cable	212	557	Satisfy
Pipe	20	120	Satisfy
Main girder	149	175	Satisfy
Tower	-28	175	Satisfy

Note: positive stress means tensile stress, negative stress means compressive stress.

As can be seen from Table 3, the stress value of the main cable of the suspension bridge is the largest, which is 294MPa. The maximum stress generated by other major components can meet strength requirements, which can ensure its safe use [8-10].

CONCLUSION

In this paper, a suspension bridge with wind cables is analyzed, mainly including dynamic and static characteristics analysis, and the conclusions are as follows:

(1) Without wind cables, the first-order natural vibration period of the suspension bridge is 14.912s, and the frequency is 0.067Hz. The natural vibration mode is first displayed as transverse vibration, indicating that it is more affected by transverse wind load; with wind cables, the first-order natural vibration period of the suspension bridge is 2.955s, and the frequency is 0.338Hz, and the transverse vibration is greatly improved.

(2) Under the influence each load, the force of the main cable element gradually decreases from the two fulcrum points to the middle of the span, and the force received by the main cable elements on both sides is the largest, and the internal force is related to the degree of horizontal tilt. For the derricks, except the units near the fulcrum, the internal force distribution of the remaining derricks is relatively uniform.

(3) Under acting each load, the vertical displacement of the main girder of the steel truss presents a parabolic distribution. Under acting load combination, the maximum mid-span displacement value is 1.24m, which meets the requirements of deformation permission.

(4) After checking the strength of the main components, the stress can meet the requirements of the allowed strength, which can ensure the safe of the structure.

ACKNOWLEDGEMENTS

This paper is supported by the Anyang Science and Technology Plan Project (2020) (grant number: 251) and Anyang Institute of Technology Research and Cultivation Fund (grant number: YPY2020021).

REFERENCES

[1] LI Deyin, 1996. Real Bridge Test of 720m Suspension Pipeline Bridge over Dnieper River. Foreign Bridges. vol.01:7-9.

[2] Chen Chong, Hou Yue, Jiao Quan, Su Junwei, Zhang Shimin, 2018. Stress Analysis of Large Span Oil and Gas Pipeline of Suspension Bridge under Wind Load. Pipeline Technology and Equipment, vol.01:45-50.

[3] Wang Lei, Yue Sanqi, Zhao Zhichao, 2020. Calculation and analysis of bearing capacity of suspension bridge of long distance natural gas transmission pipeline. Engineering Construction, vol.52(03):23-27.

[4] Wang Yongzhen, Huo Sitong, Zeng Weiguo, Lin Nan, Ju Meng, 2021. Structural Safety Analysis of Suspension Bridge Based on Scaling Model. Oil-Gas Field Surface Engineering, vol.40(01):13-17+24.

[5] Wang Lifeng, Sun Yong, Wang Ziqiang, 2010. Comparative analysis of dynamic characteristics of self-anchored suspension bridge and ground anchored suspension bridge. Chinese and foreign highways, vol. 4:156-159.

[6] Zhang Jie. Structural Safety Analysis of Large Span Suspension Pipeline. Chongqing: Chongqing University, 2008.

[7] Huang Lihua, Li Bing, Lei Gang, Shi Dongdong, 2010. Analysis of Dynamic Characteristics of Long Span Suspension Pipeline Bridge. Industrial Building, vol.S1:271-273+348.

[8] Yin Shutao. Study on Wind-induced Response of Long-span Pipe Suspension Bridge. Dalian, Dalian University of Technology, 2010.

[9] LI Bing. Static, Dynamic and Buffeting Analysis of Suspension Pipe Bridge. Dalian, Dalian University of Technology, 2010.

[10] Ni Yuewu, Zhang Xinyu, Tian Yu, 2010. Test and Evaluation Analysis of a Pipeline Bridge. World Bridge, vol. 03:74-77.

CIVIL ENGINEERING JOURNAL

Article no. 44

THE CIVIL ENGINEERING JOURNAL 2-2021

STUDY ON THE DESIGN OF HEATING AND ENERGY SAVING OF ENCLOSURE STRUCTURE OF RURAL SELF-BUILT HOUSES

Weixian Chang[1] and Hui Dong[2]

1. *Shangluo Vocational and Technical College, Shangluo, Shaanxi 726000, China; changche3483@yeah.net*
2. *Forestry College of Inner Mongolia Agricultural University, Hohhot, Inner Mongolia 010051, China*

ABSTRACT

For severe cold areas, indoor heating in winter is very important, and it is also important to achieve energy saving and emission reduction in the heating process. This paper briefly introduced a kind of heating envelope structure, the geothermal energy-based phase change wall, and analyzed two rural self-built houses in Shangluo city, Shaanxi province. One self-built house was built without the phase change wall, and the other was built with the geothermal energy-based phase change wall by the municipal government. The results showed that the self-built house that adopted the phase change wall had a better heat preservation effect and relieved the indoor temperature fluctuation; after the heating equipment was turned on, the self-built house that adopted the geothermal energy-based phase change wall had a higher and more stable indoor temperature, and the power consumption during the experiment was less.

KEYWORDS

Self-built house, Heating, Enclosure structure, Phase change wall

INTRODUCTION

The rapid development of the economy promotes the further development of cities and also drives the development of rural areas under the radiation of economic development, making rural areas develop in the direction of urbanization [1]. The acceleration of rural urbanization is not only reflected in the increase of the types of goods that can be purchased but also in the design of buildings. Different from the commercial housing series built by various real estate developers in big cities, rural houses are usually built on the homestead by the construction team, according to the experience. Although rural houses can meet the conventional living needs, the energy-saving need is usually not considered [2]. In the face of high temperatures in summer and low temperatures in winter, in order to make the living environment more comfortable, self-built housing residents will use equipment such as an air conditioner to adjust the indoor temperature environment. Air conditioning equipment will consume energy in the process of use, which is not conducive to sustainable development. Therefore, self-built houses not only need to meet the needs of conventional comfortable living but also meet the needs of energy-saving. Taking winter heating as an example, heating energy consumption accounts for a considerable proportion of building energy consumption. Part of the building heat comes from solar radiation, but the sunshine intensity in winter is relatively low, and the time is limited. Additional heat that comes from coal stoves, air conditioners, heating

radiators, etc. is needed to meet indoor comfort [3]. However, the above equipment will consume a lot of energy in the process of use, and the use of coal stoves is dangerous; moreover, reducing the use of heating equipment for the sake of energy consumption will reduce the indoor comfort. A good solution to the above situations is to improve the material and structure of the enclosure to enhance the heat insulation capacity, reduce the loss of indoor heat, and maintain the stability of comfort under low energy consumption. Petrichenko et al. [4] defined the influence of external temperature fluctuation on the temperature of the enclosure structure, gave a selection of the best energy-saving heating system, defined the thickness of the penetrating layer of the temperature wave, and solved and analyzed the Fourier differential equation of solid heat conduction process. Feng et al. [5] analyzed the influence of thermal characteristics of the enclosure structure on the indoor thermal environment and building thermal stability, evaluated the practicability of existing energy-saving methods of building envelope from the aspects of energy-saving effect, safety, reliability, practicability, and economy, and proposed the climatic-suitable thermal design and structure type of the envelope. Kong et al. [6] proposed a coupling strategy of hourly computational fluid dynamics simulation of indoor airflow and dynamic building energy simulation of heat transfer of the building envelope based on real-time information exchange and carried out a joint simulation of an office room with a ventilating and radiant floor cooling system. The results showed that the dynamic heat transfer characteristics of the outdoor wall and indoor air changed with the change of outdoor weather conditions. This paper briefly introduced a geothermal energy-based phase change wall heating envelope and analyzed two rural self-built houses in Shangluo city, Shaanxi province, China. One was built by villagers without the phase change wall, and the other was built with the geothermal energy-based phase change wall by the municipal government.

THE GEOTHERMAL ENERGY-BASED PHASE CHANGE WALL HEATING ENVELOPE

Compared with the commercial houses with unified specifications on different floors built by real estate developers in cities, most of the houses in rural areas are self-built. The building style of self-built houses is decided by the residents themselves, which is relatively free. However, in the process of construction, the construction workers generally will not get more scientific guidance, and the construction will be carried out according to the past construction experience. Self-built houses can meet conventional living needs, but there is no strict requirement for energy saving [7]. In the low-temperature environment in winter, the indoor residents need enough heating to maintain the indoor temperature and comfort. The most basic heating comes from sunlight, but the sunshine time is short in winter. Even if the building orientation is adjusted to receive the light as much as possible, it is difficult to maintain the whole-day heating. In order to maintain the indoor temperature, in addition to sunshine, additional heat sources are needed for heating. The relatively primitive way is to obtain heat by burning wood or fossil fuel, but this kind of heating method is dangerous in relatively closed rooms. With the popularization of electric power, relatively safer electric heating (electric furnace, air conditioner, etc.) has been gradually applied in winter, but the consumption of electric power will also increase the consumption of fossil energy, which is not conducive to sustainable development [8]. In order to achieve energy-saving and emission reduction in the process of building heating, we can start from supplying heat and preserving heat. In the aspect of supplying heat, we can upgrade the technology of heating equipment, including improving the efficiency of electric heating conversion and the intelligent level of operation. In short, the purpose is to provide enough heating with as little energy consumption as possible or use clean energy for heating. Preserving heat should focus on the structure and materials of the building, i.e., enhancing the heat insulation of the building envelope to reduce the indoor heat loss and ensure limited heat to maintain a comfortable temperature as long as possible. This paper mainly analyzed the design of the building envelope in heating energy saving.

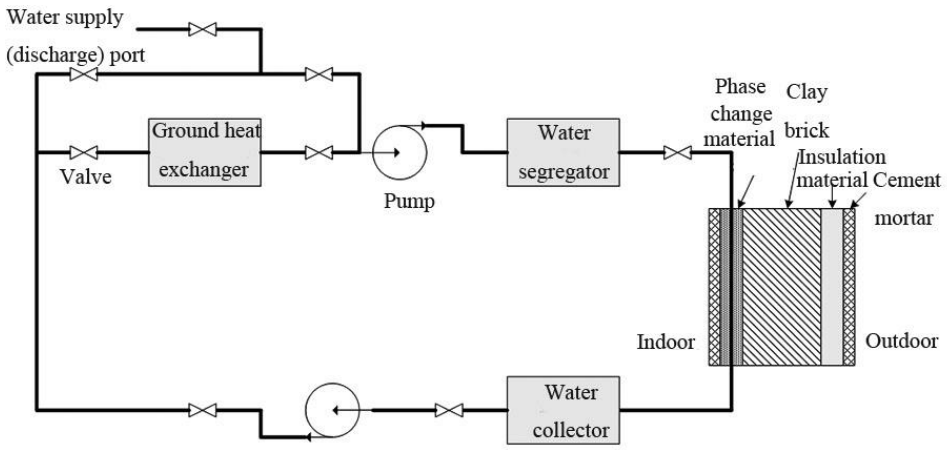

Fig. 1 – The basic structure of the geothermal energy-based phase change wall system

The envelope structure of a self-built house includes a roof, doors, windows, and walls. The wall has the largest contact area with the external environment; therefore, the overall thermal insulation of the building can be improved by strengthening the thermal insulation performance of the wall. In recent years, the improvement of building materials has improved the thermal insulation performance of walls. This study improved the thermal insulation performance of walls from the perspective of the structure. The traditional wall structure from the outside to the inside is cement mortar, brick, cement mortar, and lime [9]. In this study, phase change materials were used to improve the structure of the traditional wall. The improved phase change wall structure and the auxiliary heating system are shown in Figure 1. The basic structure of the phase change wall includes the cement mortar layer, the insulation material layer, the clay brick layer, the phase change layer [10], and the cement mortar layer. The main function of the cement mortar layer is to protect the internal materials of the wall. The function of the insulation material layer is to use the thermal insulation performance of the insulation material to reduce the heat loss in the phase change material and clay brick. Clay brick is the main structure of the wall. The phase change material of the phase change material layer is an important part of the phase change wall to improve the insulation performance. Compared with conventional materials, the phase change material has more excellent latent heat storage performance, i.e., it can store more heat. When the indoor temperature decreases, the heat stored by phase change materials will radiate to the room as much as possible under the barrier of insulation materials.

In order to further improve the heating energy-saving effect of phase change walls, this study combined geothermal energy with phase change walls. Figure 1 shows the basic structure after the combination. Its basic principle is to realize the heat exchange between the phase change material and the ground through the water flowing in the pipeline buried in the phase change material layer [11]. Taking winter heating as an example, in the daytime, the heat in the room comes from solar radiation, and part of the heat will be absorbed by the phase change material in the phase change wall. In addition, the medium water heated by the ground heat exchanger will pass through the pipe buried in the phase change material layer by the water distributor. After the phase change material absorbs the heat, the temperature will rise. When it reaches the melting point, it will melt to absorb heat, thereby storing geothermal energy. After the heat is absorbed by the phase change material, the medium water flows back to the ground heat exchanger through the water collector for heating. Due to the absence of solar radiation at night, the ambient temperature decreases, and the phase change material in the phase change wall will release the stored heat. Due to the barrier of the insulation layer, most of the heat will be transferred indoors to maintain the indoor temperature

stability [12]. In addition, a temperature sensor can be set in the water outlet or phase change layer of the phase change wall. When the temperature of the phase change material is lower than the threshold, the ground heat exchanger will be turned on again, and the phase change wall will be heated by medium water. However, the phase change material can absorb more latent heat by virtue of the phase change properties, i.e., it can store more heat, which can reduce the continuous start-up time of the ground heat exchanger and further reduce energy consumption.

CASE ANALYSIS

Case overview

The rural self-built houses analyzed in this paper are located in Shangluo city, Shaanxi province, China. Shaanxi Province is located in the middle of China and the middle reaches of the Yellow River. The overall terrain is high in the south and north and low in the middle, with various types of landforms. In terms of climate, Shaanxi is divided into three climatic zones: subtropical climate, warm temperate climate, and middle temperate climate from south to north [13]. On the whole, it is dry and rainless in spring, hot and rainy in summer, cool and humid in autumn, and cold and dry in winter. Shangluo city is located in the southeast of Shaanxi province and at the southern foot of Qinling Mountains and the junction of Hubei and Henan provinces. Figure 2 shows the rural self-built house for example analysis in this paper. The right picture is the self-built house built by Shangluo villagers, without adding a special thermal insulation structure, and it is a conventional enclosure structure. The left picture is the self-built house designed and planned by Shangluo municipal government, whose enclosure structure adopted the geothermal energy-based phase change wall mentioned above. The floor area and configuration of the two self-built houses used for case analysis were nearly the same. The two self-built houses were located about 1 km apart; thus, they were regarded as in the same weather environment.

(a) A self-built house designed and built by Shangluo municipal government

(b) A self-built house built by villagers in Shangluo

Fig. 2 – The rural self-built houses in Shangluo city

Related equipment parameters

Water - water-source heat pump main unit: there were three units; the rated heat capacity was 54 kW, the heating input power was 7.6 kW, the rated cooling water flow rate was 7.5 m^3/h, the rated refrigerant water flow rate was 12.3 m^3/h, and the heat pump supply and return water temperature under heating condition was 45/40 ℃.

Ground heat exchanger: the ground pipe was a single U-shaped aluminum-plastic composite pipe [14], with a diameter of 25 mm and a length of 2.3 m; the water demand of the ground pipe was 37.52 m^3/h; the pipe was embedded in parallel [15], with a borehole depth of 65 m, a bore diameter of 100 mm, and a distance of 2.5 m between the boreholes; there were 35 boreholes.

Circulating water pump: there were four circulating water pumps; the flow rate was 12 m^3/h, the lift was 25 m, the rotational speed was 3000 r/min, and the power was 2.0 kW.

The doors and windows of the self-built house (a) and the self-built house (b) faced south. In terms of enclosure structure, except for the east and west walls, the materials and structural parameters of the two buildings were the same. The difference in the east and west walls between the two self-built houses was that the east and west walls of the self-built house (a) designed and built by the government were geothermal energy-based phase change walls, but the east and west walls of the self-built house (b) built by villagers were conventional structures. From the outside to the inside, the east and west walls of the self-built house (b) were composed of a cement mortar layer (5 mm thick), an insulation layer (50 mm thick), a red clay brick layer (300 mm thick), and a cement mortar layer (5 mm thick). From the outside to the inside, the east and west walls of the self-built house (a) were composed of a cement mortar layer (5 mm thick), an insulation layer (50 mm thick), a red clay brick layer (270 mm thick), a phase change layer (30 mm thick), and a cement mortar layer (5 mm thick); the phase change material was paraffin. The thermal conductivity of cement mortar, benzene board, red clay brick, paraffin in the solid state, and paraffin in the liquid state was 0.93 W/(m·K), 0.05 W/(m·K), 0.81 W/(m·K), 0.18 W/(m·K), and 0.14 W/(m·K), respectively.

Experimental methods

The two-self built houses had the same floor area, and the structural parameters of the internal rooms are nearly the same. The basic structure of the first floor of the two houses is shown in Figure 3, including a living room, a master bedroom, a secondary bedroom, a toilet, a dining room, and a kitchen. The first floor of the self-built house had a total length of 9.6 m, a width of 8.1 m, and a height of 3.0 m. The door of the living room faced south. The east and west walls of the self-built house designed by the Shangluo municipal government were the phase change walls designed in this study, and the other envelope structures were conventional. The envelope structures of the self-built house built by villagers were also conventional.

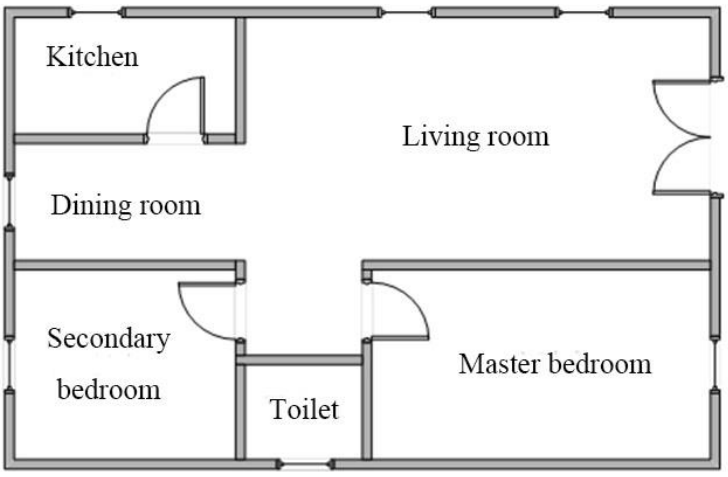

Fig. 3 – The basic structure of the first floor of two self-built houses

In this study, the energy-saving design of the self-built house with a phase change wall enclosure structure was analyzed. The indoor temperature stability and overall heating consumption in the self-built house with a phase change wall enclosure structure were compared with the traditional self-built house without phase change walls. The specific method is as follows. Temperature sensors were set every 0.6 m on the wall of the room and also set outside the room to collect the indoor and outdoor temperature changes. The resolution of the temperature sensor was 0.01 ℃, and the range was - 35 ℃ ~ 80 ℃. The electricity consumption of the two self-built houses was detected by an electricity meter.

Test item ①: when the self-built house with phase change walls did not turn on the water source heat pump host, the temperature sensors collected the indoor and outdoor temperature changes of the two self-built houses in two weeks, and the temperature changes of the self-built house in one day were reflected by the average temperature value at the same time of each day in two weeks.

Test item ②: the water-source heat pump host of the self-built house with phase change walls was turned on, and the two self-built houses used the central air conditioner with the same specifications and parameters to assist heating. The temperature sensors collected the indoor and outdoor temperature changes of the two self-built houses in two weeks, and the average temperature at the same time of each day in two weeks was used to reflect the temperature changes of the self-built houses in one day. In addition, the accumulated power consumption of the two self-built houses in two weeks was detected by an electricity meter.

Experimental results

In order to verify the thermal insulation performance of phase change walls, the two self-built houses did not use heating equipment such as geothermal and air conditioners in the two-week experiment but used natural light as the only heat source. The final results are shown in Figure 4. Within one day, the outdoor temperature showed a downward trend in the period of 0-8 o'clock, an upward trend in the period of 8-14 o'clock, and a downward trend again in the period of 14-24 o'clock. The minimum outdoor temperature was 6 ℃, and the maximum outdoor temperature was 12 ℃within one day. The temperature change trends of the self-built houses designed by the villagers and the municipal government in one day were consistent with that of the outdoor. The reason for the above result was that the heating only depended on the light and was greatly affected by the external temperature. The temperature change in the self-built house built by villagers was closer to the outdoor temperature change, but the envelope had an insulation property; thus, the indoor temperature was slightly higher than the outdoor temperature. The difference between the temperature in the self-built house designed by the municipal government and the outdoor temperature was larger, and the temperature dropped more slowly in the period of temperature drop, which was because the latent heat absorbed and stored by the phase change material in the phase change wall was released at night when the indoor temperature decreased to slow down the decrease of temperature.

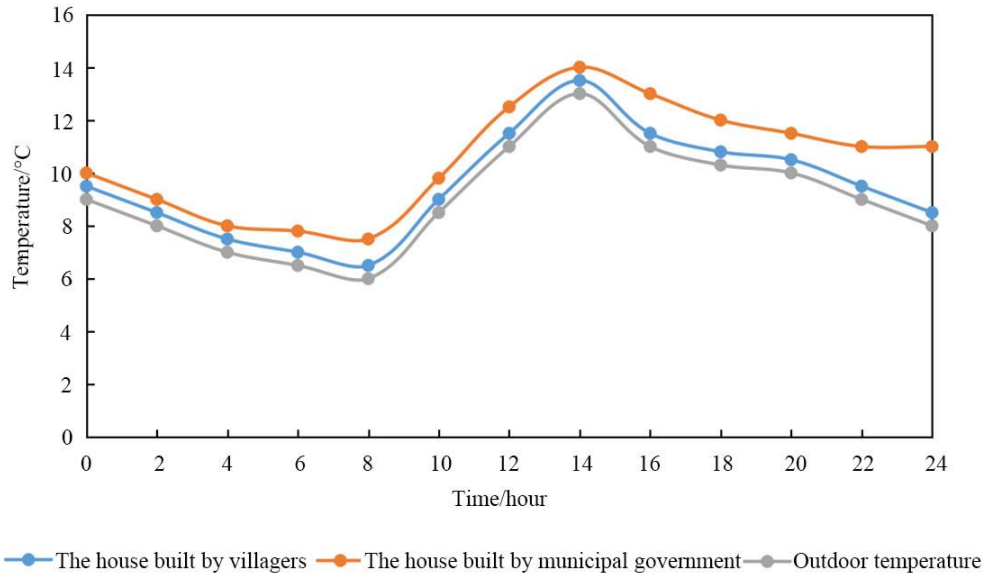

Fig. 4 – Temperature changes inside and outside two self-built houses without geothermal and air conditioner heating in one day

In order to verify the heating performance of the geothermal energy-based phase change walls, two self-built houses turned on heating equipment such as geothermal and air conditioner in the two-week experiment, and the changes of indoor and outdoor temperatures in one day are shown in Figure 5. It was seen from Figure 5 that the outdoor temperature showed a downward trend in the period of 0-8 o'clock, an upward trend in the period of 8-14 o'clock, and a downward trend in the period of 14-24 o'clock. After using the heating equipment, the indoor temperature of the two self-built houses was significantly higher than the outdoor temperature, and the indoor temperature change within one day was more stable than the outside temperature change. In addition, the comparison of the indoor temperature changes of the two self-built houses showed that the self-built house with geothermal energy-based phase change walls had a higher temperature and more stable temperature changes. The reason for the above result was that the phase change material in the phase change wall had good heat storage performance, which stored the excess heat and released it to reduce the indoor temperature fluctuation and the external heat loss; the self-built house without phase change walls lost more heat because of the limited thermal insulation capacity even if there was an air conditioner for heating, resulting in significant temperature fluctuations and lower overall temperature.

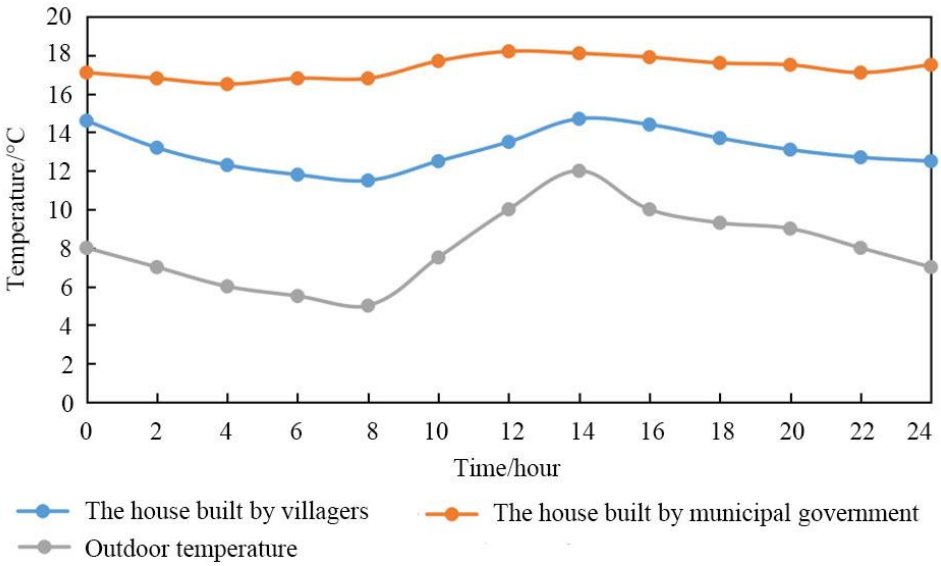

Fig. 5 – Temperature changes inside and outside two self-built houses with geothermal and air conditioner heating in one day

In order to test the heating energy-saving effect of the geothermal energy-based phase change wall as an enclosure structure, the power consumption of two self-built houses using heating equipment in two weeks was compared, and the results are shown in Figure 6. The power consumption of self-built houses without phase change walls was 2556.4 kWh in the two weeks, and that of the house with phase change walls was 1544.2 kWh in the two weeks. It was seen from the comparison that the power consumption of the self-built house with phase change walls was significantly smaller than that of the self-built house without phase change walls. The reason for the above result is as follows. The phase change material of phase change walls provided better thermal insulation performance, thus reducing the frequency of indoor active heating. In addition, the phase change wall was combined with geothermal energy in this study; thus, the heat stored and released in the phase change material of the phase change wall was not only from daylight but also from geothermal energy. The power consumed in this process mainly came from the circulating pump and control equipment. The self-built house without phase change walls had poor thermal insulation performance; thus, it needed more heating to maintain the stability of indoor temperature, and the operation of the air conditioner consumed power.

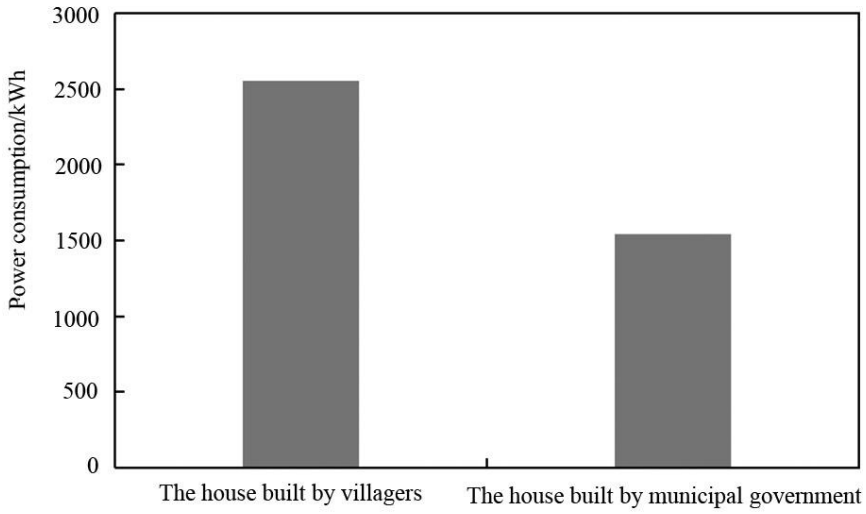

Fig. 6 – Power consumption of two self-built houses with geothermal or air conditioner heating in two weeks

CONCLUSION

This paper briefly introduced a geothermal energy-based phase change wall heating envelope and analyzed two rural self-built houses in Shangluo city, Shaanxi province, China. One self-built house was built by villagers, without phase change walls, and the other was built by a municipal government, with geothermal energy-based phase change walls. The final test results are as follows. (1) Under the premise of not using the heating equipment, the temperature change trend of the two self-built houses in one day was similar to that of the outdoor, but the indoor temperatures in the two houses were higher than the outdoor temperature, among which the indoor temperature of the self-built houses built by the municipal government was higher and changed more slowly. (2) After the heating equipment was turned on, the temperature changes of the two self-built houses tended to be stable, and the temperature of the two buildings was significantly higher than the outdoor temperature; the temperature in the self-built house built by the municipal government was higher and changed more stably. (3) After a two-week operation of the heating equipment, the power consumption of the self-built house built by the municipal government was significantly lower than that of the house built by villagers.

ACKNOWLEDGMENT

This study was supported by Shangluo City Science and Technology Plan Project 2020-Z-0002 “Shangluo City Rural Ecological Agriculture Planning and Design Technology Research under the Rural Revitalization Strategy”.

REFERENCES

[1] Woodson R., 2015. Radiant Floor Heating, Second Edition. JAMA: The Journal of the American Medical Association, vol. 313: 93-94

[2] Yang E., 2015. Research on Control Property of Low-Temperature Floor Radiant Heating System. Open Construction & Building Technology Journal, vol. 9: 311-315

[3] Kim S.H., Chung K.S., Kim Y.I., 2015. Thermal Comfort Range of Radiant Floor Heating System by Residential Style. Transactions of the Korea Society of Geothermal Energy Engineers, vol. 11: 7-14

[4] Petrichenko M., Tarasova D., Nemova D., 2015. Unsteady Temperature Condition of the Enclosure Structure. Applied Mechanics & Materials, vol. 725-726: 57-62
[5] Feng Y., Nan Y., Zhong H., 2017. Energy-saving and thermal design of the nontransparent enclosure structure for the buildings in southern China. Journal of Civil, Architectural & Environmental Engineering, vol. 39: 33-39
[6] Kong Q.X., Feng J., Yang C.L., 2017. Numerical Simulation of a Radiant Floor Cooling Office Based on CFD-BES Coupling and FEM. Energy Procedia, vol. 105: 3577-3583
[7] Du Y., 2014. Feasibility Analysis of Radiant Floor Cooling and Heating System Applications. Applied Mechanics and Materials, vol. 716-717: 428-430
[8] Ma H., Li C., Lu W., Zhang Z., Yu S., Du N., 2016. Experimental study of a multi-energy complementary heating system based on a solar-groundwater heat pump unit. Applied Thermal Engineering, vol. 109: 718-726
[9] Yu B.H., Seo B.M., Moon J.W., Lee K.H., 2015. Analysis of the Part Load Ratio Characteristics and Gas Energy Consumption of a Hot Water Boiler in a Residential Building under Korean Climatic Conditions. Korean Journal of Air Conditioning & Refrigeration Engineering, vol. 27
[10] Hong S.K., Cho S.H., 2015. The Experimental Study of the Heat Flux and Energy Consumption on Variable Flow Rate for Secondary Side of DHS. Korean Journal of Air-Conditioning and Refrigeration Engineering, vol. 27: 247-253
[11] Shaw B.H., 2018. Infection in Mental Hospitals, with Special Reference to Floor Treatment. Journal of Mental Science, vol. 69: 24-45
[12] Toyoda S., Fujiwara T., Uchida A., Ihibashi J., 2016. ESR dating of sea-floor hydrothermal barite: contribution of 228Ra to the accumulated dose. Nephron Clinical Practice, vol. 43: 201-206
[13] Barzin R., Chen J.J.J., Young B.R., Farid M.M., 2015. Application of PCM underfloor heating in combination with PCM wallboards for space heating using price based control system. Applied Energy, vol. 148: 39-48